SOME APPLICATIONS OF CAM-CLAY IN NUMERICAL ANALYSIS

By

Heng-Kong TAM

A Thesis submitted for the degree of
Doctor of Philosophy

THE CITY UNIVERSITY

Civil Engineering Department

MAY 1992

TABLE OF CONTENTS

LIST OF TABLES

LIST OF FIGURES

ACKNOWLEDGEMENTS

I am indebted to Professor J.H. Atkinson and Mr. R.I. Woods for the opportunity to join the Geotechnical Engineering Research Centre. The financial assistance provided by the SERC for the initial part of this research is acknowledged. My time in the Centre has opened up for me an infinite source of knowledge in computer applications in soil mechanics. My appreciation is extended to Professor Atkinson for his guidance and encouragement in the course of the research and writing up. My gratitude goes to Dr. S.E. Stallebrass for her critical review and comments on the draft thesis and her help in using the computing facilities in the GERC.

I am grateful particularly to Mr. R.A. Rallings, Executive Engineer Materials, Mr. A.H. Wilson, Deputy Secretary Roads, Roads Division, and Mr. K. Drew, Secretary of the Department of Roads and Transport, Tasmania, Australia for allowing me on sabbatical leave to complete my research.

My thanks also go to Dr. H.K. Mhach for our friendship and many discussions when we both were members of the GERC. Sincere thanks are extended to all the members of the GERC for their tolerance and patience in giving me priority in using the facilities of the GERC, especially Dr. R.N. Taylor for his comments on some aspects of the research. I would also like to thank Dr. W. Powrie, Mr. M.J. Gunn and Mr. R.I. Woods for giving helpful comments, information and suggestion on certain aspects of the research.

I would like to thank my wife, Yin-Ha Tam for her many encouragement and continuing support, without which this thesis would not have been completed.

DECLARATION

I grant powers of discretion to those University Librarian to allow this thesis to be copied in whole or in part without reference to the author. This permission covers only single copies for study purposes, subject to normal contribution of acknowledgement.

ABSTRACT

The research described in this thesis investigated some applications of Cam-clay in numerical analyses. Single element analysis using the program CASIS was conducted to model undrained and drained triaxial compression tests to investigate the relative importance of the critical state soil parameters and stress history on the calculated soil behaviour. The values of these parameters covered the range of most commonly occurring natural soils. The investigation was extended to finite element modelling of plate loading tests using the computer program CRISP to examine the relative importance of the critical state soil parameters and stress history on the calculated undrained plate-soil behaviour. The capability of finite element coupled consolidation analysis of boundary value problems was demonstrated by the simulation of laboratory hydraulic fracturing experiments. The effects of rate of cavity water pressure increase, bore size, confining pressure and overconsolidation ratio on fracturing pressures were examined.

The results of the parametric study of triaxial compression tests and plate loading tests were quantified in terms of stiffness (or tangent modulus), strength (or bearing pressure) and strain (or settlement) at the initial, yield, peak and ultimate states in the stress-strain (or pressure-settlement) response and allowed the comparison of these quantities for changing values of the soil model parameters. The studies revealed that the parameter κ/λ was the most influential because the initial states of soil were dependent on the values of κ and λ and this dependence affected the subsequent stress-strain behaviour. In the prediction of movements of soil structures, the parameters κ, λ and α' are the most influential and their values should be critically evaluated for input in numerical analyses. In prediction of stability, the values of κ, λ and M are the most important ones.

The work showed that the hydraulic fracturing phenomenon can be modelled by finite element coupled consolidation analysis. The computer program CRISP was validated against closed-form solutions and was found to predict the hydraulic fracturing phenomenon with a reasonable degree of accuracy when the results were compared with the experimental data obtained by Mhach (1991). It was found that the rate of cavity water pressure increase had a significant influence in the prediction of fracturing pressure. The confining pressure was an important factor whereas the effects of bore size and overconsolidation ratio had some effects but were not as significant as the first two.

LIST OF SYMBOLS

A, b	soil parameters used in Atkinson and Crabb (1991)
$\mathbf{a}_e$	nodal displacement vector
c_u	cohesion
d	displacement vector at any point in a finite element
d_w	depth of ground water table
e	void ratio
k_x, k_y, k_z	permeability of soil in x, y and z directions
p'	effective mean stress
p_c'	preconsolidation pressure
p_o'	in-situ effective overburden pressure
p_Ω'	effective mean pressure of the omega point
p	total mean stress
p_w	cavity water pressure
q'	deviator stress
q	applied pressure
q_f	ultimate bearing pressure
q_y	bearing pressure immediately after yield
Δr_1	boundary/body force components
Δr_2	boundary flow components
s_u	undrained shear strength
u	pore pressure
u_o	initial steady state pore pressure
δu_w	incremental pore water pressure vector
v	specific volume
v_λ	current value of specific volume equivalent to p' = 1 kPa
v_κ	specific volume of isotropically overconsolidated soil swelled to p' = 1 kPa
v_Ω	specific volume of the omega point
w	water content of soil
B	strain matrix relating nodal displacement and strain
B	diameter of plate for plate loading test
D, D'	constitutive matrix
E, E'	Young's modulus
E_i	initial tangent modulus of the plate-soil system
G^*	shear modulus in stiffness matrix derived by Graham & Houlsby (1983) for a transverse isotropic elastic soil

G, G' shear modulus

G_o initial shear modulus

G_s specific gravity

G_y shear modulus immediately after yield

J modulus coupling shear and volumetric strains in stiffness matrix derived by graham and Houlsby (1983)

K stiffness matrix

K^* bulk modulus in stiffness matrix derived by Graham & Houlsby (1983) for a transverse isotropic elastic soil

K' bulk modulus

K_{nc} K_o during one-dimensional normal consolidation

K_o coefficient of horizontal earth pressure at rest

K_s bulk modulus of the solid phases

K_u bulk modulus of the soil composite

K_y bulk modulus immediately after yield

L relation of pore pressure changes to strain

N shape function

N_c bearing capacity factor

OCR overconsolidation ratio

R nodal force vector

S ratio of the size of the yield surface to the history surface of the three-surface model

T ratio of the size of the history surface to the bounding surface

U_F fracturing pressure

α' elastic parameter = $G'/K' = [3(1-2\nu')]/[2(1+\nu')]$

ϵ_a axial strain

ϵ_r radial strain

ϵ_s shear strain

ϵ_v volumetric strain

ϵ_{sp} plastic shear strain

ϵ_{vp} plastic volumetric strain

σ_a' effective axial stress

σ_c' effective confining pressure

σ_h' effective horizontal stress

σ_r' effective radial stress

σ_v' effective vertical stress

σ_θ' effective hoop stress

σ_1' σ_2' σ_3' effective principal stresses

σ_c	total confining pressure
η'	stress ratio = q'/p'
τ_{xy}	shear stress
ϕ'	effective stress friction angle
ϕ_p'	effective stress friction angle at peak stress
ϕ_b	bore diameter of hydraulic fracturing sample
θ	Lode angle
δ	nodal displacement vector
δ	settlement of plate
δ_y	settlement of plate immediately after yield
δ_f	settlement of plate at failure defined at the intersection of the tangents to the initial and final sections of the pressure-settlement curve
δ_f'	settlement of plate at failure on the pressure-settlement curve at q_f
ν, ν'	Poisson's ratio
ψ	exponent in the hardening modulus for both two-surface and three-surface models
γ	bulk unit weight of soil
γ_w	unit weight of water
λ	slope of the normal compression line in v:ln p' space
κ	slope of a swelling line in v:ln p' space
Γ	specific volume of soil at critical state when p' = 1 kPa
N	specific volume of isotropically normally consolidated soil when p' = 1 kPa
M	critical state frictional coefficient

CHAPTER 1 INTRODUCTION

1.1 Background to the Project

The research described in this thesis investigated the application of Cam-clay in numerical analysis. The critical state family of soil models has been developed since the 1960's at Cambridge University (Roscoe, Schofield and Thurairajah, 1963; Schofield and Wroth, 1968; Roscoe and Burland, 1968). The theoretical concept of the critical state soil models has received wide acceptance and has been successfully implemented in finite element programs (Simpson, 1973; Naylor, 1975; Gunn and Britto, 1982, 1984; Britto and Gunn, 1987). Various modifications of the Cam-clay model have been suggested and they have been expanded within the framework of critical state theory (Roscoe and Burland, 1968, Atkinson and Bransby, 1978 and Schofield, 1980). The critical state soil models are characterised by a few fundamental soil parameters, the values of which will affect the prediction of soil behaviour in a numerical analysis. Very little fundamental research has been conducted to examine the effects of the variation of these soil model parameters on the predicted soil behaviour so it is important to extend the knowledge in this area.

In a site investigation programme, an engineer may face the difficulty of selecting only a limited amount of soil testing owing to the constraint of funds and techniques and so he has to decide which fundamental soil parameters are more critical and important in analysing the particular problem. Some of these parameters cannot be easily measured. When he understands the relative importance of the fundamental soil parameters in the prediction of the concerned behaviour parameters, he can concentrate his limited resources to evaluate them.

The first part of the research reported in this thesis was a parametric study of undrained and drained triaxial compression tests because these tests are the most common ones from which stiffness and strength of soil are derived. The dependence of the undrained and drained behaviour on the fundamental soil parameters was evaluated and provided guidelines of relative importance of these soil parameters in the prediction of the undrained and drained soil behaviour.

In the second part, the parametric study was extended to numerical modelling of plate loading tests and provided the same guidelines of relative importance of the fundamental soil parameters, stress history and depth of ground water table in the prediction of undrained plate-soil behaviour.

Undrained and drained behaviour are considered as the extreme conditions in the analysis of most categories of problems in geotechnical engineering but often loading and drainage occur at the same time. The failure of some old dams in U.K. is attributed to the hydraulic fracturing of clay cores during rapid rise of reservoir level and this is considered as one of the events in which coupled loading and drainage occur. A laboratory investigation of the hydraulic fracturing phenomenon on puddle clay was carried out and reported in Mhach (1991) and a numerical simulation was carried out to extend the understanding of soil behaviour in a fracturing test.

The third part of the numerical parametric study examined the effects of rate of cavity water pressure increase, confining pressure, cavity size and overconsolidation ratio on the predicted fracturing pressures. The program CRISP was validated against closed-form solutions of undrained cavity expansion. These numerical studies were useful to understand the stress and pore pressure distributions within the test samples and helped to understand the soil behaviour in the fracturing phenomenon.

1.2 Numerical Analyses in Geotechnical Engineering

Numerical analysis is a versatile tool to obtain solutions for boundary value problems in which there may not be any closed-form solutions. There are a number of different categories of numerical methods including the finite difference method, finite element method and boundary element method. The finite element method is one of the most common numerical methods used by researchers, engineers and scientists and the finite element programs are often implemented with constitutive models to describe material non-linear behaviour. The constitutive relations of the critical state soil models can be formulated and implemented in a relatively short computer program to

calculate the stress-strain behaviour for soil in a single element analysis following a pre-determined stress path. These constitutive relations can also be implemented into finite element codes so that soil behaviour in boundary value problems can be predicted.

It is recognised that coupled loading and drainage problems are an important category of analysis but there is comparatively very little published literature on coupled consolidation analysis of boundary value problems. This was due to the inaccessibility of computer hardware and software in the past but with the recent development and advances in these two aspects, finite element analysis can now be run on desk-top micro-computers. Computer programs incorporating both critical state soil models and Biot's fully coupled consolidation theory (Biot, 1941) are now available.

With the availability and easier accessibility of the computing facilities, numerical analysis has now become a more common tool to extend knowledge in understanding soil behaviour by performing numerical experiments. The research described in this thesis used the numerical analyses to perform parametric studies as discussed in Section 1.1 and the methods used to evaluate the coupling effects of the soil behaviour with the fundamental parameters are described in Section 1.4. Before finite element modelling can be applied successfully and give sensible and correct answers, the programs and the finite element mesh discretisation require validation against closed-form theoretical solutions and physical observation in the laboratory and in the field.

1.3 Objectives of the Research

The objectives of the research reported in this thesis were as follows:

- To investigate the variations of the calculated soil behaviour predicted by the original Cam-clay model. The parametric study examined the behaviour of an element of soil following an undrained or drained triaxial compression loading path with changing values of the soil model parameters covering the full range of values

for the most commonly occurring soils. The purpose of the work was to provide guidelines for the relative importance of fundamental soil parameters and to indicate which were the most influential in the prediction of stiffness and strength.

- To investigate the variations of the undrained plate-soil behaviour of plate loading tests by the finite element simulation using the original Cam-clay model. The purpose of the parametric study was to provide guidelines of the relative importance of the fundamental soil parameters and to indicate which were the most influential in the prediction of the plate-soil behaviour.

- To investigate the coupled consolidation behaviour during hydraulic fracturing of a triaxial specimen which was subjected to internal cavity water pressure increase causing fracturing of the sample. The modified Cam-clay model was used. The purpose of the work was to demonstrate that the laboratory hydraulic fracturing phenomenon can be modelled by the finite element simulation and the hydraulic fracturing pressure can be predicted after a fracturing criterion was established. The parametric study examined the effects of rate of cavity water pressure increase, bore size, confining pressure and overconsolidation ratio on the predicted fracturing pressures.

1.4 Methods Used in the Research

The research described in this thesis used the theory of critical state soil mechanics to model the behaviour of soil under loading, together with Biot's fully coupled consolidation theory to evaluate the soil behaviour under combined loading and drainage conditions. The original Cam-clay model (Schofield and Wroth, 1968) was used for the parametric studies of triaxial compression tests and plate loading tests. The modified Cam-clay model (Roscoe and Burland, 1968) was used for the numerical analysis of hydraulic fracturing in a triaxial sample because there have been successful applications of these models in numerical modelling (e.g. Wroth, 1977; Almeida, 1984).

In the first part of the parametric study, computations following the undrained and drained triaxial compression loading paths in a single element analysis were performed using the computer program CASIS developed for this research. The stress-strain response was considered to describe the soil behaviour and was characterised by different states. The stress-strain response was calculated by the program following a pre-determined stress path. In the second part on the parametric study of plate loading tests on Cam-clay and in the third part of the research on the numerical investigation of the hydraulic fracturing phenomenon, the finite element program CRISP was used to perform a finite element modelling and simulation of the phenomena. Detailed description of these programs is given in Chapter 4. The computation results were analysed using the basic theory of critical soil mechanics described in Chapter 2.

1.5 Outline of This Thesis

In the following chapters, applications of Cam-clay in parametric studies of undrained and drained triaxial compression tests, laboratory hydraulic fracturing and plate loading tests are presented.

In Chapter 2, the basic theories of soil mechanics, critical state soil models and the application of the finite element method in the solutions for effective stresses and pore pressures, non-linear behaviour and coupled events will be presented. Chapter 3 reviews the published literature on numerical analyses, with particular reference to those covering the applications of the critical state soil mechanics. In Chapter 4, the hardware and software used in the research described in this thesis are described.

Chapter 5 presents a numerical parametric study of soil behaviour in conventional undrained and drained triaxial compression tests using the original Cam-clay model. The variations of calculated soil behaviour with changing values of the soil model parameters are presented. It summarises the relative importance of the fundamental soil parameters and stress history in the prediction of undrained and drained behaviour in terms of stiffness, strength and strain. Chapter 6 describes the finite element simulations of the laboratory hydraulic

fracturing experiments and the investigation of the effects of rate of cavity water pressure increase, bore or cavity sizes, confining pressures and overconsolidation ratios in the prediction of fracturing pressures for puddle clay.

In Chapter 7, a numerical modelling of plate loading tests using the Cam-clay model to study the undrained plate-soil behaviour is described. The variations of the calculated soil behaviour with changing values of the soil model parameters are presented. It summarises the relative importance of the fundamental soil parameters, stress history and depth of ground water table in the prediction of the undrained behaviour of the plate-soil system. The main points of this thesis are summarised in Chapter 8.

CHAPTER 2 BASIC THEORIES

2.1 Introduction

Critical state soil models have been implemented in finite element computer programs for prediction of soil behaviour in geotechnical engineering problems covering a broad area in numerical modelling in soil mechanics and foundation engineering. The method involves calculating stresses and displacements within a soil domain subjected to an applied loading, a change in effective stress, or a displacement at the boundary of the domain using the finite element procedure with critical state soil mechanics models describing the soil behaviour. This Chapter describes the basic theories of soil mechanics, critical state models and the application of the finite element method in the solutions for effective stresses and pore pressures, non-linear behaviour and coupled events. Soil behaviour has been examined within the framework described in Critical State Soil Mechanics (Atkinson and Bransby, 1978).

2.2 Soil Behaviour and Critical State Soil Mechanics

Saturated soil is a two-phase continuum consisting of solid particles and water in the pores. Soil behaviour is governed by effective stresses which are defined by

$$\sigma' = \sigma - u \tag{2.1}$$

$$\tau' = \tau \tag{2.2}$$

where σ and τ are any total normal and shear stresses, u is the pore water pressure.

Terzaghi's principle of effective stress states that all measurable effects of a change in stress in soils, such as compression, distortion, or a change in shearing resistance, are due to changes in effective stresses. Thus changing the pore water pressure and normal total stresses by equal amounts produces no strains.

Soil particles are usually considered rigid. Each particle is in physical contact with some of its neighbouring grains to form a skeletal, cellular framework. The range of possible particle sizes is large: clay particles have a typical dimension of less than 2 μm whereas coarse gravel has a typical dimension up to 60 mm. The range of particle shapes is also great: clay particles are often flat and plate-like whereas sand and gravel are more likely to be sub-spherical. For a given soil type, there could be a range of particle sizes and shapes in it. Its strength and deformation properties depend on the packing of these soil particles, the voids and some other parameters to be explored in this research.

A soil derives its strength from friction and dilation of the soil grains. Its stiffness depends on the effective stress level and relative compactness of the packing of the soil particles and voids. The past history of the soil deposit is expected to be reflected in its present structure and the present structure will control the future response. When there is an increase in effective stresses in a soil element, the soil particles and the voids rearrange in position. The soil composite is compressed if drainage is permitted. The void ratio reduces with an increase in effective stress but the rate slows down with further increases in effective stress. The compression line (and swelling line) is idealised as a straight line in the specific volume versus logarithmic stress plot in Fig. 2.1.

The state of soil may be described fully by the stresses acting on it and by its specific volume v. The critical state soil model was formulated in terms of the stress invariants p' and q'. For general states of stress, p' and q' are defined as

$$p' = \frac{1}{3}(\sigma_1' + \sigma_2' + \sigma_3') \tag{2.3}$$

$$q' = \frac{1}{\sqrt{2}}[(\sigma_1' - \sigma_2')^2 + (\sigma_2' - \sigma_3')^2 + (\sigma_3' - \sigma_1')^2]^{1/2} \tag{2.4}$$

where σ_1', σ_2' and σ_3' are the effective principal stresses.

In triaxial apparatus where axial and radial directions are axes of principal stress with $\sigma_2' = \sigma_3' = \sigma_r'$, p' and q' are reduced to

$$p' = \frac{1}{3}\left(\sigma_a' + 2\sigma_r'\right) \tag{2.5}$$

$$q' = \sigma_a' - \sigma_r' \tag{2.6}$$

The corresponding strain invariants are

$$\epsilon_v = \epsilon_a + 2\epsilon_r \tag{2.7}$$

$$\epsilon_s = \frac{2}{3}\left(\epsilon_a - \epsilon_r\right) \tag{2.8}$$

where σ_a' and σ_r' are effective axial and radial stresses, ϵ_a and ϵ_r are the corresponding axial and radial strains; ϵ_v and ϵ_s are the volumetric and shear strains.

The parameter used to describe the volumetric state of soil is the specific volume which for fully saturated soil is defined as

$$v = 1 + e = 1 + wG_s \tag{2.9}$$

where e is the void ratio and G_s is the specific gravity of the soil grains.

In the critical state model, ultimate state occurs when the state of soil reaches the critical state line. The locus of critical states for soil is found to project to a straight line in q':p' plane defined as

$$q' = Mp' \tag{2.10}$$

where M is the frictional parameter and shown diagrammatically in Fig. 2.1.

In a triaxial compression test, M is given by

$$M = M_c = \frac{6 \sin\phi'_c}{3 - \sin\phi'_c} \tag{2.11}$$

The undrained shear strength, s_u, which corresponds to the maximum shear stress at the critical state is given by

$$s_u = \frac{1}{2} q'_f = \frac{1}{2} M p'_f \tag{2.12}$$

Many soils have been deposited over areas of large extent. The loading and unloading they have experienced during and after deposition are essentially one-dimensional. The anisotropic properties of the soil reflect this history and the soil may respond differently if it is stressed in vertical or horizontal directions. This special form of anisotropic behaviour was explored by Graham and Houlsby (1983). From the general constitutive equation, they deduced the stiffness equation for a soil element under triaxial condition to be

$$\begin{bmatrix} \delta p' \\ \delta q' \end{bmatrix} = \begin{bmatrix} K^* & J \\ J & 3G^* \end{bmatrix} \begin{bmatrix} \delta \epsilon_v \\ \delta \epsilon_s \end{bmatrix} \tag{2.13}$$

where K^* and G^* are modified values of bulk modulus and shear modulus and the presence of the two off-diagonal terms J represents the cross modulus and shows that there is some cross-coupling between volumetric and shear effects. The parameters K^*, G^* and J are functions of the shape of the stress-strain or stiffness-strain curve obtained for a given loading path, state and stress history. It should be noted that Eqn. (2.13) is a specific formulation which assumes axial symmetry and is appropriate for the analysis of a triaxial test.

The compliance form of Eqn. (2.13) is

$$\begin{bmatrix} \delta\epsilon_v \\ \delta\epsilon_s \end{bmatrix} = \frac{1}{D} \begin{bmatrix} 3G^* & -J \\ -J & K^* \end{bmatrix} \begin{bmatrix} \delta p' \\ \delta q' \end{bmatrix} \tag{2.14}$$

where $D = 3K^*G^* - J^2$

Equation (2.14) shows that volumetric and shear effects are coupled, and soils cannot satisfactorily be described as isotropic and elastic. A more elaborate model is required to describe soil response. Since there is plastic irrecoverable deformation in addition to the elastic deformation, such models should also account for the elasto-plastic deformation characteristics of soils.

When soil is loaded or unloaded, the pore pressure responds to the changes of total stress. Excess pore pressures develop and cause consolidation with time. The soil compresses and deforms as the effective stresses change. The relationships between stress, distortion, seepage and volume change are complex and are dependent on many factors such as the rate of loading compared with the rate of consolidation. Undrained and drained conditions are the two limiting cases for the rate of loading of soil. The former is one in which the loading is so quick that there is no time for any dissipation of excess pore pressure and the soil deforms at constant volume. The latter is one in which the loading is so slow that there are no excess pore pressures during loading and the pore pressures remain constant. When the application of loading and drainage or consolidation of soil occur at the same time, the condition is called coupled consolidation.

As discussed earlier the soil particle sizes and shapes, and their packing with the voids affect the soil permeability which in turn influences the drainage characteristics of the pore fluid when the soil is under loading. The rate of flow of water through soil is controlled by the pore sizes and the gradient of water pressure causing the flow. When loading is applied to saturated soil, excess pore water pressures develop and start dissipating with time. Generally, excess pore pressures dissipate rapidly in coarse grained soils but slowly in fine grained soils. However, for very quick loadings that may occur during earthquakes, coarse grained soils may

behave in an undrained manner. Thus, the soil behaves differently under different drainage conditions, namely, undrained, drained, or coupled consolidation. In many geotechnical engineering problems, the drainage condition is more likely to be a coupled event rather than a totally undrained or totally drained event.

2.3 Constitutive Equations for Soils

In the previous section, it was shown that a more elaborate model is required capable of describing the elasto-plastic response, yielding and hardening of soil behaviour. A constitutive model for soil relates increments of strains to increments of stress. It contains theoretical stress-strain relationships with components in the tangent modulus matrix expressed in terms of the parameters describing the model. Common models are the isotropic linear elastic model, models with non-linear elastic behaviour such as hyperbolic model and the 'K-G' model (Naylor, 1978). With the introduction of plasticity theory various forms of yield surfaces such as the Mohr-Coulomb, Tresca, Von Mises, and Drucker-Prager yield surfaces are available. The critical state model is an elasto-plastic model with a volumetric strain hardening yield surface. The family of critical state soil models includes yield surfaces of different shapes such as log spiral (Cam-clay), elliptical (Modified Cam-clay) and a three-part model combining the Roscoe surface, the Hvorslev surface and the tension cut-off. Their mathematical relationships can be found in Atkinson and Bransby (1978).

In the critical state models, the state boundary surface provides a conceptual model for soil behaviour. It represents a boundary to all possible states of shear stress q', normal stress p' and specific volume v. In Section 2.4, mathematical relations are developed to quantify description of soil behaviour. Figure 2.2 shows a view of the state boundary surface for soil in triaxial compression in q':p':v space. It is assumed that the behaviour of soil samples where states are inside the state boundary surface is purely elastic. When the state is on the state boundary surface, plastic strains occur as the soil yields and the state boundary surface serves as a yield surface. The yield surface may change in size when plastic yielding occurs. If

it gets larger strain hardening occurs. If it gets smaller strain softening takes place. The total strain increment is the sum of the elastic and plastic strain increments in which the elastic strain increments are related to stress increments by the theory of elasticity, whereas the plastic strain increments are related by the flow rule. The flow rule provides a relation between the plastic shear strain increments and the plastic volumetric strain increments. It can be represented by a vector normal to a plastic potential which is a surface defined in the same stress space as the yield surface. If the plastic potential and the yield curve coincide, the flow rule is associative and the normality condition applies such that vectors of plastic strain increment are normal to the yield curve. When the state of the soil reaches ultimate failure at the critical state line in Fig. 2.2, the failure of soil is given by Eqn. (2.10). The soil relies entirely on its frictional component for resistance at critical state.

2.4 Cam-Clay and Modified Cam-Clay

Cam-clay (Schofield & Wroth, 1968) is a mathematical description of soil behaviour, formulated within the framework of Critical State Soil Mechanics (CSSM). Requiring only relatively few parameters, Cam-clay is an incremental elasto-plastic model with a volumetric strain hardening yield surface. A wide variety of constitutive models based on Cam-clay have been developed over the past 25 years, each adding a particular refinement usually empirical in an attempt to match observed soil behaviour more closely (e.g. Roscoe & Burland, 1968). The Cam-clay (Schofield & Wroth, 1968) and modified Cam-clay models (Roscoe & Burland, 1968) are chosen in this research on the grounds of the simplicity of the models, the availability of large amount of laboratory test data in the development of the models, and their successful application in geotechnical engineering problems despite their simplicity. This section describes the fundamental soil parameters, stress history and the basic equations which characterise the model.

2.4.1 Fundamental Soil Parameters

The critical state models predict incremental stress-strain relations based on a small number of fundamental critical state soil parameters, the current state of effective stress and specific volume. The Cam-clay and modified Cam-clay models require four critical state soil parameters plus an elastic parameter α' used in the current investigation. They are

κ	the slope of the unload/reload line in v:ln p' space,
λ	the slope of the virgin compression line in v:ln p' space,
M	the slope of the critical state line in q':p' space,
Γ	the specific volume on the critical state line at p' = 1 kPa.
(or N	the specific volume on the isotropic normal compression line at p' = 1 kPa)
α'	= G'/K', the ratio of the elastic shear modulus G' to the elastic bulk modulus K'

These fundamental soil parameters are shown in Fig. 2.1.

The frictional parameter M is the slope of the critical state line (CSL) in the q':p' plane and is a function of the critical state frictional angle ϕ_c'. The slopes λ and κ of the normal compression and swelling lines in the v:ln p' plane are functions of soil plasticity (Atkinson and Bransby, 1978) and are given by

$$v = N - \lambda \ln p' \qquad (2.15)$$

$$v = v_\kappa - \kappa \ln p' \qquad (2.16)$$

These are also indices indicating the degree of compressibility of the material. High plasticity clays are associated with high compressibility.

The volumetric strain ratio κ/λ is a ratio between the slopes of the swelling line and the normal compression line in v:ln p' space. A low value in this ratio indicates that the material has a higher proportion of plastic strain during normal compression while a high value shows that the material has lower proportion of plastic strain.

The elastic stiffness ratio α' is the ratio of the elastic shear modulus G' to the elastic bulk modulus K' and is related to the Poisson's ratio as $\alpha' = [3(1 - 2\nu')]/[2(1 + \nu')]$. The ratio also relates the elastic shear and volumetric response of the soil as these two moduli are associated with the deviatoric and spherical stress-strain increments respectively.

Figure 2.3 shows a family of critical state lines for five soils after Schofield and Wroth (1968). These critical state lines can be extrapolated to intersect at a single point known as the "Omega (Ω) point". From this an empirical relationship may be established.

$$\Gamma = v_\Omega + \lambda \ln p_\Omega' \qquad (2.17)$$

where $v_\Omega = 1.25$, $\ln p_\Omega' = 9.21$ and Γ is the specific volume of the critical state line corresponding to unit mean pressure. Therefore,

$$\Gamma = 1.25 + 9.21 \lambda \qquad (2.18)$$

In the original Cam-clay model, the separation of the normal compression line and the critical state line is given by

$$N - \Gamma = \lambda - \kappa \qquad (2.19)$$

Combining Eqns. (2.18) and (2.19) gives

$$N = (1.25 + 9.21 \lambda) + (\lambda - \kappa) \qquad (2.20)$$

This leads to an expression for N in terms of the slopes of the normal compression line and the swelling line. Hence of the parameters N, Γ, λ, κ, M and α', only four (λ, κ, M and α') are independent.

Cherrill (1990) examined the validity of the Omega point concept using results from triaxial tests for 14 different soils by researchers at the City University. The results showed considerable scatter and it was difficult to determine a single point. However, the critical state lines intersected at a cluster near a point with $v = 1.17$ and $p' = 9900$ kPa ($\ln p' = 9.2$) and so is close to the values in Schofield

and Wroth (1968). In this research, the original relationship from Schofield and Wroth (1968) was used.

2.4.2 Stress History

Cam-clay and modified Cam-clay are models which work better for isotropically consolidated soil, and the stress history is defined by the isotropic preconsolidation pressure p_c'. For normally consolidated soils $p' = p_c'$, whereas for overconsolidated soils $p' < p_c'$ (and $OCR = p_c'/p'$).

2.4.3 Basic Equations of Cam-clay and Modified Cam-clay

The formulations of the constitutive relations for the Cam-clay model are based on a number of basic equations. The yield curve is a function specifying the state of stress corresponding to the start of plastic flow. The equation of the yield surface of Cam-clay is

$$\frac{q'}{(Mp')} + \ln\left(\frac{p'}{p_f'}\right) = 1 \qquad (2.21)$$

in which p_f' is the effective mean pressure at failure (Fig. 2.1). The flow rule relates the plastic strain increments to the current stresses and the stress increment subsequent to yielding. For Cam-clay this is given by

$$\frac{d\epsilon_v^p}{d\epsilon_s^p} = (M - \eta') \qquad (2.22)$$

in which η' is the stress ratio, q'/p'. The state boundary surface joins all the yield loci and separates possible states from impossible states (Fig. 2.2). It is given by

$$q' = \frac{Mp'}{(\lambda - \kappa)}\left(\Gamma + \lambda - \kappa - v - \lambda \ln p'\right) \qquad (2.23)$$

and it relates the stresses and volume for a soil which is yielding. The complete state boundary surface is shown diagrammatically in q':p':v space in Fig. 2.2. An elastic wall is the intersection of a surface through a swelling line perpendicular to the v:p' plane. The intersection of an elastic wall with the state boundary surface forms a yield surface when projected onto the q':p' plane. When a state point is on a current elastic wall and inside the yield surface, behaviour is elastic. When the state point moves on the state boundary surface, plastic yielding takes place. The expansion and retraction of the yield surface are referred to as hardening or softening. For states inside the state boundary surface strains are elastic and are given by

$$\delta\epsilon_s^e = \frac{\kappa}{(vp' 3\alpha')}\,\delta q' \tag{2.24}$$

$$\delta\epsilon_v^e = \frac{\kappa}{(vp')}\,\delta p' \tag{2.25}$$

The plastic components of the strain increments are

$$d\epsilon_v^p = \frac{(\lambda - \kappa)}{(Mvp')}\,[\delta q' + (M - \eta')\,\delta p'] \tag{2.26}$$

$$d\epsilon_s^p = \frac{(\lambda - \kappa)}{(Mvp')}\,[\delta p' + \frac{1}{(M - \eta')}\,\delta q'] \tag{2.27}$$

The total strains are given by

$$\delta\epsilon_s = \delta\epsilon_s^p + \delta\epsilon_s^e \tag{2.28}$$

$$\delta\epsilon_v = \delta\epsilon_v^p + \delta\epsilon_v^e \tag{2.29}$$

So the constitutive equations are given by

$$\begin{bmatrix} \delta\epsilon_v \\ \delta\epsilon_s \end{bmatrix} = \frac{1}{vp'} \begin{bmatrix} \kappa + \frac{\lambda - \kappa}{M}(M - \eta') & \frac{\lambda - \kappa}{M} \\ \frac{\lambda - \kappa}{M} & \frac{\kappa}{3\alpha'} + \frac{\lambda - \kappa}{M(M - \eta')} \end{bmatrix} \begin{bmatrix} \delta p' \\ \delta q' \end{bmatrix} \quad (2.30)$$

The detailed derivation of these relations is given in Appendix 1. The modified Cam-clay model is a modification from the original Cam-clay model. It has an elliptical geometry for the yield locus as compared with the log-spiral shape of the original Cam-clay. The constitutive equations are given by

$$\begin{bmatrix} \delta\epsilon_v \\ \delta\epsilon_s \end{bmatrix} = \frac{1}{vp'} \begin{bmatrix} \kappa + \frac{(\lambda - \kappa)(M^2 - \eta^2)}{(M^2 + \eta^2)} & \frac{2\eta'(\lambda - \kappa)}{M^2 + \eta^2} \\ \frac{2\eta'(\lambda - \kappa)}{M^2 + \eta^2} & \frac{\kappa}{3\alpha'} + \frac{4\eta^2(\lambda - \kappa)}{(M^4 - \eta^4)} \end{bmatrix} \begin{bmatrix} \delta p' \\ \delta q' \end{bmatrix} \quad (2.31)$$

The derivation of the constitutive relations in Eqn. (2.31) is given in Appendix 2.

2.4.4 Comments

The incremental stress-strain relations for the Cam-clay and modified Cam-clay models relate the strain increments to stress increments via a compliance matrix given by Eqns. (2.30) and (2.31). The terms in the compliance matrix are the fundamental soil model parameters (M, λ, κ and α') and the current stress ratio (η'). The specific volume v and effective mean stress p' of the current state are common terms to all these terms so in the normalising procedure discussed in Section 5.2.2, use is made of the term vp' in normalising the 'parameters' characterising soil states.

For an elastic soil, $\lambda = \kappa$ and Eqns. (2.30) and (2.31) reduce to the same equations as

$$\begin{bmatrix} \delta\epsilon_v \\ \delta\epsilon_s \end{bmatrix} = \frac{1}{vp'} \begin{bmatrix} \kappa & 0 \\ 0 & \frac{\kappa}{3\alpha'} \end{bmatrix} \begin{bmatrix} \delta p' \\ \delta q' \end{bmatrix} \tag{2.32}$$

Eqns. (2.30) and (2.31) are in terms of the stress invariants. Transformation is required to convert the components of the principal stress to the components of stresses in the Cartesian coordinates before they can be implemented for use in a finite element program. However, these equations can be used to formulate the algorithm in the single element numerical analysis in Chapter 5.

2.5 Finite Element Method

The finite element method started with structural applications and it is a formulation for relating loads to the displacement of a structure. There are displacement methods, force methods and hybrid formulations. Basic concepts of different types of formulation can be found in Zienkiewicz (1977).

The basis of the method is the representation of a body or a continuum by an assemblage of subdivisions called finite elements. These elements are considered to be interconnected at joints which are called nodes or nodal points. The displacements inside each finite element are expressed as functions of the displacements of nodal points and position within the element. This relationship is given by

$$\mathbf{d} = \mathbf{N}\,\mathbf{a}_e \tag{2.33}$$

where $\mathbf{d} = [\ dx \quad dy\ ]^T$ and $\mathbf{a}_e$ is a vector listing all the nodal displacements associated with an element. The matrix **N** is the displacement or shape functions for the element.

If ϵ is the vector of the relevant strain components at an arbitrary point within the finite element, the strains inside the element can be written in terms of the nodal displacements from the equations of compatibility. These are given by

$$\epsilon = \mathbf{B}\, \mathbf{a}_e \tag{2.34}$$

where **B** is the strain matrix which contains derivatives of the displacements with respect to the x and y axes. For plane strain applications, it is written as

$$B_i = \begin{bmatrix} \frac{\partial N_i}{\partial x} & 0 \\ 0 & \frac{\partial N_i}{\partial y} \\ \frac{\partial N_i}{\partial y} & \frac{\partial N_i}{\partial x} \end{bmatrix} \quad , \; i = 1,n \tag{2.35}$$

where n = number of nodes.

The stress-strain relation for the material is given by

$$\sigma = \mathbf{D}\, \epsilon \tag{2.36}$$

and this is used to express the stresses inside the elements in terms of the nodal displacements:

$$\sigma = \mathbf{D}\, \mathbf{B}\, \mathbf{a}_e \tag{2.37}$$

The principle of virtual work is then used to find the nodal forces, $\mathbf{F}_e$ which are in equilibrium with this state of internal stress. These nodal forces do not represent actual concentrated forces in the body, rather they represent resultants similar to the concepts of an axial force, shear force and bending moment describing the state of stress in a beam. A set of virtual nodal displacements $\mathbf{a}_e^*$ applied to the element accompanies a set of virtual strains ϵ^* within the element according to the relation

$$\epsilon^* = \mathbf{B}\, \mathbf{a}_e^* \tag{2.38}$$

The principle of virtual work gives

$$a_e^{*T} F_e = \int_V \epsilon^{*T} \sigma \, d(vol) \tag{2.39}$$

Substituting for σ and ϵ^* using Eqns. (2.37) and (2.38), Eqn. (2.39) becomes

$$a_e^{*T} F_e = a_e^{*T} \int_V (B^T D B) \, d(vol) \, a_e \tag{2.40}$$

and

$$F_e = \int_V (B^T D B) \, d(vol) \, a_e$$

$$= K a_e \tag{2.41}$$

where

$$K = \int_V (B^T D B) \, d(vol) \tag{2.41a}$$

is the element stiffness matrix. The equivalent nodal forces F_e balance loads due to self-weight and boundary stresses, taking into account overall equilibrium, the resulting equation is

$$\int_V (B^T D B) \, d(vol) \, a_e = \int_V N^T w \, d(vol) + \int_S N^T \tau \, d(area) \tag{2.42}$$

where $\tau = [\sigma_n \; \tau_{nt}]^T$ represents normal and shear stresses acting on an element boundary. These equations have been developed for a single element, the N and B matrices are used for each element in turn when performing an integration over the whole finite element mesh.

The above equilibrium equations (Eqns. 2.41 and 2.42) of the assemblage are then solved for displacements at the inter-element nodes in the assemblage. The stress and strain components can be computed at any location within an element by using Eqns. (2.37) and (2.34) respectively.

2.6 Finite Element Formulations for Effective Stresses, Pore Pressure and Coupled Consolidation

As discussed in Section 2.2, Terzaghi's effective stress principle suggests that when soil, either dry or saturated is to be described by the stress-strain relations, the equations must refer to effective, rather than total stresses. Thus the stress-strain relation in Eqn. (2.36) becomes

$$\sigma' = D' \epsilon \tag{2.43}$$

where the matrix D' contains elastic moduli E' and ν', the Young's modulus and Poisson's ratio in effective stress terms. In soil mechanics, it is usual to express incremental strains caused by increments in effective stresses

$$\delta\sigma' = D' \delta\epsilon \tag{2.44}$$

For dry soils when an all-round total pressure is applied to the sample the strains can be calculated by Eqn. (2.44). In this case the effective stresses are the same as the imposed total stresses since the pore water pressure is zero. If the shear strains are zero, the volumetric strain can be calculated from

$$\frac{\delta V}{V} = \frac{\delta\sigma'}{K'} \tag{2.45}$$

The elastic bulk modulus K' is a measure of the bulk stiffness of the soil matrix rather than the stiffness of the individual particles.

For saturated soils, the volume of the soil V is comprised of V_s and V_w the volumes of the solid and water phases, then

$$V = V_s + V_w \tag{2.46}$$

When an all-round pressure is applied to the sample, the soil decreases in volume by δV. This overall decrease in volume consists of decreases in the solid and water phases δV_s and δV_w respectively and so

$$\delta V = \delta V_s + \delta V_w \tag{2.47}$$

It is assumed that saturated soil is incompressible when drainage is not allowed and, for a small change in volume,

$$\frac{\delta V}{V} = \frac{\delta \sigma}{K_u} \tag{2.48}$$

$$\frac{\delta V_w}{V_w} = \frac{\delta u}{K_w} \tag{2.49}$$

$$\frac{\delta V_s}{V_s} = \frac{\delta u}{K_s} \tag{2.50}$$

where K_u, K_w and K_s are the elastic bulk moduli of the soil composite, the water and solid phases respectively. Equations (2.48) and (2.49) are definitions of K_u and K_w. Equation (2.50) expresses the volumetric compression of the solid soil particles caused by the increase in pore water pressure. The change in effective stress $\delta\sigma'$ must be consistent with

$$\delta \sigma = \delta \sigma' + \delta u \tag{2.51}$$

$$\frac{\delta V}{V} = \frac{\delta \sigma'}{K'} \tag{2.52}$$

From Eqn. (2.47), making use of Eqns. (2.48) to (2.52), the following is obtained

$$K_u = K' + K_w \left(\frac{V}{V_w}\right) \frac{1}{\left(\frac{K_w}{K_s}\right)\left(\frac{V_s}{V_w}\right) + 1} \tag{2.53}$$

Since the elastic bulk modulus of the grains is about 30 times as large as that of water (Britto and Gunn, 1987), Eqn. (2.53) can be written as

$$K_u = K' + K_w \left(\frac{V}{V_w}\right) \tag{2.54}$$

A further simplification follows from the observation that K' is much smaller than K_w (about 50 to 500 times smaller according to Britto and Gunn, 1987). Hence

$$K_u = K_w \left(\frac{V}{V_w}\right) \tag{2.55}$$

Since the void ratio $e = V_w/V_s$, then

$$K_u = \left(1 + \frac{1}{e}\right) K_w \tag{2.56}$$

Thus the bulk compressibility of saturated soil is effectively due to the bulk compressibility of the water phase alone. Therefore undrained loading produces no change in the effective stresses because the external load is carried by the pore water pressure.

When the pore water in soil is allowed to drain, outflow takes place at a rate controlled by the pore size of the soil and the pore water pressure in the sample eventually returns to its steady state pressure. The change in the effective stress is now equal to the change in the total stress ($\delta\sigma' = \delta\sigma$) and the volumetric strain can be calculated from

$$\frac{\delta V}{V} = \frac{\delta\sigma'}{K'} \tag{2.57}$$

which is identical to Eqn. (2.45) for dry soil.

In the implementation of effective stress and pore pressure calculations in a finite element package, the constitutive matrix is constructed in two parts: the soil skeleton and the pore fluid. Drained loading permits overall changes of volume to occur without the generation of excess pore pressures while undrained loading gives rise to changes in pore pressure whilst maintaining constant volume. The computer program CRISP permits fully drained, fully undrained and

coupled consolidation (Biot, 1941) analyses by means of the effective stress method (Naylor, 1975).

Effective stresses are calculated explicitly by Eqn. (2.44) and pore pressures by

$$\delta u_w = K_u \, m^T \, \delta \epsilon \tag{2.58}$$

where δu_w is the incremental pore water pressure and m is a vector indicating which stress terms participate in the effective stress relation, i.e. $m^T = [1 \quad 1 \quad 1 \quad 0 \quad 0 \quad 0]$ for three dimensional applications. K_u is the bulk modulus of the "equivalent" pore fluid and K_u is related to the bulk modulus of the pore water K_w by Eqn. (2.56).

The effective stress law can be written in matrix notation

$$\delta \sigma = \delta \sigma' + m \, \delta u_w \tag{2.59}$$

Combining this with the incremental effective stress-strain relation the constitutive equation relating increments of strains and total stresses for undrained loading is

$$\delta \sigma = D' \, \delta \epsilon + m \, K_u \, m^T \, \delta \epsilon \tag{2.60}$$

$$\delta \sigma = (D' + m \, K_u \, m^T) \, \delta \epsilon \tag{2.61}$$

The stiffness matrix K for a particular element is given by the integral $\int B^T \, D \, B$ over the volume of the element, where B relates changes of internal strain to nodal displacement in Eqn. (2.34) as described in Sec. 2.5, and D relates changes of internal stress and strain (Eqn. 2.44). The D matrix is expressed in terms of total stresses, and represents the combined response of the soil skeleton and pore fluid. If the effective stress stiffness of the soil skeleton is known, a matrix D' may be defined. D' is related to D through the expression

$$D = D' + m \, K_u \, m^T \tag{2.62}$$

In the effective stress method D is obtained from Eqn. (2.62). A drained analysis is achieved by setting $K_u = 0$, implying that the pore water is infinitely compressible and all applied stress is taken by the soil skeleton. An undrained analysis is achieved by setting $K_u >> 0$ (typically 50 to 500 K' where K' is the effective bulk modulus of the soil skeleton) implying that the water is virtually incompressible and can carry applied total stress.

In the analysis of coupled consolidation problems, the most common approach is to use Biot's (1941) equation governing excess pore pressures together with the equations of equilibrium and an appropriate constitutive law.

In Biot's coupled consolidation theory, the soil is assumed to be saturated and both the soil grains and pore water are taken to be incompressible. Thus all volume changes are due to the flow of water into and out of the soil skeleton. For the simplified case of an orthotropic soil, Biot's equation governing excess pore pressure is:

$$\frac{K'}{\gamma_w}\left[k_x\frac{\partial^2 u}{\partial x^2} + k_y\frac{\partial^2 u}{\partial y^2} + k_z\frac{\partial^2 u}{\partial z^2} \right] = \frac{\partial u}{\partial t} - \frac{\partial p}{\partial t} \qquad (2.63)$$

where K' = bulk modulus of soil

γ_w = unit weight of water

k_x, k_y, k_z = coefficients of permeability in x, y and z direction respectively

u = excess pore water pressure

p = mean total stress

The equation of equilibrium are:

$$\frac{\partial \sigma'_x}{\partial x} + \frac{\partial \tau_{xy}}{\partial y} + \frac{\partial \tau_{xz}}{\partial z} + F_x = 0$$
$$\frac{\partial \tau_{yx}}{\partial x} + \frac{\partial \sigma'_y}{\partial y} + \frac{\partial \tau_{yz}}{\partial z} + F_y = 0 \qquad (2.64)$$
$$\frac{\partial \tau_{zx}}{\partial x} + \frac{\partial \tau_{zy}}{\partial y} + \frac{\partial \sigma'_z}{\partial z} + F_z = 0$$

The strains are related to the effective stresses in Eqn. (2.44) via an incremental constitutive law which, in general, should allow for elasto-plastic behaviour.

Equations (2.63), (2.64) and (2.44) together with the boundary conditions provide the basis for analysing any three dimensional problem of coupled loading and consolidation. The implementation of coupled consolidation theory in the finite element method has been described by Sandhu and Wilson (1969), Small et al (1975) and Booker and Small (1976). The governing equation is given in matrix form by:

$$\begin{bmatrix} K & L \\ L^T & S \end{bmatrix} \begin{bmatrix} \delta \\ u \end{bmatrix} - \begin{bmatrix} \Delta r_1 \\ \Delta r_2 \end{bmatrix} \qquad (2.65)$$

where δ = nodal displacements
u = nodal excess pore pressure
Δr_1 = boundary/body force components
Δr_2 = boundary flow components
K = stiffness matrix of soil skeleton
L = relation of pore pressure changes to strains, and
S = fluid compressibility

Detailed derivation and discussion of the Biot's coupled consolidation theory is found in Gunn and Britto (1987).

2.7 Finite Element Method for Non-linear Behaviour

Soil is not a linear material. The relations between stress and strain are much more complicated than the simple, linear elastic ones described by the theory of elasticity. Therefore, in order to represent geotechnical problems realistically some form of non-linear relation must be used, and the development and application of such relations have been important areas of research in recent years. The various schemes for defining the constitutive behaviour of soils can be divided into two main groups: (1) representation of measured strain curves by using curve-fitting methods, interpolation, or mathematical functions, and (2) plasticity theories.

There are a number of solution techniques for analysing non-linear problems using finite elements. The most important of these are the incremental or tangent stiffness approach, the Newton-Raphson method and the modified Newton-Raphson method. A graphical representation of these solution schemes is shown in Fig. 2.4 to 2.6.

The programs CASIS and CRISP used in the research described in this thesis were developed from algorithms of the theory of plasticity applied to soil mechanics. They were implemented with the incremental stiffness approach to the solution of the stress-strain relations in which the total load or displacement is divided into a number of small increments. The programs apply each of these increments in turn. During each increment the stiffness properties appropriate for the current stress levels are used in the calculations. If only a few increments are used and the stress or displacement increment is large, this method produces a solution which tends to drift away from the true or exact solution. This means a stiffer response results for a strain-hardening model and the displacements are always under-predicted. Consequently it is necessary to check that the increment size is sufficiently small in the computation.

2.8 Summary

Soil particles cover a range of particle sizes, the packing of which with the voids, and the stress history influence its permeability,

stress-strain and strength characteristics. When a saturated soil is loaded undrained or partly drained, excess pore water pressure develops. If drainage is permitted, the excess pore water pressure dissipates and the effective stress increases with gradual consolidation of the soil. In practice in geotechnical engineering problems, both undrained and drained conditions are the extreme conditions and they are more likely to be coupled, e.g. stage construction of embankment on soft soil and heave of an excavation with time. These are mostly associated with the dissipation of excess pore water pressure as time goes by. Soils are mostly anisotropic, elasto-plastic with volumetric and shear effects coupled. Hence, a more elaborate model than the linear elastic model is necessary to describe the soil behaviour fully.

The critical state soil model is probably the simplest and easiest to begin with. It uses the stress history, effective stresses, volume change and elasto-plastic behaviour in the description of soil materials. It provides a framework for evaluating the strength and stiffness characteristics for most commonly occurring soils.

The finite element displacement method provides a powerful numerical technique for modelling geotechnical boundary value problems. The solution of the problem using modern computer hardware allows engineers to examine soil behaviour and the performance of structures. With the implementation of the effective stress stiffness equations and the excess pore water pressure components, undrained, drained or coupled consolidation problems can be examined using a finite element program.

CHAPTER 3 LITERATURE SURVEY ON NUMERICAL ANALYSES

3.1 Introduction

Previous research has investigated numerical techniques to analyse problems in soil mechanics and foundation engineering. Numerical experiments are conducted to evaluate theoretical soil behaviour and to analyse laboratory experiments and problems of soil-structure interaction. This chapter reviews the application of the finite element technique in general, the range of applications and the developments in implementing the critical state models in finite element programs. In particular, the review concentrates on the literature published on the applications of the critical state soil mechanics relating to the parametric study of Cam-clay for the research discussed in Chapter 5, coupled events and cavity expansion in the numerical study of hydraulic fracturing in the laboratory triaxial samples discussed in Chapter 6, and the parametric study of plate loading tests on Cam-clay discussed in Chapter 7.

3.2 Applications of Finite Element Methods

In a design process, numerical analysis is performed to evaluate the behaviour and performance of an engineering structure. This is as important in a geotechnical engineering analysis and design. With the development in computer hardware and software, numerical methods have been formulated in computer codes, implementing finite difference procedures, finite element methods, boundary element methods or coupled finite element and boundary element methods. Most of these numerical methods were originally developed for structural engineering applications but structural engineering programs may not be suitable for analysis in geotechnical engineering. Among all these numerical techniques, the finite element method has a very wide range of applications in addition to structural engineering. These include applications in fluid flow, electricity, magnetism, heat transfer and geotechnical engineering (Zienkiewicz, 1977).

In the finite element method for stress deformation problems, there are different types of formulations, namely displacement, force and

hybrid methods with the first one as the most common one (Zienkiewicz, 1977). The method involves the division of a continuum into elements. Section 2.5 briefly dealt with the basic ingredients of the finite element displacement formulations and details of the formulations and solution techniques can be found in Zienkiewicz (1977) and Hinton and Owen (1979).

Different types of elements are available to describe the displacement fields in the finite element methods (Irons and Ahmad, 1980). There are linear, triangular, quadrilateral and brick elements etc. which are used for modelling different geometries and features in engineering problems. Different orders of displacement field are available within an element e.g. constant strain, linear strain or cubic strain functions. Higher order elements with more than one mid-side node may give better accuracy in the solution with a coarser mesh compared with lower order elements in the same discretisation at the expense of computer resources (Sloan and Randolph, 1982). Selection of the size and shape of elements is a matter of experience and intuition. In general, elements should be smaller where the stress and strain gradients are the greatest. There have been discussions and suggestions on whether one should use more numbers of lower order elements or fewer numbers of higher order elements in mesh discretisation (Sloan and Randolph, 1982). This is a matter of assessing which can provide a cost-effective analysis to a problem.

3.3 Applications of Critical State Models in Finite Element Methods

3.3.1 Introduction

Saturated soil is a two-phase material comprising soil grains and water. Its behaviour was discussed in Section 2.2. Roscoe and his research team developed the critical state soil models in Cambridge University in the 1960's, namely the original Cam-clay and modified Cam-clay models described in Section 2.4 to model the behaviour of soft clays. Roscoe was aware of the possible use of finite elements formulations to implement the critical state theories in practical problems and invited the collaboration of Zienkiewicz of Swansea

University (Zienkiewicz and Naylor, 1972). Zienkiewicz and Naylor (1972) tackled the general coupled problem which was discussed in Section 2.6 and presented a general finite element formulation of the two models.

3.3.2 Cam-clay and Modified Cam-clay Models

The original Cam-clay and modified Cam-clay models are non-linear models unifying the concepts of critical state, volume change and effective stress relationships, and plastic deformation characteristics. In the implementation of the models in the finite element procedure, explicit expressions for volumetric and deviatoric strain rate invariants are obtained in terms of the corresponding stress invariants, and also for the principal strain rate components in terms of principal stresses in both two and three dimensions (Roscoe, Schofield and Thurairajah, 1963; Schofield and Wroth, 1968 and Roscoe and Burland, 1968). All components of the stress and strain rate tensors must be related. Use was made of the normality law of associative plasticity to obtain the plastic strain components which are then used to compute stress increments.

Research workers have successfully implemented these critical state models into finite element programs (Simpson, 1973, Naylor, 1975). There are now many geotechnical program packages incorporating critical state soil models and those which are found in the published literature include CAMFE (Carter, 1978), SAFE (Simpson, 1979), CRISP (Britto and Gunn, 1982, 1984 and 1987), ICFEP (Potts and Ganendra, 1991). Some of these programs are accessible to users in geotechnical engineering and they are used to evaluate or predict the behaviour of real geotechnical engineering problems. In this research, the package CRISP was used and the program is described in Section 4.4.

3.3.3 Other Soil Models

Many other numerical models for soil behaviour exist and are described in the literature. Murayama (1985) provided a comprehensive survey of

available models. The models for the stress-strain behaviour of overconsolidated soil can generally be divided into two groups:

-Models which assume all deformations inside the state boundary surface are elastic.

-Models which allow plastic yielding to occur inside the state boundary surface.

Stallebrass (1990) gave a detailed evaluation of some of the models in these categories and the only models that will link the changes in stress-strain response with changes in recent stress history are those which incorporate kinematic hardening, for example Mröz et al (1979) or Hashiguchi (1985), or Model LC devised by Simpson et al (1979).

3.3.4 Geometric Non-linear Behaviour

Non-linear behaviour may arise due to either geometric non-linearity or material non-linearity, or a combination of both. The stiffness is not constant but dependent on stress or strain. Carter (1977) and Carter et al (1977) examined the importance of non-linear geometric effects in geotechnical analysis. They examined the influence of a large strain formulation on the load-deformation response calculated by the finite element method using elastic perfectly plastic models of soil behaviour. The general conclusion appeared to be that the influence of large strain effects was not very significant for the range of material parameters associated with most soils. In most situations the inclusion of large strain effects led to a stiffer load-deformation response near failure and some enhancement of the load carrying capacity of the soil. If an analysis is concerned mainly in the estimation of a collapse load using an elastic perfectly plastic soil model then it is probably best to use the normal infinitesimal strain assumption to avoid the occurrence of the stiffening effect (Carter, 1977).

3.3.5 Limitations of the Cam-clay and Modified Cam-clay Models

In the Cam-clay and modified Cam-clay models deformations within the state boundary surface are purely elastic. An undrained loading path on an isotropic overconsolidated soil has a stress path which rises vertically in p':q' space to the yield surface where plastic strains begin and the stress path moves along the yield surface to the critical state. Real soils do not conform exactly to this behaviour and the strains within the state boundary surface are not purely elastic with some plastic strains occurring as the yield surface is approached. The undrained stress path described above may not be vertical and could deviate from the vertical within the state boundary surface. Anisotropy may also cause the stress path not to be vertical but this effect is generally small.

The Cam-clay and modified Cam-clay models were developed to model very small homogeneous soil elements each one behaving in accordance with critical state soil mechanics theory described in Section 2.4. However, in practice soil is not completely homogeneous and this leads to localised deformations and the formation of slip planes particularly in overconsolidated samples in triaxial tests. The Cam-clay and modified Cam-clay models do not predict these deformations and are therefore unable to model the overall behaviour of a soil element when slip planes are formed. The models are however still valid for elements outside a slip plane. In an undrained loading path on an overconsolidated material in a triaxial test slip planes normally form when the sample reaches the yield surface. Soil elements near the middle of the sample generate negative excess pore pressures causing local drainage (Atkinson and Richardson, 1987) towards this zone of elements. This increases the water content and weakens the soil in this zone. Further deformations are concentrated in these elements and slip planes form. A similar situation occurs in drained loading paths on overconsolidated soils in triaxial tests when soil elements in the middle of the sample where stresses are greatest pass their peak strength after reaching the yield surface and then weaken causing slip planes to form in these elements. The consequence of this behaviour is that the Cam-clay and modified Cam-clay models do not model the overall behaviour of overconsolidated materials very

accurately once the yield surface is reached and slip planes have formed as the effects of slip planes are not taken into account.

3.3.6 Limitations of the Package CRISP

The theory of critical state soil mechanics has been developed since the 1960's and there have been many modifications proposed. Many deficiencies of the Cam-clay models have been pointed out and though the models have limitations as discussed in Section 3.3.5, they require few soil parameters to characterise and provide reasonably consistent results for normally consolidated and lightly overconsolidated soils. The package CRISP (Gunn and Britto, 1982 and 1984; Britto and Gunn, 1987) to be discussed in Section 4.4 and used in the work described in this thesis was implemented with the Cam-clay family of models and employed an incremental tangent stiffness approach to solve the non-linear finite element equations described in Section 2.7. There have been many comments made on the formulations and implementation of the finite element procedures in the program and Potts and Ganendra (1991) in their discussion on the work by Hird et al (1990) pointed out that it was their experience when sophisticated constitutive models were used, this solution strategy worked only if many increments were employed and even this did not guarantee agreement with closed-form solution for some problems. This was because the stiffness matrix was based on the stress state at the beginning of the increment so it was difficult to establish when an integration point changes from elastic to plastic behaviour, or from loading to unloading. However, this deficiency can be circumvented by a check on the solution from the finite element computation results until it is independent of the increment size.

Potts and Ganendra (1991) illustrated that the way the modified Cam-clay model was implemented in CRISP resulted in the angle of shearing resistance ϕ' being a function of the Lode angle which is given by

$$\theta = \arctan\left[\frac{(2b - 1)}{\sqrt{3}}\right] \qquad (3.1)$$

where

$$b = \frac{(\sigma'_2 - \sigma'_3)}{(\sigma'_1 - \sigma'_3)}$$

This leads to inconsistent calculated and input values of ϕ' so the user has to be very careful in this respect. The way the modified Cam-clay model was implemented did not readily allow a linear undrained shear strength with depth profile to be adopted but the value of undrained shear strength varied with the Lode angle and hence also with the intermediate principal stress. This may result in a strongly non-linear strength profile near the soil surface. However, the reply in Hird et al (1991) to the discussion of Potts and Ganendra (1991) suggested that they had checked on the effect of this non-linearity of the strength profile actually used and the effect on the solution was negligible.

The program CRISP 84 version was implemented with a constant permeability algorithm. This is not the case for a real soil for which drainage leads to changes in specific volume and permeability. Cherrill (1990) found that in the drained tests the changes in specific volume were very small and were of the order of 5% in elements immediately adjacent to drainage boundaries. The errors involved in assuming a constant permeability were therefore not considered to be great though this must be borne in mind when analysing results. The main consequence of assuming a constant permeability was that CRISP was likely to underestimate the magnitude of excess pore pressures after a reduction in specific volume due to drainage. Almeida et al (1986) modified the standard version of CRISP and correlated the coefficient of permeability with the void ratio using the following relationship

$$k_v = k_{vo} \cdot 10^{(e - e_o)/C_k} \qquad (3.2)$$

where k_{vo} is the initial coefficient of permeability in the vertical direction and e_o is the initial void ratio and C_k is the slope of the log k_v:e plot. Almeida et al (1986) compared the results from the finite element computation with the above variable permeability assumption and constant permeability assumption. The results indicated that better agreement was obtained between measurements and the calculation with the variable permeability assumption. The predicted excess pore pressures for the constant permeability assumption dissipated faster than those from the variable permeability assumption and the predicted displacements for the two different assumptions were more or less the same.

3.4 Parametric Studies of Critical State Soil Model Parameters

The Cam-clay constitutive model offers a complete description of soil behaviour and is defined by a small number of physically meaningful parameters. To assess the relative importance of the fundamental soil parameters on soil behaviour characterising initial, yield, peak and ultimate states, numerical parametric studies need to be carried out.

Cherrill (1990) performed numerical analyses to model triaxial tests using the CRISP finite element program and examined the influence of sample drainage conditions, the type and rate of loading, the stress history and the fundamental soil parameters on the excess pore pressures, non-uniformities of stress, specific volume and axial strain within the sample, and the stiffness measured. The study is considered as coupled consolidation problem and a more detailed review of the findings in Cherrill (1990) is given in Section 3.6.1.

Stallebrass (1990) investigated the sensitivity of the three-surface yielding model to some of the model parameters. The predictions were compared with some experimental data for three loading paths. The behaviour parameters shear modulus G' and bulk modulus K' were examined and the study showed that the parameters T and ψ, and the product TS have the greatest influence on behaviour predicted by the three-surface model. A typical illustration of the results is shown Figs. 3.1(a) and 3.1(b). Stallebrass (1990) gave a more detailed description of the influence of the other parameters.

Other types of parametric studies for some of the soil model parameters exist such as in Powrie and Li (1991a) in the finite element analysis of an in situ wall. They used the Schofield three-part model (Schofield, 1980) incorporating the original Cam-clay yield surface on the wet side of the critical state and the Hvorslev surface and a no-tension cut-off on the dry side (Fig. 3.2). The Hvorslev surface and the no-tension cut-off were used because of the overestimation of the elastic response of soils on the dry side by conventional Cam-clay models. Though Powrie and Li (1991a) used a fixed set of soil parameters based mainly on laboratory and in situ test data on stiff overconsolidated boulder clay described in Li (1990), they examined the effect of varying the critical state frictional coefficient M using 0.76 and 1.03, and the slope of the no-tension cut-off line S using 2 and 3, the difference in the computation results was found to be insignificant.

There have been other types of parametric studies in soil mechanics and foundation engineering such as those reported by Potts and Fourie (1984) in which the influence on the behaviour of retaining wall due to the variations of K_o was examined. These did not fall into the category of parametric studies in the research described in this thesis and are not described here.

No other publications in the literature on numerical parametric studies have been found similar to those reported in Atkinson and Tam (1988) and Tam and Woods (1989) which were publications of part of the research to be described in Chapter 5.

3.5 Cavity Expansion

The numerical studies of cavity expansion to be described in Chapter 6 modelled the laboratory experiments reported in Mhach (1991). A cavity was formed in a cylindrical specimen and cavity pressure via water was increased at a pre-determined rate and caused cracking of the specimen. The laboratory experiment is discussed in Chapter 6. The following sections review some of the published literature which describe the use of finite element programs to model the cavity expansion problem.

3.5.1 Pressuremeter Tests and Piezocone Insertion and Dissipation Tests

Lee Goh and Fahey (1991) applied a one-dimensional cavity expansion model to investigate the stress and pore pressure changes due to the expansion of a self-boring pressuremeter (SBP) and the insertion of a piezocone. A one-dimensional finite element program CAMFE (Carter, 1978) was used. The program incorporated the modified Cam-clay model with Biot's coupled consolidation theory. The expansion was modelled as a one-dimensional plane strain axisymmetric problem. No details of the finite element mesh were given in the paper but it was described that the radius to the outer boundary of the finite element mesh was set at 200 times the final expanded radius. This was established as "more than sufficient to achieve results insensitive to the mesh radius". The prediction was compared with field measurements and modelled the following situations: SBP-Fast test, Undrained SBP test, SBP-Slow test, Piezocone tests at 5.0 and 5.5 m depths.

In the SBP tests, there was good agreement between the predicted and measured total pressure versus strain data, but poor agreement in the pore pressures. The pore pressure dissipation phase was also compared poorly with the CAMFE predictions. It was found that at the beginning of the strain holding phase on reaching the required cavity strain, the cavity pressure had to be dropped almost instantaneously to maintain a constant cavity size. The magnitude of this drop was dependent on the expansion rate, with a greater drop being required for faster expansion and Lee Goh and Fahey (1991) believed that this was mainly a stress relaxation effect. That was, even in a perfectly impermeable soil, the total stress would drop at the start of a strain holding test, with the rate and amount of the reduction being dependent on the rate of expansion.

For the piezocone tests, the total radial stress on the cone shaft after installation was significantly over-predicted by the cavity expansion model. The peak excess pore pressure, and the subsequent dissipation were much better predicted by CAMFE but it was believed that this was likely coincidental.

It was concluded in the paper that numerical modelling of SBP holding tests and piezocone dissipation tests requires a model which incorporates stress relaxation effects.

3.5.2 Driven Piles in Clay

Randolph, Carter and Wroth (1979) described the results of numerical analysis of the effects of installing a driven pile. Pile installation was modelled as the undrained expansion of a cylindrical cavity and the excess pore pressures generated were subsequently assumed to dissipate by means of outward radial flow of pore water. The geometry of the problem was simplified by assuming plane strain conditions in addition to axial symmetry. Modified Cam-clay model was adopted. No details of the finite element meshes used were given in the paper and were probably discussed in two unpublished reports (Randolph and Wroth, 1978 and Carter, Randolph and Wroth, 1979). They performed a parametric study of the effect of the past consolidation history of the soil on the stress changes due to installation of the pile. The results indicated that for any initial value of overconsolidation ratio, the final stress state adjacent to the pile was similar to that in a one-dimensionally normally consolidated soil except that the radial stress was the major principal stress. They presented a method which was used to predict changes in the strength and water content of soil adjacent to a driven pile. The prediction compared well with measurements from two field tests on driven piles. The rate of increase of bearing capacity might be estimated with reasonable accuracy from the rate of increase in shear strength of the soil predicted from the analysis.

3.5.3 Summary

The work described in Sections 3.5.1 and 3.5.2 modelled an undrained cavity expansion in which the changes in stresses and pore water pressure were examined. The numerical analyses appeared to be displacement controlled by assuming a certain rate of expansion at the inner radius. Though the boundary condition is different from that of the hydraulic fracturing described in Chapter 6, in the latter the

pore pressure degree of freedom at the nodes in the cavity was increased with time, it is demonstrated that the finite element mesh chosen in Chapter 6 can also be used to simulate the extreme condition of undrained cavity expansion phenomenon for which closed-form solution is available for validation purpose.

3.6 Coupled Events

There are a number of cases in which it is recognised that coupled loading and drainage problem is an important category of analysis in soil mechanics and foundation engineering. With the implementation of Biot's coupled consolidation theory in the finite element program CRISP (Gunn and Britto, 1982 and 1984; Britto and Gunn, 1987), it is possible to conduct numerical study of such events. Most researchers are only interested in undrained and drained cases which are the extreme conditions in a geotechnical engineering problem and are not concerned about the conditions in-between. This may well be true in certain classes of problems but in the time and drainage dependent behaviour, the stress paths and stress strain conditions of soil are very much affected. This may cause non-uniformities in the internal stresses and strains and thus variations in soil strength in the materials. The numerical studies in Chapter 6 are basically a consolidation problem with the change in the pore pressure degree of freedom at the nodes in the central cavity. Water pressure was increased with time thus simulating a certain rate of loading increase and causing changes in the internal stresses within the cylindrical sample. Hence a coupled analysis is thought to be more relevant. The following sections review some of the published literature which described the use of finite element programs to model coupled events.

3.6.1 Non-uniformities in Triaxial Tests

Carter (1982) predicted non-uniformities in internal stresses and variations in soil strength in triaxial drained compression samples of Weald clay under different axial strain rates using the finite element mesh shown in Fig. 3.3(a). The modified Cam-clay soil model and the Biot's coupled consolidation theory were adopted. He found that as

the strain rate was increased, the response changed from drained to undrained as less and less of the soil sample was able to achieve pore pressure equilibrium. He illustrated the non-uniformity in the triaxial sample for a test conducted at an axial strain rate of 8.33×10^{-6}/s in Fig. 3.3(b), with drainage from the whole surface of the sample. Non-uniformities were shown on the computed contours of the effective mean stress p', deviator stress q', excess pore water pressure u and specific volume v at axial strain of 5%. He demonstrated that the computed effective stress paths for three elements inside the specimen were all different.

Woods (1986a) performed numerical experiments using CRISP to study the loading and consolidation of triaxial test samples. Two groups of analysis were examined: rapid loading followed by consolidation (with drainage conditions as: radial only, radial only and all-round); and loading at different rates with simultaneous drainage (loading rate between 20 and 20000 kPa/hr). The finite element mesh used was similar to the one reported in Carter (1982). Linear strain triangles with pore pressure nodes were used and the modified Cam-clay model was adopted to model the soil. The tests were simulated by applying rapid undrained loading with an increment of total stress $\Delta\sigma_y$ (K_o condition) or Δp (isotropic condition) of 200 kPa. The drainage was 'switched on' by reducing boundary pore pressure to zero in a number of time steps. The time steps must be long enough to allow those nodes nearest the boundary to experience changes in excess pore pressure.

Consolidation time increments were kept small enough to ensure that changes in effective stress were not so large as to cause the yield locus to grow by more than 2 to 4%. The increment of total stress ($\Delta\sigma_y$ or Δp) was subdivided into a number of smaller increments applied over finite time steps. Pore pressures at the drainage boundaries were set to zero from the start. The loading sub-increments were small enough to satisfy the above restrictions on yield locus growth. He reported the development of significant radial variations in water content, and hence shear strength and soil stiffness. These non-uniformities were shown to be a consequence of the boundary conditions for drainage and displacement, and of the rate of application of total stress. The results illustrated the importance of coupled consolidation analysis to improve the understanding of soil behaviour.

Cherrill (1990) used CRISP to perform further numerical analyses to model the triaxial test examining a range of loading types and rates, different drainage conditions and soil states. The modified Cam-clay model was used. Two-dimensional axisymmetric finite element meshes were used and drained and undrained triaxial compression tests were simulated to investigate the magnitude of undissipated and unequalised excess pore pressures, non-uniformity of stress, specific volume and axial strain and the effect of loading rate and excess pore pressure on the values of stiffness measured.

The prediction indicated that the end restraint on triaxial samples significantly reduced shear stresses at the ends although the shear stress distribution over the middle third of the sample was generally reasonably uniform and unaffected by end restraint. The concentration of shear stress in the middle third of a triaxial sample caused greater deformation in this region than in the sample as a whole. Axial strains measured as the relative movement of the platen and top cap can therefore seriously underestimate the axial strains in the middle third of the sample. This error was greatest for undrained analyses on normally consolidated soils and analyses on yielding of overconsolidated soils. The finite element prediction indicated that the axial strains over the middle part of the sample may be 40-50% greater than the overall axial strain for these cases. The degree of dissipation or equalisation of excess pore pressure had little effect on this error except for the case of drained analyses on normally consolidated soils where large excess pore pressures increase the error significantly. The consequence was, provided there were no other errors due to bedding of the sample onto the platens or compliance of the apparatus, the stiffness measured across the middle third of the sample will be less than the stiffness measured across the platens.

3.6.2 Model Tunnel Tests

De Moor (1989) and De Moor and Taylor (1991) reported investigations of time dependent movements associated with tunnelling in Speswhite kaolin clays using small scale model tests and finite element analysis using the program CRISP and full details are described in De Moor

(1989). The three dimensional heading problem was simplified by the conditions of axial symmetry. The geometry was defined by a radial section through the cylindrical model and discretised as shown in Fig. 3.4 and modified Cam-clay model was used. Removal of the face support system was represented by the reduction of the tunnel face boundary pressure to zero in a number of very short time increments in the coupled consolidation analysis and it was found that the magnitude of pressure reduction in each increment had to be sufficiently small to prevent excessive changes in yield ratio. Maintaining a small yield ratio was achieved on a 'trial and error' basis using the STOP/RESTART facility in CRISP until the face support pressure was reduced to zero. The analysis was then continued on an incremental time basis, allowing dissipation of the negative excess pore pressures around the unsupported boundary. The size of the time steps was steadily increased as the pore pressure gradients near the unsupported boundary decreased. A large number of very small time steps was needed to allow the analysis to progress without numerical instability.

3.6.3 Summary

This chapter reviews the published literature which give reasonable results on the applications of finite element analyses incorporating critical state soil models. The numerical modelling of triaxial testing by Carter (1982) and Woods (1986) described in Section 3.6.1 adopted a finite element mesh with smaller finite elements at locations with greatest changes in stress and strain. The axisymmetric mesh used in the numerical studies in Chapter 6 was adapted from this. Carter (1982), Woods (1986) and Cherrill (1990) studied the effects of loading rates on non-uniformities within triaxial samples. The rate effect on the predicted fracturing pressure was similarly examined in the numerical modelling of the hydraulic fracturing experiments. It was pointed out in Woods (1986), Cherrill (1990) and De Moor and Taylor (1991) that the increment size on loading must be sufficiently small to prevent excessive changes in the computed yield ratio. The same approach was used in the numerical modelling described in Chapters 6 and 7.

It was demonstrated the finite element numerical technique, incorporating a critical state soil model with Biot's coupled consolidation theory is capable of making reasonable predictions of non-homogeneous behaviour of normally consolidated clay in triaxial compression and consolidation tests, and time-dependent behaviour of excavation for tunnel heading.

3.7 Parametric Studies on Plate Loading Tests

Sloan and Randolph (1982) performed a numerical prediction of undrained collapse loads on circular footings using the finite element method. The performance of different types of elements: 8-noded and 12-noded quadrilaterals, constant, linear and cubic strain triangles to model the elements under a smooth rigid footing on a plane strain domain with an elastic perfectly plastic Tresca yield criterion was evaluated. The cubic strain triangle was the only element found to be suitable. With lower order elements, the cumulative effect of not being able to satisfy the incompressibility constraints may cause the entire pressure-settlement response to be in error.

Work on numerical analysis of field plate loading tests was reported by Woods & Contreras (1987, 1988). Woods and Contreras (1987) performed benchmarking of the finite element program CRISP for modelling the field plate loading test. They conducted simulation of circular plates at both the ground surface and at the base of a borehole. They tested seven finite element mesh discretisations with a domain size of 14 × 14 plate-radii square. Figure 3.5 shows the boundary conditions of the domain with restraints in movement in both horizontal and vertical movement, except the centre-line where movement was free vertically and the soil surface where movement was unrestrained. Coupled consolidation was not considered so boundary conditions of displacement and loading were specified. Four meshes using linear strain triangles (LST) and three of cubic strain triangles (CuST) were investigated. The benchmarks chosen were those of a flexible and a rigid circular load on an homogeneous, isotropic semi-infinite elastic half-space given by Poulos and Davis (1974). An acceptable agreement with theoretical vertical stress distribution was obtained with mesh CP-07 having 39 CuST's. This mesh was subsequently

adopted in the research described in Chapter 7 in this thesis. In the analysis, linear elastic, homogeneous isotropic and homogeneous anisotropic, elastic-perfectly plastic undrained Tresca and drained Mohr-Coulomb models were used in turn. The analyses with Mohr-Coulomb model produced highly erratic load-settlement curves whereas other analyses generally validated the program in such application.

The down-hole plate analysis was modelled with the same domain size as that of the surface plate analysis with an extra zone included to represent the ground above the level of the plate. The meshes used were based on CP-07 with additional elements to simulate the borehole excavation and overburden. Six CuST meshes were used providing for six different borehole depths (D/B = 0 to 10 in which D and B are the depth and diameter of the borehole). The borehole excavation sequence was modelled as accurately as the stress-strain characteristics demand. One or more elements can be removed in a single step of analysis. It was found if the elements concerned were rather large, removal in one step caused a load change too large for non-linear stress-strain models. In such cases, sub-increments were used in which the elements were physically removed at the start of the analysis increment, but the effects of self weight removal were spread over a number of smaller increments. There were no published analytical solutions available for down-hole loaded plates but there were solutions for the case of a circular flexible or smooth-rigid plate buried in the soil at some depth below the ground surface. Benchmarking was performed by undrained analysis for a flexible plate in an isotropic linear elastic half-space and compared with the analytical solutions obtained by Nishida (1966), and for a smooth-rigid plate in an isotropic elastic half-space and compared with the analytical solutions by Butterfield and Banerjee (1971). Excellent agreement was found in the former whereas the results were within acceptable limits in the latter case when compared with the exact solution. In the analysis, borehole excavation was modelled and provided a means of obtaining the post-excavation soil stress-state. Collapse load computation was obtained using Tresca criterion. The results indicated the important role played by borehole lining and the size of the annular gap between the plate and the borehole wall.

Woods and Contreras (1988) continued to investigate various factors in the plate load test influencing the evaluation of stiffness and strength parameters from field data. A brief investigation of the boundary conditions adopted in their earlier work was undertaken. They based their work on the findings in Carrier and Christian (1973) in which the boundary conditions were relaxed with the bottom boundary free to move horizontally, and the remote vertical boundary was completely unrestrained. They observed that although it demonstrated superior performance, the boundary condition at the bottom was only feasible for linear elastic analysis where self weight effects were not being taken into account. The unrestrained side became unstable in an elasto-plastic soil as it was essentially an unsupported vertical cutting. Hence, these boundary conditions were of little use where more realistic constitutive models were used for the soil. They went on and studied the influence on the evaluation of stiffness and strength parameters from field data by the pore water compressibility, anisotropy, relative plate stiffness, plate/borehole gap at the base of a borehole, borehole lining, overburden pressure and constitutive model. Details of their findings can be found in the report but the point related to pore water compressibility relevant to the work described in Chapter 7 is summarised. They evaluated that for all degrees of anisotropy, $K_f/K' > 100$ can be seen to result in an undrained response.

3.8 Summary

Parametric studies of critical state soil model parameters were studied by some researchers. These examined the influence of the soil model parameters on a particular soil model in making numerical predictions. Stallebrass (1990) found that the parameters T, ψ and the product TS have the greatest influence on the calculated bulk modulus K' and shear modulus G' predicted by the three-surface model. Powrie and Li (1991a) examined the influence of model parameters of the Schofield three-part model in the finite element analysis of an in situ wall using the program CRISP and found that the critical state frictional coefficient and the slope of the no-tension cut-off line had insignificant influence in the numerical solution of the in situ wall problem.

Numerical experiments have many applications in soil mechanics and geotechnical engineering. Researchers have been applying the techniques and performing numerical experiments to evaluate theoretical soil behaviour or analyse the laboratory experiments, model or field tests. There are published works on the applications of finite element analysis in retaining walls (Potts and Fourie, 1984; Fourie and Potts, 1985), direct shear box test (Potts et al, 1987), centrifuged embankment (Almeida, 1984; Almeida et al, 1986), rate effects in triaxial compression test (Carter, 1982), loading and consolidation of triaxial sample (Woods, 1986a; Cherrill, 1990), time dependent movement of tunnel heading (De Moor, 1989; De Moor and Taylor, 1991), application of cavity expansion theory on pressuremeter test (Lee Goh and Fahey, 1991) and driven pile installation (Randolph and Wroth, 1978; Randolph et al, 1979), collapse loads of circular footings (Sloan and Randolph, 1982), surface and borehole plate loading tests (Woods and Contreras, 1987 and 1988). Only those related to the research described in Chapters 5, 6 and 7 were reviewed. Some of the recent modelling studies fall into the coupled consolidation type of analysis, reflecting this has become an important class of investigation in soil mechanics, in addition to the conventional undrained and drained analysis.

In almost all the literature studied, it was found that continued deformation occurred as a function of time or water flow through the porous media and non-uniformities exist within the soil mass, the magnitude of which depends on the rate of load application, and permeability of soil such as in the triaxial compression and consolidation tests. In numerical modelling, numerical difficulties were experienced if the increment of time steps and loading were too large (De Moor and Taylor, 1991). Observation on the calculation of the computed yield ratio and equilibrium percentage error was required to check on the modelling computation accuracy and potential ill-conditioning of the finite element equations. It was only with these checks plus adequate benchmarking then the numerical modelling could provide accurate and meaningful results to complement the experimental and field test data.

CHAPTER 4 COMPUTER HARDWARE AND COMPUTER PROGRAMS

4.1 Introduction

The equipment used in the research includes the hardware and software facilities. A computer program CASIS was developed (Tam, 1987) and run on a micro-computer and a finite element package CRISP was run on the mini-computers. This section describes the hardware used and the algorithm of the program CASIS, its input and output formats, solution strategy, capability and control of drift. The program CRISP has been discussed elsewhere (Britto and Gunn, 1987) and is briefly summarised.

4.2 Hardware

The two types of computer used in this research were a BBC Model B+ micro-computer and a Gould series mini-computer. The former was used to conduct the work in Chapter 5 and the latter was used for the finite element analysis described in Chapters 6 and 7.

The configuration of the Gould mini-computers is shown in Fig. 4.1. The four machines, the main PN9005 and the three PN6040's were linked by the Ethernet. The three PN6040's were integrated by a Network File System which enabled them to be viewed as a single system. The user accessed the system by logging into one of three PN6040's. Each PN6040 computer has an 8 Mbytes RAM with a 680 Mbytes disk storage, whereas the PN9005 has 8 Mbytes RAM but four storage disks each of 340 Mbytes. The machines used the UNIX operating system. They are multi-user systems in which the Computer Unit maintains centralised control. Two 600 line-per-minute printers were connected to the PN9005 and a Hewlett Packard HP7586B plotter provided the central plotting services.

4.3 Computer Program CASIS

This program was developed for the BBC micro-computer using an algorithm implementing the original Cam-clay and modified Cam-clay models (Tam, 1987). It calculated stresses and strains in triaxial

tests using the incremental constitutive equations developed in Section 2.4. It was used to generate the raw data of principal stress or strain components following a specified stress path. The data was stored on disk and used for calculation of the desired parameters using the program BEEBAN (Clinton, 1986).

The original version of the program described in Tam (1987) has been updated so that strain-controlled triaxial drained compression tests for overconsolidated samples can be modelled (Atkinson and Tam, 1988). The implementation allows either model to be chosen for stress-controlled or strain-controlled analyses. The program was used to predict the behaviour of isotropically normally consolidated and lightly overconsolidated soils as a single element. Axial strain or radial strain increments can be controlled in a strain-controlled analysis; while total axial stress, pore pressure or total radial stress increments were controlled in a stress-controlled analysis. A complete listing of the program is given in Tam (1987). The following sections describe the solution strategy, and the input and output formats of the program. Examples using this program are given in Tam (1987). Figure 4.2 shows the flow diagram of the program.

The program was validated by checking its computed results from both models against manual computation of the theoretical solutions. The examples given in Appendix D in Tam (1987) presented the deviator stress q' vs shear strain ϵ_s plots for undrained analysis from which the ultimate deviator stresses q_f' were extracted from the final section of the curves. The shear strength at ultimate state is half this value and it was compared with the theoretical solution of shear strength given in Eqn. (5.1). The results were very close to the theoretical ones and were on the average within 0.5% for Cam-clay and 1.5% for modified Cam-clay in these examples.

4.3.1 Equations of Models

The basic equations of the original Cam-clay and the modified Cam-clay models implemented in the program CASIS were discussed in Section 2.4 and their derivations have been given in Appendices 1 and 2.

4.3.2 Solution Strategy

An incremental solution strategy without equilibrium iteration is used in the program. Accurate and reliable results can only be obtained when the increment size is small enough. However, if the increment size is too small, the computation time becomes excessive. Hence a compromise should be reached in such a manner that the increment size is sufficiently small to yield results in which errors are within an acceptable limit, and yet the computation time would not be too long.

4.3.3 Increment Size on Drift and Growth of Yield Locus

Since the solution strategy adopted an incremental tangent stiffness approach, the stiffness matrix is assembled by assuming piecewise linearity over the increment, whereas the actual characteristics are non-linear. The computed stress or strain increments therefore "drift" away from the true solution. The drift of the stress strain curve increases as larger increments are specified but there is a limit at which the decrease in increment size does not have significant benefit in gaining more accurate results.

The control of this drift was achieved by making use of the calculation of the yield ratio YR, which is the ratio of the pressure at which the loading surface intersects the mean stress axis (p_y') at the end of a typical increment, to the preconsolidation pressure (p_c') corresponding to the current yield locus at the beginning of this increment ($YR = p_y'/p_c'$) (Figure 4.3). If the soil is yielding and hardening then a value of YR greater than one is obtained. Values of YR less than one mean that the soil is either behaving elastically or yielding and softening. When the stress condition changes from A1 to A2 as shown in Fig. 4.3, it remains elastic so a fictitious yield locus is constructed through A2 to give the corresponding p_y' value, YR is therefore equal to p_{yA}'/p_c'. When the stress state changes from B1 to B2, the soil yields and hardens with $p_y' = p_{yB}'$, $YR = p_{yB}'/p_c'$ and is greater than one. The growth of the yield locus is monitored by the numerical computation of YR in order to limit the drift of the stress strain curve.

A study of the effect of the increment size on drift and growth of the yield locus was conducted by computing undrained triaxial compression tests and constant p' compression tests using the original Cam-clay model in CASIS. Figures 4.4(a) and 4.4(b) show the calculated deviator stress at failure q_f plotted against the strain increments and the corresponding stress-strain curves for axial strain increments in the range 0.01% to 2.5% computed for undrained compression analyses. The calculated maximum deviator stress became constant at about 90.5 kPa when the strain increment reduced to a value below about 0.3% and converged to the theoretical solution of q_f = 90.5 kPa by Eqn. (5.1) using the corresponding critical state parameters and the initial specific volume. Figures 4.5(a) and 4.5(b) show the calculated maximum deviator stress plotted against the yield ratio (YR), and the yield ratio plotted against the input strain increments respectively. The computed maximum deviator stress became constant with a yield ratio close to 1.0 (See Fig. 4.5(a)). The yield ratio converged when the increment size was below 0.3% (Fig. 4.5(b)); and the corresponding yield ratio was 1.03 when first yield took place. Hence with a strain increment of 0.3%, a calculated value of maximum deviator stress about 1.2% higher than the true solution was obtained and the drift of the stress-strain curve was regarded acceptable. A maximum yield ratio of 1.03 was therefore set in CASIS to limit the drift of the stress-strain curve in undrained analysis.

Figure 4.6 shows the stress ratio η' plotted against the shear strain for constant p' compression loading calculated for deviator stress increments of 0.1 kPa to 10.0 kPa. Figure 4.7 shows the corresponding computed yield ratio plotted against the stress increments. The increment $\delta q'$ = 1.0 kPa gave a value of shear strain of 16.7% at η' = 0.8 compared with a shear strain of 17.2% for $\delta q'$ = 0.1 kPa. This was about 2.8% less than the true solution at a stress ratio close to η' = M of 0.9 and drift of the stress strain curve was acceptable. The yield ratio had a value of 1.01 when first yield took place. Hence, a maximum yield ratio of 1.01 was set in the program to control the drift in stress-controlled analysis. These limits in maximum yield ratio permit the control of the increment step size by restricting the growth of the yield locus to a fixed value. Values of 1.03 and 1.01 or less for the yield ratio in strained-controlled and stress-

controlled analysis respectively are regarded as leading to sufficiently accurate calculations.

4.3.4 Input

Both interactive keyboard input and file input are available in the program. The interactive input is self explanatory. In the file input, four records are necessary and are described in Tam (1987). These are summarised as follows

(a) Input material parameters M, λ, κ, ν', N (or Γ), and choice of either the original Cam-clay or modified Cam-clay model.

(b) Select either stress- or strain-controlled analysis, and choose either screen or disk-file output.

(b1) Input output data file name (FILE$) if disk-file output is required.

(c) Input initial stress conditions: σ_a, u, σ_r, p_c'.

(d1) Input axial and radial stress and pore pressure increments: $\delta\sigma_a$, δu, $\delta\sigma_r$, and total number of increments in stress-controlled analysis, or

(d2) Input axial and radial strain increments: $\delta\epsilon_a$, $\delta\epsilon_r$, and total number of increments in strain-controlled analysis.

4.3.5 Output

The output for a typical undrained analysis and a constant p' analysis is reported in Tam (1987). The parameters in the output are: κ/λ ratio, G'/K' ratio, the overconsolidation ratio, the values of initial v, κ, λ, N - the specific volume of the NCL at ln p' = 1, and p_c' - the preconsolidation pressure.

The output could be stored in file on disk as requested by the user (See Section 4.3.4 (b)). The user can then use the triaxial test analysis program BEEBAN to calculate the desired parameters. Typical outputs are found in Tam (1987).

Example runs of the program have been performed. The results of a programme of undrained triaxial compression analyses can be found in Tam (1987).

4.4 Computer Program CRISP

The finite element package used for the work described in Chapters 6 and 7 was CRISP. The package, formerly called CRISTINA was developed by the Cambridge Soil Mechanics Group. It was first released in 1982 and updated in 1984 incorporating 3D modelling. Both users and programmers documentation is available for the two versions (Gunn and Britto, 1982 and 1984). Britto and Gunn (1987) documented the theory and the computer code in book form and released the micro-computer version CRISPS on floppy disks. The numerical work described in this report was carried out with the CRISP 1984 version. Validation of the program was conducted before a particular application was examined. The associated work is described in Chapters 6 and 7.

4.4.1 Package Structure

The CRISP package comprises two distinct programs, GEOM (or CRISP GP) and MAIN (or CRISP MP). Both programs are written in Standard FORTRAN IV.

(a) GEOM program

GEOM is a pre-program which reads the geometric details of the finite element mesh defined by the user in terms of vertex node co-ordinates, element-node connectivity, and element types. GEOM generates mid-side and interior nodes, derives the optimised solution order for the

frontal solver and creates a permanent "link" file of geometric data to be subsequently read in by the program MAIN.

(b) MAIN program

MAIN calculates the displacements, stresses and pore pressures caused by the (boundary) loading of a soil body. User input defines the material properties, applied loads, and boundary conditions to be used with the mesh specified in GEOM and stored in the "link" file.

4.4.2 Program Features

(a) Drainage condition

The program can handle calculation of undrained, drained and coupled consolidation events. Section 2.6 has described the finite element application of effective stresses and pore pressure. According to Britto and Gunn (1987), the constitutive matrix in Eqn. (2.61) is used in the following manner:

(i) In an undrained analysis, it expects that the material properties input relate to changes in effective stress.

(ii) When calculating the element stiffness matrices the program adds in the terms corresponding to the volumetric stiffness of the pore water.

(iii) After the finite element equations are solved, the program calculates the changes in effective stresses and pore water pressures separately as shown in Eqn. (2.61).

In an undrained analysis, the bulk modulus of the equivalent pore fluid K_u given in Eqn. (2.56) is normally set to a value between 50 and 500 times K'. The second term in Eqn. (2.61) is the change in pore water pressure due to the volumetric strain experienced by the pore water. Hence, the program calculates the incremental stress and excess pore water pressure separately.

In a drained analysis, K_u is set to zero and no changes in the pore pressures are calculated. In a coupled consolidation analysis, the value for K_u is set to the value of the unit weight of water γ_w.

(b) Element types

CRISP 84 offers two main types of isoparametric triangular elements, linear strain triangles (LST) and the cubic strain triangles (CuST). The LST has 6 nodes (3 vertex, 3 mid-side) giving a total of 12 degrees of freedom, Fig. 4.8(a). Seven Gauss point integration is used, giving exact solutions for a quadratic displacement field. The LST/U element includes excess pore pressure unknowns at the vertex nodes with a total of 15 degree of freedom, and can be used for consolidation analysis, Fig. 4.8(b).

The CuST has 15 nodes (3 vertex, 9 edge and 3 interior) giving a total of 30 degree of freedom per element, Fig. 4.8(c). Sixteen Gauss points are used, and up to 4th order (quartic) displacement fields can be modelled exactly. The CuST/U has 10 additional pore pressure degree of freedom (3 vertex, 6 edge and 1 centroid), as shown in Fig. 4.8(d).

Other element types available include linear strain quadrilateral (LSQ), LSQ with linearly varying excess pore pressures, linear strain brick (LSB), LSB with linearly varying excess pore pressures. They are not described here because only LST and CuST are chosen in the numerical studies in the research described in this thesis.

(c) Soil Models

The following constitutive models are available in CRISP 84:

(i) linear elastic, anisotropic (isotropic being a special case)

(ii) linear elastic, linear variation with depth (Gibson soil)

(iii) elastic-perfectly plastic with Von Mises, Tresca, Drucker-Prager, or Mohr-Coulomb yield criteria

(iv) Cam-clay

(v) Modified Cam-clay

(vi) Schofield's three-part yield surface soil model

(d) Solution Scheme

A tangent stiffness solution scheme is used, in which the global stiffness matrix K is updated in each increment. As no iterative corrections are applied, increments must be kept small for non-linear materials to prevent drift from the true solution. For elastic perfectly plastic models, the stress state may be corrected back to the yield surface at the end of every increment, for those elements in which yield has occurred. The increment size of loading, displacements or time chosen in the research is described in the sections where the problem is examined.

It is claimed that the program can accommodate geometric non-linearity due to large displacements by updating nodal coordinates and revising the B matrix which relates internal strains to nodal displacements in each load increment. This facility was not used in the present work.

(e) Applied Loading

Applied loads can take any of the following forms:

(i) forces applied directly at nodes, in terms of X,Y components,

(ii) tractions along element edges - shear and normal components, or

(iii) self weight body forces, i.e. gravity loading.

(f) Boundary Conditions

Nodes can be fixed in the X and/or Y directions along the appropriate mesh boundaries. Displacement controlled loading is modelled by prescribing movements in the X and/or Y directions. For nodes with excess pore pressure unknowns, drainage boundaries and impermeable interfaces can be simulated; it is also possible to conduct "known change of pore pressure" analysis, by prescribing changes of u.

(g) Initial Stress State

CRISP permits 3 methods of specifying initial stresses:

(i) all stresses set to zero,

(ii) interpolate from values specified at discrete vertical locations in the mesh, or

(iii) specify values directly at every integration point in every element in the mesh.

4.5 Pre- and Post-Processors

The pre- and post-processing programs are: MESHGEN, MPLOT, DISPLAY, DPLOT, CPLOT, GPLOT. They were used to generate meshes, plot undeformed finite element meshes, display numerical results of a CRISP analysis, plot deformed meshes and displacement vectors, plot contours of the results, and plot graphs of any two variables such as calculated stress and strain. They were developed in-house in the Geotechnical Engineering Research Centre by Woods (1986b to 1987f). The programs are written in FORTRAN 77 and make use of the GINO graphics library: GINO-F, GINOGRAF, and GINOSURF (University of Salford, 1981, 1982, 1983).

4.6 Summary

Two computer programs were used in this research. The program CASIS runs on a BBC micro-computer whereas CRISP84 runs on the Gould series mini-computer.

The algorithm of the program CASIS was based entirely on the two critical state soil mechanics models: the original Cam-clay and modified Cam-clay model. The program can simulate either isotropically consolidated undrained or drained triaxial compression loading or unloading following a specified stress path. The loading can be either stress-controlled or strain-controlled by inputting either stress increments or strain increments. The solution strategy adopts an incremental or tangent stiffness method. The control of drift from the true solution is based on the growth of the yield locus from which the yield ratio is computed. Values for strain-controlled undrained and stress-controlled drained tests were examined and appropriate values were chosen in the program as checking point when yielding takes place.

The package CRISP 84 also uses a tangent stiffness solution strategy so increment size chosen in analysing an engineering or experimental problem is crucial to obtain a reasonably accurate solution. Before an increment size was accepted as satisfactory, a series of analysis testing for its effect on the stress-strain behaviour of a soil element was performed. The choice of element types and the mesh discretisation was made after a check on the degree of accuracy obtained and the computer time required in the execution of the program. In the analyses in which CRISP was used, these checks were conducted and will be reported in the corresponding sections in Chapters 6 and 7.

The program CASIS was installed on a personal desk-top micro-computer which was a dedicated system. Hence it is affordable to use an increment size even finer than what is actually required to satisfy the yield ratio control requirement. On the contrary, the Gould series computer was a multi-user system serving the users of the whole City University. There were often times when the execution of CRISP84 was terminated halfway due to the long running time in solving a

problem. In these cases some coarser mesh was chosen provided that this did not significantly reduce the accuracy in the analysis.

CHAPTER 5 PARAMETRIC STUDY OF CAM-CLAY IN TRIAXIAL TESTS

5.1 Introduction

This Chapter describes a numerical parametric study of soil behaviour using the Cam-clay model. Some of the results were presented in Atkinson and Tam (1988) and Tam and Woods (1989). The purpose of the investigation was to examine the variation of calculated soil behaviour with changing values of the soil model parameters over the full range found for most commonly occurring soils. Strength and stiffness characteristics in conventional drained and undrained 'triaxial' compression stress paths have been investigated using the computer program CASIS described in Section 4.3. The program calculated increments of stress (or strain) from increments of strain (or stress) using the simple Cam-clay equations and summed increments to give a calculated stress-strain response. The soil model parameters described in Section 2.4.1 were used and the constitutive equations have been discussed in Section 2.4. The results of the numerical study are grouped under two main headings: undrained compression loading and drained compression loading. The results indicate the degree of relative importance of each of the individual soil model parameters on the selected soil behaviour parameters.

5.2 Characterisation of Soil Behaviour in Undrained and Drained Triaxial Compression Tests

The characteristics of stress, strain and strength in soil can be investigated by examining the state paths and the stress-strain responses under undrained or drained conditions. Numerical modelling of single element conventional undrained and drained triaxial compression loading tests was performed for this study because numerous experimental data from analyses following these two types of stress paths are available for comparison. The total stress path in an undrained compression loading test is defined by $dq/dp = 3$ in q:p space and by definition, there is no volume change. In a drained compression loading test, the effective stress path is defined by $dq'/dp' = 3$ in q':p' space and there are no excess pore water pressures.

5.2.1 States in Cam-clay

It has been discussed in Section 2.2 that the characteristics of soil behaviour in terms of stress-strain response and soil strength depend on the current state of the soil and the stress history. They are also dependent on the direction of the stress path. Figure 5.1 illustrates idealised behaviour of isotropically normally consolidated soil in conventional undrained and drained triaxial compression tests according to the Cam-clay model. For the undrained tests in Fig. 5.1(a) to (d), stress paths and stress-strain curves OYPF and NF correspond to overconsolidated and normally consolidated samples respectively at the same specific volume. Ideally both samples reach the same state on the critical state line (CSL) at F at which they continue to strain at constant state as illustrated in Figs. 5.1(b) and (c). The state paths NF in Figs. 5.1(a) and (d) define part of the state boundary surface on the 'wet' side of critical. The form of the stress path in Fig. 5.1(a) and the stress-strain curve in Fig. 5.1(b) is a function of the elastic volumetric strain ratio κ/λ and this will be discussed in Section 5.2.2. In Fig. 5.1(c) there is a well defined peak stress ratio at Y for the overconsolidated sample. The point Y corresponding to the peak stress ratio lies on the part of the state boundary surface 'dry' of critical. The path OY lies inside the state boundary surface and ideally the path YF lies on the log spiral shaped state boundary surface.

For the drained tests in Figs. 5.1(e) to (h), paths and stress-strain curves NF_1 correspond to a normally consolidated sample and paths and stress-strain curves OPF_2 correspond to an overconsolidated sample with the same specific volume. Ideally both samples reach different critical states (F_1 and F_2 respectively) on the critical state line where they continue to strain at constant state as illustrated in Figs. 5.1(f) and (g). The state path NF_1 in Fig. 5.1(h) indicates compression (reduction in specific volume) for the normally consolidated sample and the state path OPF_2 shows an initial compression followed by dilation for the overconsolidated sample.

From Fig. 5.1, it is demonstrated that three or four states: the initial, yield, peak (for overconsolidated materials on the dry side of critical) and ultimate states could be identified during shearing

as characteristic states for comparison of soil behaviour in triaxial tests.

5.2.2 Selection of Behaviour Parameters to Characterise Soil Behaviour

To characterise soil behaviour, it is essential to choose certain parameters which allow comparison of the same basic properties at the four selected states, the initial, yield, peak and ultimate states as discussed in the previous section.

Figure 5.2 illustrates the idealised stress-strain curve of an isotropically overconsolidated sample in an undrained triaxial compression test. The differences between the tangent modulus and secant modulus at the same stress and strain level are shown. Because the constitutive relationships in Cam-clay are incremental and the stiffness parameters are expressed over small increments, the tangent stiffness has been used throughout this study.

Figure 5.3 shows the stress-strain and pore pressure-strain responses used to characterise soil behaviour in an undrained test and volumetric strain-shear strain relationship in a drained test. The deviator stress q' and pore pressure u have been normalised by the specific volume v and effective mean pressure p' at the current state of soil. Equations (2.24), (2.25), (2.26) and (2.27) show the advantage of this normalising procedures as this enables the stress state or strain state to be dependent only on the critical state soil parameters (M, λ, κ and α') and the current stress ratio $\eta' = q'/p'$. In Fig. 5.3(b), the normalised pore pressure response is plotted against shear strain for undrained tests for normally consolidated and heavily overconsolidated samples. The slopes of the curves show the rates of pore pressure change. The slopes of the volumetric strain-shear strain curves in Fig. 5.3(c) for drained tests show the rates of dilatancy.

In the initial elastic range soil usually exhibits a much stiffer response than after yielding has taken place. When the state reaches A in the stress-strain curve in Fig. 5.3(a), this corresponds to point

Y in Fig. 5.1(a) where the state of the soil reaches the state boundary surface. The range from initial loading to yielding defines the initial elastic range within the state boundary surface. In an undrained test, the initial normalised tangent shear modulus $3G_o/(vp')$ and the initial normalised rate of pore pressure change $[du/(vp'd\epsilon_s)]_o$ have been chosen to characterise the initial state. In a drained test, in addition to the initial normalised tangent modulus, the initial normalised bulk modulus $K_o/(vp')$ and the initial rate of dilatancy $(d\epsilon_v/d\epsilon_s)_o$ have been selected.

After the soil yields at A (Fig. 5.3(a)), the stress state moves along the path ABC in which plastic deformation starts to take place. From this level of straining the state moves along YP on the state boundary surface in Fig. 5.1(a). Thus A is the point at which plastic irrecoverable strains first occur. The strain ϵ_{sy}, the normalised tangent modulus $3G_y/(vp')$, the normalised rate of pore pressure change $[du/(vp'd\epsilon_s)]_y$ for an undrained test, the normalised bulk modulus $K_y/(vp')$ and the rate of dilatancy $(d\epsilon_v/d\epsilon_s)_y$ for a drained test, all at this yield strain, have been selected for comparison.

When the state reaches C the deviator stress reaches its peak value and is related to the peak shear strength. This corresponds to the peak point at the state boundary surface in Fig. 5.1(a) for undrained tests. The peak shear strength is associated with soil at states dry of critical. The state at the peak stress ratio coincides with that of the yield state in Figs. 5.1(a) and 5.1(c). The strains ϵ_{sp} at which the deviator stress reaches its peak, the peak deviator stress q_p', the normalised rate of pore pressure change $[du/(vp'd\epsilon_s)]_p$ in an undrained test have been chosen. For drained tests the state at peak deviator stress coincides with that immediately after yield as illustrated in Fig. 5.1(e).

On passing the peak point C, the state approaches the ultimate condition E along CDE. This corresponds to the path PF in Fig. 5.1(a) for an undrained test or PF_2 in Fig. 5.1(e) for a drained test. The ultimate state usually occurs at very large strains at which the rate of pore pressure change in an undrained test and the rate of dilatancy in a drained test are zero. The strain ϵ_{sf} at this critical state and the ultimate deviator stress q_f' are selected. This ultimate deviator

stress is related to the critical state undrained shear strength in Eqn. (2.12) and may also be expressed simply as

$$s_u = \frac{1}{2} M \exp\left[\frac{(\Gamma - v)}{\lambda}\right] \tag{5.1}$$

In order to examine the state boundary surface state paths should be normalised with respect to the equivalent pressure p_e' or the equivalent specific volume v_λ. These parameters have been shown geometrically in Fig. 2.1. For a particular state S at which the current values of stress and specific volume are p' and v respectively, the relationships for p_e' and v_λ are given by

$$p_e' = \exp\left[\frac{(N - v)}{\lambda}\right] \tag{5.2}$$

$$v_\lambda = v + \lambda \ln p' \tag{5.3}$$

As indicated in Section 5.2.1, the form of the undrained effective stress path is a function of the elastic volumetric strain ratio κ/λ. This is given by the following equation:

$$q' = \frac{Mp'}{1 - \frac{\kappa}{\lambda}} \left(\ln \frac{p_e'}{p'}\right) \tag{5.4}$$

Higher values of κ/λ produce stress paths and stress-strain curves with higher peak q' values after yielding but before the critical state in undrained paths for overconsolidated materials dry of critical. The dependence of the undrained stress path on κ/λ and other critical state soil parameters are derived in Appendix 3. From Eqn. (5.4), the shape of the undrained effective stress path depends on the value of the factor $(1 - \kappa/\lambda)$ or κ/λ while the value of p_e' determines the size of the yield locus.

In this Section, behaviour parameters have been selected to characterise soil behaviour at initial, yield, peak and ultimate conditions. These have been plotted against the fundamental soil

model parameters, e.g. λ, M, κ/λ and α' to investigate relative sensitivity of soil behaviour to these basic soil model parameters.

5.3 Choice of Values for Input Parameters

The fundamental soil parameters and stress history discussed in Section 2.4 were varied in this parametric study to investigate the effects on the soil behaviour described in Section 5.2. These soil parameters can be determined from appropriate laboratory testing and their values fall within limits governed by the soil type. The range of values selected in this study is based on a review of laboratory test data summarised in Table 5.1. The program of study is tabulated in Table 5.2.

5.3.1 The Range of Values of Fundamental Soil Parameters

The frictional parameters M discussed in Section 2.4.1 is a function of the friction angle ϕ_c', the value of which is governed by a number of factors. Firstly, whether the material type is clay, sand or mixed soil. The value of ϕ_c' generally ranges from low values for clay to higher values for sand. Secondly, for a clay material, it varies with its plasticity, from around 18° for higher plasticity clay to about 25° for low plasticity clay. For granular materials, ϕ_c' varies with mineralogy, from around 33° for quartz to about 40° for feldspar (Bolton, 1986). Some unusual soils such as carbonate sands have ϕ_c' values as high as 45° but these were not considered in this study. A range of friction angle between 20° to 35° was chosen. The corresponding M values in triaxial compression are between 0.77 and 1.4. This range covers the soil types in Table 5.1.

The slope of the isotropic normal consolidation line in v:ln p' plane is directly proportional to the plasticity index PI (λ = PI/171 given by Schofield and Wroth, 1968). Table 5.1 shows that the undisturbed lodgement till has the lowest value of 0.037 (Little, 1985) while the Thameside alluvial clay at East Ham tested by Pickles (1989) has a high value of 0.33 with an average of 0.27 due to large variation in organic contents between 2% and 10%. A range of values 0.05 to 0.35

has been chosen, covering materials from very low compressibility such as sands to highly compressible materials such as clays.

The elastic volumetric strain ratio κ/λ describes the proportion of elastic to total volumetric strain during normal consolidation. Sands usually have low values of both λ and κ, while clays have higher values. However, the differences between κ values for clay and sand materials may not be very much. The result is that sands have higher values of κ/λ than clays. Table 5.1 shows that the lodgement till has the highest κ/λ value of 0.51 (Little, 1985) while the deep ocean sediment tested by Ho (1985) has the lowest value of 0.018. A range from 0.1 to 0.5 has been chosen.

Values for the elastic stiffness ratio α' chosen were between 0.75 and 0.33 which correspond to Poisson's ratios between 0.2 and 0.35. These generally cover the range of values for sandy soils which have Poisson's ratios of 0.15 to 0.25 and for clays which have values in the range 0.30 to 0.40 (Barkan, 1962). Pickles (1989) reported a Poisson's ratio of 0.25 for the reconstituted organic clay from East Ham, whereas De Moor (1989) reported a value of 0.3 for Speswhite kaolin. Unusual carbonate sands which have Poisson's ratios of near zero were not considered in this study.

The specific volume of the normal consolidation line corresponding to unit mean pressure is defined by N. Since λ and κ were taken as the independent parameters and varied as described above, the values of N were calculated using Eqn. (2.20) developed from the Omega (Ω) point described in Section 2.4.1. It varied in the range between 1.735 and 4.788. Values of Γ were calculated using Eqn. (2.19) and varied in the range between 1.710 and 4.473. These ranges contain the experimental values of N and Γ given in Table 5.1.

5.3.2 The Stress History

A preconsolidation pressure of 200 kPa was used in all the numerical analyses. Isotropically normally consolidated soil was loaded in triaxial compression from this initial pressure of 200 kPa without any prior swelling. Overconsolidation was achieved by allowing the soil

to swell to a pre-determined pressure before loading in triaxial compression stress paths. In CASIS, this was specified in the initial stress conditions as discussed in Section 4.3.4. Confining pressures of 150 kPa and 50 kPa after swelling were selected corresponding to lightly overconsolidated samples (on the wet side of critical) with OCR = 1.33 and overconsolidated samples (on the dry side of critical) with OCR = 4.0.

5.4 Numerical Computations

5.4.1 Computer Program (CASIS) and Modifications

The program CASIS described in Section 4.3 was used in all the numerical analyses. The program has the facilities to use both the Cam-clay and the modified Cam-clay models, but only the former model was used in this study. The program can be used to calculate stress or strain increments in either strain- or stress-controlled analyses. The desired stress path was defined by the user by specifying the appropriate stress or strain increments. The original version has been updated such that strain-controlled computation of drained compression loading for overconsolidated samples may be performed. This was implemented simply by expressing the stress increments in terms of the strain increments. An incremental solution strategy without equilibrium iteration (Sec. 4.3.2) was used. Accurate and reliable results can only be obtained when the increment size is small enough as discussed in Section 4.3.3.

5.4.2 Selection of Increment Size

As discussed in Section 4.3.3, the control of drift was achieved by selecting small enough increments of stresses or strains. In this study, strain increments from 0.005% to 0.01% were used to achieve sufficient accuracy in strain-controlled analyses, while stress increments varying from 0.1 kPa to 1.0 kPa were used in stress-controlled analyses. These increments were smaller than the required values discussed in Section 4.3.3 because of the advantage of using a totally dedicated micro-computer as described in Section 4.6.

5.4.3 The Numerical Experiments

Undrained and drained triaxial compression loading tests were modelled in the numerical experiments. To model the undrained triaxial compression test, a shear strain increment was applied such that there was no volumetric strain. The corresponding deviator stress increment and mean stress increment were calculated and summed to give a stress-strain response. In modelling the drained triaxial compression test, a stress-controlled analysis required the input of the stress increments, i.e. dq' and $dp' = dq'/3$ to compute the strain increments and then summed to give a stress-strain response. If strain-controlled analyses were used in drained compression tests, axial and radial strain increments were input to compute stress and volumetric strain increments. The latter had to be used for drained compression analyses on overconsolidated materials because instability occurred when strain softening took place in stress-controlled computation.

The parameters tabulated in Table 5.2 were used to calculate the stress-strain response in these two types of loading paths. The numerical results were examined at the initial, yield, peak and ultimate states as discussed in Section 5.2 and the results for undrained and drained behaviour are presented separately.

5.5 Numerical Results and Discussion - Undrained Behaviour

Table 5.3 was derived after detailed observation and analyses on the normalised plots of the behaviour parameters versus the fundamental soil model parameters for the undrained compression loading and summarises the ranges and form of changes (or variations). The form of the variations is categorised as linear or non-linear. The ranges are tabulated in terms of magnitude of increase or decrease (denoted as 'i' or 'd' respectively in Table 5.3 after the magnitude of variations) of the value of the behaviour parameters over the chosen full range of critical state soil model parameters. The magnitude of the variations were derived from the normalised plots. Table 5.4 presents the relative degree of dependence of each undrained behaviour parameter on the fundamental soil model parameters based on a rating

system discussed later in Section 5.7. Representative curves are selected for illustration in Figure 5.4 to 5.27(b).

5.5.1 Initial States

The Cam-clay model assumes that materials exhibit elastic behaviour when the stress state is inside the state boundary surface. Equations (2.24) and (2.25) illustrate that when the elastic shear and volumetric strain increments are separated from the total strain increments, the normalised tangent modulus $dq'/(d\epsilon_s^e vp')$ is a function of α' and κ. The variations in values in Fig. 5.4 are very large and in the order of 10 times at the lower range of κ from 0.005 to 0.05. For the full range of κ between 0.05 and 0.175, the variations are as high as 36 times (see Table 5.3). Equation (2.24) could be re-written as

$$\frac{dq'}{(vp'\ d\epsilon_s^e)} = \frac{3\alpha'}{\kappa} \qquad (5.5)$$

which shows that the normalised tangent modulus is a linear function of $(1/\kappa)$. Because of normalising by the specific volume v and effective mean pressure p' at the current state, the initial normalised tangent modulus is independent of the overconsolidation ratio OCR.

Figures 5.5 and 5.6 show that the initial rate of pore pressure change $[du/(vp'd\epsilon_s)]_o$ is independent of OCR and M when the state is inside the state boundary surface and there is no change in effective mean stress p'. The Cam-clay model also predicts that the initial rate reduces 7 times with increasing λ over the range between 0.05 and 0.35 (Fig. 5.7 and Table 5.3). Figures 5.5 to 5.7 illustrate that $[du/(vp'd\epsilon_s)]_o$ has strong dependence on λ and κ/λ. It is moderately dependent on α'. For normally consolidated material, the model predicts that the initial rate of pore pressure change is the same as that immediately after yield because the material starts yielding as soon as strains develop. The rate depends slightly on M because the pore pressure is implicitly a function of M which is contained in the effective stress equations.

5.5.2 Yield States

Figures 5.8 to 5.16 show typical plots of the behaviour parameters immediately after yield against the fundamental soil model parameters. When the state reaches the state boundary surface, plastic irrecoverable strains begin to develop. The soil behaviour is characterised by the normalised tangent modulus, the shear strain and the normalised rate of pore pressure change at this strain or stress level as discussed in Section 5.2.2. Figures 5.8 to 5.11 show that the model predicts the normalised tangent modulus increases when M and α' increase, and λ, κ/λ and OCR decrease for materials on the wet and dry sides of critical. The most influential parameters are κ/λ and OCR. It is moderately dependent on M, λ and α'.

The model predicts that normally consolidated materials yield as soon as shearing takes place. Therefore, the yield strain is infinitesimally small. Figures 5.12 to 5.15 show the typical yield strains for materials on the wet and dry sides of critical. In Fig. 5.12, the yield strains for these ranges of M, λ, κ/λ of lightly overconsolidated materials with $\alpha' = 0.75$ would range from 0.05% to 1% which is a relatively low strain level. For the same ranges of materials with $\alpha' = 0.33$ in Fig. 5.13, these range from 0.1% to 2.5%. The results for overconsolidated materials dry of critical in Figs. 5.14 and 5.15 show the yield strains ranging from 0.2% to 5% and 0.4% to 11% for $\alpha' = 0.75$ and 0.33 respectively. The most influential parameters are κ/λ, OCR and λ; the parameters M and α' are of moderate importance.

Figure 5.16 shows that the normalised rate of pore pressure change varies with λ and M. The data points of normally consolidated and lightly overconsolidated materials are positive values while those of the overconsolidated materials dry of critical are negative. This indicates that the model predicts heavily overconsolidated materials tend to dilate as soon as yielding occurs. For the normalised rate of pore pressure change, λ and κ/λ are the most influential parameters followed by OCR and α'. The parameter M is of slight importance.

5.5.3 Peak States

As discussed in Section 5.2.2, the peak states are associated with overconsolidated materials dry of critical and with κ/λ ratios greater than zero. The peak states refer to states at peak deviator stress q'. For materials on the wet side of critical, the peak states coincide with the ultimate states. The strains ϵ_{sp} at peak deviator stress in Figs. 5.17 and 5.18 are typical for $\alpha' = 0.75$ and 0.33 with OCR = 4.0. Inspection of Figs. 5.14 and 5.17, Figs. 5.15 and 5.18 indicates that the strains immediately after yield and at peak are the same for materials with $\kappa/\lambda = 0.367$ and 0.5. The strains at peak deviator stress for materials with $\kappa/\lambda = 0.1$ and 0.233 are higher than those immediately after yield. The parameter κ/λ is the most influential while λ and α' are of moderate importance. The OCR and M have a slight degree of influence on the peak strain.

The rate of pore pressure change reached its peak on yielding and started to decrease after the yield state. Comparison of Figs. 5.16 and 5.19 shows that when the peak state is reached, the rate has decreased by about 2 to 3 times for materials having $\alpha' = 0.75$ and $\kappa/\lambda = 0.1$. The most important parameter is λ followed by M and then κ/λ. It is independent of α'.

The peak shear strength shown in Figs. 5.20 and 5.21 is based on the peak deviator stress. The parameter M is important in the prediction of the peak shear strength while κ/λ is only slightly important. λ and α' appear to have no influence at all on the shear strength although Eqn. (5.1) shows that the undrained strength is expressed in terms of λ. This is due to a constant ratio of the difference between the chosen input parameters Γ and the specific volume v, to the λ value.

5.5.4 Ultimate States

The ultimate or critical state is reached when the material continues to suffer shear strains at constant state - that is, at constant deviator stress, at constant stress ratio and at constant excess pore pressure. The normalised ultimate deviator stress plots shown in

Figs. 5.22(a), 5.23(a) and 5.24(a) for normally consolidated materials reveal that the ultimate strength has strong dependence on λ followed by M. The parameters κ/λ, α' and OCR have no influence at all on strength as the data points cluster almost on a smooth line irrespective of the κ/λ values. This is the same for samples on the dry side of critical.

The undrained shear strength s_{uf} plots shown in Figs. 5.22(b), 5.23(b) and 5.24(b) indicate its moderate dependence on M, κ/λ and OCR. It does not depend on λ due to the constant term $(N - \kappa)/\lambda$ as discussed in the previous sub-section for the peak shear strength.

Figures 5.25 and 5.26 show the strain ϵ_{sf} at ultimate or critical state for a normally consolidated and an overconsolidated material both with $\alpha' = 0.75$. They show the ultimate strain ranges from 2% to 28% for the normally consolidated, 2% to 24% for the overconsolidated materials. It has strong dependence on λ and κ/λ. It is moderately dependent on M. Comparison of the results in Figs. 5.25 and 5.26 indicates that the OCR is of slight importance. It is independent of α'.

5.5.5 State Boundary Surfaces

Figures 5.27(a) and 5.27(b) show the constant volume sections through the normalised state boundary surfaces of the range of κ/λ values for two typical M values of 0.77 and 1.4 respectively. The state paths have been normalised with respect to the equivalent pressure p_e' and the equivalent specific volume v_λ based on Eqns. (5.2) and (5.3). The model predicts the normally consolidated materials having state paths followed the appropriate curves of the state boundary surface on the wet side of critical depend on κ/λ and approach the ultimate or critical state. For lightly and heavily overconsolidated materials, the state paths are vertical and straight when the state is inside the state boundary surface. Figure 5.27(a) illustrate two state paths, both for $M = 0.77$, $\lambda = 0.35$ and $OCR = 4.0$ at the dry side of critical, one with $\kappa/\lambda = 0.1$ (Path (1)) and the other with $\kappa/\lambda = 0.367$ (path (2)). Their paths inside the state boundary surface do not coincide. When these state paths meet the state boundary surface, they follow a

log spiral path and approach the ultimate state. The state path with $\kappa/\lambda = 0.1$ rises towards a peak value after yield and then reduces to the ultimate state. The one with $\kappa/\lambda = 0.367$ has a yield point which coincided with the peak state.

5.6 Numerical Results and Discussion - Drained Behaviour

Figures 5.28 to 5.39 show some of the results from the Cam-clay prediction on the drained behaviour. Table 5.5 summarises the observation and analyses on the ranges and form of changes (or variations) in the drained behaviour parameters. Table 5.6 presents the relative degree of dependence of each drained behaviour parameter on the fundamental soil model parameters based on the same rating system for undrained behaviour parameters to be discussed in Section 5.7.

5.6.1 Initial States

The initial states in drained analyses are characterised by the initial normalised tangent and bulk moduli, and the rate of dilatancy. The initial tangent moduli in drained analyses are the same as those in Figs. 5.4 presented for undrained analyses. The theoretical relationship of the initial normalised bulk modulus is obtained by rewriting Eqn. (2.25) as

$$\frac{dp'}{(vp'\ d\epsilon_v^e)} = \frac{1}{\kappa} \qquad (5.6)$$

Therefore, the initial normalised bulk modulus $K_o/(vp')$ is equal to $(1/\kappa)$. Figure 5.28 shows the plot of this relation and indicates the strong dependence of this behaviour parameter on κ.

On resolving Eqns. (2.24) and (2.25) the initial rate of dilatancy is expressed as

$$\left(\frac{d\epsilon_v}{d\epsilon_s}\right)_o - \frac{d\epsilon_v^e}{d\epsilon_s^e} - 3\alpha' \left(\frac{\delta p'}{\delta q'}\right) \qquad (5.7)$$

However, normally consolidated materials yield as soon as strains develop. Therefore, the initial rate of dilatancy is the same as the rate of dilatancy immediately after yield for normally consolidated materials. Figures 5.29 and 5.30 show the typical plots of $(d\epsilon_v/d\epsilon_s)_o$ versus λ and M respectively. The rate of dilatancy has strong dependence on OCR and α', and is moderately dependent on M and slightly dependent on κ/λ. It is independent of λ.

5.6.2 Yield States

The yield states are characterised by the normalised tangent and bulk moduli, the yield strain and the rate of dilatancy. The typical normalised tangent modulus $3G_y/(vp')$ for $\alpha' = 0.75$ and OCR = 1.0 shown in Fig. 5.31 indicates significant variations at the lower range of λ from 0.05 to 0.15. Figure 5.32 shows the decrease in normalised tangent modulus with increasing OCR. The most influential parameter on the normalised tangent modulus is λ followed by M and OCR. It is slightly dependent on κ/λ and α'.

The normalised bulk modulus $K_y/(vp')$ shown in Fig. 5.33 for OCR = 1.0 decreases significantly at the lower range of λ from 0.05 to 0.15. It is independent of α'. The variations of $K_y/(vp')$ are small with respect to OCR as shown in Fig. 5.34. λ is the most influential, M and κ/λ are moderately important, and OCR is only slightly important in the prediction of the normalised bulk modulus.

Figures 5.35 and 5.36 show the typical yield strain ϵ_{sy} for overconsolidated materials on the wet side and dry side of critical respectively. The yield strains in Figs. 5.35 and 5.36 range from 0.1% to 0.8% and 0.1% to 4% for overconsolidated materials wet and dry of critical respectively. The data points show that the materials yield at a relatively low strain level. The yield strain is strongly dependent on λ and κ/λ, moderately dependent on α' and OCR and slightly dependent on M.

The rate of dilatancy immediately after yield has been illustrated together with the initial rate in Figs. 5.29 and 5.30. The OCR is the most influential parameter, M is moderately influential, α' and κ/λ are slightly influential. The rate is independent of λ.

As discussed in Section 5.2.2 for drained characteristic states, the yield state coincides with the peak state for states on the dry side of critical. The peak state coincides with the ultimate state for states at the wet side of critical.

5.6.3 Ultimate States

At ultimate state, the soil behaviour is characterised by the ultimate deviator stress, the normalised deviator stress and the shear strain. The normalised ultimate deviator stress $q_f'/(vp')$ shown in Fig. 5.37(a) is moderately dependent on λ and M. It is independent of α', κ/λ and OCR. The ultimate deviator stress q_f' increases with increasing M, but decreasing OCR as shown in Fig. 5.37(b). It is independent of α', λ and κ/λ .

Figure 5.38 to 5.39 illustrate the ultimate shear strains ϵ_{sf} plotted against λ. These range from 17% to over 400% for normally consolidated materials, and from 8% to over 70% for materials dry of critical. These results indicate the high level of straining before the ultimate or critical state is reached for some materials in drained tests as predicted by the Cam-clay model. The ultimate shear strain has moderate dependence on λ and M, and is independent of κ/λ, α' and OCR.

5.7 Summary

The parametric study of the undrained and drained behaviour using the Cam-clay model has generated a very large amount of data, even with extensive use of normalising techniques. Tables 5.3 and 5.5 summarise the analyses and observation on the ranges and form of the changes in the undrained and drained behaviour parameters from Cam-clay predictions. Tables 5.4 and 5.6 are produced after an assessment on

the quantitative data in Tables 5.3 and 5.5. A rating system is used in Tables 5.4 and 5.6 to indicate the dependence of any given behaviour parameters on a fundamental soil model parameter as follows:

*	no dependence
**	slight dependence (1 to 1.5 times over the full range)
***	moderate dependence (1.5 to 2 times over the full range)
****	strong dependence (>2 times over the full range)

The degree of relative dependence in the above rating system is based on the degree to which the behaviour parameters vary over the full range of values of the fundamental soil model parameters chosen. This provides a qualitative assessment on which fundamental soil model parameters are critical or important in the determination of the behaviour parameters in real testing in geotechnical engineering analysis and design. In determining independent parameters, use was made of the Omega point concept (Schofield and Wroth, 1968) described in Section 2.4.1 which essentially relates N and Γ to λ. The initial specific volume and hence strength are therefore dependent to some extent on λ.

5.7.1 Undrained Behaviour

The initial state is characterised by the normalised tangent modulus and the initial rate of pore pressure change. On the whole, they have strong dependence on the elastic volumetric strain ratio κ/λ and the elastic stiffness ratio α'. This is so because the behaviour parameters in the initial state are functions of the elastic soil model parameters.

The yield state is characterised by the yield strain, the normalised tangent modulus and the rate of pore pressure change. They have strong dependence on most of the Cam-clay soil model parameters in the order κ/λ, λ, OCR, α' and M. Before the soil starts yielding and immediately after yield, the elastic soil parameters have dominant influence in the stress-strain response of the soil in the Cam-clay prediction. This is reflected by the order of dependence in the above.

The peak state is characterised by the peak strain, the peak shear strength and the peak rate of pore pressure change. They have strong dependence on the soil model parameters in the following order: κ/λ, M, λ, α' and OCR.

The ultimate state is characterised by the ultimate strain, the ultimate shear strength and the normalised deviator stress. The soil model parameter M is equally influential to the three behaviour parameters. λ has strong influence on the ultimate strain and normalised deviator stress while κ/λ has strong influence on the ultimate strain and moderate influence on the ultimate shear strength. Finally, OCR has moderate influence on the ultimate shear strength, and slight influence on the ultimate strain. The behaviour parameters at ultimate state are independent of the elastic stiffness ratio α'.

As discussed in Section 5.2.2, the form of the stress path in Fig. 5.1(a) and the stress-strain curve in Fig. 5.1(b) would be a function of the elastic volumetric strain ratio, κ/λ. Figures 5.27(a) and (b) have demonstrated this for M = 0.77 and 1.4. The height of the yield locus grows with increasing κ/λ values. Higher values of κ/λ produce stress paths and stress-strain curves with higher peak q' values after yielding but before the critical state in undrained paths for overconsolidated materials. This indicates that materials having higher values of κ/λ behave elastically in a large proportion of their stress state.

5.7.2 Drained Behaviour

The initial state is characterised by the normalised tangent modulus, the normalised bulk modulus and the initial rate of dilatancy. The moduli have strong dependence on κ/λ and are independent of other soil model parameters except that the normalised tangent modulus is also strongly dependent on α'. The initial rate of dilatancy has strong dependence on α' and OCR, and is moderately dependent on M and slightly dependent on κ/λ.

The yield state is characterised by the yield strain, the normalised tangent and bulk moduli and the rate of dilatancy immediately after

yield. The normalised tangent modulus has strong dependence on λ, M and OCR, and slight dependence on κ/λ and α'. The normalised bulk modulus has strong dependence on λ, moderate dependence on κ/λ and M, and slight dependence on OCR. The yield strain has strong dependence on λ and κ/λ. It is moderately dependent on α' and OCR and slightly dependent on M.

The ultimate state is characterised by the ultimate strain, the deviator stress and the normalised deviator stress. The ultimate strain is strongly dependent on λ, M and OCR, and is moderately dependent on κ/λ. The ultimate deviator stress is strongly dependent on M and OCR; whilst the normalised ultimate deviator stress is moderately dependent on λ and M. All the behaviour parameters at ultimate state are independent of α'.

CHAPTER 6 NUMERICAL EXAMINATION OF HYDRAULIC FRACTURING IN A TRIAXIAL SPECIMEN

6.1 Introduction

One of the primary causes of failure in embankment dams is believed to be the hydraulic fracturing of the clay core. A program of work has been carried out to assess the susceptibility of a number of older embankment dams to this manner of failure. The research involved experimental studies of the mechanisms involved in hydraulic fracturing (Mhach, 1991). Numerical investigation of the phenomenon was also conducted to model the laboratory experiments. The numerical results provide some understanding of the hydraulic fracturing phenomenon and complement the laboratory testing. In the laboratory experiments, water pressures were increased at a given rate in the central cavity of a cylindrical clay sample via a hypodermic probe as shown in the experimental set-up in Fig. 6.1 until fracturing occurred, and as there was strong evidence of dependency of fracturing pressure on this rate of increase the problem may be classified as coupled. Paraffin as injecting fluid was used in some other series of the laboratory experiments in order to achieve an undrained effect. The latter work was not simulated and the experimental work is described in Mhach (1991). The effect of overconsolidation on the fracturing pressures was also examined (Tam et al 1988, Atkinson and Tam, 1991a).

This Chapter describes the finite element computations designed to simulate the laboratory experiments and to permit the investigation of rate, bore size and overconsolidation effects. Validation of the finite element meshes and soil models is also presented.

6.2 Finite Element Simulation

Numerical studies have been made of the hydraulic fracturing tests on cylindrical specimens using the CRISP finite element package, developed by the Cambridge Soil Mechanics group (Gunn & Britto, 1982, 1984). The program CRISP was described in Section 4.4 and its limitations were described in Section 3.3.6. In the laboratory

experiments, sand was placed in a 25 mm long by 6 mm or 16 mm diameter cavity in the clay specimen to prevent collapse of the cavity during consolidation stage. The outer diameter of the cylindrical sample was 38.2 mm. When an equilibrium condition was achieved, water pressure in the sand cell was increased by injecting water into the cavity via a hypodermic probe through the top cap (Fig. 6.1). The volume of water which entered the system was observed with time, and the test specimen cracked when there was a sudden increase in water inflow into the system (Mhach 1991, Tam et al 1988). In the finite element modelling, simulations have been carried out by discretising both the clay specimen and sand cell. Several loading simulations were attempted: undrained and drained applied pressure loading in the cavity, and cavity water pressure increment at the needle/sand contact (or nodes). These were tested to obtained the best approach to simulate the actual conditions in the experiments.

6.2.1 Finite Element Mesh

Two different types of mesh were used: plane strain mesh from Figure 6.2(a) to 6.2(d), and axisymmetric mesh in Figure 6.3(a) and 6.3(b).

Due to symmetry the plane strain mesh only models one quadrant of a plan cross-section through the soil sample. Both the sand and clay are modelled with 6-noded linear strain triangle consolidation elements (LST/U shown in Fig. 4.8(b)) for Mesh HF005 (6 mm diameter cavity) in Fig. 6.2(a) and for Mesh HF211 (16 mm diameter cavity) in Fig. 6.2(d). There are eighty elements in the Mesh HF005 and one hundred elements in the Mesh HF211. The meshes are graded in the radial direction, being finer near the cavity. The pore pressure degree of freedom in the sand element nodes adjacent to the probe was increased incrementally over uniform time steps in the simulation.

In the axisymmetric mesh, a radial section has been modelled. The sand and clay are modelled with eighty-eight linear strain triangle consolidation elements whereas the top platen and hypodermic probe are modelled with sixteen linear strain triangles (Mesh HF100 for 6 mm diameter cavity in Fig. 6.3(a) and Mesh HF101 for 16 mm diameter cavity in Fig. 6.3(b)).

The plane strain mesh HF005 was primarily used in the plane strain analyses. It was tested for its degree of accuracy with respect to fineness, possible stress concentrations and adequacy in evaluating the stress-strain-pore pressure changes by comparing results from two finer meshes: HF105 and HF205 (Figs. 6.2(b) and 6.2(c)) with respectively 100 and 140 LST/U's. The results are discussed in Section 6.3.1.

The axisymmetric mesh was derived after a review of the work in Carter (1982) and Woods (1986) discussed in Section 3.6.1. The mesh is graded finer near the hypodermic probe where the pressure gradient is expected to be the highest. There are no discontinuities or corners in the two meshes HF100 and HF101. The results in displacements and deformations were closely examined and it was observed that the problem did not induce significant displacements and the calculated deformations will be shown later in Section 6.5.3.

6.2.2 Constitutive Models and Soil Properties

In the selection of material models to describe soil behaviour, the modified Cam-clay model was used to model the clay behaviour in the meshes described above. The modified Cam-clay model was chosen because it has been used successfully for modelling normally consolidated and lightly overconsolidated materials (Wroth 1977; Almeida, 1984 and Almeida et al 1986). In the programme of analyses discussed in Section 6.2.7 and summarised in Table 6.1, Groups A and B were analyses for the normally consolidated materials. It is shown later in Section 6.3.2 that in the modelling of hydraulic fracturing, the choice of a soil model may not be so important in the evaluation of the fracturing pressure. For other elements, an elastic perfectly plastic model with the Mohr-Coulomb yield criterion was used for the sand, and linear elastic models for both the platen and probe.

The modified Cam-clay model (Roscoe and Burland, 1968) requires five basic soil parameters: κ, λ, M, Γ and α' discussed in Section 2.4.1. The soil parameters used in the majority of the analyses described in this Chapter are for a reconstituted puddle clay and they were

obtained from triaxial tests in the stress path cells as part of the laboratory investigation by Mhach (1991). The values used were:

$\kappa = 0.03$ $\quad\quad$ $\nu' = 0.3$

$\lambda = 0.12$ $\quad\quad$ $M = 1.275$

$\Gamma = 2.314$ $\quad\quad$ $\gamma_w = 10.0\ kN/m^3$

The initial effective stress state and a measure of overconsolidation were specified in terms of vertical and horizontal effective stresses and preconsolidation pressure p_c' in order to solve boundary value problems. Since a consolidation analysis was performed, coefficients of permeability in the coordinate directions were also required. The values of permeability for the clay were obtained from the results of the consolidation stage of the triaxial tests. There were no distinct measurement of horizontal and vertical permeabilities so the value used for both k_v and k_h was 2.7×10^{-9} m/min.

For the analyses in Group D, revised values of $\Gamma = 2.338$ and $M = 1.2$ reported in Mhach (1991) were used. For the sand cell the following were used:

$E' = 7500\ kN/m^2$

$\nu' = 0.3$ $\quad\quad$ $k_x = 2.7 \times 10^{-5}$ m/min

$\phi' = 30°$ $\quad\quad$ $k_y = 2.7 \times 10^{-5}$ m/min

The permeability of the sand was given a value four orders of magnitude larger than that of the clay. This was done deliberately so that the sand did not impede the propagation of pressure front in the numerical analysis. Finally, very stiff linear elastic parameters were used for the top platen and probe in the axisymmetric mesh.

For one of the plane strain analyses (Case A1), additional analyses using the linear elastic model and the elasto-plastic model with the Tresca yield criterion were performed in the later part of this research to study the effect of the choice of models on the results of computations of stresses. The discussion of results is given in Section 6.3.3. The parameters used were:

(1) Linear elastic analysis

Clay: $E' = 5000$ kPa, $\nu' = 0.3$, $G' = 1920$ kPa.

Sand: $E' = 7500$ kPa, $\nu' = 0.3$, $G' = 2500$ kPa.

(2) Elasto-plastic analysis with Tresca yield criterion

Clay: $E' = 5000$ kPa, $\nu' = 0.3$, $c_u = 100$ kPa.

Sand: $E' = 7500$ kPa, $\nu' = 0.3$, $c_u = 100$ kPa.

6.2.3 Initial Stress State

In the laboratory tests, the samples were isotropically consolidated to total confining pressures of either $\sigma_c = 200$ kPa or 400 kPa. The total stress was then held constant throughout the remainder of the test. Since the initial pore pressure was set to zero, the initial total and effective stresses were the same. In the numerical study, an in-situ stress equal to these confining stresses was imposed on the element boundaries. The degree of overconsolidation was achieved by specifying the in-situ stresses with the corresponding preconsolidation pressures to provide the desired overconsolidation ratios. Two groups of analyses (Groups A and B) examined normally consolidated materials and two other groups (Groups C and D) examined overconsolidated materials with different degrees of overconsolidation (OCR between 2 and 12). The initial stresses are summarised in Table 6.1.

6.2.4 Boundary Conditions

Neither undrained nor drained applied loading at the cavity boundary appeared to provide an accurate physical simulation of the experiments. They would be more appropriate when there is a moisture separation membrane between the water and sand elements. Therefore, the increase in water pressure in the cavity was thought to be better simulated by applying water pressure increments at the nodes between the probe needle and the sand elements.

In the plane strain case, Figures 6.2(a) to 6.2(d), boundaries B and D were fixed in the tangential direction and free to move in the

radial direction. Boundary A simulated the edge of the hypodermic probe and cavity water pressures were increased incrementally at the vertex nodes of the element along boundary A.

In the axisymmetric case in Figures 6.3(a) and 6.3(b), boundary A was the axis of symmetry of the sample and was fixed horizontally. Cavity water pressures were increased incrementally at the vertex nodes of the sand elements along boundary A.

In both cases, the total confining stress was kept constant throughout the analysis.

6.2.5 Rate of Loading

The rate at which the cavity water pressure is increased has a significant effect on the fracturing pressure U_F (defined as the water pressure at which the sample begins to crack). The influence of loading rate was studied by using different time intervals for fixed increments of water pressure. Rates between the limits of 1000 kPa/min (effectively undrained) and 0.01 kPa/min (effectively drained) were examined in Groups A and B. Table 6.1 summarises the rates of loading in the different cases in these two groups of tests.

The cavity water pressure increment adopted in all the analyses was 10 kPa and there was no equilibrium error detected in all the analyses. The time increment was used to control the rate of loading and the results of pore pressure distribution in each increment were checked to ensure that there was no zigzag distribution due to the type of compensating error described in Britto and Gunn (1987). The time increments used to produce the desired rates in all the analyses were acceptable and will be shown in Section 6.4.2.

6.2.6 Failure Criteria

In the analyses adopting the modified Cam-clay model, the failure criteria for fracturing to take place are defined when either one of the following criteria is reached:

(1) When the critical state line is reached at the integration point in any one element,

(2) When the shear stress at the edge of the clay specimen adjacent to the sand cell reaches the maximum value, and

(3) when the effective hoop stress σ_θ' (effective minor stress σ_3') at the edge of the clay specimen adjacent to the sand cell reduces to zero.

6.2.7 Programme of Analyses

A programme of analyses was set up and consisted of numerical studies of rate, bore size, confining pressure, geometry and overconsolidation effects. There were groups of numerical analyses and they were grouped under A, B, C and D. Groups A and B were designed to examine the effects of rate of cavity water pressure increase, bore size and confining pressures for normally consolidated materials with plane strain and axisymmetric conditions respectively. Groups C and D were set up to examine the effects of overconsolidation and briefly for the bore sizes assuming plane strain conditions only. The programme is summarised in Table 6.1.

From the four groups of analyses, there are large amount of data generated and plotted. Some of the plots of stress variations are similar so only representative results are selected and presented in Sections 6.4 to 6.7. The calculated fracturing pressure U_F and the ratio of U_F/σ_c' are summarised in Tables 6.2 to 6.5.

6.3 Validation of the Program CRISP, Finite Element Meshes, and Soil Models in Numerical Modelling of Cavity Expansion and Hydraulic Fracturing

6.3.1 Modelling of Undrained Cavity Expansion

The hydraulic fracturing phenomenon is one of the coupled consolidation events. The finite element meshes adopted were then

validated against the closed-form solutions in undrained cavity expansion. De Moor (1989) provided a detailed review on the cavity contraction theory of a thick wall cylinder and the equations in De Moor (1989) were used to compute results and compare with those from the finite element calculations. Mesh HF005 in Fig. 6.2(a) and Mesh HF205 in Fig. 6.2(c) were used to model the thick wall cylinder problem using the linear elastic model and elastic perfectly plastic model with the Tresca yield criterion. The parameters used for the material properties were E = 7500 kPa, ν' = 0.3, G' = 2885 kPa and K_w = 6.25×10^5 kPa for the linear elastic model, and E = 7500 kPa, ν' = 0.3 and c_u = 50 kPa for the elastic perfectly plastic model with the Tresca yield criterion. The geometry of the thick wall cylinder was that of a cylindrical triaxial sample in the hydraulic fracturing experiments described in Section 6.2 with the internal and external diameters of 1 mm and 38.2 mm respectively.

The in-situ stresses were set to zero and the internal pressure was increased at 10 kPa increments. The results from the analyses for Mesh HF205 are presented in the following figures (Figs. 6.4 to 6.7). Figure 6.4 shows the variations of internal stresses with the increase in cavity water pressure at the centroid of element 9 in an undrained elastic analysis. There is no pore pressure developed and the effective radial and hoop stresses coincide with the total radial and hoop stresses. Figure 6.5 shows the stress distribution of effective radial and hoop stresses and pore pressures at the centroids across the mesh at the cavity pressure of 200 kPa. The stress distribution conforms to the theoretical distribution and the percentage errors in the finite element calculations at the cavity pressure of 200 kPa were 4.5% and 1.3% lower respectively for the radial and hoop stresses at the centroid of element 9.

Finite element calculations using the elastic perfectly plastic model with the Tresca yield criterion were also performed for an undrained cavity expansion using the same cavity pressure increments of 10 kPa. Percentage errors on equilibrium checks as high as 10% were observed. Figure 6.6 shows the variations of the effective radial and hoop stresses, total radial and hoop stresses and pore pressure at the centroid of element 9. The total and effective radial stresses (similarly for the total and effective hoop stresses) coincide when

the material is elastic. When the material shear strength of 50 kPa was reached, pore pressure began to develop and both the total radial and hoop stresses increased. Figure 6.7 shows the variations of the total radial and hoop stresses, effective radial and hoop stresses and pore pressure at the centroids of the elements across the mesh at the cavity pressure of 200 kPa. For zones where the shear strength is reached, pore pressures develop and the total stresses increase. The theoretical plastic radius using the equations in De Moor (1989) at the cavity pressure of 200 kPa was 2.24 mm which is in-between the centroids of the elements 49 and 51 and the finite element result in Fig. 6.7 show that the material yields at a location between the centroids of these two elements. The theoretical pore pressure at the centroid of element 9 was about 134.5 kPa whereas the finite element results gave a value of 131.2 kPa at this cavity pressure, an underestimate of about 2.5%. However, the percentage errors increased as the comparison moved further from the cavity wall, with an underestimate of about 16% at the centroid of element 29. Analyses were performed with smaller cavity pressure increments of 5 kPa, 2 kPa and 0.5 kPa. The results of the computed stresses remained the same as those in the analysis with the 10 kPa cavity pressure increments but the equilibrium errors were proportionately reduced. Hence, this discrepancy in computed results is thought to be related to the discretisation of the finite element mesh rather than the increment size of the cavity pressure.

Similar analyses were carried out for the coarser mesh HF005 and the finite element predictions of stresses for the undrained cavity expansion phenomenon deteriorated and erratic results of calculated radial and hoop stresses and pore pressures were observed. This is as expected because the mesh has coarser discretisation near the central cavity. Although the mesh HF005 is not superior in the prediction of stresses in the undrained cavity expansion problem, it will be demonstrated in Section 6.3.2 that the effect in the prediction of the fracturing pressure in the hydraulic fracturing simulation was not significant.

6.3.2 Validation of the Finite Element Meshes

As discussed in Section 6.2.1, the plane strain mesh HF005 and HF211 in Figs. 6.2(a) and 6.2(d) were primarily used in the numerical modelling of hydraulic fracturing. Validation of the Mesh HF005 was conducted to compare predictions of the fracturing pressure with those from the meshes HF105 and HF205 in Figs. 6.2(b) and 6.2(c) respectively. Analyses for Cases A1, A7 and D1 with the initial conditions summarised in Table 6.1 were performed using the modified Cam-clay model and the material parameters given in Section 6.2.2 to examine the capability and shortcomings of the plane strain meshes. The results are discussed as follows:

Case D1

In Case D1, the overconsolidation ratio was 2 and the rate of cavity water pressure increase was 1000 kPa/min. It was found that in the analysis for Case D1 using the three meshes, the computed results were very similar in the prediction of the fracturing pressures based on the effective hoop stress equal to zero criterion to be demonstrated in Section 6.4.1. Figure 6.8 shows the reduction in the effective hoop stresses at the centroid of the clay element adjacent to the cavity wall with the increase in the cavity water pressure and the values of the fracturing pressures were 335 kPa, 320 kPa and 320 kPa respectively for Mesh HF005, HF105 and HF205, and the percentage difference between these values was about 4.5%. Figure 6.9 shows the variations in the stress ratio q'/p' with the increase in the cavity water pressure. The finer meshes produced results with higher stress ratios at the same cavity water pressure. It is seen that the values of the predicted fracturing pressure are very much the same in these three meshes.

Case A1

The initial condition of the soil was normally consolidated in Case A1 and the rate of cavity water pressure increase was 1000 kPa/min. Two analyses were performed and the effective stress paths in q':p' space for the integration points 5 and 7 in element 37 shown in Fig. 6.2(a) adjacent to the cavity wall in Mesh HF005, and those for the

integration points 5 and 7 in element 69 shown in Fig. 6.2(d) adjacent to the cavity wall in Mesh HF205 are shown in Fig. 6.10 to 6.13. The variations of the effective hoop stresses are also plotted in the corresponding figures to examine the state of the stress paths when the effective hoop stresses become zero. The primary objective of the modelling was to predict the fracturing pressures which range between 330 kPa and 345 kPa for Mesh HF005, and between 330 kPa and 335 kPa for Mesh HF205 so the values of prediction are very similar and within 3% between the two meshes. The effective stress paths in Fig. 6.10 to 6.13 all move to the dry side of critical and so it is necessary to assess the effects of the locations of the yield surfaces on the dry side on the prediction of the fracturing pressures. This is discussed in Section 6.3.3.

Case A7

The Case A7 modelled the normally consolidated sample with the rate of cavity water pressure increase of 0.01 kPa/min. Figures 6.14 and 6.15 show the effective stress paths together with the reduction of the effective hoop stresses at the centroids of element 37 and 69 adjacent to the cavity wall in the q':p' space respectively for Meshes HF005 and HF205. The stress paths for the integration point 5 in these two elements are identical to those of the corresponding centroids suggesting that the rate of cavity water pressure increase is slow enough to allow pore pressure in these two locations to reach equilibrium when fracturing occurs. The predicted fracturing pressures were about 200 kPa which was the same as the confining pressure.

Since the determination of the fracturing pressure was governed by the effective hoop stress criterion, the computations using Mesh HF005 were considered acceptable in all the plane strain analyses.

6.3.3 Assessment of Soil Models Used

Analysis using linear elastic model for the sand and clay was performed for Case A1 with the material parameters given in Section 6.2.2. The variations in stresses in the clay element 37 and sand

element 35 are illustrated in Fig. 6.16. It is noted that the shear stress τ_{xy} developed is very small. The reduction of the effective hoop stress σ_θ' is slightly slower than the analysis using the modified Cam-clay model and σ_θ' becomes zero at the cavity water pressure of 365 kPa for the linear elastic model comparing with 340 kPa for the modified Cam-clay model and this is about 7% higher in the prediction of the fracturing pressure.

A corresponding elasto-plastic analysis with the Tresca yield criterion was performed for Case A1. The variations in stresses in the clay element 37 and sand element 35 are exactly the same as those plotted in Fig. 6.16. The shear stress developed as predicted by the model is about 6 kPa maximum so it does not exceed the shear strength of 100 kPa given for the Tresca model in Section 6.2.2. The analysis was virtually an elastic analysis.

The computer program CRISP using the critical state soil models conveniently computes and outputs the void ratio which is required in the analysis and these models can describe the behaviour of normally consolidated clays as discussed in Section 6.2.2, so it is logical to use one of those in the critical state family of soil models. In Figs. 6.10 to 6.15, all the effective stress paths move to the dry side of the critical so it is important to assess the effects of the locations of the yield surfaces on the fracturing pressure. Since the modified Cam-clay model was used, the other types of yield surfaces: the Hvorslev surface and no-tension cut-off line were superimposed in the same plot to examine the stress state in relation to these yield surfaces when the effective hoop stress became zero. The modified Cam-clay surface on the dry side of critical lies above the Hvorslev surface and the no-tension cut-off line so the elastic response of a soil at a state dry of critical may be overestimated.

The slope of the no-tension cut-off is 3:1 in the q':p' space representing the limiting condition of no tension beyond the line. Bolton et al (1989) suggested that a slope of 2:1 for the no-tension cut-off would be more appropriate in plane strain condition and both are plotted in Fig. 6.10 to 6.15. The slope of the Hvorslev surface is dependent on the angle of friction at peak stress ϕ_p' (Schofield and Wroth, 1968). Schofield and Wroth (1968) examined the data from tests

on Weald clay and evaluated the slope of the Hvorslev surface on the dry side of critical to be 0.72 in triaxial compression, which was equivalent to ϕ_p' of about 19°. Atkinson and Crabb (1991) examined the friction angle ϕ_p' for a range of clayey soils from Reading Bed clay to London clay and they found that the peak failure envelope became curved at very low effective stresses. The envelope may be represented by an equation

$$\tau_p' = A\,(\sigma_n')^b \qquad (6.1)$$

where A and b are soil parameters. From Eqn. (6.1), it is found that the values of ϕ_p' range between 11° and 24° with the majority of 19°, so the average value of the finding was similar to the value derived by Parry (1960) and reported in Schofield and Wroth (1968), and similar to the triaxial data from Powrie (1986) in which 19° was reported. The derivation of ϕ_p' using Eqn. (6.1) is shown in Fig. 6.17. A value of 0.6 for the slope of the Hvorslev surface is therefore used in the plots in Figs. 6.10 to 6.15. The modified Cam-clay model predicts a higher shear strength on the dry side of critical and the difference in the prediction between the two models is about 6% and 10% in Case A1 and A7 respectively. If the Schofield three part model (Schofield, 1980) was used, the two criteria i.e. zero hoop stress and peak shear strength may be reached more or less at the same cavity water pressure. The stress paths fall within the region bounded by the 2:1 and 3:1 no-tension lines indicating that the soil is in a state of tensile rupture when the effective hoop stress is reduced to zero.

Had the Schofield three part model been used instead of the modified Cam-clay, the criteria of zero hoop stress and peak shear strength may have been reached more or less at the same time, but it should not make very much difference in the prediction of the fracturing pressure.

6.4 Numerical Results and Discussion - Group A (Plane Strain)

This group of analyses assumes a plane strain condition for normally consolidated materials examining the effect of rate of cavity water pressure increase, bore size and confining pressures. There are three subgroups, namely A1 to A7, A8 to A13 and A14 to A19 in this group. Analyses with two confining pressures, 200 kPa and 400 kPa were performed. They are numbered as Case A1 to A7, and A8 to A13 respectively. The bore size for these cases was 6 mm diameter and the finite element mesh HF005 shown in Fig. 6.2(a) was used. The simulations in Case A14 to A19 were for a bore size of 16 mm diameter with a confining pressure of 200 kPa and the finite element mesh HF211 shown in Fig. 6.2(d) was used in the analyses. Representative results are presented in Fig. 6.18 to 6.29. The results of the calculated fracturing pressure is summarised in Table 6.2.

6.4.1 Changes of Stresses

Figure 6.18 shows the variations of the effective hoop stress σ_θ', effective radial stress σ_r', pore pressure u, deviator stress q', effective mean stress p', total mean stress p at the centroid of the clay element 37 which is adjacent to the cavity wall, and the effective hoop stress σ_θ', effective radial stress σ_r' and pore pressure u at the centroid of the sand element 35 with the increase in cavity water pressure for Case A1. In the clay element 37, there are reductions in effective hoop, radial, and mean stress whereas pore pressure, deviator stress and stress ratio increase as the cavity water pressure is increased. The fracture criterion which is satisfied first is that of zero effective hoop stress at a cavity water pressure p_w of 340 kPa which is taken as the fracturing pressure U_F. No peak is observed in the deviator stress and no elements reach critical state (although stress ratios higher than critical are achieved as the stress path for elements near the cavity takes the soil into states "dry" of critical). The rate at which the cavity water pressure is raised produces consistent trends in the data; of great significance is the increasing lag in pore pressure behind the cavity pressure at higher rates to be discussed in Section 6.4.2.

The variations of stresses in other cases are similar to those in Fig. 6.18 and all the analyses predicted that the effective hoop stress criterion is the governing criterion. Some of these plots were reported in Atkinson and Tam (1991a). Figure 6.19 shows the variations of the effective hoop stresses with the increase in cavity water pressure at the centroid of element 37 for Case A1 to A7 for the range of rates between 1000 kPa/min and 0.01 kPa/min summarised in the programme in Table 6.1. The cavity water pressure at which the effective hoop stress reduces to zero is taken as the fracturing pressure U_F and the results are summarised in Table 6.2.

Figure 6.20 shows similar variations of the effective hoop stresses as the cavity water pressure is increased for the Case A8 to A13 with confining stress of 400 kPa and bore diameter 6 mm. Figure 6.21 shows a similar plot for the clay element 49 adjacent to the sand element 47 for a 16 mm bore diameter with confining pressure of 200 kPa for Case A14 to A19.

6.4.2 Propagation of Pressure Front

The pore pressure response across the radius of the clay sample was examined at the different rates of cavity pressure increase and Figures 6.22, 6.23 and 6.24 show the results for Cases A1, A3 and A7 respectively. These show the radial variations of pore pressure at cavity water pressure $p_w = 0$ to the point of hydraulic fracturing (i.e. $p_w = U_F$ at $\sigma_\theta' = 0$). Faster rates of increase allow less time for the pore pressure front to traverse the sample radius, as expected, Figure 6.22. At slower rates the pore pressures become virtually uniform across the sample, as more time has been allowed for drainage, Figure 6.24. Figure 6.23 shows the corresponding pore pressure response across the sample for an intermediate rate of 50 kPa/min (typical laboratory rate) and the response falls intermediate between the two rates shown in Figs. 6.22 and 6.24. The smooth nature of the computed pore pressure response in Figs. 6.22 to 6.24 indicates that the time stepping sizes and loading steps in these analyses were acceptable.

6.4.3 Rate Effects

It was shown in Section 6.4.1 that the effective hoop stress criterion with $\sigma_\theta' = 0$ is the governing criterion in hydraulic fracturing. It was possible to define the fracturing pressure for the various rates of cavity pressure increase and plot these out in Figures 6.25 and 6.26 for these three subgroups in Group A. A smooth curve is obtained, asymptotic to the drained and undrained limits. This type of curve is typical of coupled (rate dependent) problems and indicates, for example, the range of rates which could produce an effectively undrained response in laboratory tests. Such information is important to the experimentalist, as very little guidance exists on appropriate rates of loading in laboratory (or field) tests.

6.4.4 Bore Size Effects

On comparing the two curves for Cases A1 to A7 and A14 to A19 for the two bore sizes of 6 mm and 16 mm in Figs. 6.25, it is seen that the bore size has an influence on the predicted fracturing pressure. Towards the undrained condition, the fracturing pressure is about 10% higher for the sample with 6 mm bore diameter than the one with 16 mm diameter. The fracturing pressure at the drained condition is the same irrespective of the cavity size.

6.4.5 Void ratio Variations

Figures 6.27 to 6.29 show the variations of void ratio across the mesh for the rates of loading 1000, 50 and 0.01 kPa/min respectively (Cases A1, A3 and A7). The values of void ratio are those at the centroid of the elements across the finite element mesh. Figure 6.27 shows the changes of void ratio with the fastest rate of cavity pressure increase equivalent to undrained condition at six values of cavity water pressure. The plots show that the void ratio in the first clay element 37 increases as water is forced into the material while all other elements have a reduction in void ratio indicating that they are compressed. This would suggest a dilation of volume in the clay nearest to the sand while those which were further away from the

cavity wall would experience compression when an almost undrained water pressure loading is applied. Similar trends are observed in Fig. 6.28 for a rate of pore pressure increase of 50 kPa/min and the thickness of clay experiencing dilation is larger. With the rate of 0.01 kPa/min (Fig. 6.29), the analysis predicts the void ratio across the whole mesh increases and the whole specimen dilates under a much slower rate or a cavity water pressure close to a drained loading.

The void ratios in the element adjacent to the cavity increase with increasing cavity water pressure and the increase is the greatest in the elements closest to the cavity wall. The increase is about 7% and 9% in the analyses with rates of 1000 kPa/min and 0.01 kPa/min respectively. This change in void ratio increases the permeability of the soil in this zone and would affect the prediction of pore pressure response as discussed in Section 3.3.6. An algorithm with variable permeabilities is more appropriate in analysing coupled consolidation problems.

6.4.6 Effects of Confining Pressure

The predicted fracturing pressures by the finite element simulation for the confining pressures of 200 kPa and 400 kPa are shown in Fig. 6.30 for the single rate of 50 kPa/min. An empirical correlation can be obtained for the best fit line as

$$U_F - u_o = 1.5\ (\sigma_c - u_o) \qquad (6.2)$$

where u_o is the initial steady state pore pressure in the clay, U_F is the fracturing pressure which is the cavity water pressure at zero effective hoop pressure and σ_c is the total confining pressure. It is observed that the fracturing pressure is directly proportional to the effective confining pressure more or less linearly. The results of the axisymmetric analysis in Group B and the laboratory results from Mhach (1991) are also plotted in Fig. 6.30 and will be discussed in Sections 6.5.4 and 6.8.1.

6.5 Numerical Results and Discussion - Group B (Axisymmetric)

The numerical analysis with axisymmetric condition was briefly investigated for bore diameter ϕ_b of 6 mm (Mesh HF100) and 16 mm (Mesh HF101) with OCR = 1. Fracturing analyses with confining pressures of either 200 kPa or 400 kPa were studied. They are numbered as Case B1 to B7, B8 to B11 and B12 summarised in Table 6.1. Typical results are shown from Fig. 6.31 to 6.37. The calculated fracturing pressure is summarised in Table 6.3.

6.5.1 Changes of Stresses

Figure 6.31 shows the variations of stresses in the clay element 53 adjacent to the sand cell as the cavity water pressure is increased at the rate between 1000 and 0.01 kPa/min for Case B1 to B7 summarised in Table 6.1. Similar to the plane strain case discussed in Section 6.4.1, zero effective hoop stress governs the fracturing as neither a peak deviator stress nor the critical state is reached in any element before the effective hoop stress $\sigma_\theta' = 0$. The results of other cases (B8 to B12) are similar.

6.5.2 State of Stresses at Fracture

Contour plots of effective hoop stress, deviator stress, and excess pore pressure are presented in Figures 6.32 to 6.34 respectively, for a rate of 50 kPa/min (typical laboratory rate). The plots were obtained at the cavity pressure of 290 kPa causing hydraulic fracture at which the effective hoop stress becomes zero. The locations of minimum effective hoop stress coincide fairly closely with those of highest deviator stress (Compare Figs. 6.32 and 6.33). Figure 6.32 shows that the region with lowest effective hoop stress is at the zone between the clay, sand and brass probe. The perspex platen and the bottom fixity of the mesh provide certain restraint. There is a stress concentration in the clay at the contact with the bottom of the sand element but is not significant in the prediction of the hydraulic fracturing pressure. Figure 6.33 shows that the region of highest deviator stress (higher than 100 kPa) is in the region between the

clay, sand and brass probe. Similarly there is some stress concentration in the clay below the sand cell. It would be beneficial to fine-tune the discretisation of the finite elements in these two zones if a detailed investigation of the stress gradients is required. Figure 6.34 shows the pore water pressure distribution within the clay material at a cavity water pressure of 290 kPa. The distribution across the clay is reasonably uniform from the centre of the sand cell with some local variations. There is a region in the clay towards the middle of the brass probe with pore water pressure response higher than the cavity water pressure. This zone corresponds to the regions in Figs. 6.32 and 6.33 in which highest deviator stress and lowest effective hoop stress are observed. This suggests that the pore water pressure response in the clay dominates the magnitude of the predicted fracturing pressure and the location corresponds to the weakest zone where crack would first develop. All the three figures (Figs. 6.32 to 6.34) show non-uniformities in pore pressure and stress distributions across the sample.

6.5.3 Rate and Bore Size Effects

A plot of fracturing pressure against rate of increase of cavity water pressure has been obtained for the bore diameter of 6 mm and 16 mm in the axisymmetric analyses, Figure 6.35. The trend has a higher value at the fastest rate of 1000 kPa/min and a value closest to the confining pressure at the slowest rate of 0.01 kPa/min similar to the corresponding plane strain analyses shown in Figure 6.25, there is a difference in the predicted values of fracturing pressures between the plane strain and axisymmetric assumptions and the difference becomes more marked at higher rates. However, there is no significant difference in the two curves for the 6 mm and 16 mm bore with the results for axisymmetric assumption in Fig. 6.35. Figure 6.36 and 6.37 shows the deformed mesh and the displacement vectors respectively at U_F = 300 kPa for Case B8 plotted without exaggeration and indicate that the magnitude of movement is very small. This is expected in a fracturing phenomenon for soils because soils do not have very much tensile strength thus the resistance to tensile rupture is low. Very small tensile displacement would mobilise full tensile strength.

6.5.4 Effects of Confining Pressure

The predicted fracturing pressures by the finite element axisymmetric analysis for the confining pressures of 200 kPa and 400 kPa are plotted in Fig. 6.30 together with the results from the plane strain analysis discussed in Section 6.4.6. The correlation obtained for the best fit line is

$$U_F - u_o = 1.42\ (\sigma_c - u_o) \qquad (6.3)$$

The correlation equation in Eqn. (6.3) is very similar to Eqn. (6.2) by the plane strain analysis.

6.6 Numerical Results and Discussion - Group C (Plane Strain) - Overconsolidated Sample

Fracturing tests were performed on 6 mm diameter cavity overconsolidated sample with OCR of 2, 4, 8 and 12. These are numbered Case C1 to C4. The sample in Case C5 was of 16 mm diameter cavity and the OCR was 12. This group of samples was modelled using the plane strain assumption. The rate of loading of 1000 kPa/min was used to simulate fast undrained loading condition. The initial conditions were summarised in Table 6.1. Figure 6.38 to 6.39(b) show typical plots of results of the analyses. Table 6.4 summarises the calculated fracturing pressure U_F and U_F/σ_c' ratios. The derivation of the stress conditions for the corresponding OCR is given in Appendix 4. The aim of the derivation was to simulate the same initial specific volume as that with OCR = 1 at different initial stress conditions at the start of each analysis. It is to be shown later that they produced slightly more consistent numerical results in Figure 6.39(a) when compared with those in Group D.

6.6.1 Changes of Stresses

The pattern of stress changes in overconsolidated soils is similar to those soils having OCR = 1 discussed in Sections 6.4.1 and 6.5.1. Similar to Groups A and B, zero effective hoop stress is taken to

define the point of fracturing, as neither a peak deviator stress nor the critical state is reached in any element before the effective hoop stresses σ_θ' becomes 0. Figures 6.38 shows the variations of effective hoop stresses σ_θ' in the clay element 37 adjacent to the sand cell as the cavity water pressure is increased for Cases C1 to C5. The fracturing pressures reduce with increasing OCR's as the confining pressure reduce from OCR = 2 to 12.

6.6.2 Bore Size Effects

Figure 6.38 shows the corresponding effective hoop stress variations having bore diameter of 6 mm (Case C4) and 16 mm (Case C5) respectively, both with OCR = 12. The fracturing pressures U_F are 74 kPa and 72 kPa and the U_F/σ_c' ratios are 2.39 and 2.32 respectively (summarised in Table 6.4) and show insignificant difference for the two different bore diameters.

6.6.3 OCR and Confining Pressure Effects

Figure 6.39(a) shows the fracturing pressure U_F normalised by the confining pressure σ_c' plotted against ln(OCR). The plot indicates that the normalised fracturing pressure increases with increasing OCR, however, the rate of increase reduces at the OCR range higher than 4 approximately. When the fracturing pressure U_F is plotted against the confining pressures in Fig. 6.39(b), a linear relationship is obtained and is given by

$$U_F - u_o = 2.36\ (\sigma_c - u_o) \qquad (6.4)$$

6.7 Numerical Results and Discussion - Group D (Plane Strain) - Modelling Laboratory Experiment on Overconsolidated Samples

Fracturing tests modelling the laboratory experimental OCR condition were performed and numbered as Case D1 to D4. The OCR's are 2, 6, 8 and 12 and the samples were analysed assuming plane strain condition

having 6 mm diameter cavity. The rate of cavity water pressure increase of 1000 kPa/min was used to simulate a fast undrained pressure loading. The initial conditions are summarised in Table 6.1. Figure 6.40 shows the variations of effective hoop stresses with increasing cavity water pressure for Cases D1 to D4. Table 6.5 summarises the calculated U_F and U_F/σ_c' ratios.

6.7.1 Changes of Stresses

The pattern of stress changes is similar to those having OCR = 1. As before, zero effective hoop stress is taken to define the point of fracturing, as neither a peak deviator stress nor the critical state is reached in any element before the effective hoop stress $\sigma_\theta' = 0$. Figure 6.40 shows the variations of effective hoop stresses σ_θ' at the centroid of the clay element 37 adjacent to the sand cell as the cavity water pressure is increased for Cases D1 to D4.

6.7.2 OCR and Confining Pressure Effects

Figure 6.39(a) shows the fracturing pressure U_F normalised by the confining pressure σ_c' plotted against ln(OCR). The plot indicates that the normalised fracturing pressure increases with increasing OCR, however, the rate of increase reduces at the OCR range higher than 4 approximately. The finding is the same as those discussed in Section 6.6 for the analyses in Group C but the numerical prediction shows slightly more scattered in Fig. 6.39(a). This is believed due to the difference in the initial specific volume at the start of each analysis.

The normalised fracturing pressures from laboratory observations are also presented in Figure 6.39(a). The numerical experiments provide a similar trend of the OCR effect on U_F/σ_c' as the laboratory tests. The correlation between the predicted hydraulic fracturing pressures and the confining pressures for this group of analysis shown in Fig. 6.39(b) is given by

$$U_F - u_o = 2.3\ (\sigma_c - u_o) \qquad (6.5)$$

The correlation in Eqn. (6.5) is very similar to that in Eqn. (6.4) for Group C analysis.

6.7.3 Yield Locus

Again in all the analyses, the fracturing pressure is always governed by the zero hoop stress criterion discussed in Section 6.2.6. Figure 6.41 shows the plots of effective stress paths q':p' and σ_θ':p' in one graph together with the corresponding modified Cam-clay yield locus for Case D1. This is similar to those in Fig. 6.6 to 6.11 for the normally consolidated materials in Cases A1 and A8. The Schofield three part yield surface is also plotted based on the discussion in Section 6.3.3. The patterns of the changes in effective hoop stress and the stress path are similar to those in Figs. 6.6 and 6.11. This plot again confirms that the prediction of the fracturing pressures is not sensitive to the choice of soil model in the prediction of the hydraulic fracturing pressure.

6.8 Comparison of Numerical Results with Experimental Results

6.8.1 Normally Consolidated Materials

All Group A and B analyses were performed with different confining pressures of either 200 kPa or 400 kPa discussed in Sections 6.4 and 6.5 and the results of the finite element simulation with the plane strain and axisymmetric assumptions were shown in Fig. 6.30. Similar patterns were obtained for both stress changes and pressure front propagation in the clay elements when the results of the analyses for different confining pressures were compared. In Figure 6.30, fracturing pressure has been plotted against confining pressure for the single rate of 50 kPa/min. The Group F1-B experimental results reported in Mhach (1991) is also shown. The correlation in the laboratory results was given by

$$U_F - u_o = 1.6\ (\sigma_c - u_o) \qquad (6.6)$$

Assuming the zero effective hoop stress criterion to be valid, both the plane strain and axisymmetric finite element results underestimate the experimental results by about 6% to 11% respectively.

6.8.2 Overconsolidated Materials

The Group D of the numerical analyses in the research described in this thesis simulated the hydraulic fracturing tests on Group F5 in Mhach (1991). The experimental and finite element results are shown in Figs. 6.39(a) and 6.39(b). The finite element results underestimated the values of fracturing pressure by about 8 to 9% for analyses with OCR between 2 and 6 when compared with the experimental results. The highest underestimate was about 22% for the analysis with OCR = 12. Although the finite element results flattened off at higher values of overconsolidation ratios, an idealised straight line is fit through the results from the finite element computations for Group D and a correlation equation for these points is given as

$$\frac{(U_f - u_o)}{(\sigma_c - u_o)} = 0.36 \ln (OCR) + 1.6 \qquad (6.7)$$

6.9 Summary

This chapter describes the numerical modelling of the laboratory hydraulic fracturing in a triaxial cylindrical sample. The modelling was a coupled consolidation event with cavity water pressure increased with time. The time increment was controlled to produce a desired rate of cavity water pressure increase. Two types of mesh, plane strain and axisymmetric were used in the finite element simulation. The modified Cam-clay model was used to describe the behaviour of puddle clay as the model has been applied successfully in modelling behaviour of normally consolidated and lightly overconsolidated clay (e.g. Wroth, 1977; Almeida et al 1986).

The plane strain meshes HF005 (coarser mesh) and HF205 (finer mesh) were validated against the closed-form solutions in undrained cavity expansion of a thick wall cylinder with a linear elastic model and

then an elastic perfectly plastic model with a Tresca yield criterion. The external pressure was set to zero and the internal pressure was increased at 10 kPa increments. Other increment sizes of cavity pressure of 5 kPa, 2 kPa and 0.5 kPa were also examined. The distribution of the total and effective radial and hoop stresses, and pore pressure were studied and compared with the theoretical equations summarised in De Moor (1989). The results of calculated pore pressure from Mesh HF205 in the elastic perfectly plastic analysis were compared with the theoretical calculation and was about 2.5% less than the theoretical at an element adjacent to the cavity wall at a cavity pressure of 200 kPa. The percentage underestimate in pore pressure increased as the comparison moved further from the cavity wall. The percentage error in equilibrium checks at the end of each increment step was as high as 10% in the analysis with 10 kPa increments of cavity pressure. The percentage errors were proportionately reduced in the analyses using smaller increment sizes but the prediction of the internal stresses and pore pressure remained the same. This would suggest even a finer discretisation than those of Mesh HF205 may be necessary in order to improve the prediction of stresses and pore pressures if undrained cavity expansion problem is performed. The results of total and effective radial and hoop stresses and pore pressures for Mesh HF005 were erratic due a coarser discretisation adjacent to the cavity. This mesh will give a much higher percentage errors in the modelling of undrained cavity expansion problem.

Mesh HF005 shown in Fig. 6.2(a) was used in the plane strain analysis of the 6 mm bore size model. Validation of the plane strain mesh in modelling the hydraulic fracturing phenomenon was conducted to assess the accuracy of the mesh by comparing predicted results of fracturing pressure with those from the finer meshes (HF105 and HF205 in Figs. 6.2(b) and 6.2(c) respectively). It was demonstrated that the results from Mesh HF005 were within 4.5% for the three cases (Cases A1, A7 and D1) examined.

The validity of using modified Cam-clay was also investigated. It was found in an analysis for Case A1 using the linear elastic model that the prediction of fracturing pressure was about 7% higher than that of using the modified Cam-clay model. The state of stress at the dry side of critical was also examined by plotting the Hvorslev surface

and no-tension cut-off line together with the modified Cam-clay yield surface. It was found that when the effective hoop stress became zero, the state of stress was in a region very close to the no-tension cut-off line and the Hvorslev surface thus confirming that the zero hoop stress criterion was the controlling criterion.

In the parametric study, the effects of rate of cavity water pressure increase, bore size and degree of overconsolidation on the predicted fracturing pressure were studied. Failure was deemed to take place when either the zero effective hoop stress or maximum deviator stress at the edge of the clay specimen adjacent to the cavity wall was reached, or the critical state line was reached at the integration point in any one element. The zero effective hoop stress criterion was found to be the governing one, so the cavity water pressure at which the effective stress reduced to zero was taken as the fracturing pressure U_F.

Two bore or cavity sizes of 6 mm and 16 mm were modelled to examine the effect on the predicted fracturing pressure. The prediction in the plane strain case was about 10% higher for the analysis of the 6 mm bore than those for the 16 mm bore towards the undrained condition. The prediction of fracturing pressure was almost identical in the axisymmetric case (Case B).

The effect of the rate of cavity water pressure increase on the predicted fracturing pressure was examined in two groups (Groups A and B) in the programme of analyses. Rates between 1000 kPa/min and 0.01 kPa/min were chosen. The analysis with the fastest rate produced the highest fracturing pressure and the one with the slowest rate predicted the fracturing pressure more or less the same as the confining pressure. The pore pressure distributions across the mesh were different for different rates of cavity water pressure increase with the most lag in the pore pressure response across the sample for the fastest rate, whereas the pore pressure across the sample reached equilibrium for the slowest rate more or less at the end of each increment of cavity water pressure increase. The clay adjacent to the cavity wall dilated more than that further away for the fastest rate, whereas the dilation was more or less uniform for the slowest rate.

The effect of the degree of overconsolidation was examined in two groups (Groups C and D) in the programme of analyses and values of OCR between 2 and 12 with a fast rate of 1000 kPa/min for the cavity water pressure increase were chosen. Group C modelled a series with identical initial void ratio whereas Group D modelled the actual laboratory test condition in Mhach (1991). The predicted fracturing pressure increased with increasing OCR with flattening off of predicted hydraulic fracturing pressure at OCR higher than 4.

The predicted fracturing pressure U_F and the fracturing pressure normalised by the confining pressure U_F/σ_c' are summarised in Table 6.2 to 6.5 for the four groups of analyses. The predicted fracturing pressures were compared with the experimental results and the results from the plane strain and axisymmetric analyses for the normally consolidated materials underestimated the experimental results by about 6% and 11% respectively. A linear relationship between the fracturing pressure and the confining pressure was obtained. The plane strain analyses for the overconsolidated materials generally underestimated the fracturing pressures when compared with the experimental results. A linear relationship between the predicted fracturing pressures normalised by the effective confining pressures and the logarithm of overconsolidation ratios was obtained but the correlation was not ideal.

CHAPTER 7 PARAMETRIC STUDY OF PLATE LOADING TESTS ON CAM-CLAY

7.1 Introduction

The plate loading test is a full scale load test often conducted to assess the strength and deformation characteristics of ground under an applied pressure on a plate. From the test results, the bearing capacity and deformation modulus of the subsoil are evaluated.

This Chapter describes numerical modelling of plate loading tests using the original Cam-clay model to study plate-soil behaviour. The computer program CRISP 84 (Gunn & Britto, 1984) was used. The purpose of the investigation was to examine the variation of calculated soil behaviour with changing values of the soil model parameters over the full range found for most commonly occurring soils. Only behaviour of stiffness, settlement and strength of the plate-soil system under undrained loading have been investigated. This study did not cover other types of behaviour such as drained loading or coupled consolidation. Some results were presented in Atkinson and Tam (1991b). A domain of soil was idealised by a finite element mesh of 39 cubic strain triangles (CuST) based on earlier work by Woods & Contreras (1987). Results of the numerical study are evaluated at the initial, yield and ultimate states defined earlier in Chapter 5 and indicate the degree of relative importance of each of the individual soil model parameters on the selected soil behaviour parameters.

7.2 Surface Plate Loading Test

7.2.1 Introduction

The basic purpose of the plate loading test is that a loaded plate gives rise to settlement which is a function of the modulus of deformation of the ground beneath it. There are different assumptions in the conditions of a plate loading analysis with respect to the flexibility of a plate relative to the subsoil, the conditions of the plate-soil contact and the rate of applied loading. It is generally assumed that the load is uniformly distributed, and total load and average ground displacement are measured. Different diameters of

plates are available ranging in sizes up to 865 mm. Two types of tests are usually performed: constant rate of penetration (CRP) and maintained load tests (ML) (Marsland and Butcher, 1983) and during ML testing, the loads are applied in increments and as far as possible a standard loading sequence is followed for every test. In typical field CRP tests the plate is loaded so as to give a constant rate of vertical displacement of 2.5 mm/min and reload cycles are carried out at bearing pressures of about 250, 450 and 660 kPa prior to taking it to a final settlement equal to 15% of the plate diameter. For the ML tests, the loads are maintained at average pressures of 250, 450 and 660 kPa and reload cycles are carried out both prior to and after each maintained load. All load changes including the cyclic loading and final loading to a settlement equal to 15% of the plate diameter are carried out so as to give a constant rate of vertical displacement of the plate of 2.5 mm/min. Most of these tests are considered as undrained but in reality, this assumption is doubtful.

In this numerical study, only the condition with a smooth contact between the plate and soil, and a uniform displacement of plate simulating a rigid plate was investigated.

7.2.2 Interpretation of Field Plate Loading Test Results

In general, the results of field tests are presented in pressure-settlement plots. The shapes of the curves are normally non-linear and are difficult to interpret and the behaviour may be idealised as shown in Fig. 7.1 for the present investigation. On first loading, the curve relating settlement to applied pressure is taken as initially linear with an initial tangent modulus E_i. At a pressure q_y, the curve bends slightly and becomes non-linear suggesting that yielding of the material has started and the settlement at this point is defined as δ_y. When the plate is loaded further the pressure-settlement curve bends over sharply and enters a roughly linear portion with a lower modulus E_f. The material is considered as undergoing general yield. The pressure-settlement curve for this stage may be extended back to intersect the tangent to the initial portion of the curve at a pressure of q_f and a settlement of δ_f which are defined as the pressure and settlement at failure. The actual

settlement (δ_f' in Fig. 7.1) from the curve at q_f was not used in this study because the gradient of the final portion of the pressure-settlement curves is relatively flat so the value of δ_f is very sensitive to a small change in q_f. These parameters are often normalised by the bulk unit weight of soil γ and plate diameter B in order to provide non-dimensional plots and this is discussed in Section 7.3.8.

7.3 Finite Element Simulation

7.3.1 Finite Element Mesh

Previous researchers such as Toh and Sloan (1980) and Sloan and Randolph (1982) have generally used an axisymmetric domain of square diametral half-section with the far boundaries at 10 plate radii from both the base and the centre-line of the plate. Woods & Contreras (1987) tested seven mesh arrangements and compared results with theoretical solutions using elastic and elastic perfectly plastic model with the Tresca yield criterion. In the finite element simulation, the far boundaries were set at 14 plate radii from the base and the centre-line of the plate. They adopted the mesh CP-07 shown in Fig. 7.2 with 39 CuST's as the optimal numbers of elements having an acceptable agreement with theoretical elastic solutions for vertical stress distributions. The mesh CP-07 was therefore used in the current investigation and the mesh concentrated 23 elements in zone I where most of the deformation occurred. The density was lower elsewhere in the domain (Fig. 7.3). Since coupled consolidation was not considered in any of the present work, the only boundary conditions to be specified were those of displacement and loading. Displacement fixities along the mesh boundaries are shown in Fig. 7.3. Boundaries A and C were fixed in the horizontal direction. Boundary B was fixed in the vertical direction. The sides D and E of element 1 and 3 were prescribed to move in the vertical direction and free to move horizontally (except at the centre-line). The downward displacement was increased incrementally to simulate a rigid plate of 865 mm diameter under an applied loading with uniform displacement. The nodes 2 and 3 were free to move laterally and there were no shear stresses on the ground surface. This simulated a model of smooth and

This simulated a model of smooth and rigid plate. The equivalent plate load was obtained by summing nodal reactions.

7.3.2 Drainage Conditions

The solutions published in the literature are generally given in terms of total stresses (Sloan & Randolph, 1982). This assumption is questionable. However in this study, a high bulk water modulus K_w equal to 100 times those of the bulk modulus (K′) of the soil skeleton was chosen in all the analyses to simulate undrained loading conditions. The values of K′ are pressure dependent and can be derived from Eqn. (2.25) as

$$K' = \frac{v\,p'}{\kappa} \tag{7.1}$$

The K_w value computed at mid-depth was used in the numerical analyses.

7.3.3 Constitutive Model

Original Cam-clay used in the research work described in Chapter 5 was used to model the clay behaviour in all the analyses. The model as discussed in Section 2.4.1 requires five basic soil model parameters: κ, λ, M, Γ, and α' and the choice of values for these parameters is discussed in Section 7.3.6.

7.3.4 In-situ Stresses and Stress History

In the selection of values to specify the in-situ stress state in the analysis described in this thesis, isotropic states were assumed. But initially, calculations were carried out with the in-situ stresses derived from the stress history of the deposit based on the second approach described in Chapter 4 of Gunn and Britto (1984).

This approach was based on an empirical method developed from Wroth (1975). The in-situ stresses were taken as anisotropic and the value of K_{nc} was calculated from Jaky (1944) equation:

$$K_{nc} = 1 - \sin\phi' \qquad (7.2)$$

Wroth (1975) then proposed two relationship between K_o, K_{nc} and OCR and their values can be calculated. The in-situ vertical stress σ_v', horizontal stress σ_h' and preconsolidation pressure p_c' were then evaluated based on these predicted values of K_o and OCR. Figure 7.4(a) shows the variations of K_o for a material having critical state soil parameters $\lambda = 0.15$, $\kappa/\lambda = 0.1$, $\Gamma = 2.632$ and $\alpha' = 0.75$ with OCR = 4 at 0.75 m but different M values of 0.77 and 1.4. Figure 7.4(b) shows the variations of in-situ vertical and horizontal stresses and the preconsolidation pressure with depth. The values of K_o, σ_h' and p_c' for M = 0.77 are larger than those for M = 1.4. Figure 7.5 shows the pressure-settlement curves from the numerical analyses for these two materials. The pressure-settlement response for the material having M = 0.77 has a lower sustained pressure at the same settlement, but the curve shows a stiffer response in the early stage of deformation. The stiffer response is due to higher horizontal stresses as shown in Fig. 7.4(b). So in order to provide comparison between idealised pressure-settlement behaviour, isotropic states were therefore assumed.

The effects of stress history were investigated by varying the overconsolidation ratio. The effects of stress history on computed plate settlement were examined for normally consolidated and overconsolidated materials, taking values of OCR = 1, 4 and 40. For overconsolidated materials, these OCR values were assumed at a depth of 0.75 m below the ground surface and reduce with increasing depth. Figure 7.6(a) shows the variations of OCR with depth for an OCR = 4 at a depth of 0.75 m and Fig. 7.6(b) shows the corresponding variations for an OCR of 40 at 0.75 m. The in-situ stresses used in the numerical analyses for the condition of these three OCR's are shown in Fig. 7.7(a) to 7.7(c).

7.3.5 Ground Water Table

The effects of depth of ground water table d_w were investigated for two levels, taking values for d_w = 0.5 m and 2 m. The variations of the depth of ground water table allow the study of the effects of the increase in effective stresses in an analysis with a deeper ground water table on the performance of the plate-soil system.

7.3.6 Choice of Values for Input Parameters

The fundamental soil model parameters and stress history discussed in Section 7.3.3 and 7.3.4 were varied in this parametric study to investigate the effects on the plate-soil performance described in Section 7.2.2. These soil model parameters can be determined from appropriate laboratory testing and their values fall within limits governed by the soil type. The ranges of values selected in this study are based on a review of laboratory test data and are the same as the ranges of soil parameters discussed in Section 5.3.1. The bulk unit weight of soil was taken as 20 kN/m^3 in the numerical analyses. These values are summarised in Table 7.1.

7.3.7 Increments of Displacement

In the simulation of a rigid plate loading test, a uniform vertical settlement was enforced to the plate-soil boundary discussed in Section 7.3.1. Different magnitudes of displacement increment (0.5 mm, 0.125 mm and 0.0625 mm per increment) were tested until the pressure-settlement response curve did not show any drift in the analysis (See Fig. 7.8). The two curves with displacement increments of 0.125 mm and 0.0625 mm were almost identical so the displacement increment of 0.125 mm per increment was therefore adopted in all subsequent analyses. Generally, a total displacement of 60 mm (480 steps and about 7% of the plate diameter) is adequate to provide a picture of the pressure-settlement curve sufficient to define the failure point for normally and lightly overconsolidated materials. For extremely heavily overconsolidated soils with OCR = 40, sometimes even a total settlement of 120 mm (960 steps and about 14% of the

plate diameter) could not produce a clearly defined yield and failure point in the pressure-settlement curve and this will be illustrated later in Section 7.4.1.

7.3.8 Choice of Parameters for Presentation

The initial tangent modulus E_i, the applied pressure q_y and settlement δ_y immediately after yield, and the applied pressure q_f and settlement δ_f at failure defined in Section 7.2.2 were derived from all the basic pressure versus settlement curves as illustrated in Fig. 7.1. These were then plotted against the fundamental soil model parameters so that the variations of their values within the ranges of these soil model parameters can be observed.

The initial tangent modulus or elastic deformation modulus is derived from the equation based on the elastic solution (Poulos and Davis, 1974):

$$\delta = \frac{\pi}{4} \frac{qB(1 - \nu^2)}{E_i} \tag{7.3}$$

where

δ = settlement
q = applied pressure
B = plate diameter which is 865 mm
ν = Poisson's ratio of soil and is 0.5 in undrained case
E_i = initial tangent modulus of the plate-soil system

With further reduction by substituting $\nu = 0.5$ into Eqn. (7.3), the equation can be expressed in the following form:

$$E_i = \frac{0.59\ qB}{\delta} \tag{7.4}$$

The values of the initial tangent modulus E_i and pressures q_y and q_f are normalised by the bulk unit weight of soil γ and plate diameter B to provide a dimensionless parameter and the settlements δ_y and δ_f are

normalised by the plate diameter to provide the settlement ratio in percentage. This has the potential to enable the use of some of the plots to assess the initial tangent modulus, bearing capacity and settlement for shallow foundations when the critical state soil parameters, stress history and depth of ground water table are known and this is discussed in Section 7.4.6. This non-dimensional normalisation of the numerical results is also shown in the representative results in Section 7.4.

7.3.9 Programme of Analyses

Four series of numerical experiments were conducted. The parameters tabulated in Table 7.1 were used in the computations in the plate loading tests. This programme was similar to the one for the parametric study of Cam-clay described in Chapter 5 (Table 5.1). Not all the analyses included the intermediate values of the soil model parameters, only the analyses in series 2 covered the intermediate values of κ/λ, λ and M.

The computation for each test took at least 10 to 15 hours on the Gould series machines. The programme covered the range of soil model parameters discussed in Section 5.3.1 and provides numerical results to illustrate the influence of the critical state soil model parameters on the calculated performance of a loaded plate.

7.4 Numerical Results and Discussion

The numerical results were examined at the initial, yield and failure states as discussed in Sec. 7.2.2. Table 7.2 was derived after detailed observation and analyses of the undrained behaviour parameters versus the fundamental soil model parameters and summarises the ranges of variations for normally consolidated materials while Table 7.3 is for overconsolidated materials. The ranges are tabulated in terms of magnitude of increase or decrease, denoted as 'i' or 'd' similar to those in Section 5.5. Tables 7.4 and 7.5 summarise the results of the parametric study showing the dependence of the undrained behaviour parameters on the fundamental soil parameters,

stress history and depth of water table for the normally consolidated and overconsolidated materials respectively. They were derived using the same rating system as the one used in the parametric study of Cam-clay in Chapter 5, in which * indicates no dependence and **** indicates strong dependence (Section 5.5.3). Representative results are presented for illustration.

7.4.1 Pressure-Settlement Response

The pressure-settlement curve is the basic information derived from the plate loading analyses. Typical results are shown in Fig. 7.9 to 7.15. They are extracted from the different series in the programme of analyses to illustrate the variations in the pressure-settlement response predicted by the Cam-clay model by varying one single soil parameter, ground water table or stress history.

The applied pressure was calculated by summing the nodal reactions in the vertical direction at a specific increment of settlement. The pressure-settlement curves show that the trend of settlement with the applied loading follows a similar pattern for all the four series of numerical experiments as in Fig. 7.1.

Figure 7.9 shows the pressure-settlement curves for four analyses with varying λ between 0.05 and 0.35. The curves illustrate that the plate-soil system shows a stiffer and stronger response for the analysis with smaller values of λ. A lower λ value leads to a material with lower initial water content for the same stress history and the value of the corresponding strength is higher. Since the value of κ/λ is constant so for a lower value of λ, the corresponding κ value is lower. As discussed in Section 5.5.1, κ value has a significant influence on stiffness. Consequently, the initial tangent stiffness derived from the pressure-settlement curve with a lower κ value is higher.

The pressure-settlement curves in Fig. 7.10 are of four analyses with varying κ/λ values between 0.1 and 0.5 and constant λ. Lower values of κ/λ show a stiffer and stronger response and this is because a lower κ/λ value results in a lower κ value which has significant

effects on the stiffness of soil. This is consistent with the findings in Chapter 5 and has been discussed in Section 5.5.1.

Figure 7.11 shows the pressure-settlement curves of the analyses with varying M values between 0.77 and 1.4. The Cam-clay model predicts that the strength is higher for higher M values and this is as expected but the initial tangent stiffness remains constant for different M values.

The pressure-settlement plots in Fig. 7.12 for OCR of 1, 4 and 40 illustrate the effects of stress history on the performance of the plate-soil system on the subsoil. The analysis with OCR of 40 predicts much higher values of yield pressure and settlement, ultimate bearing pressure and settlement when compared with the results of the analysis for OCR of 4 and 1. The effect on the initial tangent modulus is not significant.

Figure 7.13 shows the pressure-settlement curves of varying α' between 0.75 and 0.33. The main influence is on the initial tangent modulus and settlements, whereas the effects on the yield and ultimate pressure are not significant.

The pressure-settlement curves for the two depths of ground water level at 0.5 m and 2 m shown in Fig. 7.14 illustrate the significant increase in the initial tangent modulus and ultimate bearing pressure for normally consolidated materials. This is expected because of the increase in effective stresses for the analysis with d_w = 2 m when compared with the analysis with d_w = 0.5 m.

Figure 7.15 shows the pressure-settlement curves for two analyses with OCR = 40 and M = 0.77 or 1.4. The pressure-settlement curve for soil with M = 1.4 has not entered the ultimate state even though the plate has settled 120 mm, 14% of the plate diameter. In general, there is not any peak condition followed by strain softening during the loading of the plate-soil system, even for soils with OCR of 40. This is because the shear strength of more and more soil elements further below the plate is mobilised with increasing plate settlement, and the growth of the yield zone is slower and requires much higher

settlements in heavily overconsolidated materials before yielding occurs.

7.4.2 Plate-Soil Behaviour at Initial States

The original Cam-clay model predicts that materials exhibit elastic behaviour when the stress state is inside the state boundary surface. In this plate-soil system, the subsoil is comprised of 39 elements and they interact together when the soil deforms. The initial tangent modulus E_i discussed in Sections 7.2.2 and 7.3.8 characterises the whole plate-soil system. Figures 7.16 to 7.18 show some representative results of the initial tangent modulus E_i plotted against the fundamental soil parameters. These figures are also shown with the ordinate of the normalised initial tangent modulus by the unit weight of soil and plate diameter $E_i/(\gamma B)$. The modulus values shown in Fig. 7.16 reduce by about 2.3 to 4.1 times with increasing λ values between 0.05 and 0.35 for materials with OCR = 4 and the influence of λ is strong.

Figure 7.17 shows the reduction of the modulus with increasing κ/λ values for normally consolidated materials and overconsolidated materials. When the plots of variation between $E_i/(\gamma B)$ and κ/λ for all the λ and α' values are compared, the full range of reduction is found to be 3.7 to 8.5 times for normally consolidated materials and between 4.5 to 6.7 times for overconsolidated materials and the influence of κ/λ is significant. The values of OCR have negligible influence on E_i.

Figures 7.16 and 7.17 also show the variations of the modulus with varying M between 0.77 and 1.4. The modulus increases slightly with increasing M for normally consolidated materials and is relatively constant for overconsolidated materials.

The increase in the modulus with the increase in the depth of ground water table from 0.5 m to 2 m shown in Fig. 7.18 is about 2 and 3.2 times respectively. The modulus is expected to increase because the effective stresses are larger for the latter case. These observations are summarised in Tables 7.2 and 7.3 for normally consolidated and overconsolidated materials respectively.

The model predicts that for normally consolidated materials, the initial tangent modulus E_i increases when λ and κ/λ decrease, and M, α' and d_w increase. The most influential parameters are λ, κ/λ, α' and d_w. For overconsolidated materials, the modulus increases when λ and κ/λ decrease and OCR and α' increase whereas it is independent of M. The most influential parameters are λ, κ/λ and α' whereas OCR is of slight importance and it is independent of M.

7.4.3 Plate-Soil Behaviour at Yield States

When the state reaches the state boundary surface, plastic irrecoverable strains begin to develop. The plate-soil behaviour is characterised by the normalised pressure $q_y/(\gamma B)$ and settlement ratio $100\delta_y/B$ immediately after yield as discussed in Section 7.3.8. For normally consolidated materials, yielding occurs as soon as the plate-soil system is loaded and so there is no information derived at the yield states. Figures 7.19 and 7.20 illustrate the typical results of settlement ratio immediately after yield $100\delta_y/B$ plotted against varying λ values for OCR = 4 and 40 respectively. The values of $100\delta_y/B$ tend to increase with increasing λ values although for low κ/λ values and high λ, this trend appears to reverse for OCR = 4. The variations of $100\delta_y/B$ with κ/λ values are also shown and for materials with OCR = 4, the values of $100\delta_y/B$ increase with increasing κ/λ values, but reduce for materials having OCR = 40 and M = 1.4 (Fig. 7.20). The variations of $100\delta_y/B$ values with M, OCR and α' for overconsolidated materials are summarised in Table 7.3. The settlement ratio immediately after yield generally increases when λ, κ/λ (except for OCR = 40 and M = 1.4), M and OCR increase, and α' decreases. The most influential soil model parameters are λ, κ/λ, α' and OCR; M is moderately influential. For materials with OCR = 40, κ/λ is slightly influential.

Figure 7.21 shows the normalised bearing pressure immediately after yield $q_y/(\gamma B)$ plotted against λ values. The plots show some erratic variations of $q_y/(\gamma B)$ values and this is likely due to the difficulty in the extraction of the yield point from the pressure-settlement curve. However, a horizontal line could be fitted through the data points. Figure 7.22 shows a similar plot but for OCR = 40. A similar

pattern of variations is observed with the decrease in $q_y/(\gamma B)$ when λ values increase. Table 7.3 summarises the ranges of variations of $q_y/(\gamma B)$ with the fundamental soil model parameters. The model predicts that the normalised pressure immediately after yield $q_y/(\gamma B)$ increases when OCR, M and α' increase, and κ/λ and λ decrease. The most influential parameters are OCR and κ/λ, whereas M is moderately influential. λ and α' are only slightly influential.

7.4.4 Plate-Soil Behaviour at Failure States

The failure state is defined by the intersection of the two tangents to the initial and final segments of the pressure-settlement curve as discussed in Section 7.2.2. Initially, the settlement δ_f' on the pressure-settlement curve corresponding to q_f shown in Fig. 7.1 was used in the observation of the variations but it produced highly variable results for the reason described in Section 7.2.2. Hence, use was made of the intersection point of the two tangents to the initial and final straight segments of the pressure-settlement curve at a point with q_f and δ_f and typical results are illustrated.

Figures 7.23 and 7.24 show the settlement ratio at failure $100\delta_f/B$ plotted against λ values and the values of settlement ratio increase significantly for materials with OCR = 4 and high κ/λ value of 0.5 in Fig. 7.23 and for OCR = 40 in Fig. 7.24. The full range of variations is summarised for normally consolidated materials in Table 7.2 and for overconsolidated materials in Table 7.3.

Figure 7.25 shows the plot of $100\delta_f/B$ against the depth of ground water table d_w. The increase and decrease in settlement ratio at failure are found to be insignificant with the change in the depth of water table between 0.5 m and 2 m. There was no analysis for overconsolidated materials with variations in the depth of ground water table. The ranges of variations of the settlement ratio with the other parameters, i.e. κ/λ, M and α' for normally consolidated materials and κ/λ, M, OCR and α' for overconsolidated materials are summarised in Tables 7.2 and 7.3 respectively.

Figure 7.26 show the normalised pressure at failure $q_f/(\gamma B)$ plotted against varying λ values for OCR = 4. The increase in λ values has slight effects on the predicted $q_f/(\gamma B)$ values for overconsolidated materials. Figure 7.27 shows the plot of $q_f/(\gamma B)$ plotted against varying M and the $q_f/(\gamma B)$ values increase moderately with increasing M values. Figure 7.28 shows the plots of $q_f/(\gamma B)$ against d_w of 0.5 m and 2 m. The $q_f/(\gamma B)$ values increase significantly with increasing depth of ground water table. The ranges of variations are summarised in Tables 7.2 and 7.3 for normally consolidated and overconsolidated materials respectively.

For normally consolidated materials, the settlement ratio at failure $100\delta_f/B$ increases when λ, κ/λ, d_w (except for κ/λ = 0.5) and M increase, and α' decreases. The most influential parameters are κ/λ, λ and α'; M and d_w are slightly influential. For overconsolidated materials, the settlement ratio increases when λ, κ/λ, M and OCR increase, and α' decreases. The most influential parameters are λ, κ/λ and OCR; M and α' are moderately influential.

The model predicts that for normally consolidated materials the normalised pressure at failure $q_f/(\gamma B)$ is relatively constant or decreases slightly when λ increases. The model also predicts that $q_f/(\gamma B)$ increases when OCR, M, α' and d_w increase, and κ/λ decreases. For normally consolidated materials, the most influential parameter is d_w, M is moderately influential whereas κ/λ, λ and α' are slightly influential. For heavily overconsolidated materials, the parameters κ/λ and OCR are the most influential, M is moderately influential and α' and λ are slightly influential.

7.4.5 Stress Paths and Stress Distribution Under the Plate

Figures 7.29 to 7.40 show typical plots of stress paths, deviator stress versus settlement, contours of pore pressure, shear stress and shear strain at a chosen increment of loading for two typical numerical plate loading analyses. The pressure-settlement curves of the analyses are also included. The plots are typical of each single computer analysis for a fixed set of fundamental soil model parameters.

Figure 7.29 shows the pressure-settlement curve of an analysis having soil parameters with $\lambda = 0.35$, $\kappa/\lambda = 0.1$, $\alpha' = 0.75$, $M = 0.77$, OCR = 4 and $d_w = 0.5$ m. From the curve, $q_y = 19$ kPa, $\delta_y = 4$ mm and $q_f = 36$ kPa. The deviator stress q' at the centroid of five elements (Element No. 1, 2, 3, 4 and 9) under the plate versus the plate settlement is shown in Fig. 7.30. The deviator stress in element 4 was the largest among the five elements and was the first element to reach a constant value of 11.8 kPa. The theoretical undrained shear strength s_u of the material at this level was about 5.7 kPa so the calculated deviator stress by CRISP consistently approached the theoretical $2s_u$ values. Similar patterns of deviator stress are observed in the other elements in Figure 7.30 and the values of $2s_u$ fall within a range between 11 kPa and 12 kPa. For a shallow foundation, the ultimate bearing pressure is given by

$$q_f = N_c s_u + p_o' \tag{7.5}$$

where N_c is the bearing capacity factor, s_u is the undrained shear strength and p_o' is the contribution from the effective overburden which can be ignored in this case. Hence, the value of N_c for this analysis can be evaluated as $N_c = q_f/s_u = 36/5.5$ or $36/6$, so the N_c values vary between 6 and 6.5 and these values are consistent when they are compared with the theoretical N_c value of 6.15 for a circular foundation given by the theory of bearing capacity.

Figure 7.31 shows the computed effective stress paths for elements 1,2 and 4 under the plate. They were vertical when they were inside the state boundary surface. As soon as they reached the state boundary surface, they moved along it and approach the critical state line which has a slope of $M = 0.77$. Figure 7.32 shows the pore pressure distribution with depth near the centre-line of the domain at plate settlements of 10 mm, 30 mm and 60 mm. The static water pressure is shown as a straight line in the diagram and the difference is the excess pore water pressure. About 90% of the excess pore water pressure was generated when the plate settled 10 mm. Figure 7.33 shows the pore pressure contours within a 2 m × 2 m zone from the plate at the vertical settlement of 10 mm. The pore pressure gradient is seen to be the greatest under the edge of the plate. Figure 7.34 shows the corresponding shear stress contours at 10 mm of settlement

illustrating the concentration of high shear stresses at the edge of the plate. Figure 7.35 shows the shear stress contours at a settlement of 30 mm and the zone with high shear stresses has grown larger under the edge of the plate. Figures 7.36 and 7.37 show the corresponding shear strain contours, again with the highest shear strain occurred at the edge of the plate.

Figure 7.38 shows the pressure-settlement curve of another analysis with $\lambda = 0.25$, $\kappa/\lambda = 0.5$, $M = 1.4$, $\alpha' = 0.75$, OCR = 4 and $d_w = 0.5$ m. The values of q_y and δ_y were 21 kPa and 17 mm respectively and $q_f = 41$ kPa. The deviator stress q' at the centroid of four elements (Element No. 1,2,3 and 4) under the plate versus the plate settlement is shown in Fig. 7.39 and element 4 reached the highest peak value before other elements. Other elements reached the peak value at larger settlements while the element 4 reached its critical state at that time. On passing their corresponding peak deviator stresses they approached their corresponding critical state undrained strength. Similar to the previous analysis, they consistently approached the theoretical value of $2s_u$ ranging between 13.2 kPa and 14.3 kPa depending on the void ratio of the materials. The corresponding bearing capacity factor N_c can be calculated as between 5.73 and 6.21, compared with the theoretical N_c value of 6.15 for a circular foundation given by the bearing capacity theory (Skempton, 1951).

When this is expressed in p':q' plots in Fig. 7.40, the shape of the effective stress paths illustrates that the peak strength was reached as the stress paths reached the state boundary surface. Then they moved down along it approaching the critical state line with $M = 1.4$. The shapes of these stress paths in Figs. 7.31 and 7.40 depend on the κ/λ values as discussed in Section 5.5.5, in which the same behaviour was observed in the undrained triaxial compression stress paths in Fig. 5.27(a). The stress paths for the three elements under the plate (Elements 1, 2 and 4) in both figures (Figs. 7.31 and 7.40) were all on the dry side of critical and they were vertical until they met their corresponding original Cam-clay yield loci. There was a significant proportion of peak soil strength derived from this part of the stress paths and the percentage of elastic response may be overestimated. Powrie and Li (1991a and 1991b) carried out a finite element analysis of an in situ wall propped at formation level and

adopted the Schofield three part model (Schofield, 1980) for this reason. It was shown in Section 6.3.3 that there is a wide range of values for the slope of the Hvorslev surface and it is not easy to select a correct value for the slope. Assuming the slope of the Hvorslev surface for the material is 0.6 used in Powrie and Li (1991a) in Figs. 7.31 and 7.40, the overestimation of the deviator stress q' in element 4 was about 46% for materials with $\kappa/\lambda = 0.1$ (Fig. 7.31). For materials with $\kappa/\lambda = 0.5$ (Fig. 7.40), the overestimation was about 30%. The assumption in using the original Cam-clay model is likely to lead to an overestimation in pressure and settlement immediately after yield. However, it is unlikely that the initial tangent modulus, the ultimate bearing pressure and settlement are affected very much since these quantities are selected at the initial and final portions of the pressure-settlement curves and they correspond to the elastic state and the critical state of the original Cam-clay and Schofield three part models.

7.4.6 Normalised Tangent Modulus, Settlement Ratio and Bearing Capacity

The value of initial tangent modulus E_i in settlement computations can be extracted from the plots of the normalised initial tangent modulus $E_i/(\gamma B)$ versus the soil model parameters and stress states in Figs. 7.16 to 7.18. The settlement ratio discussed in Section 7.3.8 is the ratio of settlement to the plate diameter expressed in percent (settlement ratio = $100\delta/B$) and the settlement ratio immediately after yield are shown in Figs. 19 and 20. The normalised bearing pressures at failure are presented in Figs. 7.25 to 7.28. These normalised parameters are often used in the presentation of field plate loading test results and these non-dimensional plots produced by the parametric study have the potential for use to predict the initial tangent modulus, settlements immediately after yield and at failure, and the bearing pressures immediately after yield and at failure when the size of a footing and the soil parameters are known.

7.5 Summary

This chapter describes a numerical parametric study of plate loading tests using original Cam-clay. A smooth and rigid circular plate under a displacement controlled undrained analysis was simulated. The parametric study has generated a very large amount of data similar to the work described in Chapter 5. Tables 7.2 and 7.3 summarise the analyses and observations on the ranges of the variations in the undrained behaviour parameters from Cam-clay predictions for normally consolidated and overconsolidated materials respectively. Tables 7.4 and 7.5 were produced after an assessment of the quantitative data in Tables 7.2 and 7.3 respectively. The same rating system which was introduced in Section 5.5.3 is used here. In determining independent parameters, use was made of the Omega point concept (Schofield and Wroth, 1968) described in Section 2.4.1 which essentially relates N and Γ to λ. The initial specific volume and hence strength are therefore dependent to some extent on λ.

The bearing pressure-settlement curve is the basic information derived from the plate loading analysis and from which the plate-soil behaviour at different states can be evaluated. It was demonstrated that the initial state of the subsoil has significant effects on the initial tangent modulus. The initial water content or specific volume of a material is a function of the critical state soil parameters, stress history and current stress state and it affects the strength of the soil. For a fixed set of values of the critical state soil parameters with varying κ/λ values, an analysis with lower values of κ/λ shows a relatively stiffer response. This is because the value of κ has a significant influence on the tangent modulus of the soil.

The initial state is characterised by the normalised initial tangent modulus $E_i/(\gamma B)$. For normally consolidated materials, it has strong dependence on κ/λ, λ, α' and d_w and has slight dependence on M. For overconsolidated materials, it has strong dependence on λ, κ/λ and α', slight dependence on OCR and is independent of M.

The yield state is characterised by the settlement ratio $100\delta_y/B$ and normalised pressure $q_y/(\gamma B)$ immediately after yield for overconsolidated materials only because for normally consolidated

materials yielding starts as soon as the plate-soil system is loaded. The settlement ratio has a strong dependence on λ, α' and OCR, and also on κ/λ for OCR = 4, but only a slight dependence on κ/λ for OCR = 40. It has moderate dependence on M. The normalised yield pressure has a strong dependence on κ/λ and OCR, a moderate dependence on M and a slight dependence on α' and λ.

The ultimate state is characterised by the settlement ratio $100\delta_f/B$ and normalised pressure $q_f/(\gamma B)$ at failure. For normally consolidated materials, the settlement ratio has a strong dependence on λ, κ/λ and α', a slight dependence on M and d_w. For overconsolidated materials, the settlement ratio has a strong dependence on λ, κ/λ and OCR, and a moderate dependence on M and α'. For normally consolidated soils, the normalised bearing pressure has a strong dependence on d_w, a moderate dependence on M, and a slight dependence on λ, κ/λ and α'. For overconsolidated soils, the normalised bearing pressure has a strong dependence on κ/λ and OCR, a moderate dependence on M, and a slight dependence on α' and λ.

Although there were limitations in the assumptions made in this research of the effects of the variations in the fundamental soil model parameters on the plate-soil behaviour, the finite element simulation of the plate loading test incorporating a critical state soil model indicates which fundamental soil parameters are more critical in the prediction of the undrained behaviour parameters. The results showing the relative importance of the fundamental soil parameters on the undrained behaviour can be used to assess which fundamental soil parameters are relatively more important and so the appropriate soil testing can be chosen in the site investigation programme such that the more important parameters are critically assessed before they are input in a design analysis.

The non-dimensional plots of the normalised initial tangent modulus $E_i/(\gamma B)$, settlement ratio $100\delta_y/B$ and normalised pressures $q_y/(\gamma B)$ and $q_f/(\gamma B)$ given in Fig. 7.16 to 7.28 have the potential to provide a preliminary assessment of the initial tangent modulus, settlement and bearing pressure immediately after yield, and ultimate bearing pressure when the fundamental soil model parameters, stress history and depth of ground water table are known.

CHAPTER 8 SUMMARY AND CONCLUSIONS

8.1 Methodology

Numerical modelling has become one of the essential and most powerful tools in extending knowledge to evaluate and understand soil behaviour. The investigation reported in this thesis used numerical analysis to perform parametric studies to examine the influence of soil parameters in the prediction of soil behaviour. The parametric studies were extended to the modelling of some boundary value problems in geotechnical engineering. In the numerical analyses, the critical state soil models were used.

The work examined a number of aspects:

- A parametric study of Cam-clay investigated the variations of the calculated soil behaviour with changing values of the soil model parameters predicted by the Cam-clay model in a single element analysis. A computer program CASIS (Tam, 1987 and Atkinson and Tam, 1988) developed for this purpose was used and it calculated stress and strain increments in either strain or stress-controlled undrained and drained triaxial compression analysis.

- A parametric study of plate loading tests on Cam-clay investigated the variations of the plate-soil behaviour predicted by the Cam-clay model with changing values of the soil model parameters. A finite element simulation of the problem was performed and the computer program CRISP (Gunn and Britto, 1984) was used. Isotropic in-situ stress conditions were assumed.

- A parametric study of a coupled loading and drainage event examined the hydraulic fracturing phenomenon in a triaxial specimen. The numerical modelling studied the effects of the rate of cavity water pressure increase, bore size, confining pressure and overconsolidation ratio in the prediction of the fracturing pressures. The computer program CRISP was used.

8.2 Influence of Soil Parameters and Other Factors on Predicted Soil Behaviour

8.2.1 Triaxial Compression Loading Tests

In the parametric study of Cam-clay a wide range of fundamental soil parameters has been considered to examine their influence on stiffness and strength. Computations were performed for the single element triaxial compression loading paths in both undrained and drained analyses using CASIS. The soil behaviour at the initial, yield, peak and ultimate states was evaluated. Normalising procedures using the current specific volume v and current effective mean pressure p' enabled the stress state or strain state to be related to the critical state soil parameters (M, λ and κ) and the current stress ratio $d\eta' = dq'/dp'$. Tables 5.4 and 5.6 summarise the relative importance of the fundamental parameters on the predicted undrained and drained behaviour respectively.

In the study for the triaxial loading paths, it was revealed that in almost all the states, the parameter κ/λ had major influence on most of the soil behaviour parameters. The values of κ and λ determined the initial states of soil in v:ln p' space thus affecting its subsequent stress-strain response when the soil was loaded. Generally, M had relatively moderate influence on most of the predicted undrained behaviour parameters whereas it had strong influence on soil behaviour at ultimate state for drained loading behaviour. As expected, the parameter α' had a significant influence during the early part of the shearing process and this was reflected by its strong influence on the predicted initial tangent modulus. The influence of α' on the predicted soil behaviour reduced as the soil state moved from the initial to ultimate state.

There are some unexpected results revealed. For example, the parameter λ was coupled with the normalised rate of pore pressure increase, yield and ultimate strain in the undrained behaviour and its influence was strong. The parameter M was coupled with the strains, the rate of pore pressure increase in undrained analyses and the rate of dilatancy in drained analysis immediately after yield and at ultimate state, in addition to the soil strength. These findings

revise the traditional and conventional thinking that the parameter M relates only to soil strength. The value of λ, coupled with the Omega point concept (Schofield and Wroth, 1968) described in Section 2.4.1, influenced strength principally by its influence in the initial specific volume.

The shape of the state boundary surface for constant volume sections depended on κ/λ values. For material states on the dry side of critical, the undrained state path may exhibit peak states after yielding as shown by path (1) in Fig. 5.27(a).

During undrained loading, the elastic soil model parameters κ/λ and α' played a more important role at the early stage of shearing i.e. at the initial state. At the yield state, all the soil model parameters were important in the prediction of the behaviour parameters. At the peak state, κ/λ and M became more important. Finally at the ultimate state, M and λ were the most important soil model parameters.

During drained loading, the elastic parameters κ/λ and α' again played the most important role in the prediction of the drained behaviour parameters at the initial state. At the yield state, most of the soil model parameters were important. At the ultimate state, M and OCR were the most important parameters in making the prediction.

8.2.2 Plate Loading Analyses

The parametric study of Cam-clay was extended to a finite element simulation of plate loading tests using the computer program CRISP. A smooth and rigid circular plate under a displacement controlled undrained analysis was modelled with the same range of fundamental soil parameters and similar stress history adopted in the work summarised in Section 8.2.1. Three characteristic points on the bearing pressure-settlement curve were chosen and results examined at these points: the three points were the origin, yield and ultimate described in Section 7.2.2. Tables 7.4 and 7.5 summarise the relative importance of the fundamental parameters on the predicted undrained behaviour of the plate-soil system for normally consolidated and heavily overconsolidated materials respectively.

The prediction of the initial tangent modulus was similar to the findings in the parametric study of Cam-clay in the undrained triaxial compression analysis in which the values of the modulus depended very much on the values of κ. This was reflected in the pressure-settlement responses for different values of κ/λ shown in Fig. 7.10. Even for a constant value of κ/λ, the value of κ changed for different values of λ and the stiffer response of the plate-soil system for lower κ values due to lower λ values is shown in Figure 7.9. The initial specific volume had some influence on the predicted initial tangent modulus but not as much as the parameter κ.

It was revealed that the parameter κ/λ was the most influential parameter in the prediction of the undrained behaviour of the plate-soil system and followed by λ. Stress history in terms of overconsolidation ratio was another influential parameter in the prediction. The parameter M was moderately influential and the parameter α' as expected was the most influential at the initial stage of the loading process. The influence of the depth of ground water table was examined only for the normally consolidated materials and was found to have strong influence on the prediction of the initial tangent modulus and bearing capacity. This was due to the increase in the effective stresses over the first two metres in the soil domain shown in Figure 7.3.

The shapes of the effective stress paths in p':q' space resembled those in the parametric study of Cam-clay in undrained triaxial compression analysis. They were vertical inside the state boundary surface and when they reached the state boundary surface the stress paths moved along it towards the critical state line. The shapes were dependent on the values of κ/λ and the findings were the same as those summarised in Section 8.2.1.

The bearing capacity factors for two analyses were calculated based on the ultimate bearing pressure defined by the pressure-settlement curves and the theoretical shear strength of the soil elements in the domain. The values of the bearing capacity factor were found to vary between 6 and 6.5 in one analysis, and between 5.73 and 6.21 in another, comparing with the theoretical N_c value of 6.15 for a circular foundation from the bearing capacity theory. The finite element

simulation of the plate loading tests using the Cam-clay model in CRISP produced solutions which were in the same order as the plasticity solutions.

8.2.3 Hydraulic Fracturing Analyses

Numerical modelling of the hydraulic fracturing of a triaxial specimen, using a relatively coarse mesh with the program CRISP can produce reasonably accurate results for the fracturing pressures as compared with the experimental results. However, a much more refined discretisation towards the cavity wall is required in analysing undrained cavity expansion. The predictions of fracturing pressures were not sensitive to the soil model chosen because in the hydraulic fracturing test, the stress path of the clay elements in p':q' space was inside the state boundary surface before fracturing occurred and so the soil state was almost always elastic. The computed results were within 7% when the solutions from the linear elastic model and modified Cam-clay model were compared.

It is important to use coupled consolidation analysis in modelling the hydraulic fracturing phenomenon because in the laboratory experiments, cavity pressure was applied using water within the central cavity and there was no membrane between the clay and sand. Effectively, water was injected into the cavity and it was demonstrated that even with a rate of cavity water pressure increase of 1000 kPa/min, there was swelling of the elements near the cavity. The modelling helped to understand the hydraulic fracturing phenomenon in a triaxial specimen and allowed an evaluation of the behaviour of stress changes and non-uniformities of stresses and pore pressure across the sample.

In the modelling of the hydraulic fracturing phenomenon, the zero effective hoop stress criterion was the controlling criterion on which the predicted fracturing pressure was obtained. Table 6.2 to 6.5 summarise the results of the predicted fracturing pressure U_F and the fracturing pressure normalised by the effective confining pressure U_F/σ_c'. The modelling provided a reasonably close prediction of the hydraulic fracturing pressure and was consistent with the experimental results that fracturing occurred when the effective hoop stress

reduced to zero. The analyses confirmed that the rates of cavity water pressure increase had a significant influence on the prediction of fracturing pressures. Both the plane strain and axisymmetric analyses at a rate of cavity water pressure increase of 50 kPa/min provided very similar correlations between the fracturing pressures and the (effective) confining pressures. The correlations underestimated the experimental results by about 6% and 11% respectively.

The size of the cavity had an influence on the predicted fracturing pressure. This was found to be about 10% smaller for the 16 mm diameter cavity sample when compared to that of the 6 mm diameter cavity sample in the plane strain analyses. However, the difference of the predicted fracturing pressure was insignificant in the axisymmetric analyses. For the modelling of overconsolidated materials, the normalised fracturing pressure $(U_F - u_o)/(\sigma_c - u_o)$ increased linearly with increasing ln (OCR) between OCR of 1 and 4 but the increase reduced when OCR exceeded 4 (Fig.6.39(a)). The fracturing pressure increased linearly with the confining pressure shown in Fig. 6.39(b) suggesting that the fracturing pressures were predominantly governed by the in-situ confining pressures.

8.2.4 Summary

The parametric study of Cam-clay categorised the relative importance of the critical state soil parameters and other factors in the prediction of undrained and drained soil behaviour. The results of the relative importance are summarised in Tables which can be used by engineers in a site investigation programme to determine which fundamental soil parameters are more important in the analysis in a particular geotechnical engineering problem. For instance, if prediction of movements is required, it is important to determine the values of κ, λ and α'. If prediction of stability is required, it is important to determine κ, λ and M more accurately so that better prediction of the behaviour can be obtained. The values of κ and λ are important because they determine the initial states of the soil as summarised in Section 8.2.1 and 8.2.2 and have significant influence in the model prediction of soil behaviour.

Numerical analysis has become a powerful tool in analysing boundary value problems and numerical simulation provides a quick way to assess the soil behaviour by performing numerical parametric studies. The finite element formulation with the Biot's coupled consolidation theory in the program CRISP allows the analysis of coupled loading and drainage events. The modelling of hydraulic fracturing in a laboratory triaxial specimen demonstrates that CRISP can simulate the problem and give reasonably close estimate of the fracturing pressure. In the finite element simulation of undrained cavity expansion problem a much finer discretisation of the mesh towards the cavity is necessary.

8.3 Difficulties in the Numerical Analyses and Further Work

For the parametric study of Cam-clay following a triaxial compression loading path, the analyses were for isotropic undrained and drained triaxial compression loading paths so further studies need to be carried out for states in extension and initial K_o conditions. Also in the current study, the parameters κ/λ and λ were varied so κ changed in all the analyses. It would be desirable to perform a study to vary the values of κ/λ and κ, or to vary the values of κ and λ and examine the effects on the predicted soil behaviour. In the parametric study reported in this thesis, the program CASIS was developed and it generated an enormous amount of information so some post-processing facility should be incorporated. With the available spreadsheet programs such as Quattro Pro, SuperCalc 4, Lotus 1-2-3 for instance, the program CASIS can be modified so that the generated stress-strain parameters can be stored on ASCII files and imported into the spreadsheet programs for graph plotting in the data processing. This will speed up the analysis of the data which were plotted manually in this research.

In the parametric study of plate loading tests on Cam-clay, there were difficulties in the interpretation of the pressure-settlement curves to determine the settlement and bearing pressure immediately after yield, and the settlement at failure, because of the nature of the pressure-settlement curves. Careful examination and analysis of these curves were necessary in order to obtain consistent results in the

interpretation of the yield point and ultimate bearing pressure. In a few analyses with OCR = 40, there was no clearly defined failure point even when a total settlement of 120 mm was achieved, that is equivalent to a settlement ratio of 13.8. It is therefore necessary to impose further displacements.

With the availability of CRISP90 which can now be run on 486 micro-computers, the numerical analysis can be performed relatively quickly. The program CRISP90 also comes with the Lotus interface program which can expedite the analysis of the enormous amount of information generated by the program. The calculated specific volume v and the effective mean stress p' in the post-processing files generated by the Lotus interface program can be used to normalise stress, strain and pore pressure in any soil elements so that variations due to the current stress state can be eliminated. In the current investigation reported in this thesis, the undrained behaviour of the plate-soil system was evaluated. The parametric study of plate loading tests on Cam-clay can be extended to examine the normalised deviator stress, shear strain and rate of pore pressure increase by the current specific volume and effective mean stress at the initial, yield, peak and ultimate states in any soil elements as defined in the parametric study of Cam-clay following the undrained triaxial compression loading path. This exercise will confirm the findings in the first part of the parametric study using the single element analysis.

The simulation of laboratory hydraulic fracturing phenomenon by CRISP also generated an enormous amount of information which extends the knowledge in understanding soil behaviour in the fracturing analysis. The axisymmetric meshes, briefly investigated in the research, produced results which were very similar to those from the plane strain analyses. The axisymmetric mesh could be used more in the modelling of the hydraulic fracturing experiments and validation of these meshes against available closed-form solutions is also required. The analysis should be extended to investigate the influence of the sand cell on the predicted fracturing pressures. In addition, the geometry, in particular the boundary at which the cavity water pressure is applied, requires further study before use of the program in modelling the boundary value problem of hydraulic fracturing of an embankment dam.

APPENDIX 1 DERIVATION OF CONSTITUTIVE RELATIONS FOR CAM-CLAY

For any increment of load and displacement, total strains are equal to the sum of their elastic and plastic components:

$$\delta\epsilon_s = \delta\epsilon_s^e + \delta\epsilon_s^p \tag{A1.1}$$

$$\delta\epsilon_v = \delta\epsilon_v^e + \delta\epsilon_v^p \tag{A1.2}$$

where

$$\delta\epsilon_s^e = \frac{1}{3G'}\,\delta q' \tag{A1.3}$$

$$\delta\epsilon_v^e = \frac{1}{K'}\,\delta p' \tag{A1.4}$$

For associated flow, the vector of plastic strain increment is normal to the yield curve and is given by

$$\frac{\delta\epsilon_s^p}{\delta\epsilon_v^p} = F \tag{A1.5}$$

where the flow parameter F depends on the shape of the yield curve and on the state of stress. As the state of stress moves on the yield surface it moves from one yield curve to another. It is convenient to relate the resulting increment of plastic volumetric strain $\delta\epsilon_v^p$ to the stress increments $\delta q'$ and $\delta p'$ by an equation of the form

$$\delta\epsilon_v^p = H\,\delta q' + G\,\delta p' \tag{A1.6}$$

where H and G are the hardening parameters and depend on the shape of the yield surface and the state of stress. Equation (A1.6) can be thought of as a hardening law since it relates an increment of plastic strain to the corresponding changes of stress from one yield curve to another.

Combining Eqns. (A1.5) and (A1.6),

$$\delta\epsilon_s^p = F\,H\,\delta q' + F\,G\,\delta p' \tag{A1.7}$$

From Eqns (A1.1) and (A1.2),

$$\delta\epsilon_s = (F\,H + \frac{1}{3G'})\,\delta q' + F\,G\,\delta p' \tag{A1.8}$$

$$\delta\epsilon_v = H\,\delta q' + (G + \frac{1}{K'})\,\delta p' \tag{A1.9}$$

Assuming coaxiality condition holds and the flow rule is associated

$$G = \frac{H}{F} \tag{A1.10}$$

Then Eqns. (A1.8) and (A1.9) become

$$\delta e_s = (\,FH + \frac{1}{3G'}\,)\,\delta q' + H\,\delta p' \tag{A1.11}$$

$$\delta e_v = H\,\delta q' + (\frac{H}{F} + \frac{1}{K'}\,)\,\delta p' \tag{A1.12}$$

and they are the general expressions for stress-strain relations.

The equation for the Roscoe surface is

$$\frac{q'}{Mp'} + (\frac{\lambda}{\lambda - \kappa})\,\ln p' - (\frac{\Gamma - v}{\lambda - \kappa}) = 1 \tag{A1.13}$$

This intersects the v:p' plane along the normal consolidation line (NCL) where q' = 0 and v = N - λ ln p'. Therefore,

$$N = \Gamma + \lambda - \kappa \tag{A1.14}$$

which is the separation between the normal compression line and the critical state line in the v:ln p' space.

A yield curve is the intersection of an elastic wall

$$v = v_\kappa - \kappa \ln p' \tag{A1.15}$$

with the state boundary surface.

At failure on the critical state line (CSL),

$$v_f = v_\kappa - \kappa \ln p'_f \tag{A1.16}$$

$$v_f = \Gamma - \lambda \ln p'_f \tag{A1.17}$$

Hence, eliminating v and v_κ, a yield curve is

$$\frac{q'}{Mp'} + \ln\left(\frac{p'}{p'_f}\right) = 1 \tag{A1.18}$$

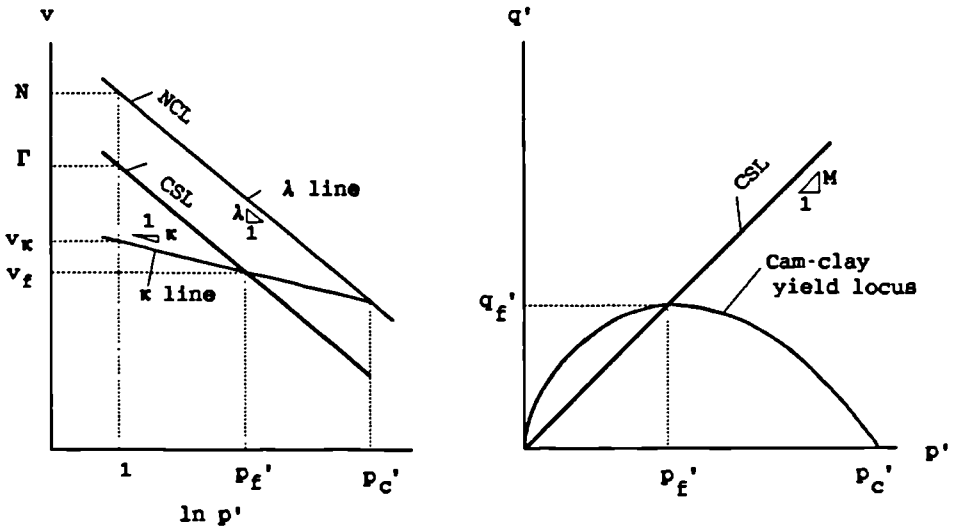

Applying the normality condition,

$$-\frac{1}{\left(\frac{de_s^p}{de_v^p}\right)} = \frac{dq'}{dp'} = \frac{q'}{p'} = M \tag{A1.19}$$

$$\frac{de_v^p}{de_s^p} = M - \frac{q'}{p'} \tag{A1.20}$$

$$\frac{1}{F} = M - \eta' \tag{A1.21}$$

Rewriting Eqn. (A1.13),

$$v = \Gamma + \lambda - \kappa - \lambda \ln p' - \frac{(\lambda - \kappa)\, q'}{Mp'} \tag{A1.22}$$

Differentiating and dividing by v,

$$\frac{\delta v}{v} = -\left(\frac{\lambda - \kappa}{vMp'}\right) \delta q' - \frac{\lambda}{vp'} \delta p' + \frac{(\lambda - \kappa)\eta'}{vMp'} \delta p' \tag{A1.23}$$

$$\delta \epsilon_v = -\frac{\delta v}{v} = \frac{\lambda - \kappa}{vMp'} \delta q' - \left[\frac{(\lambda - \kappa)\eta'}{vMp'} - \frac{\lambda}{vp'}\right] \delta p' \tag{A1.24}$$

$$\delta \epsilon_v^e = \frac{\kappa}{vp'} \delta p' \tag{A1.25}$$

$$\begin{aligned} \delta \epsilon_v^p &= \delta \epsilon_v - \delta \epsilon_v^e \\ &= \left[\frac{\lambda - \kappa}{vMp'}\right] \left[\delta q' + (M - \eta')\, \delta p'\right] \end{aligned} \tag{A1.26}$$

Comparing the terms between Eqns. (A1.6) and (A1.26), we have,

$$H = \frac{\lambda - \kappa}{vMp'} \tag{A1.27}$$

Equations (A1.11) and (A1.12) become,

$$\begin{aligned} \delta \epsilon_s &= \left[\frac{\lambda - \kappa}{(M - \eta')\, vMp'} + \frac{1}{3G'}\right] \delta q' + \frac{\lambda - \kappa}{vMp'} \delta p' \\ \delta \epsilon_v &= \frac{\lambda - \kappa}{vMp'} \delta q' + \left[(M - \eta')\frac{\lambda - \kappa}{vMp'} + \frac{1}{K'}\right] \delta p' \end{aligned} \tag{A1.28}$$

in which

$$K' = \frac{vp'}{\kappa} \tag{A1.29}$$

and

$$G' = \frac{vp'}{\kappa} \frac{[3(1 - \nu')]}{[2(1 + \nu')]} \tag{A1.30}$$

Expressing in matrix form,

$$\begin{bmatrix} \delta\epsilon_v \\ \delta\epsilon_s \end{bmatrix} = \begin{bmatrix} \frac{1}{K'} + \frac{\lambda - \kappa}{vMp'}(M - \eta') & \frac{\lambda - \kappa}{vMp'} \\ \frac{\lambda - \kappa}{vMp'} & \frac{1}{3G'} + \frac{\lambda - \kappa}{vMp'(M - \eta')} \end{bmatrix} \begin{bmatrix} \delta p' \\ \delta q' \end{bmatrix} \tag{A1.31}$$

Since

$$\alpha' = \frac{G'}{K'} = \frac{[3(1 - \nu')]}{[2(1 + \nu')]} \tag{A1.32}$$

Then,

$$\begin{bmatrix} \delta\epsilon_v \\ \delta\epsilon_s \end{bmatrix} = \frac{1}{vp'} \begin{bmatrix} \kappa + \frac{\lambda - \kappa}{M}(M - \eta') & \frac{\lambda - \kappa}{M} \\ \frac{\lambda - \kappa}{M} & \frac{\kappa}{3\alpha'} + \frac{\lambda - \kappa}{M(M - \eta')} \end{bmatrix} \begin{bmatrix} \delta p' \\ \delta q' \end{bmatrix} \tag{A1.33}$$

APPENDIX 2 DERIVATION OF CONSTITUTIVE RELATIONS FOR MODIFIED CAM-CLAY

The general expressions for stress-strain relations have been given in Eqns. (A1.11) and (A1.12) in Appendix 1.

For the modified Cam-clay model, the equation for the Roscoe surface is given by

$$\frac{p'}{p'_c} = \left[\frac{M^2}{M^2 + \eta^2}\right]^{(1 - \frac{\kappa}{\lambda})} \tag{A2.1}$$

$$\ln\left(\frac{p'}{p'_c}\right) = \left(1 - \frac{\kappa}{\lambda}\right) \ln\left(\frac{M^2}{M^2 + \eta^2}\right) \tag{A2.2}$$

$$\ln\left(\frac{p'}{p'_c}\right) + \left(\frac{\lambda - \kappa}{\lambda}\right) \ln\left[1 + \frac{\eta^2}{M^2}\right] = 0 \tag{A2.3}$$

$$\frac{1}{\left(1 - \frac{\kappa}{\lambda}\right)} \ln \frac{p'}{p'_c} + \ln\left[1 + \frac{\eta^2}{M^2}\right] = 0 \tag{A2.4}$$

$$\frac{1}{\left(1 - \frac{\kappa}{\lambda}\right)} \ln \frac{p'}{p'_c} + \ln 2 + \ln\left[\frac{1}{2}\left(1 + \frac{\eta^2}{M}\right)\right] = 0 \tag{A2.5}$$

or,

$$\lambda \ln \frac{p'}{p'_c} + (\lambda - \kappa) \ln 2 + (\lambda - \kappa) \ln\left[\frac{1}{2}\left(1 + \frac{\eta^2}{M^2}\right)\right] = 0 \tag{A2.6}$$

The intersection of the constant volume section and CSL, where

$$q' = M p'_f \tag{A2.7}$$

and

$$v = \Gamma - \lambda \ln p_f' \tag{A2.8}$$

is given by

$$\lambda \ln \frac{p_f'}{p_c'} + (\lambda - \kappa) \ln 2 + 0 = 0 \tag{A2.9}$$

$$\lambda \ln p_f' - \lambda \ln p_c' + (\lambda - \kappa) \ln 2 = 0 \tag{A2.10}$$

From Eqn. (A2.8) $v = \Gamma - \lambda \ln p_f'$,

and $v = N - \lambda \ln p_c'$ (A2.11)

Therefore, $\lambda \ln p_f' = \Gamma - v$,

and $\lambda \ln p_c' = N - v$

Hence, $\Gamma - v - N + v + (\lambda - \kappa) \ln 2 = 0$

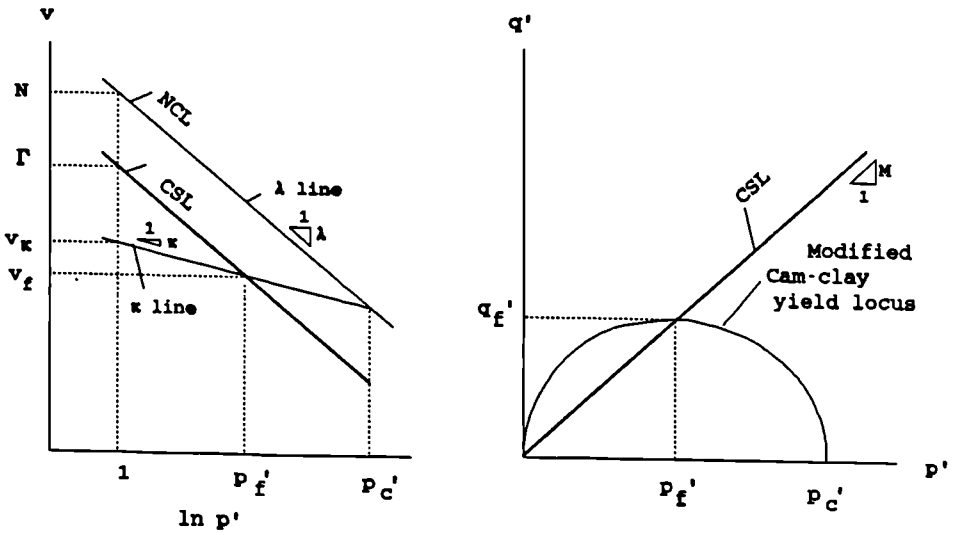

So, $N - \Gamma = (\lambda - \kappa) \ln 2$ (A2.12)

which is the separation between the normal compression line and the critical state line in the v:ln p' space.

The Roscoe surface in Eqn. (A2.6) can be written as

$$\lambda \ln p' - \lambda \ln p'_c + N - \Gamma + (\lambda - \kappa) \ln \left[\frac{1}{2}\left(1 + \frac{\eta^2}{M^2}\right)\right] = 0 \tag{A2.13}$$

or,

$$(N - \lambda \ln p'_c) = (\Gamma - \lambda \ln p') - (\lambda - \kappa) \ln \left[\frac{1}{2}\left(1 + \frac{\eta^2}{M^2}\right)\right] \tag{A2.14}$$

$$v = (\Gamma - \lambda \ln p') - (\lambda - \kappa) \ln \left[\frac{1}{2}\left(1 + \frac{\eta^2}{M^2}\right)\right] \tag{A2.15}$$

On expanding,

$$v = \Gamma - \lambda \ln p' + (\lambda - \kappa) \ln 2 - (\lambda - \kappa) \ln \left[\left(1 + \frac{\eta^2}{M^2}\right)\right] \tag{A2.16}$$

On differentiating,

$$\begin{aligned} \delta v &= -\frac{\lambda\, \delta p'}{p'} - \frac{(\lambda - \kappa)}{M^2 + \eta^2}\left[\frac{2q'\delta q'}{p^2} - \frac{2q^2}{p^3}\delta p'\right] \\ &= -\frac{\lambda}{p'}\delta p' - \frac{2\eta'(\lambda - \kappa)}{p'(M^2 + \eta^2)}\left(\delta q' - \eta'\, \delta p'\right) \end{aligned} \tag{A2.17}$$

Dividing the above equation by -v,

$$\begin{aligned} \delta \epsilon_v &= -\frac{\delta v}{v} \\ &= \frac{\lambda}{vp'}\delta p' - \frac{2\eta^2(\lambda - \kappa)}{vp'(M^2 + \eta^2)}\,\delta p' + \frac{2\eta'(\lambda - \kappa)}{vp'(M^2 + \eta^2)}\,\delta q') \end{aligned} \tag{A2.18}$$

Since,

$$\delta \epsilon_v^e = \frac{\kappa}{vp'}\delta p' \tag{A2.19}$$

And,

$$\delta\epsilon_v^p = \delta\epsilon_v - \delta\epsilon_v^e$$

$$= -\frac{\lambda - \kappa}{vp'}\,\delta p' - \frac{2\eta^2(\lambda - \kappa)}{vp'(M^2 + \eta^2)}\,\delta p' + \frac{2\eta'(\lambda - \kappa)}{vp'(M^2 + \eta^2)}\,\delta q' \qquad \text{(A2.20)}$$

Since from Eqn. (A1.6),

$$\delta\epsilon_v^p = H\,\delta q' + G\,\delta p' \qquad \text{(A2.21)}$$

$$H = \frac{2\eta'(\lambda - \kappa)}{vp'(M^2 + \eta^2)} \qquad \text{(A2.22)}$$

A yield curve is the intersection of an elastic wall

$$v = v_\kappa - \kappa \ln p' \qquad \text{(A2.23)}$$

with the state boundary surface.

At failure on the critical state line (CSL),

$$v_f = v_\kappa - \kappa \ln p_f' \qquad \text{(A2.24)}$$

$$= \Gamma - \lambda \ln p_f'$$

$$v = \Gamma - \lambda \ln p_f' + \kappa \ln p_f' - \kappa \ln p' \qquad \text{(A2.25)}$$

Equating Eqns. (A2.15) and (A2.25)

$$\Gamma - \lambda \ln p_f' + \kappa \ln p_f' - \kappa \ln p' = \Gamma - \lambda \ln p' - (\lambda - \kappa) \ln \left[\frac{1}{2}\left(1 + \frac{\eta^2}{M^2}\right)\right]$$

$$\ln \left(\frac{p_f'}{p'}\right) = \ln \left[\frac{1}{2}\left(1 + \frac{\eta^2}{M^2}\right)\right]$$

$$\frac{p_t'}{p'} = \frac{1}{2}\left(1 + \frac{\eta^2}{M^2}\right) \tag{A2.26}$$

Since,

$$p_t' = \frac{1}{2}p_c' \tag{A2.27}$$

Hence,

$$\frac{p_c'}{p'} = \left(1 + \frac{\eta^2}{M^2}\right) \tag{A2.28}$$

which is the yield curve derived from the modified Cam-clay model.

Applying the normality condition,

$$-\frac{1}{\left(\frac{de_s^p}{de_v^p}\right)} = \frac{dq'}{dp'} \tag{A2.29}$$

leading to

$$\frac{de_v^p}{de_s^p} = \frac{M^2 - \eta^2}{2\eta'} \tag{A2.30}$$

Hence,

$$\frac{1}{F} = \frac{M^2 - \eta^2}{2\eta'} \tag{A2.31}$$

And,

$$\frac{H}{F} = \frac{(\lambda - \kappa)\ (M^2 - \eta^2)}{vp'(M^2 + \eta^2)} \tag{A2.32}$$

$$H \cdot F = \frac{2\eta'\ (\lambda - \kappa)}{vp'\ (M^2 + \eta^2)} \cdot \frac{2\eta}{(M^2 - \eta^2)} \tag{A2.33}$$

$$- \frac{4\eta^4 (\lambda - \kappa)}{vp' (M^4 - \eta^4)} \tag{A2.34}$$

So,

$$\delta\epsilon_v = \left[\frac{\kappa}{vp'} + \frac{(\lambda - \kappa)(M^2 - \eta^2)}{vp' (M^2 + \eta^2)} \right] \delta p' + \frac{2\eta' (\lambda - \kappa)}{vp' (M^2 + \eta^2)} \delta q' \tag{A2.35}$$

$$\delta\epsilon_s = \frac{2\eta' (\lambda - \kappa)}{vp' (M^2 + \eta^2)} \delta p' + \left[\frac{\kappa}{vp'} \cdot \frac{2(1 + \nu')}{9(1 - 2\nu')} + \frac{4\eta^2 (\lambda - \kappa)}{vp' (M^4 - \eta^4)} \right] \delta q' \tag{A2.36}$$

Expressing Eqns. (A2.35) and (A2.36) in matrix form,

$$\begin{bmatrix} \delta\epsilon_v \\ \delta\epsilon_s \end{bmatrix} = \begin{bmatrix} \frac{\kappa}{vp'} + \frac{(\lambda - \kappa)(M^2 - \eta^2)}{vp' (M^2 + \eta^2)} & \frac{2\eta' (\lambda - \kappa)}{vp' (M^2 + \eta^2)} \\ \frac{2\eta' (\lambda - \kappa)}{vp' (M^2 + \eta^2)} & \frac{\kappa}{vp'} \cdot \frac{2(1 + 2\nu')}{9(1 - 2\nu')} + \frac{4\eta^2 (\lambda - \kappa)}{vp' (M^4 - \eta^4)} \end{bmatrix} \begin{bmatrix} \delta p' \\ \delta q' \end{bmatrix}$$

Since

$$\alpha' = \frac{G'}{K'} = \frac{[3(1 - 2\nu')]}{[2(1 + \nu')]} \tag{A2.37}$$

Then,

$$\begin{bmatrix} \delta\epsilon_v \\ \delta\epsilon_s \end{bmatrix} = \frac{1}{vp'} \begin{bmatrix} \kappa + \frac{(\lambda - \kappa)(M^2 - \eta^2)}{(M^2 + \eta^2)} & \frac{2\eta' (\lambda - \kappa)}{M^2 + \eta^2} \\ \frac{2\eta' (\lambda - \kappa)}{M^2 + \eta^2} & \frac{\kappa}{3\alpha'} + \frac{4\eta^2 (\lambda - \kappa)}{(M^4 - \eta^4)} \end{bmatrix} \begin{bmatrix} \delta p' \\ \delta q' \end{bmatrix} \tag{A2.38}$$

APPENDIX 3 DERIVATION OF THE UNDRAINED STRESS PATH FOR THE CAM-CLAY MODEL

The prediction of undrained strength based on the Cam-clay family of models depends on the constitutive equations adopted. The state boundary surface describes a surface in (q':p':v) space and is given by Eqn. (2.24):

$$q' = \frac{Mp'}{\lambda - \kappa}(\Gamma + \lambda - \kappa - v - \lambda \ln p') \tag{A3.1}$$

The separation of the normal compression line (NCL) and the critical state line (CSL) in the original Cam-clay model is:

$$N - \Gamma = \lambda - \kappa$$

Assuming that a sample is initially isotropically normally consolidated to a pressure p_o' the initial volume is given by

$$v_o = N - \lambda \ln p_o'$$

or

$$v_o = \Gamma + \lambda - \kappa - \lambda \ln p_o' \tag{A3.2}$$

Substituting Eqn. (A3.2) in (A3.1), then

$$q' = \frac{Mp'}{\lambda - \kappa}(\lambda \ln p_o' - \lambda \ln p')$$

$$q' = \frac{Mp'}{\lambda - \kappa}(\lambda \ln \frac{p_o'}{p'})$$

$$q' = \frac{Mp'}{(1 - \frac{\kappa}{\lambda})} \ln \frac{p_o'}{p'} \tag{A3.3}$$

Eqn. (A3.3) is the undrained effective stress path for a sample initially normally consolidated to a pressure p_e'. For overconsolidated samples at the same initial specific volume v_e, the effective stress paths are parallel to the q' axis until they intersect this line, they then follow the same path to the critical state. Eqn. (A3.3) shows that the shape of the undrained effective stress path depends on the value of the factor $(1 - \kappa/\lambda)$ or κ/λ while the value of p_e' determines the size of the yield locus.

APPENDIX 4 DERIVATION OF STRESS CONDITIONS FOR DIFFERENT OCR'S AT THE SAME INITIAL SPECIFIC VOLUME AT THE START OF THE ANALYSIS

The following derives the initial stress condition in the numerical analysis of hydraulic fracturing in order to have the same initial specific volume with different values of overconsolidation ratio at the start of the analysis.

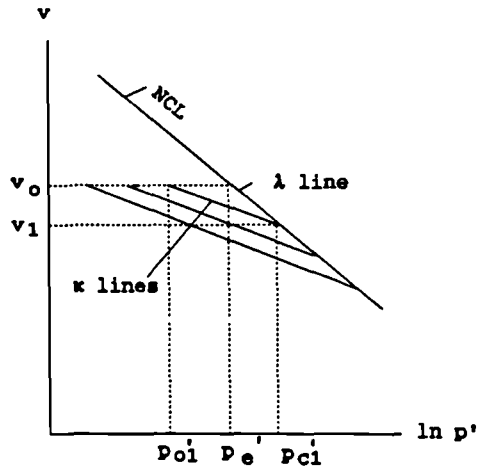

The overconsolidation ratio OCR is defined as

$$OCR = R_p = \frac{p'_c}{p'_o} \tag{A4.1}$$

The slope of the isotropic normal compression line λ is given by

$$-\lambda = \frac{(v_1 - v_o)}{\ln \frac{p'_{c1}}{p'_e}} \tag{A4.2}$$

Therefore,

$$v_1 = v_o - \lambda \ln \frac{p'_{c1}}{p'_e} \tag{A4.3}$$

The slope of the swelling line κ is given by

$$-\kappa = \frac{(v_1 - v_o)}{\ln \frac{p'_{c1}}{p'_{o1}}} \tag{A4.4}$$

Therefore,

$$v_1 = v_o - \kappa \ln \frac{p'_{c1}}{p'_{o1}} \tag{A4.5}$$

Equating Eqns. (A4.3) and (A4.5),

$$\lambda \ln \frac{p'_{c1}}{p'_e} = \kappa \ln \frac{p'_{c1}}{p'_{o1}}$$

$$\lambda \ln p'_{c1} - \lambda \ln p'_e = \kappa \ln R_p$$

$$\ln p'_{c1} - \ln p'_e + \frac{\kappa}{\lambda} \ln R_p$$

or,

$$\ln \frac{p'_{c1}}{p'_e} = \frac{\kappa}{\lambda} \ln R_p$$

or,

$$\frac{p'_{c1}}{p'_e} = [\frac{p'_{c1}}{p_{o1}}]^{\frac{\kappa}{\lambda}} \tag{A4.6}$$

For the analyses in Group C described in Chapter 6, Equation (A4.6) is used to calculate the initial in-situ stresses for a range of values of overconsolidation ratio between 2 and 12. With p_e' = 200 kPa, κ = 0.03, λ = 0.12 and κ/λ = 0.25, the following values of p_{c1}' and p_{o1}' are obtained.

Case	OCR	p_{c1}' (kPa)	p_{o1}' (kPa)
C1	2	237.8	118.9
C2	4	282.8	70.7
C3	8	336.4	42.0
C4	12	372.2	31.0

REFERENCES

Almeida, M.S.S. (1984), *Stage constructed embankments on soft clays*, Ph.D. Thesis, Engineering Department, Cambridge University, Cambridge, England.

Almeida, M.S.S., Britto, A.M. and Parry, R.H.G. (1986), Numerical modelling of a centrifuged embankment on soft clay, *Canadian Geotechnical Journal*, **Vol. 23**, pp. 103-114.

Atkinson, J.H. (1980), *Foundations and Slopes*, McGraw-Hill, London.

Atkinson, J.H. and Bransby, P.L. (1978), *The Mechanics of Soils*, McGraw-Hill, London.

Atkinson, J.H. and Crabb, G.I. (1991), Determination of soil strength parameters for the analysis of highway slope failures, *Proc. International Conference on Slope Stability Engineering - Developments and Applications*, Institution of Civil Engineers, U.K.

Atkinson, J.H. and Little, J.A. (1985), Undrained triaxial strength and stress-strain characteristics of reconstituted and undisturbed samples of a lodgement till, *Research Report GE/85/14*, City University, London.

Atkinson, J.H. and Richardson, D. (1987), The effect of local drainage in shear zones on the undrained strength of overconsolidated clay, *Geotechnique*, **Vol. 37, No. 3**, pp. 393-403.

Atkinson, J.H. and Tam, H.K. (1988), A parametric study of Cam-clay, *Research Report GE/88/11*, City University, London.

Atkinson, J.H. and Tam, H.K. (1991a), Numerical studies of hydraulic fracturing in clays, *Research Report GE/91/16*, City University, London.

Atkinson, J.H. and Tam, H.K. (1991b), Numerical investigation of plate loading tests on Cam-clay, *Research Report GE/91/17*, City University, London.

Barkan, D.D. (1962), *Dynamics of Bases and Foundations*, (Translated from the Russian), McGraw-Hill.

Biot, M.A. (1941), General theory of three dimensional consolidation, *J. Applied Physics*, **Vol. 12**, pp. 155-164.

Bishop, A.W. and Hight, D.W. (1977), The value of Poisson's ratio in saturated soils and rocks under undrained conditions, *Geotechnique*, **Vol. 27, No. 3**, pp. 369-384.

Bolton, M.D. (1986), The strength and dilatancy of sands, *Geotechnique*, **Vol. 36, No. 1**, pp. 65-78.

Bolton, M.D., Britto, A.M., Powrie, W. and White, T.P. (1989), Finite element analysis of a centrifuge model of a retaining wall embedded in a heavily overconsolidated clay, *Computers and Geotechnics*, **Vol. 7**, pp. 289-318.

Booker, J.R. & Small, J.C. (1975), An investigation of the stability of numerical solutions of Biot's equations of consolidation, *International Journal of Solids & Structures*, **Vol. 11**, pp. 907-911.

Booker, J.R. & Small, J.C. (1976), Finite element analysis of primary and secondary consolidation, *Research Report R284*, School of Civil Engineering, University of Sydney.

Britto, A.M. and Gunn, M.J. (1987), *Critical State Soil Mechanics via Finite Elements*, Ellis Horwood.

Butterfield, R. and Banerjee P.K. (1971), A rigid disc embedded in an elastic half-space, *Geotechnical Engineering*, **Vol. 2, No. 1**, pp. 35-52.

Carrier, W.D. and Christian, J.T. (1973), Rigid circular plate resting on a non-homogeneous elastic half-space, *Geotechnique*, Vol. 23, No. 1, pp. 67-84.

Carter, J.P. (1977), *Finite deformation theory and its application to elastoplastic soils*, Ph.D. Thesis, University of Sydney.

Carter, J.P. (1978), CAMFE. A computer program for the analysis of a cylindrical cavity expansion in soil, *CUED/C - Soils TR52 Report*, Cambridge University, England.

Carter, J.P. (1982), Predictions of non-homogeneous behaviour of clay in the triaxial test, *Geotechnique*, Vol. 32, No. 2, pp. 55-58.

Carter, J.P. and Young, S.K. (1985), Analysis of cylindrical cavity expansion in a strain weakening material, *Computers and Geotechnics*, Vol. 1, pp. 161-180.

Carter, J.P., Small, J.C. and Booker, J.R. (1977), A theory of finite elastic consolidation, *International Journal of Solids & Structures*, Vol. 13, pp. 467-478.

Carter, J.P., Randolph, M.F. and Wroth, C.P. (1979), Stress and pore pressure changes in clay during and after the expansion of a cylindrical cavity, *International Journal for Numerical and Analytical Methods in Geomechanics*, Vol. 3, pp. 305-322.

Cherrill, H.E. (1990), *The influence of loading rate on excess pore pressures in triaxial tests*, Ph.D. Thesis, City University, London.

Clinton, D.B. (1986), Programs for Data Analysis on the BBC micro-computer, *Research Report No. GE/86/2*, City University, London.

De Moor, E.K. (1989), *Modelling of deep tunnel behaviour in clay*, Ph.D. Thesis, City University, London.

De Moor, E.K. and Taylor, R.N. (1991), Time dependent behaviour of a tunnel heading in clay, *Proc. of the seventh International Conference on Computer Methods and Advances in Geomechanics*, Cairns, pp. 1455-1460.

Gibson, R.E. and Anderson, W.F. (1961), In-situ measurement of soil properties with the pressuremeter, *Civil Engineering and Public Works Review*, **Vol. 56**, pp. 615-618.

Graham, J. and Houlsby, G.T. (1983), Anisotropic elasticity of a natural clay, *Geotechnique*, **Vol. 33, No. 2**, pp. 165-180.

Gunn, M.J. and Britto, A.M. (1982 & 1984), *Users and Programmers Guide*, Cambridge University Engineering Department.

Hashiguchi, K. (1985), Two- and three-surface models of plasticity, *Proc. Fifth International Conference on Numerical Methods in Geomechanics*, Nagoya, pp. 285-292.

Hinton, E. and Owen, D.R.J. (1979), *An Introduction to Finite Element Computations*, Pineridge Press, Swansea.

Hird, C.C., Pyrah, I.C. and Russell, D. (1990), Finite element analysis of the collapse of reinforced embankments on soft ground, *Geotechnique*, **Vol. 40, No. 4**, pp. 633-640.

Hird, C.C., Pyrah, I.C. and Russell, D. (1991), reply to discussion, *Geotechnique*, **Vol. 41, No. 4**, pp. 630.

Ho, E.W.L. (1985), Undrained triaxial compression and extension tests on 'undisturbed' and reconstituted deep-ocean sediments consolidated under K_o conditions, *Research Report GE/85/21*, City University, London.

Houlsby, G.T. and Nageswaren, S. (1982), A study of consolidation with radial drainage, *Workshop on Finite Elements in Critical State Soil Mechanics*, Cambridge.

Irons, B.M. and Ahmad, S. (1980), *Techniques of Finite Elements*, Ellis Horwood.

Jaky, J. (1944), The coefficient of earth pressure at rest, *Magyar Mernok es Epitesz Egylet Kozlonye*.

Jardine, R.J. and Potts, D.M. (1988), Hutton tension leg platform foundations: prediction of driven pile behaviour, *Geotechnique*, **Vol. 38, No. 2**, pp. 231-252.

Jardine, R.J., Potts, D.M., Fourie, A.B. and Burland, J.B. (1986), Studies of the influence of non-linear stress-strain characteristics in soil-structure interaction, *Geotechnique*, **Vol 36, No. 3**, pp. 377-396.

Lee, I.K. (1986), Stress path tests on reconstituted deep-ocean sediments under K_o conditions, *Research Report GE/86/27*, City University, London.

Lee Goh, A. and Fahey, M. (1991), Application of a 1-dimensional cavity expansion model to pressuremeter and piezocone tests in clay, *Proc. of the seventh International Conference on Computer Methods and Advances in Geomechanics*, Cairns, PP. 255-260.

Lewin, P.I. (1970), *Stress deformation characteristics of a saturated soil*, M.Sc. Thesis, University of London.

Li, E.S.F. (1990), *On the analysis of singly-propped diaphragm walls*, Ph.D. Thesis, University of London.

Little, J.A. (1985), personal communication.

Marsland, A. and Butcher, A.P. (1983), In situ tests on highly weathered chalk near Luton, England, *Proc. Symp. International In Situ Testing*, **Vol. 2**, Paris, pp. 83-88.

Mhach, H.K. (1991), *An experimental study of hydraulic fracture and erosion*, Ph.D. Thesis, City University, London.

Mröz, Z., Norris, V.A. and Zienkiewicz, O.C. (1979), Application of an anisotropic hardening model in the analysis of elasto-plastic deformation of soils, *Geotechnique*, Vol. 29, No. 1, pp. 1-34.

Murayama, S (ed.) (1985), Constitutive laws of soil, *Report of ISSMFE Subcommittee on constitutive laws of soils and Proc. discussion session 1A, 11th International Conference on Soil Mechanics and Foundation Engineering*, San Francisco (Tokyo: Japanese Society of Soil Mechanics and Foundation Engineering).

Naylor, D.J. (1975), *Non-linear finite elements for soils*, Ph.D. Thesis, University College of Swansea, Wales.

Naylor, D.J. (1978), Finite Element Methods in Soil Mechanics (Chapter 1), *Developments in Soil Mechanics*, ed. C.R. Scott, Applied Science Publishers.

Ng, C. (1984), Personal communication.

Nishida, Y. (1966), Vertical stresses and vertical deformations of ground under a deep circular uniform pressure in the semi-infinite, *Proc. First Congress of International Society of Rock Mechanics*, Vol. 2, pp. 493-498.

Pickles, A.R. (1989), *The application of critical state soil mechanics to predict ground deformations below an embankment constructed on soft alluvium*, Ph.D. Thesis, City University, London.

Potts, D.M. and Fourie, A.B. (1984), The behaviour of a propped retaining wall: results of a numerical experiment, *Geotechnique*, Vol. 34, No. 3, pp. 383-404.

Potts, D.M. and Ganendra, D. (1991), Discussion on Finite element analysis of the collapse of reinforced embankments on soft ground, *Geotechnique*, Vol. 41, No. 4, pp. 627-630.

Potts, D.M., Dounias, G.T. and Vaughan, P.R. (1987), Finite element analysis of the direct shear box test, *Geotechnique*, Vol. 37, No. 1, pp.11-23.

Poulos, H.G. and Davis, E.H. (1974), *Elastic Solutions for Soil and Rock Mechanics*, John Wiley, New York.

Powrie, W. (1986), *The behaviour of diaphragm walls in clay*, Ph.D. Thesis, University of Cambridge.

Powrie, W. and Li, E.S.F. (1991a), Finite element analyses of an in-situ wall propped at formation level, *Geotechnique*, Vol. 41, No. 4, pp. 499-514.

Powrie, W. and Li, E.S.F. (1991b), Analysis of in-situ retaining walls propped at formation level, *Proc. I.C.E.*, Part 2, Vol. 91, December, pp. 853-873.

Randolph, M.F. and Wroth, C.P. (1978), An analytical solution for the consolidation around a driven pile. (Unpublished).

Randolph, M.F., Carter, J.P. and Wroth, C.P. (1979), Driven piles in clay - the effects of installation and subsequent consolidation, *Geotechnique*, Vol. 29, pp. 361-393.

Richardson, D.(1984), Report on progress in first year of research on threshold effects in soil mechanics, *Research Report GE/84/22*, City University, London.

Richardson, D.(1985), Report on progress in second year of research on threshold effects in soil mechanics, *Research Report GE/85/23*, City University, London.

Roscoe K.H. and Burland, J.B. (1968), On the generalised stress-strain behaviour of "wet" clay, *Engineering Plasticity*, (eds. Heyman and Leckie), Cambridge University Press, pp. 535-609.

Roscoe, K.H., Schofield, A.N. and Thurairajah, A. (1963), Yielding of clays in states wetter than critical, *Geotechnique*, Vol. 8, No. 1, pp. 22-53.

Sandhu, R.S. and Wilson, E.L. (1969), Finite element analysis of seepage in elastic media, *Proc. A.S.C.E.*, Vol. 95, No. EM3, pp. 641-652.

Schofield, A.N. (1980), Cambridge geotechnical centrifuge operations, *Geotechnique*, Vol. 20, No. 2, pp. 129-170.

Schofield, A.N. and Wroth, C.P. (1968), *Critical State Soil Mechanics*, McGraw-Hill, London.

Simpson, B. (1973), *Finite element computations in soil mechanics*, Ph.D. Thesis, University of Cambridge.

Simpson, B., O'Riordan, N.J. and Croft, D.D. (1979), A computer model for the analysis of ground movements in London clay, *Geotechnique*, Vol. 29, No. 2, pp. 149-175.

Skempton, A.W. (1951), The bearing capacity of clays, *Proceedings Building Research Congress*, Vol. 1, The Institution of Civil Engineers, London, pp. 180-189.

Sloan, S.W. and Randolph, M.F. (1982), Numerical prediction of collapse loads using finite element methods, *International Journal for numerical and Analytical Methods in Geomechanics*, Vol. 6, pp. 47-76.

Small, J.C., Booker, J.R. and Davies, E.H. (1975), Elasto-plastic consolidation of soil, *Research Report R268*, School of Civil Engineering, University of Sydney.

Stallebrass, S.E. (1990), *Modelling the effect of recent stress history on the deformation of overconsolidated soils*, Ph.D. Thesis, City University, London.

Tam, H.K. (1987), A computer program calculating stresses and strains in triaxial tests using incremental constitutive equations - CASIS, *Research Report GE/87/7*, City University, London.

Tam H.K., Mhach, H.K., Woods, R.I. (1988), Numerical investigation of hydraulic fracturing in clays, ed. G. Swoboda, *Proc. 6th International Conference on Numerical Methods in Geomechanics*, Innsbruck, pp. 563-570.

Tam, H.K. & Woods, R.I. (1989), A parametric study of Cam-clay, *Proceedings of the 3rd International Symposium on Numerical Models in Geomechanics, NUMOG III*, 8-11 May 1989, Canada, Elsevier Applied Science Publishers, pp. 264-271.

Toh, C.T. and Sloan, S.W. (1980), Finite element analyses of isotropic and anisotropic cohesive soils with a view to correctly predicting impending collapse, *International Journal of Numerical and Analytical Methods in Geomechanics*, Vol. 4, pp. 1-23.

University of Salford (1981), GINO-F users manual, Computer Laboratory Publication.

University of Salford (1982), GINOSURF users manual, Computer Laboratory Publication.

University of Salford (1983), GINOGRAF users manual, Computer Laboratory Publication.

Vesic, A.S. (1972), Expansion of cavities in infinite soil mass, *Journal of Soil Mechanics and Foundation Engineering, ASCE*, Vol. 98, pp. 265-290.

Woods, R.I. (1986a), Finite element analysis of coupled loading and consolidation, eds. Pande and Van Impe, *Proc. 2nd International Conference on Numerical Models in Geomechanics*, Ghent University, Redruth, Jackson, pp. 701-712.

Woods, R.I. (1986b), User manual for MPLOT - A computer program to plot finite element meshes, *Research Report GE/86/17*, City University, London.

Woods, R.I. (1987a), A guide to using CRISP 84 on the GOULD PN9005 under UNIX, *Research Report GE/87/15*, City University, London.

Woods, R.I. (1987b), User manual for MESHGEN - A computer program to generate simple finite element meshes, *Research Report GE/87/16*, City University, London.

Woods, R.I. (1987c), User manual for DISPLAY - A computer program to display the results of a finite element analysis, *Research Report GE/87/17*, City University, London.

Woods, R.I. (1987d), User manual for DPLOT - A computer program to plot deformed finite element meshes and displacement vectors, *Research Report GE/87/18*, City University, London.

Woods, R.I. (1987e), User manual for CPLOT - A computer program to contour the results of a finite element analysis, *Research Report GE/87/19*, City University, London.

Woods, R.I. (1987f), User manual for GPLOT - A computer program to plot the results of a finite element analysis, *Research Report GE/87/17*, City University, London.

Woods, R.I. and Contreras, L.F. (1987), Numerical modelling of field plate loading tests, *Research Report GE/87/2*, City University, London.

Woods, R.I. and Contreras, L.F. (1988), Numerical modelling of field plate loading tests (Part II), *Research Report GE/88/8*, City University, London.

Wroth, C.P. (1975), In-situ measurement of initial stresses and deformation characteristics, *Proc. of Specialty Conference in In-Situ Measurement of Soil Properties*, ASCE, Raleigh, North Carolina, pp. 181-230.

Wroth, C.P. (1977), The predicted performance of soft clay under a trial embankment loading based on the Cam-clay model, *In Finite elements in geomechanics*, ed. by G. Gudehus, John Wiley & Sons, Chap. 6, pp. 191-208.

Zienkiewicz, O.C. (1977), *The Finite Element Method in Engineering Science*, McGraw-Hill, London.

Zienkiewicz, O.C. and Naylor, D.J. (1972), The adaptation of critical state soil mechanics theory for use in finite elements, *In Stress-strain behaviour of soils, Proc. of the Roscoe Memorial Symposium*, Foulis & Co. Ltd., pp. 537-547.

Table 5.1 Summary of Experimental Soil Parameters

Soil Type	λ	κ	Γ_c	N	M_c	κ/λ	G_s	LL	PL	PI	Reference
London clay	.156	.043	2.585	2.675, $\eta'=0$ 2.665, $\eta'=.25$ 2.610, $\eta'=.75$	0.89	.28	2.75	70	27	43	Richardson (1985)
	.161	.062	2.448		0.89	.38	2.75	75	30	45	Schofield & Wroth (1968)
Cowden till	.0925	.015		2.110		.16					Ng (1984)
	.0845	.013	1.810	1.875	1.26	.15	2.65	35	17	18	
	.09	.0145		1.984	1.18	.16	2.66	35	17	18	
Slate dust	.077	.011		2.086		.14					Lewin (1970)
	.078	.0108			1.04	.14	2.78	29	18	11	
Speswhite kaolin	.18	.04		3.2		.22					Robinson (1983)
	.19	.05	3.14	3.26, $\eta'=.43$	1.0	.26	2.60	65	35	30	
Deep Ocean sediment	.165	.03	3.513	3.545, $K_o=.42$	1.6	.18	2.70	100	45	55	Ho (1985)
	.205		3.15; Γ_e =3.1	3.205, $K_o=.45$	1.4; M_e =1.1			85	40	45	Lee (1986)
Ware till	.079	.0194		2.036 2.259	1.02	.25	2.61	39	22	17	Richardson (1984)
Lodgement till											Atkinson & Little (1985)
(recon)	.065	.03	1.845	1.863	0.84	.46		40	18	22	
(undis)	.037	.019	1.68	1.695	0.86	.51					
East Ham clay	.27	.054	3.72	3.90, $\eta'=0$ 3.84, $\eta'=K_o$	1.17	.2	2.66	95	42	53	Pickles (1989)

Table 5.2 Programme of Parametric Study on Cam-Clay

λ	κ/λ	κ	Γ	N	Remarks
0.05	0.100	0.0050	1.7105	1.7555	
	0.233	0.0116		1.7489	
	0.367	0.0183		1.7422	
	0.500	0.0250		1.7355	M=0.77, 0.98, 1.20, 1.40
0.15	0.100	0.0150	2.6315	2.7665	
	0.233	0.0349		2.7466	
	0.367	0.0550		2.7265	
	0.500	0.0750		2.7065	α'=0.75, 0.60, 0.46, 0.33
0.25	0.100	0.0250	3.5525	3.7775	
	0.233	0.0582		3.7443	
	0.367	0.0917		3.7108	
	0.500	0.1250		3.6775	p_c'=200 kPa
0.35	0.100	0.0350	4.4735	4.7885	
	0.233	0.0815		4.7420	OCR=1.0,
	0.367	0.1284		4.6951	1.33,
	0.500	0.1750		4.6485	4.0

Notes:

1. κ, λ, Γ, M and α' are the critical state soil model parameters.
2. OCR denotes the overconsolidation ratio.
3. p_c' denotes the preconsolidation pressure.

Table 5.3 Ranges & Form of Variations of Undrained Behaviour Parameters

	M	λ	κ/λ	α'	OCR
	0.77-1.40	0.05-0.35	0.1-0.5	0.33-0.75	1.0,1.33 and 4.0
$3G_o'/(vp')$	indep.	indep.	36.4 d	2.3 i	indep.
			linear with $1/\kappa$	linear	
$[du/(vp' d\epsilon_s)]_o$	1.1-1.4 i*	7.0 d	4.8-5.5 d	1.3-2.2 i	indep.
	nonlin.	nonlin.	nonlin.	linear	
ϵ_{sy}	1.6-1.8 i	3.7 i	4.3-4.8 i	1.9-2.1 d	4.3-4.6 i
	linear	nonlin.	linear	linear	linear
$3G_y'/(vp')$	1.5-2.2 i	7.3 d	3.5 d	1.3-1.8 i	6.5-8.5 d
	linear	linear with $1/\lambda$	linear with λ/κ	linear	linear with 1/OCR
$[du/(vp' d\epsilon_s)]_y$	1.4 i	6.8 d	5.0-5.5 d	1.3-1.8 i	2.0-3.0 d
	linear	linear with $1/\lambda$	linear with λ/κ	linear	linear
ϵ_{sp}	1.1-1.8 i	3.5 i	2.1-3.5 i	1.4-2.2 d	indep.
	linear	nonlin.	nonlin.	linear	
s_{up}	1.8 i	indep.	1.04 d	indep.	indep.
	linear		nonlin.		
$[du/(vp' d\epsilon_s)]_p$	1.7-2.3 i	8-9 d	1.1-1.5 d	indep.	indep.
	linear	nonlin.	nonlin.		
ϵ_{sf}	1.5-1.75 d	2.4-2.9 i	2.8-3.8 i	indep.	1.1-1.2 i
	linear	nonlin.	nonlin.		linear
s_{uf}	1.8 i	indep.	1.5 i	indep.	1.2-2 d
	linear		linear		nonlin.
$q_f'/(vp')$	1.8 i	2.0 d	indep.	indep.	indep.
	linear	nonlin.			

Notes: (*) 1.1-1.4 i denotes increase in the values of $[du/(vp'd\epsilon_s)]_o$ between 1.1 to 1.4 times over the range of M between 0.77 and 1.4.

Table 5.4 Dependence of Undrained Behaviour Parameters on Cam-clay Soil Model Parameters

Parameter	λ	κ/λ	M	OCR	α'
$[3G'_o/(vp')]$	*	****	*	*	****
$[du/(vp'd\epsilon_s)]_o$	****	****	**	*	***
$[\epsilon_{sy}]$	****	****	***	****	***
$[3G_y'/(vp')]$	***	****	***	****	***
$[du/(vp'd\epsilon_s)]_y$	****	****	**	***	***
$[\epsilon_{sp}]$	***	****	**	**	***
$[s_{up}]$	*	**	***	*	*
$[du/(vp'd\epsilon_s)]_p$	****	**	***	*	*
$[\epsilon_{sf}]$	****	****	***	**	*
$[s_{uf}]$	*	***	***	***	*
$[q_f'/(vp')]$	****	*	***	*	*

Keys:

* denotes no dependence
** slight dependence (1 to 1.5 times over the range)
*** moderate dependence (1.5 to 2 times over the range)
**** strong dependence (>2 times over the range)

Table 5.5 Ranges & Form of Variations of Drained Behaviour Parameters

	M	λ	κ/λ	α'	OCR
	0.77-1.40	0.05-0.35	0.1-0.5	0.33-0.75	1.0,1.33 and 4.0
$3G_o'/(vp')$	indep.	indep.	36.4 d	2.3 i	indep.
			linear with $1/\kappa$	linear	
$K_o'/(vp')$	indep.	indep.	35.0 d	indep.	indep.
			linear with $1/\kappa$		
$[d\epsilon_v/d\epsilon_s]_o$	1.8 i	indep.	1.0-1.2 d	2.3 i	5.3 d
	linear		linear	linear	linear
ϵ_{sy}	1.3-1.7 i	3.4-3.5 i	1.8-4.7 i	1.3-2.3 d	1.8-5.0 i
	nonlin.	nonlin.	linear	linear	linear
$3G_y'/(vp')$	2.1-2.7 i	7.0 d*	1.2-1.5 i	1.1-1.2 i	2.8-4.0 d
	linear	linear with $1/\lambda$	linear with λ/κ	linear	linear
$K_y'/(vp')$	1.4-1..7 i	6.9-7.3 d	1.4-1.7 i	indep.	1.2-1.3 i
	linear	linear with $1/\lambda$	linear with λ/κ		linear
$[d\epsilon_v/d\epsilon_s]_y$	1.8 i	indep.	1.1 d	1.1-1.5 d	7.0 d
	linear		linear	linear	linear
ϵ_{sf}	1.3-3.8 d	2.6-4.0 i	1.5-1.8 d	indep.	1.0-5.8 d
	nonlin.	nonlin.	linear		nonlin.
q_f	2.6 i	indep.	indep.	indep.	4.0 d
	nonlin.				linear
$q_f'/(vp')$	1.8 i	1.7 d	indep.	indep.	indep.
	linear	nonlin.			

Note: (*) 7.0 d denotes decrease in the values of $3G_y'/(vp')$ 7.0 times over the range of λ between 0.05-0.35.

Table 5.6 Dependence of Drained Behaviour Parameters on Cam-clay Soil Model Parameters

Parameter	λ	κ/λ	M	OCR	α'
$[3G_o'/(vp')]$	*	****	*	*	****
$[K_o'/(vp')]$	*	****	*	*	*
$[d\epsilon_v/d\epsilon_s]_o$	*	**	***	****	****
$[\epsilon_{sy}]$	****	****	**	***	***
$[3G_y'/(vp')]$	****	**	****	****	**
$[K_y'/(vp')]$	****	***	***	**	*
$[d\epsilon_v/d\epsilon_s]_y$	*	**	***	****	**
$[\epsilon_{sf}]$	****	***	****	****	*
$[q_f']$	*	*	****	****	*
$[q_f'/(vp')]$	***	*	***	*	*

Keys:

* denotes no dependence
** slight dependence (1 to 1.5 times over the range)
*** moderate dependence (1.5 to 2 times over the range)
**** strong dependence (>2 times over the range)

Table 6.1 Programme of Numerical Study of Hydraulic Fracturing

Rate of pressure increase (kPa/min)	Group A (Plane strain)			Group B (Axisym)		
	σ_c' (kPa)			σ_c' (kPa)		
	200	400	200	200	200	400
	Case			Case		
1000	A1	A8	A14	B1	B8	-
100	A2	A9	A15	B2	-	-
50	A3	A10	A16	B3	B9	B12
10	A4	A11	A17	B4	-	-
1	A5	A12	A18	B5	-	-
0.1	A6	A13	A19	B6	B10	-
0.01	A7	-	-	B7	B11	-
ϕ_b (mm)	6	6	16	6	16	6

Group C (Plane strain)				Group D (Plane strain)		
Case	OCR	σ_c'(kPa)	ϕ_b (mm)	Case	OCR	σ_c'(kPa)
C1	2	118.9	6	D1	2	183
C2	4	70.7		D2	6	79
C3	8	42		D3	8	65
C4	12	31		D4	12	45
C5	12	31	16			
				ϕ_b = 6 mm		
Rate of pressure increase = 1000 kPa						

Notes: ϕ_b : Diameter of bore or cavity
σ_c' : Effective confining pressure = (σ_c - u_o)
u_o : Steady state pore pressure which is taken as zero in the analyses

Table 6.2 Summary of Numerical Prediction - Group A (Plane Strain Condition)

Case	ϕ_b (mm)	σ_c' (kPa)	OCR	Rate of pressure increase (kPa/min)	U_F (kPa)	U_F/σ_c'
A1	6	200	1	1000	340	1.7
A2				100	336	1.68
A3				50	330	1.65
A4				10	300	1.5
A5				1	235	1.18
A6				0.1	205	1.03
A7				0.01	200	1.0
A8	6	400	1	1000	580	1.45
A9				100	560	1.40
A10				50	530	1.33
A11				10	460	1.15
A12				1	410	1.03
A13				0.1	400	1.0
A14	16	200	1	1000	310	1.55
A15				100	295	1.48
A16				50	290	1.45
A17				10	255	1.28
A18				1	210	1.05
A19				0.1	200	1.0

Table 6.3 Summary of Numerical Prediction - Group B (Axisymmetric Condition)

Group	Case	ϕ_b (mm)	σ_c' (kPa)	OCR	Rate of pressure increase (kPa/min)	U_F (kPa)	U_F/σ_c'
B	B1	6	200	1	1000	295	1.48
	B2				100	295	1.48
	B3				50	290	1.45
	B4				10	275	1.38
	B5				1	240	1.2
	B6				0.1	210	1.05
	B7				0.01	200	1.00
	B8	16	200	1	1000	300	1.5
	B9				50	300	1.5
	B10				0.1	205	1.02
	B11				0.01	205	1.02
	B12	6	400	1	50	550	1.37

Table 6.4 Summary of Numerical Prediction - Group C (Plane Strain Condition)

Group	Case	ϕ_b (mm)	σ_c' (kPa)	OCR	Rate of pressure increase (kPa/min)	U_F (kPa)	U_F/σ_c'
C	C1	6	118.9	2	1000	270	2.27
	C2	6	70.7	4		168	2.38
	C3	6	42	8		100	2.38
	C4	6	31	12		74	2.39
	C5	16	31	12		72	2.32

Table 6.5 Summary of Numerical Prediction - Group D (Plane Strain Condition)

Group	Case	ϕ_b (mm)	σ_c' (kPa)	OCR	Rate of pressure increase (kPa/min)	U_F (kPa)	U_F/σ_c'
D	D1	6	183	2	1000	340	1.86
	D2		79	6		194	2.46
	D3		65	8		160	2.46
	D4		45	12		108	2.40

Table 7.1 Programme of Parametric Study of Plate Loading Tests on Cam-Clay

Series	λ	κ/λ	κ	Γ	Remarks
1	0.05	0.100 0.500	0.0050 0.0250	1.7105	M=0.77, 0.98, 1.20, 1.40 α'=0.75, 0.33 OCR=1,4, 40 d_w=0.5m, 2.0m
2	0.15	0.100 0.233 0.367 0.500	0.0150 0.0349 0.0550 0.0750	2.6315	
3	0.25	0.100 0.500	0.0250 0.1250	3.5525	
4	0.35	0.100 0.500	0.0350 0.1750	4.4735	

Notes:

1. κ, λ, Γ, M and α' are the critical state soil model parameters.
2. OCR denotes the overconsolidation ratio.
3. d_w denotes the depth of ground water table.

Table 7.2 Ranges of Variations of Undrained Behaviour Parameters Characterising Plate Loading Tests (Normally Consolidated Materials)

	λ	κ/λ	M	α'	d_w(m)
	0.05-0.35	0.1-0.5	0.77-1.4	0.33-0.75	0.5, 2.0
$E_i/(\gamma B)$	2.4-6.7 d[(1)]	3.7-8.5 d	1-1.7 i	1.4-4 i	2-3.2 i
$100\delta_f/B$	1.8-3.7 i	5-12.7 i	1-2 i	1.2-4.2 d	1.2-1.5 i for κ/λ=0.1
					1-1.1 d for κ/λ=0.5
$q_f/(\gamma B)$	1-1.3 d	1.1-1.4 i	1.7-1.9 i	1-1.2 i	2.4-3.2 i

Notes: (1) 2.4-6.7 d denotes decrease in the value of $E_i/(\gamma B)$ between 2.4 to 6.7 times over the range of λ between 0.05 and 0.35.

Table 7.3 Ranges of Variations of Undrained Behaviour Parameters Characterising Plate Loading Tests (Overconsolidated Materials)

	λ	κ/λ	M	OCR	α'
	0.05-0.35	0.1-0.5	0.77-1.4	4 & 40	0.33-0.75
$E_i/(\gamma B)$	2.3-4.1 d[1]	4.5-6.7 d	1.0	1-1.2 i or d	2.1-2.3 i
$100\delta_y/B$	2-4.4 i	(OCR=4) 2.2-3.7 i (OCR=40) 1-1.4 d	1.1-2.3 i	2.7-24 i	1.2-2.9 d
$q_y/(\gamma B)$	1-1.7 d	1.4-8.2 d	1.2-2.4 i	2.8-21.5 i	1-1.6 i or d
$100\delta_f/B$	2.2-3.1 i	1.3-3.2 i	1.6-1.8 i	4-47.5 i	1-2.6 d
$q_f/(\gamma B)$	1.1-1.7 d	1.5-4.9 d	1.6-1.8 i	2.2-9.5 i	1-1.6 i

Notes: (1) 2.3-4.1 d denotes decrease in the value of $E_i/(\gamma B)$ between 2.3 to 4.1 times over the range of λ between 0.05 and 0.35.

Table 7.4 Dependence of the Undrained Behaviour Parameters Characterising Plate Loading Tests on the Fundamental Soil Model Parameters (Normally Consolidated Materials)

	λ	κ/λ	M	α'	d_w (m)
	0.05-0.35	0.1-0.5	0.77-1.4	0.33-0.75	0.5 & 2.0
$E_i/(\gamma B)$	****	****	**	****	****
$100\delta_f/B$	****	****	**	****	**
$q_f/(\gamma B)$	**	**	***	**	****

Keys:

* denotes no dependence
** slight dependence (1 to 1.5 times over the range)
*** moderate dependence (1.5 to 2 times over the range)
**** strong dependence (>2 times over the range)

Table 7.5 Dependence of the Undrained Behaviour Parameters Characterising a Plate Test on the Fundamental Soil Model Parameters (Overconsolidated Materials)

	λ	κ/λ	M	OCR	α'
	0.05-0.35	0.1-0.5	0.77-1.4	4 & 40	0.33-0.75
$E_i/(\gamma B)$	****	****	*	**	****
$100\delta_y/B$	****	(OCR=4) ****	***	****	****
		(OCR=40) **			
$q_y/(\gamma B)$	**	****	***	****	**
$100\delta_f/B$	****	****	***	****	***
$q_f/(\gamma B)$	**	****	***	****	**

Keys:

* denotes no dependence
** slight dependence (1 to 1.5 times over the range)
*** moderate dependence (1.5 to 2 times over the range)
**** strong dependence (>2 times over the range)

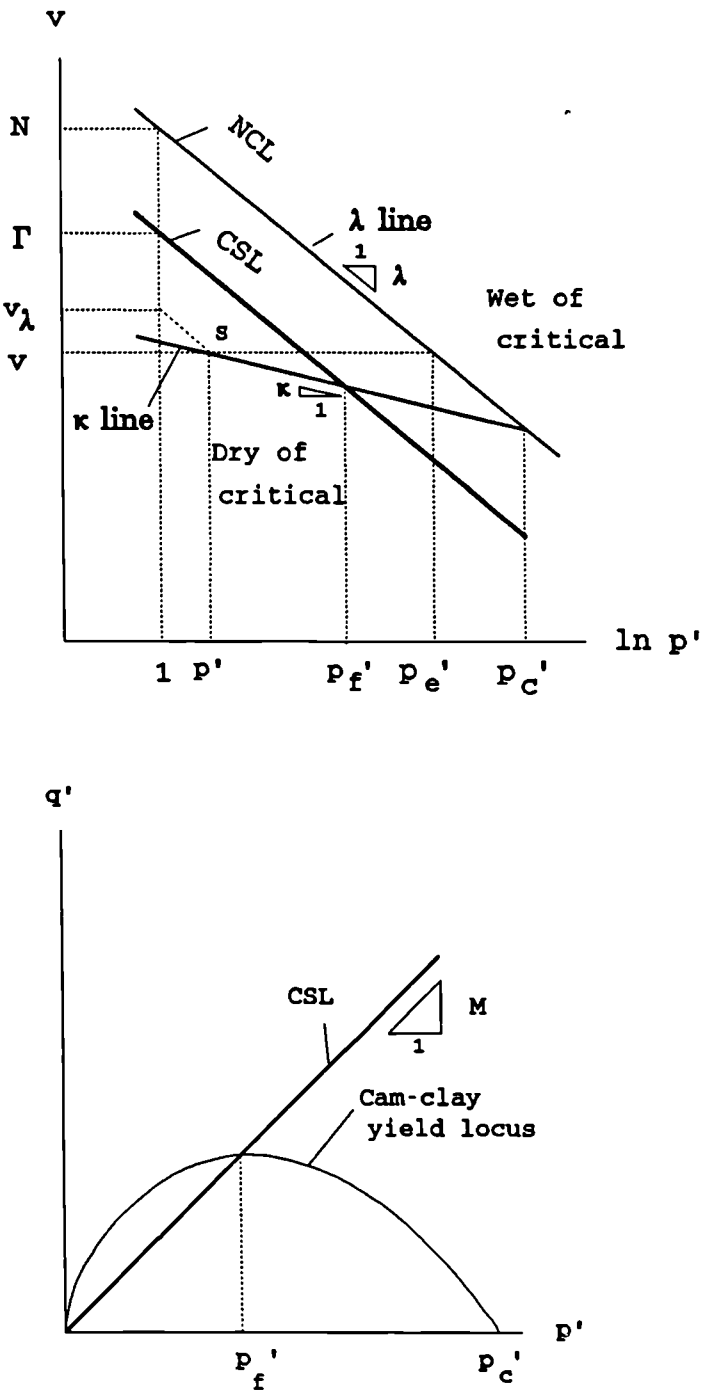

Figure 2.1 Diagram defining the critical state soil parameters used in the Cam-clay model

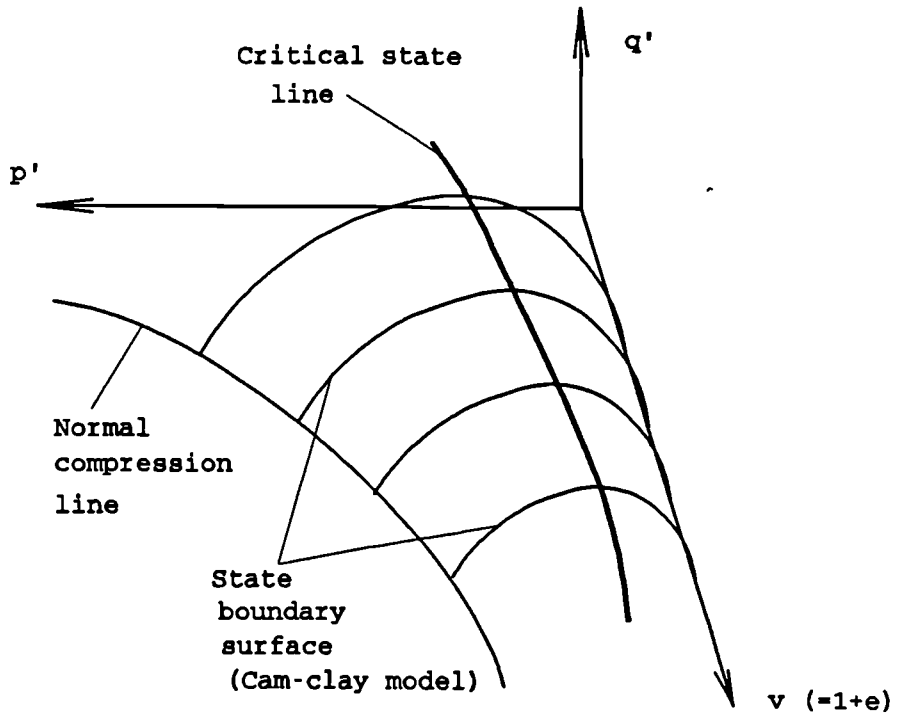

Figure 2.2 State boundary surface

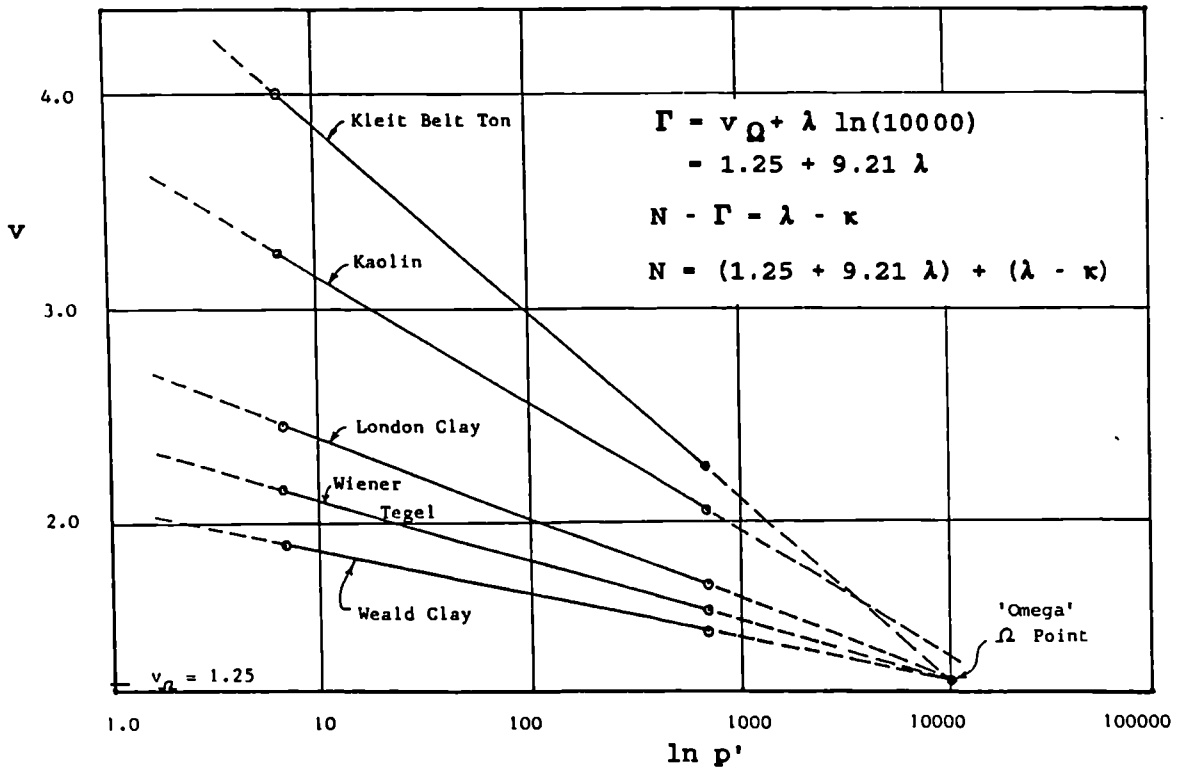

Figure 2.3 Family of experimental critical state lines (after Schofield and Wroth, 1968)

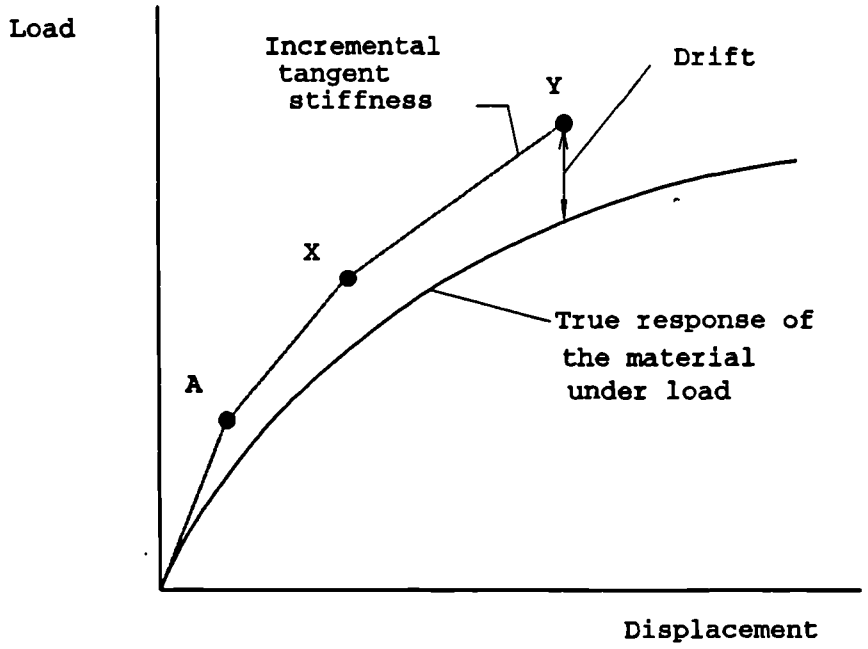

Figure 2.4 Tangent stiffness incremental solution scheme

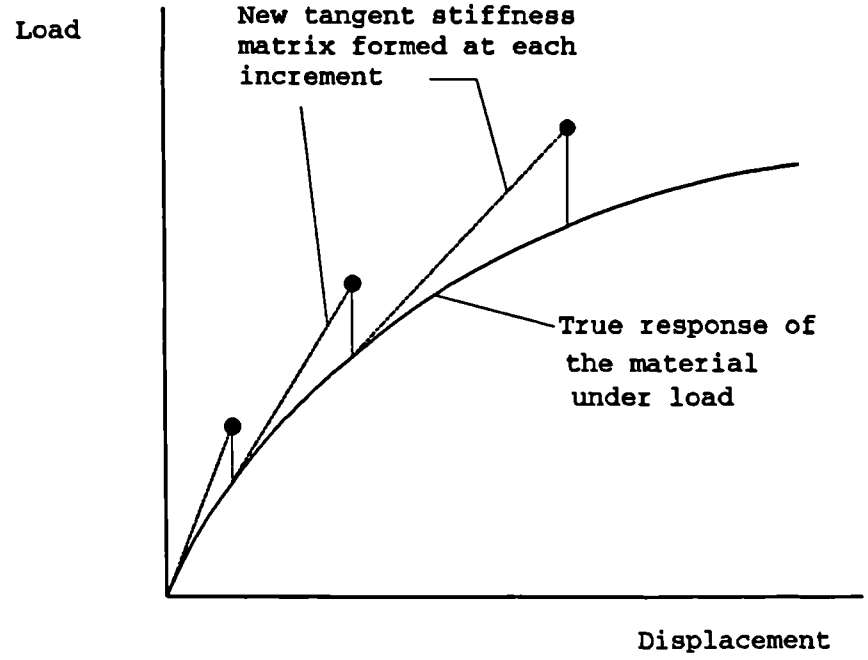

Figure 2.5 Newton-Raphson method

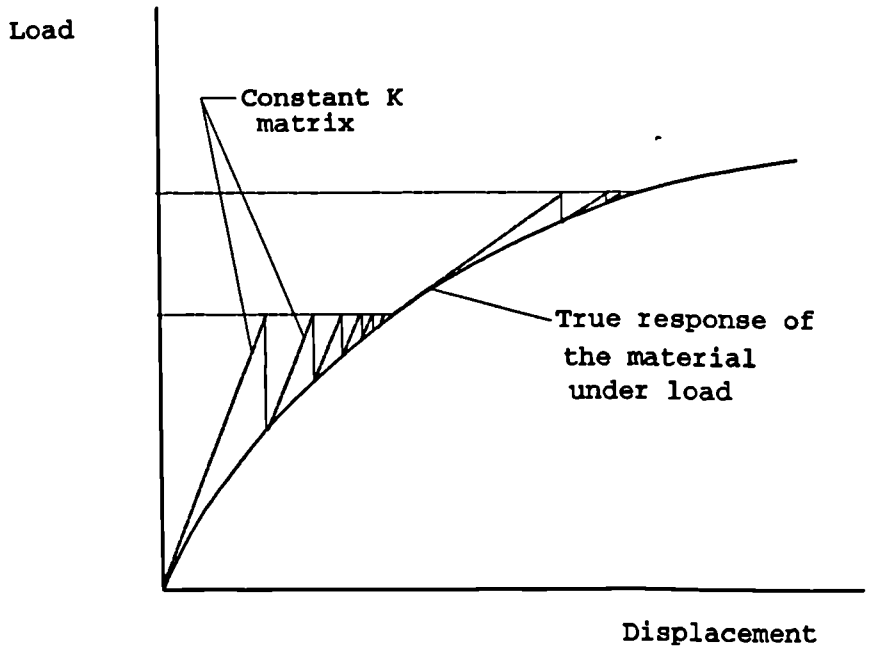

Figure 2.6 Modified Newton-Raphson method

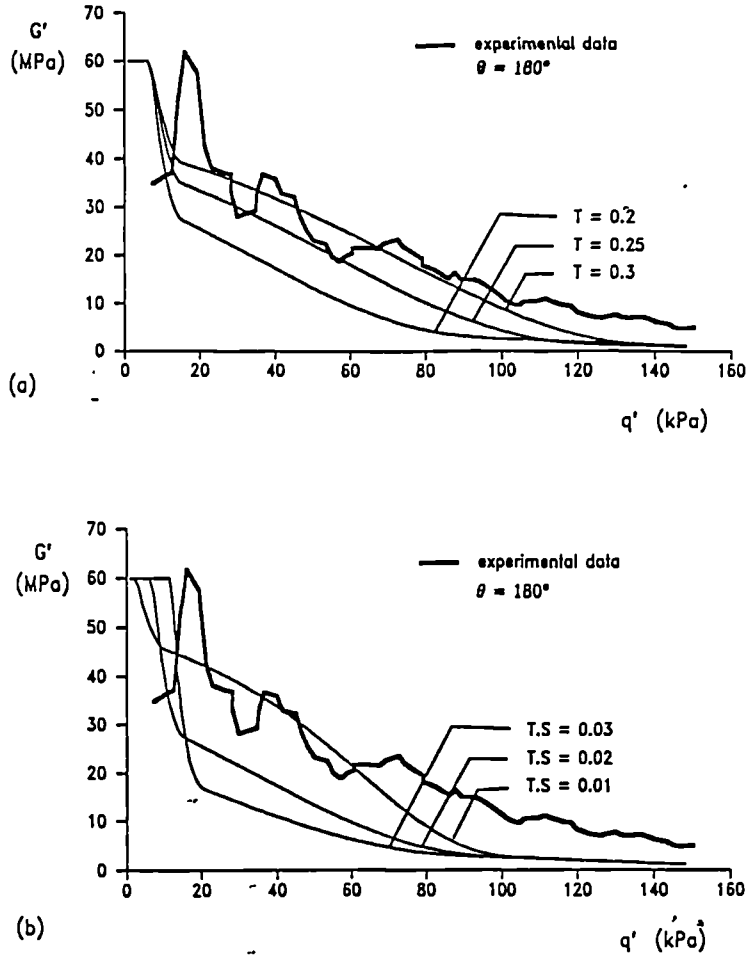

Figure 3.1 Model predictions for constant p' compression following a stress path reversal. The sets of data illustrate the effect of (a) T and (b) T.S (after Stallebrass, 1990)

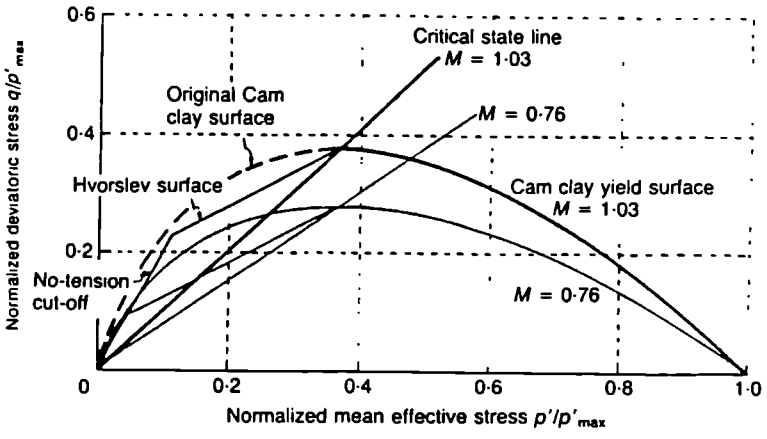

Figure 3.2 Cam-clay yield surface, Hvorslev surface and no-tension cut-off in normalised q':p' space (after Powrie and Li, 1991a)

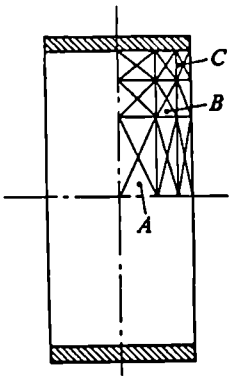

Modified Cam-clay parameters of Weald clay

λ	0.088
κ	0.031
Γ	2.0575
M	0.882
ϕ'	22.6°
G'	3000 kPa
k	1.27×10^{-12} m/s

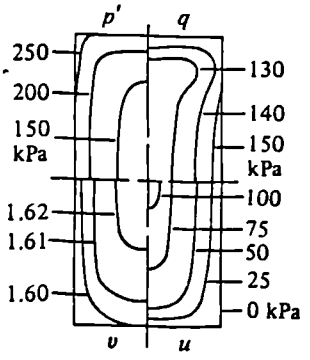

(a) (b)

Figure 3.3(a) Finite element mesh for analysis of triaxial sample (after Carter, 1982)
(b) Computed contours of stress and specific volume at axial strain e_a=0.05 during drained compression with axial strain rate 8.33×10^{-6}/s; drainage from all boundaries (after Carter, 1982)

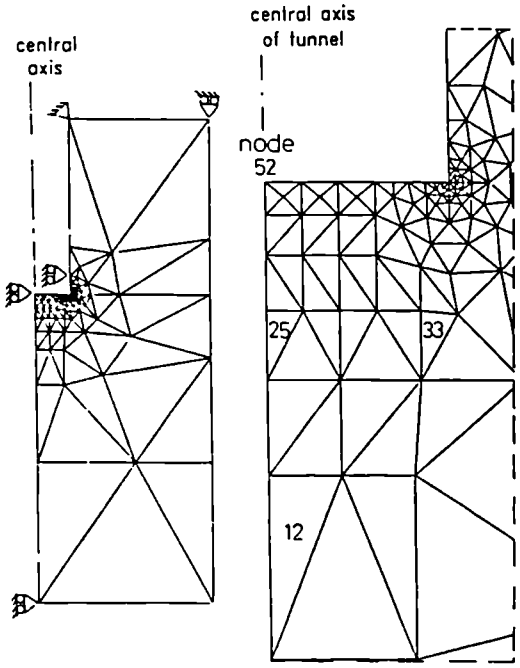

Modified Cam-clay parameters of Speswhite kaolin

M = 0.8
λ = 0.1
κ = 0.05
Γ = 3.1
ν' = 0.3
$k_v = 0.45 \times 10^{-6}$ mm/s
$k_h = 1.33 \times 10^{-6}$ mm/s

Figure 3.4 Finite element mesh for analysis of time dependent movements associated with tunnelling (after De Moor and Taylor, 1991)

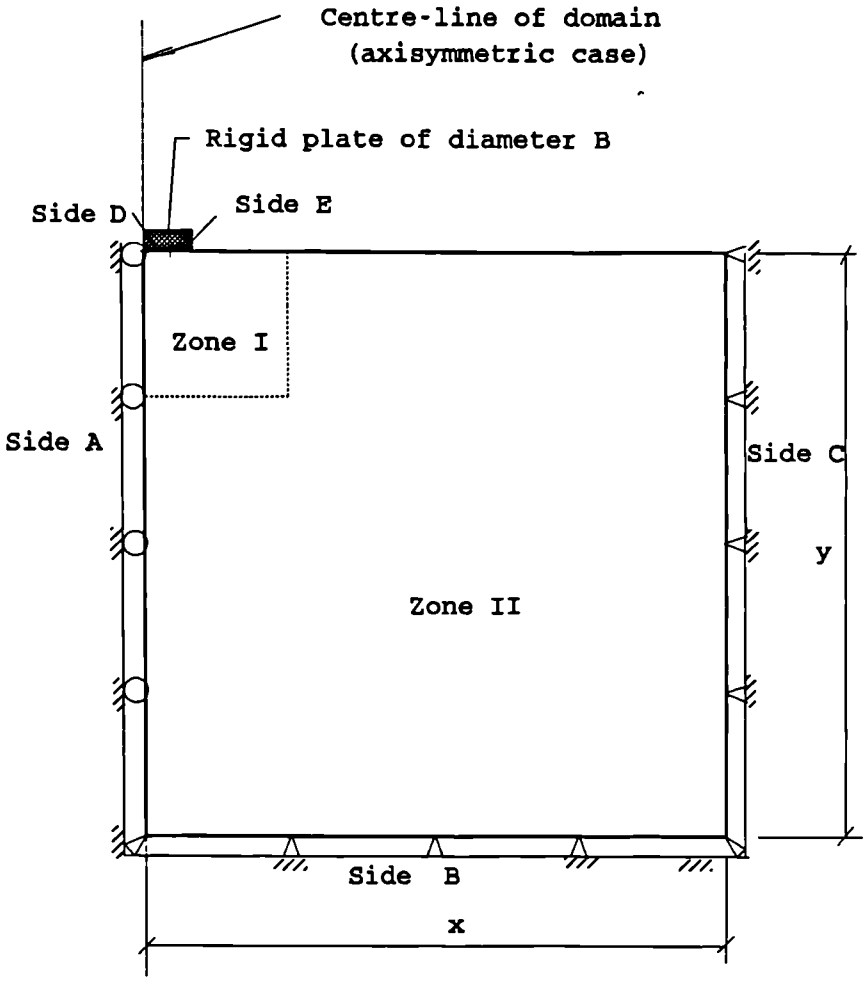

Figure 3.5 Mesh boundary conditions for plate loading analysis (after Woods and Contreras, 1987)

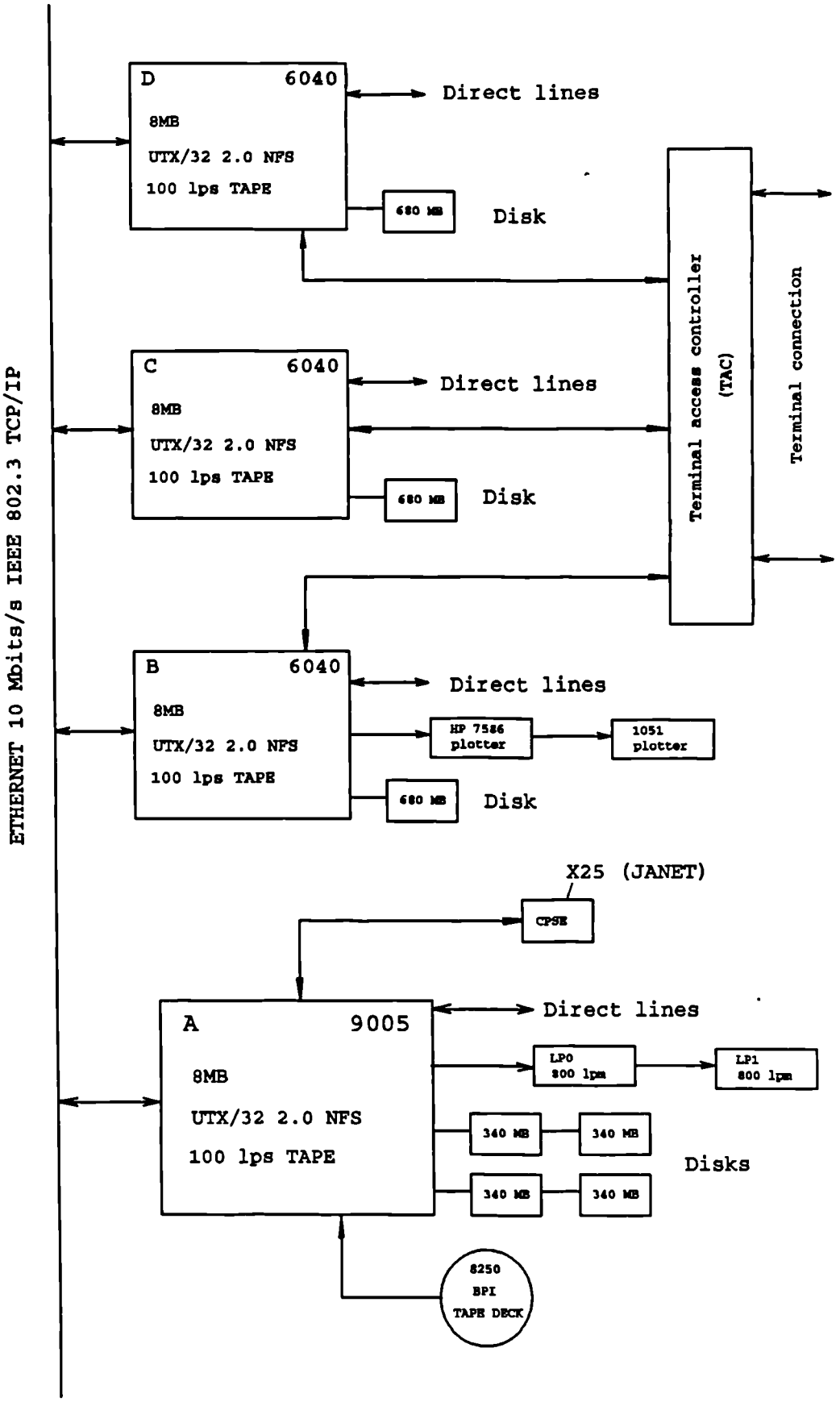

Figure 4.1 Configuration of the Gould mini-computers

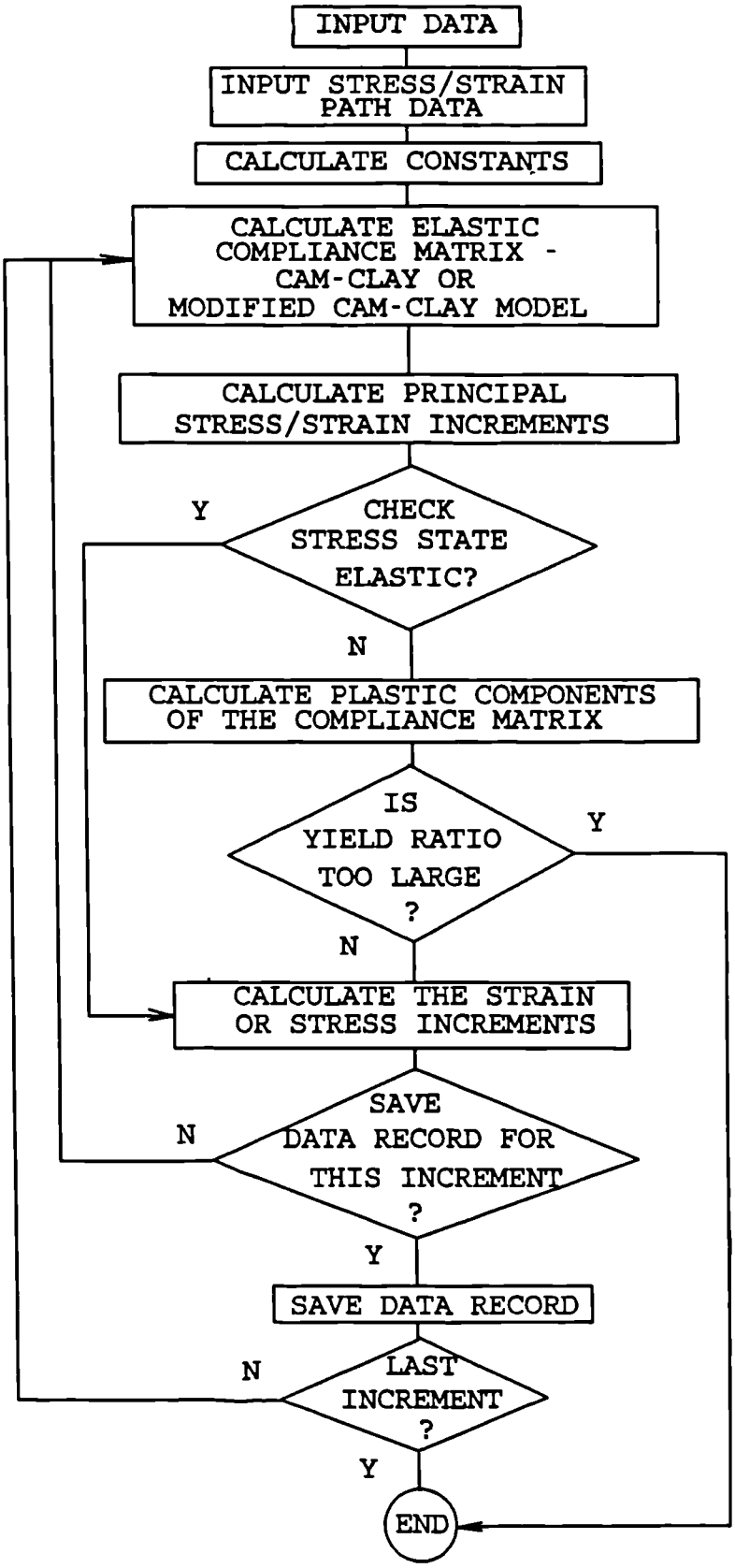

Figure 4.2 Flow diagram of computer program CASIS

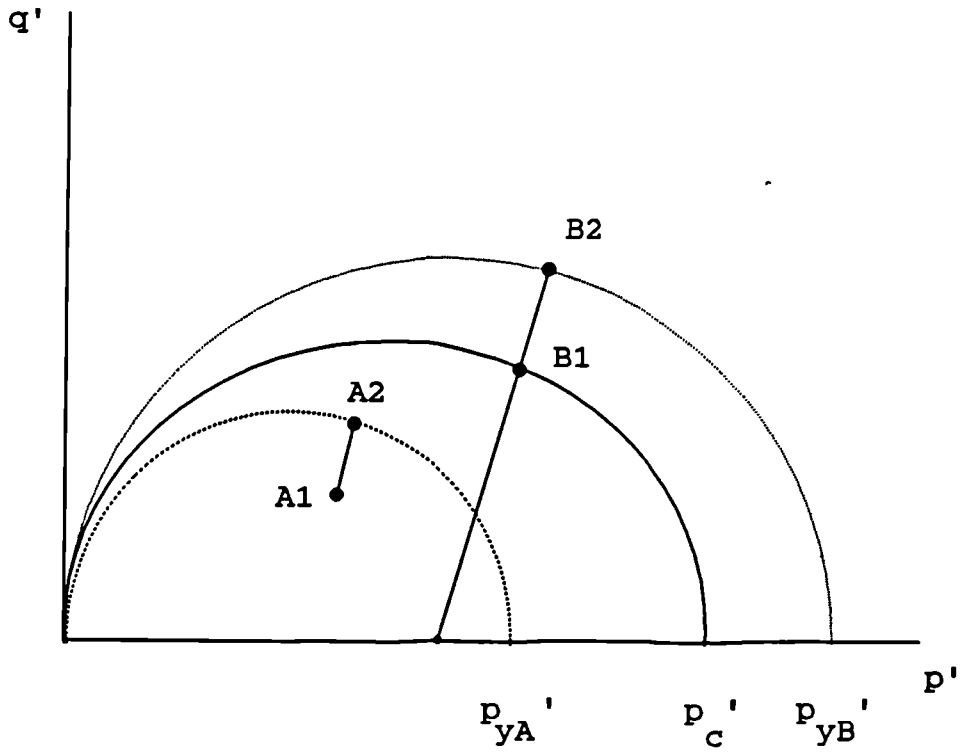

Figure 4.3 Growth of yield locus

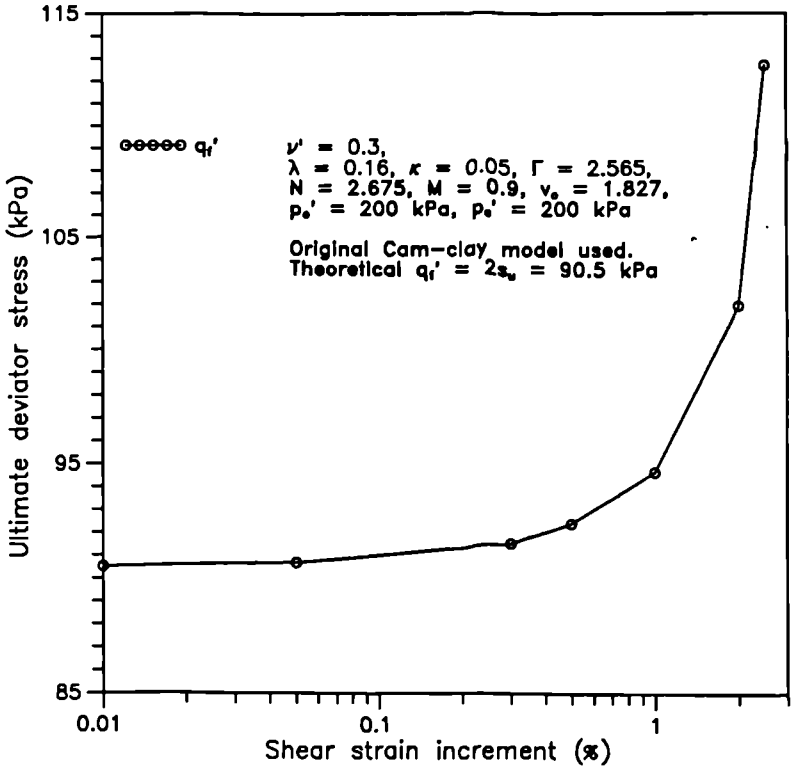

Figure 4.4(a) Calculated ultimate deviator stress by CASIS with different increment sizes of shear strain in undrained triaxial compression analyses

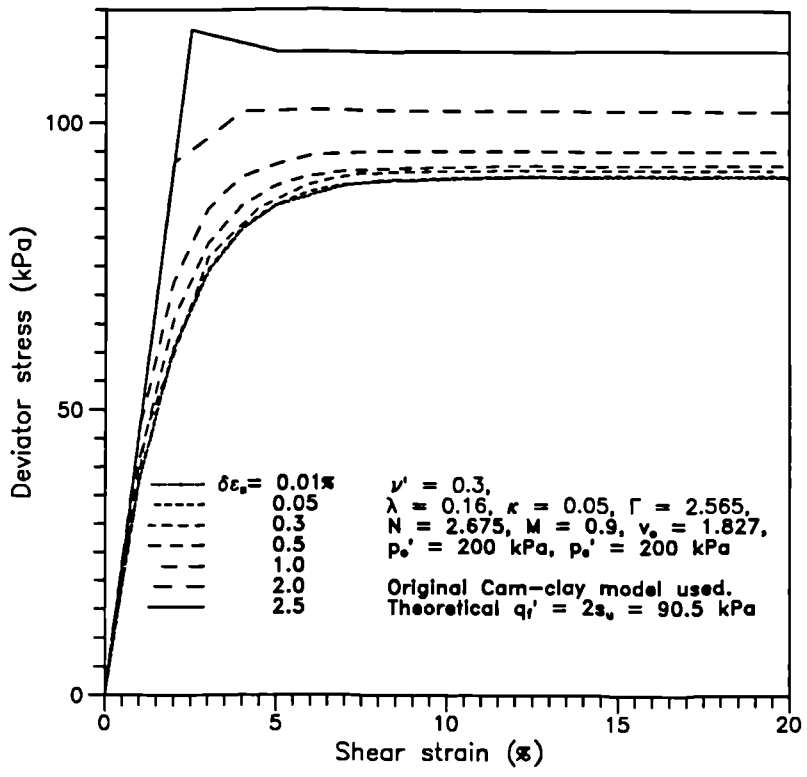

Figure 4.4(b) Stress-strain curves for different increment sizes of shear strain in undrained triaxial compression analyses

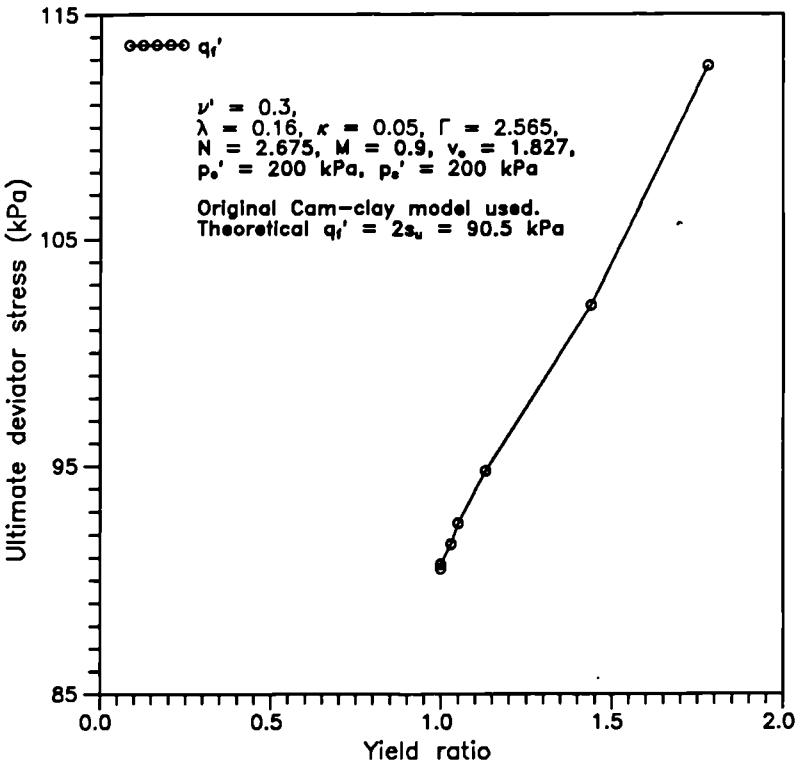

Figure 4.5(a) Calculated ultimate deviator stress versus yield ratio for different increment sizes of shear strain in undrained triaxial compression analyses

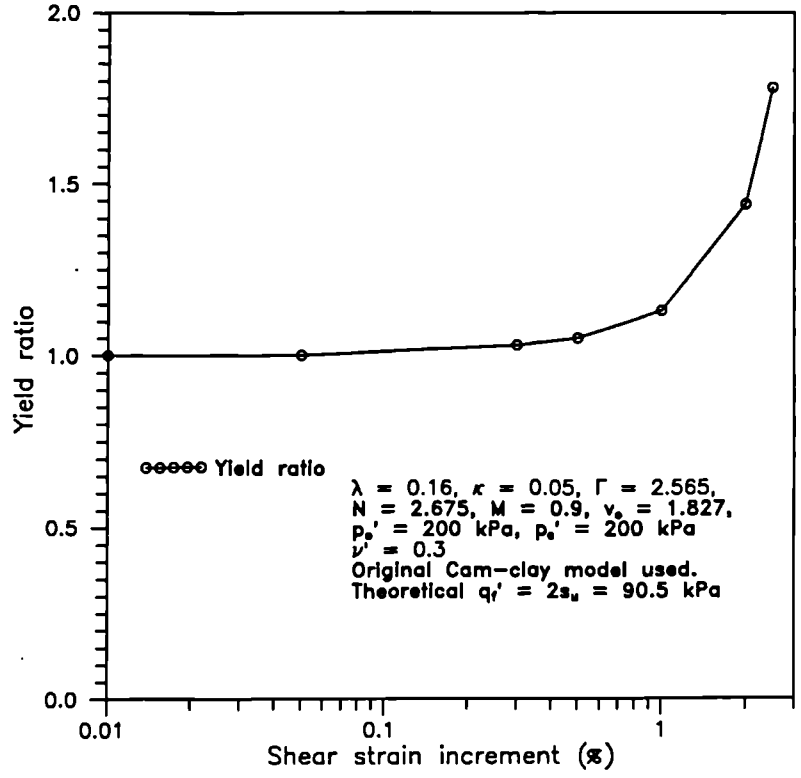

Figure 4.5(b) Variations of calculated yield ratio with different increment sizes of shear strain in undrained triaxial compression analyses

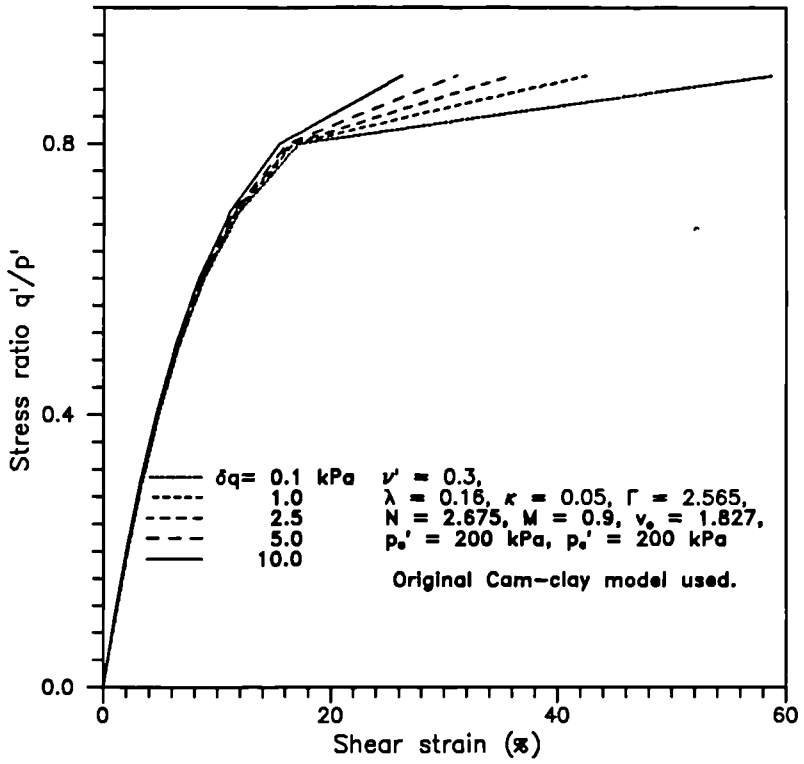

Figure 4.6 Stress ratio–shear strain curves for different increment sizes of deviator stress in constant p' analyses

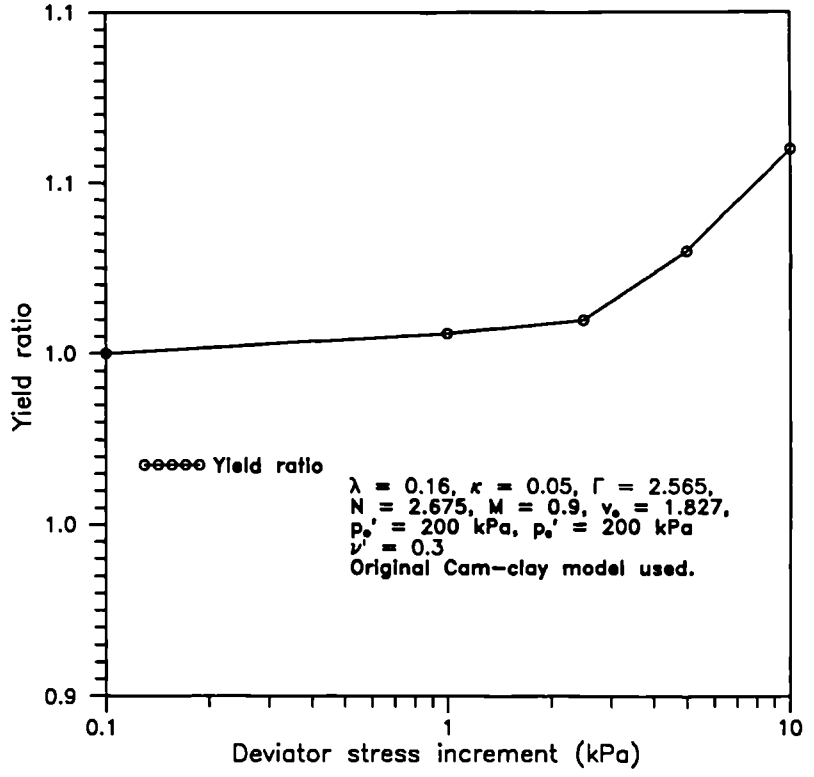

Figure 4.7 Variations of yield ratio with different increment sizes of deviator stress in constant p' analyses

○ u, v - displacements unknown

▲ p - pore-pressures unknown

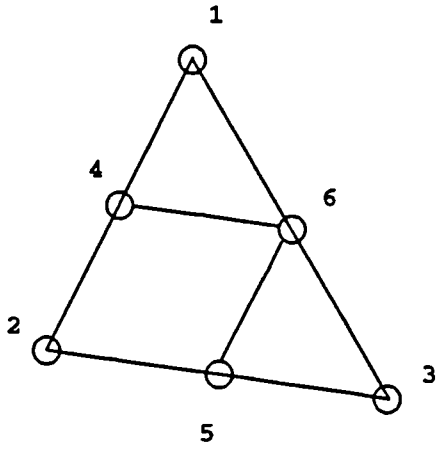

(a) LST (element type 2)
6 nodes, 12 d.o.f.

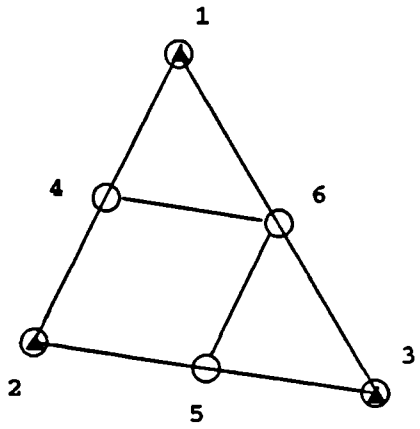

(b) LST/U (consolidation)
(element type 3)
6 nodes, 15 d.o.f.

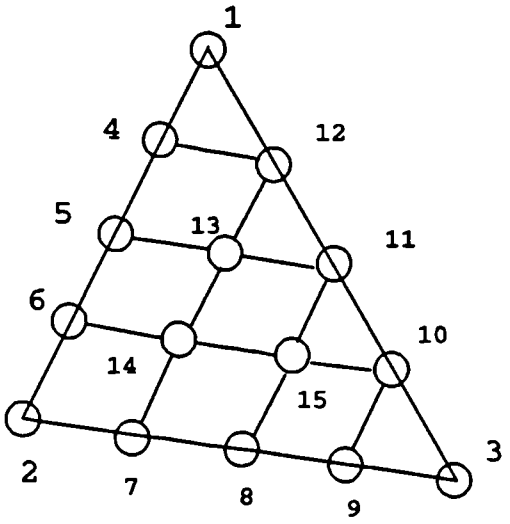

(c) CuST (element type 6)
15 nodes, 30 d.o.f.

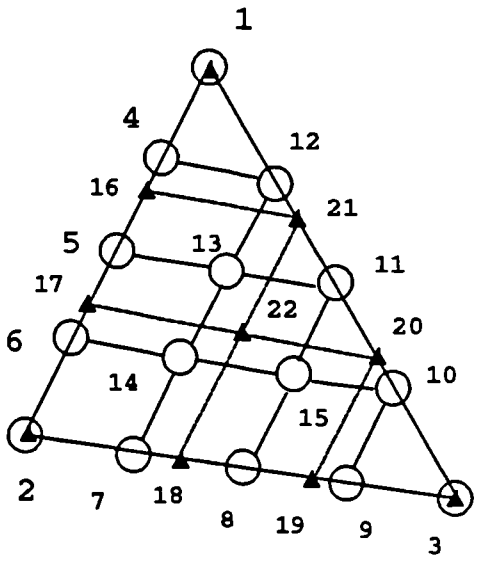

(d) CuST/U (consolidation)
(element type 7)
22 nodes, 40 d.o.f.

Figure 4.8 Different types of elements

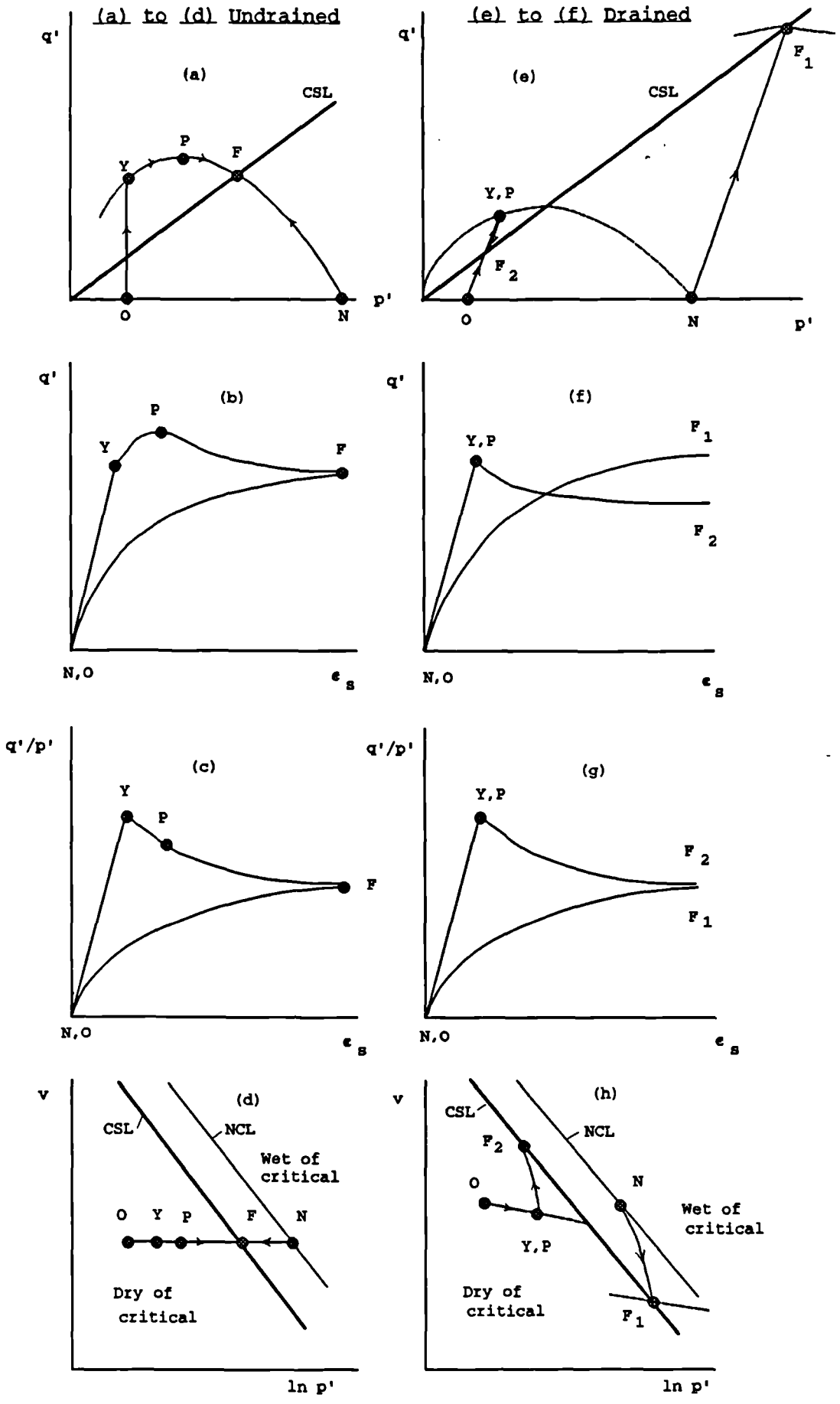

Figure 5.1 Idealised soil behaviour

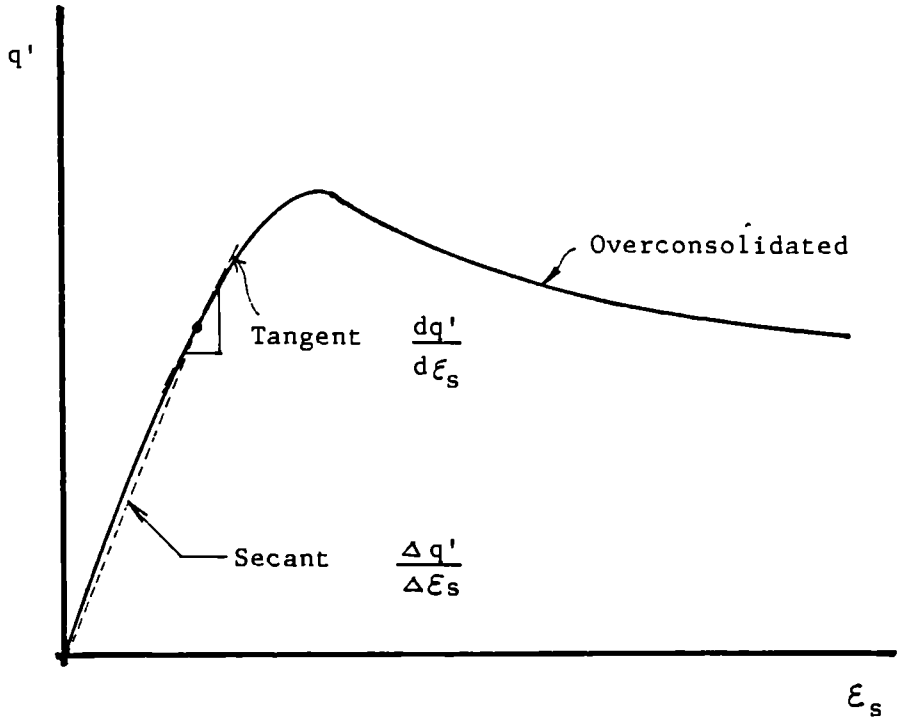

Figure 5.2(a) Stress strain response of an overconsolidated sample

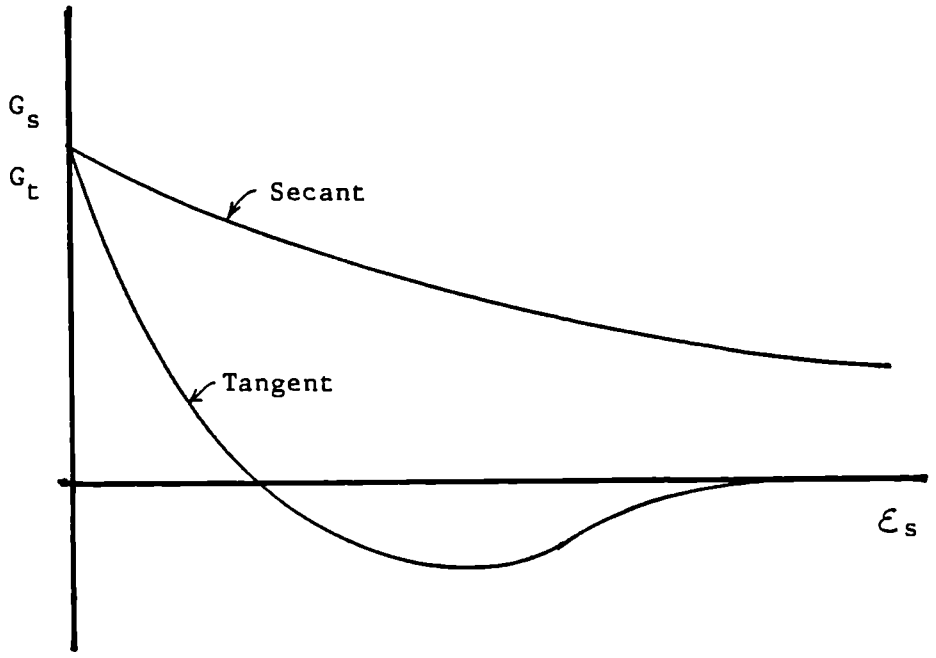

Figure 5.2(b) Variations of tangent and secant shear modulus with shear strain

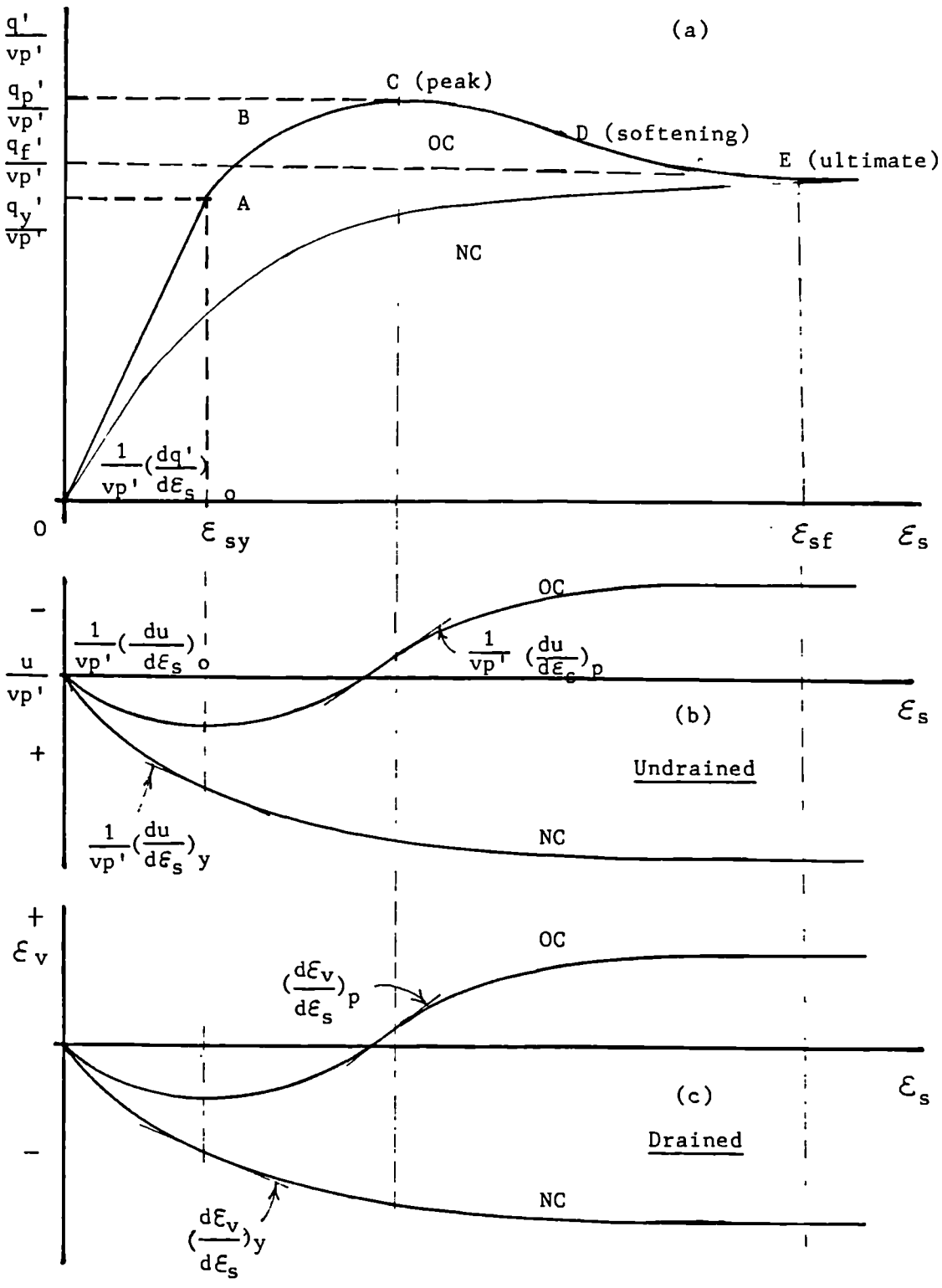

Figure 5.3 Behaviour parameters to characterise undrained and drained behaviour

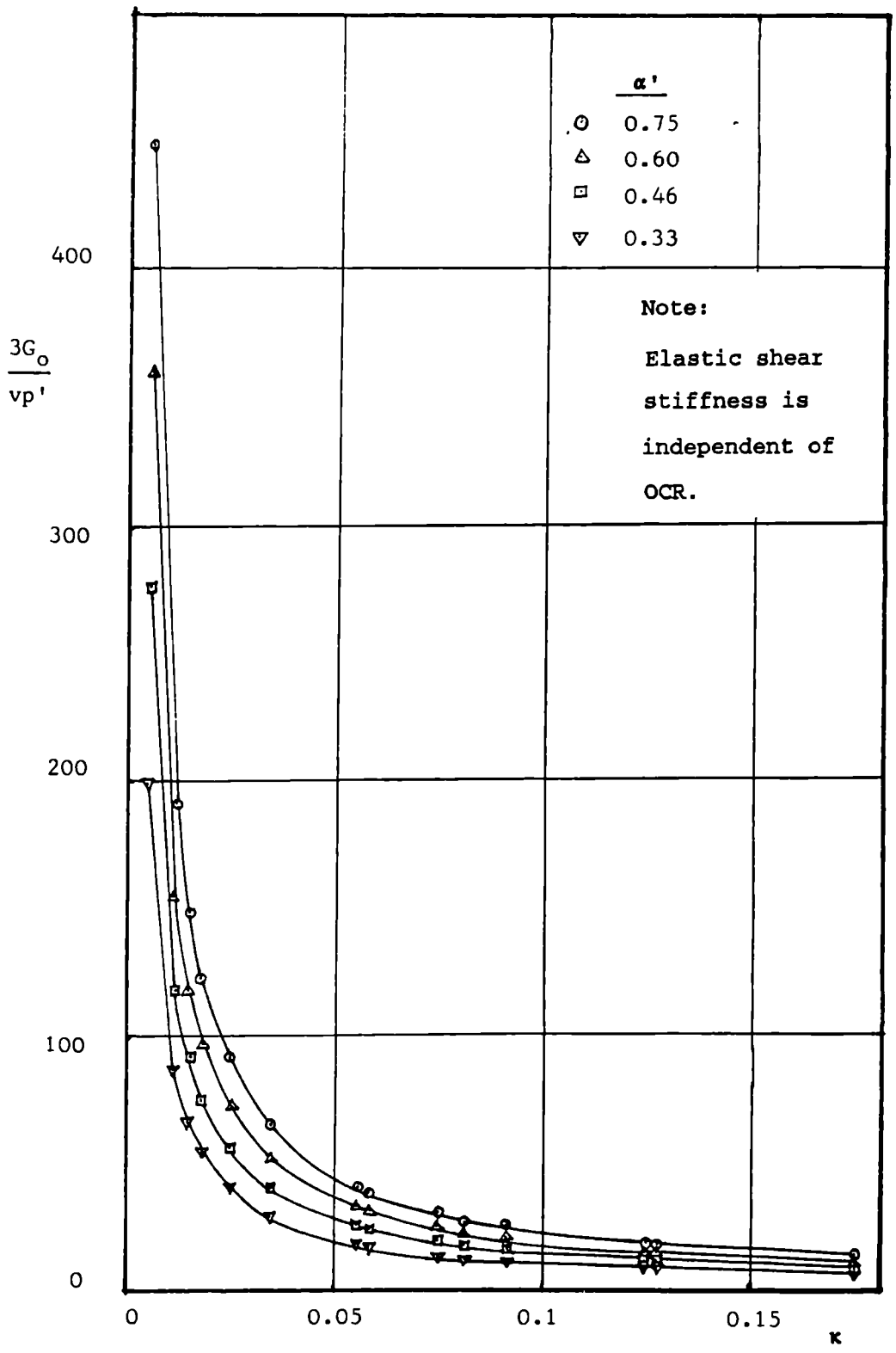

Figure 5.4 Variations of initial normalised tangent modulus $3G_o/(vp')$ with κ for fixed values of α'

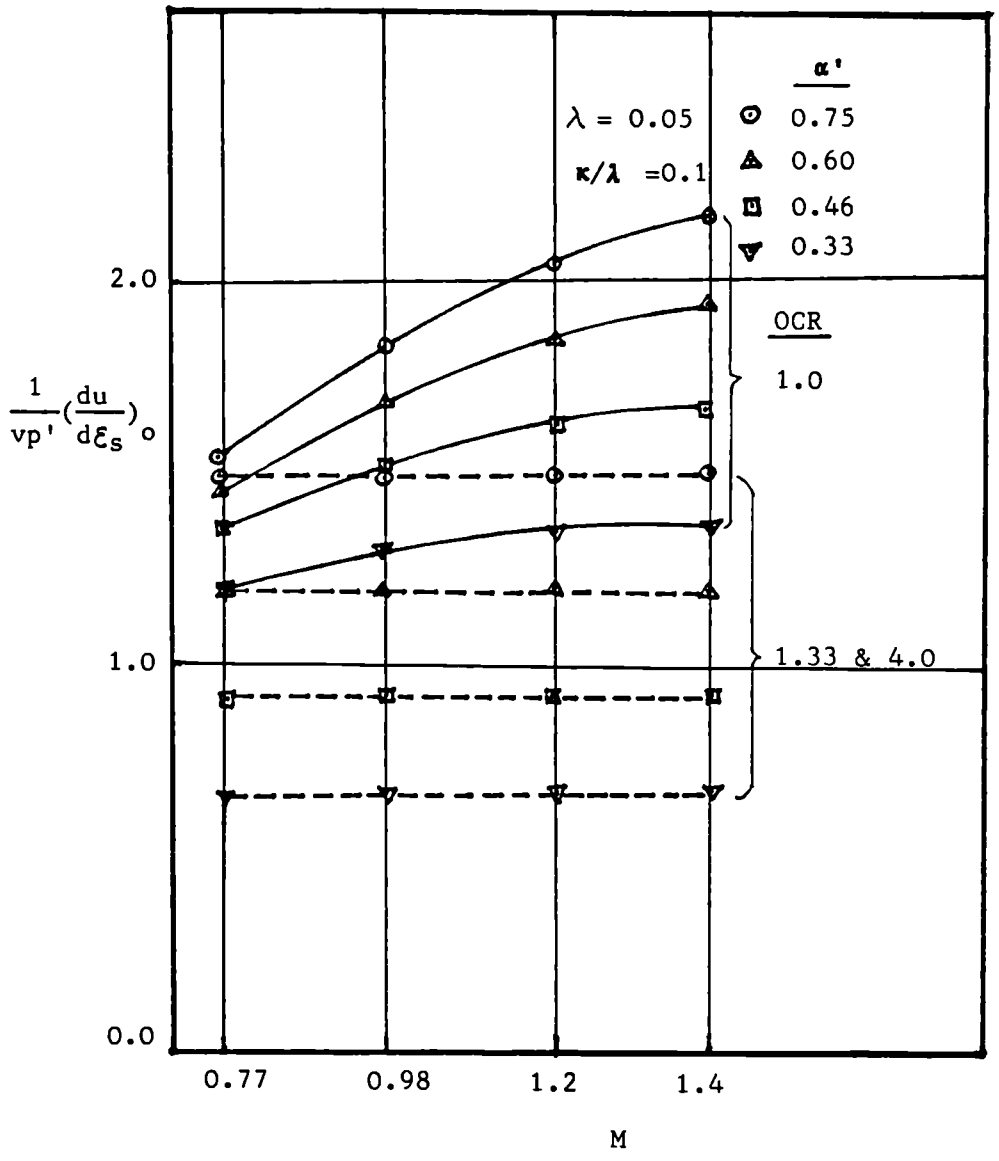

Figure 5.5 Variations of initial rate of pore pressure change $[du/(vp'd\varepsilon_s)]_o$ with M for fixed values of OCR and α'

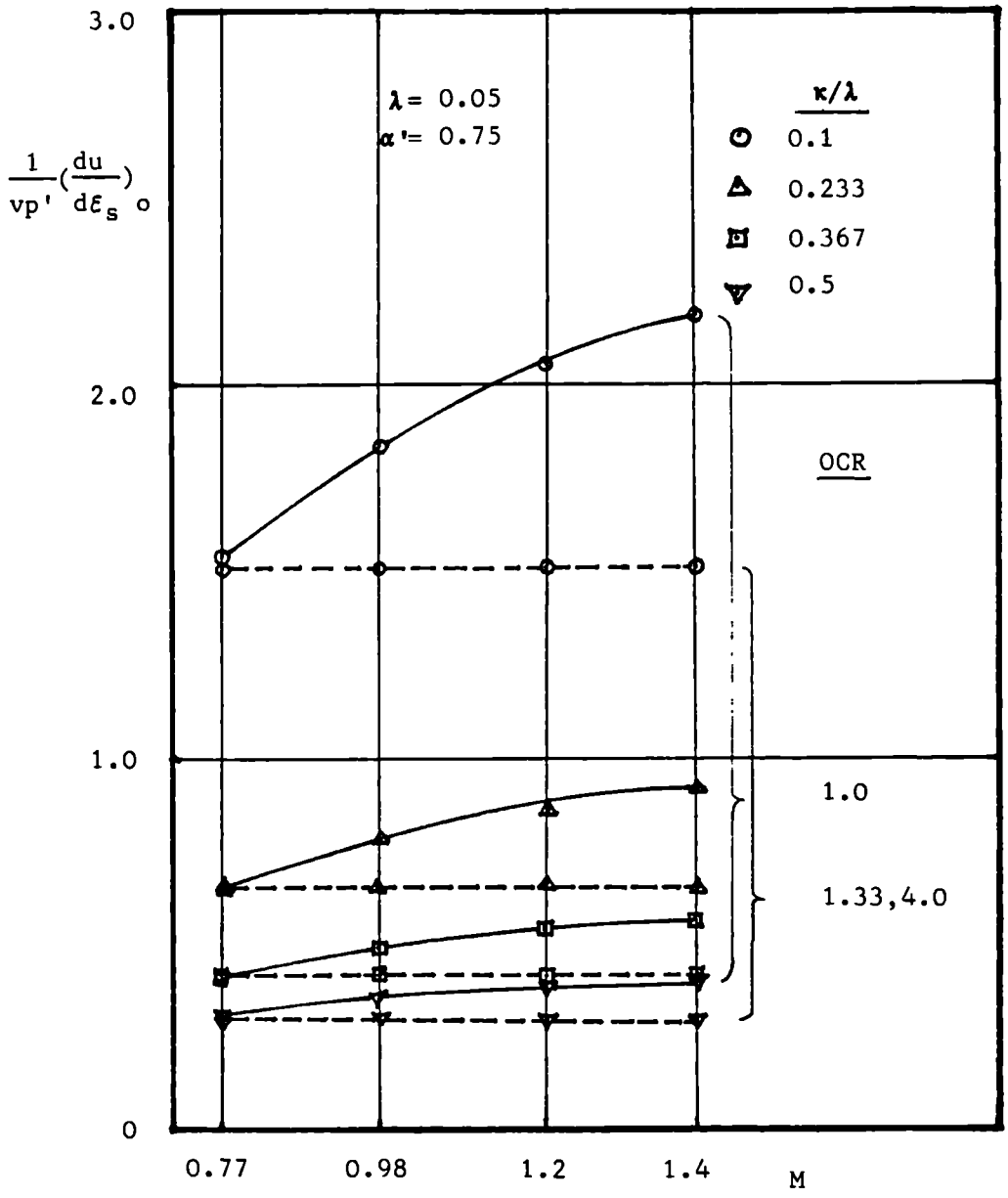

Figure 5.6 Variations of initial rate of pore pressure change $[du/(vp'd\varepsilon_s)]_o$ with M for fixed values of OCR and κ/λ

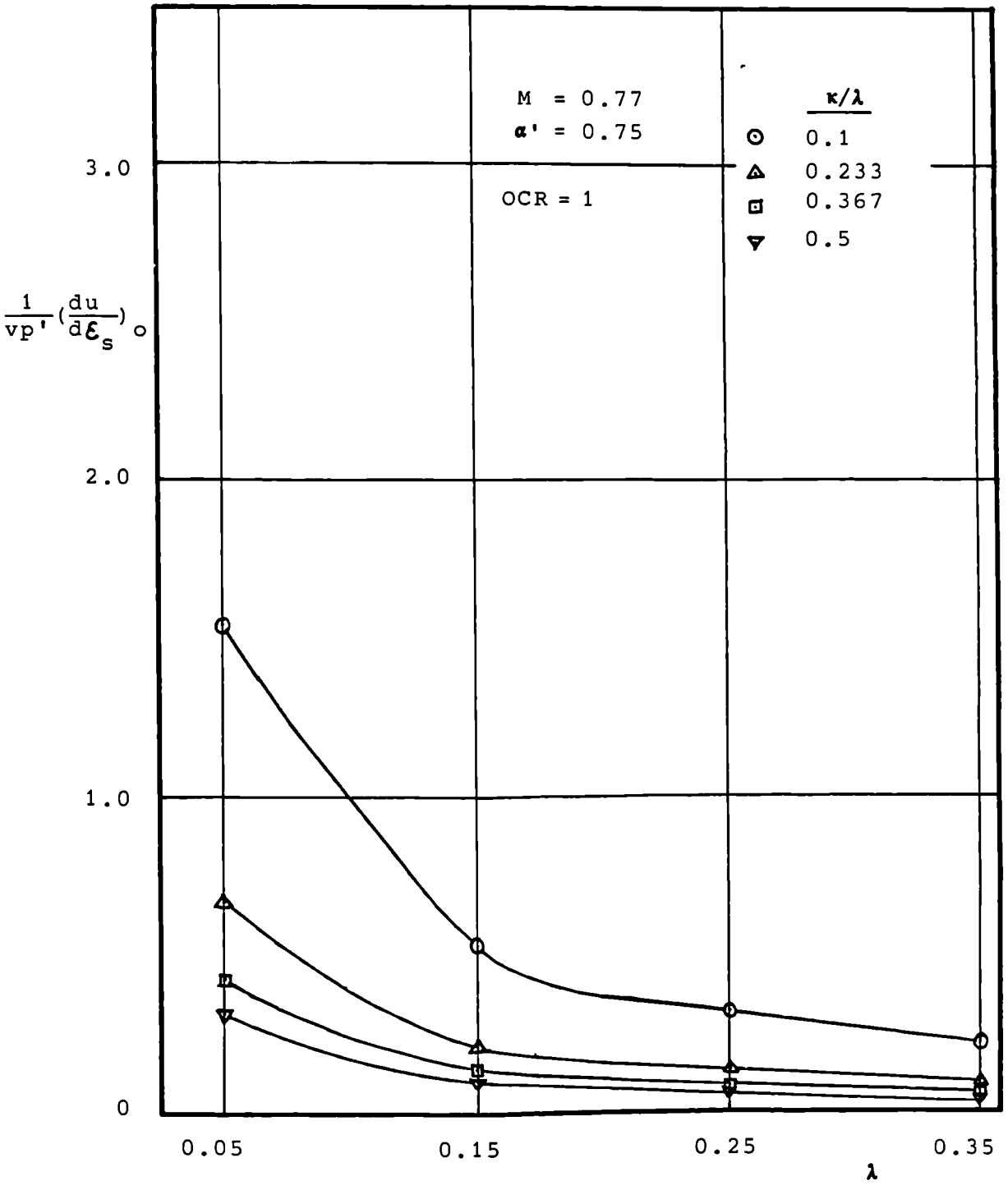

Figure 5.7 Variations of initial rate of pore pressure change $[du/(vp'd\varepsilon_s)]_o$ with λ and κ/λ

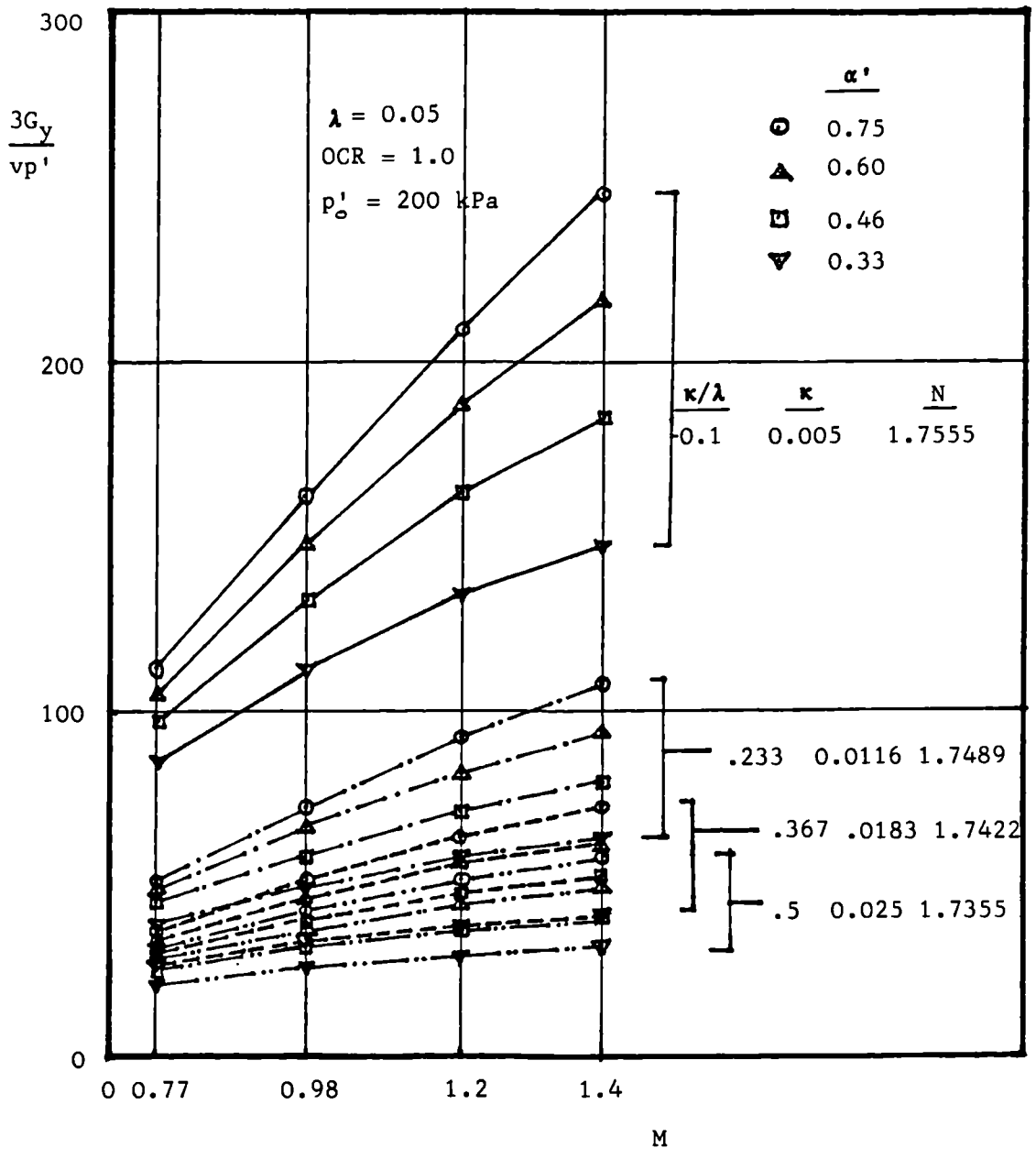

Figure 5.8 Variations of normalised tangent modulus $3G_y/(vp')$ immediately after yield with M for fixed values of κ/λ and α'

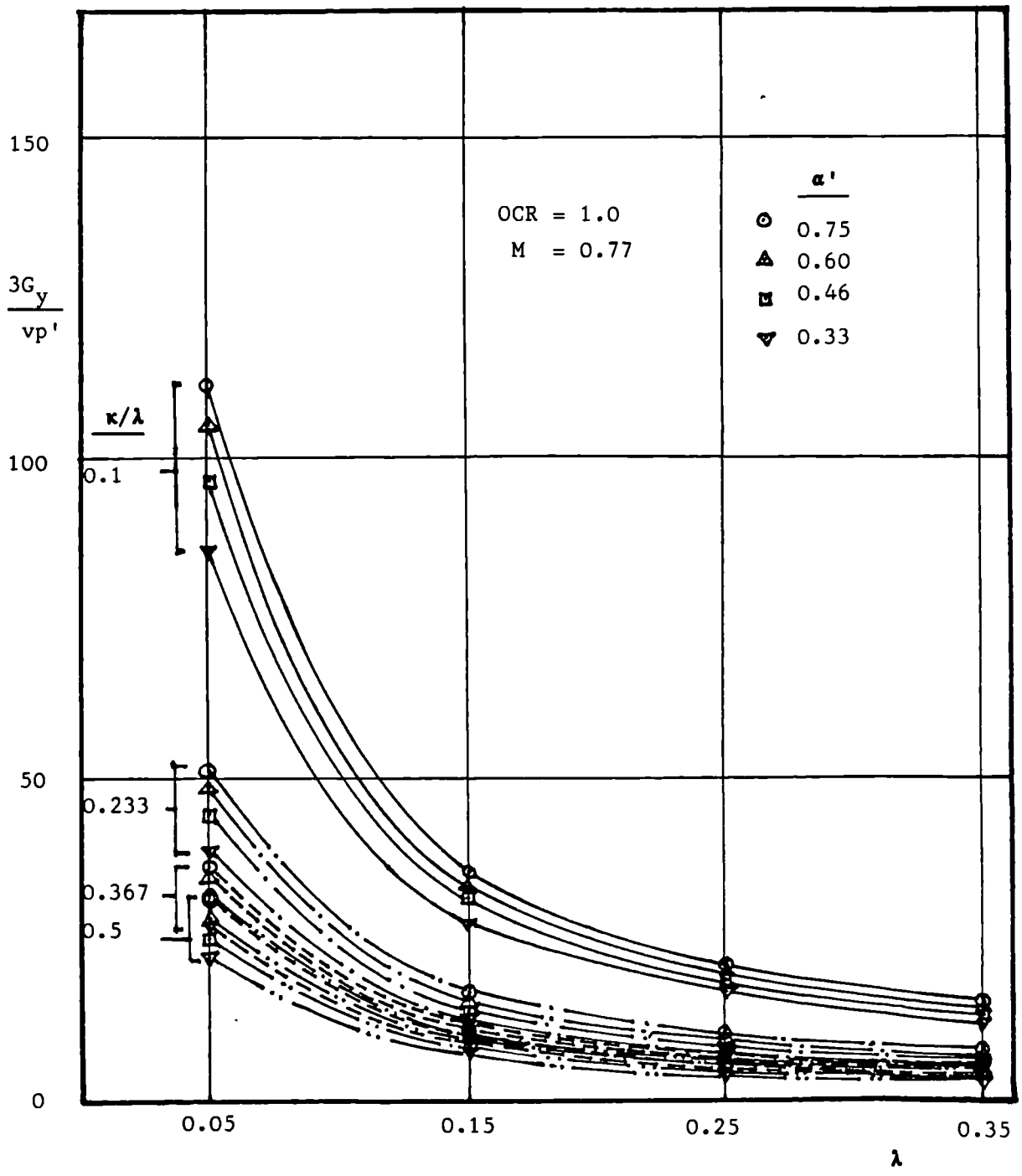

Figure 5.9 Variations of normalised tangent modulus $3G_y/(vp')$ immediately after yield with λ for fixed values of α'

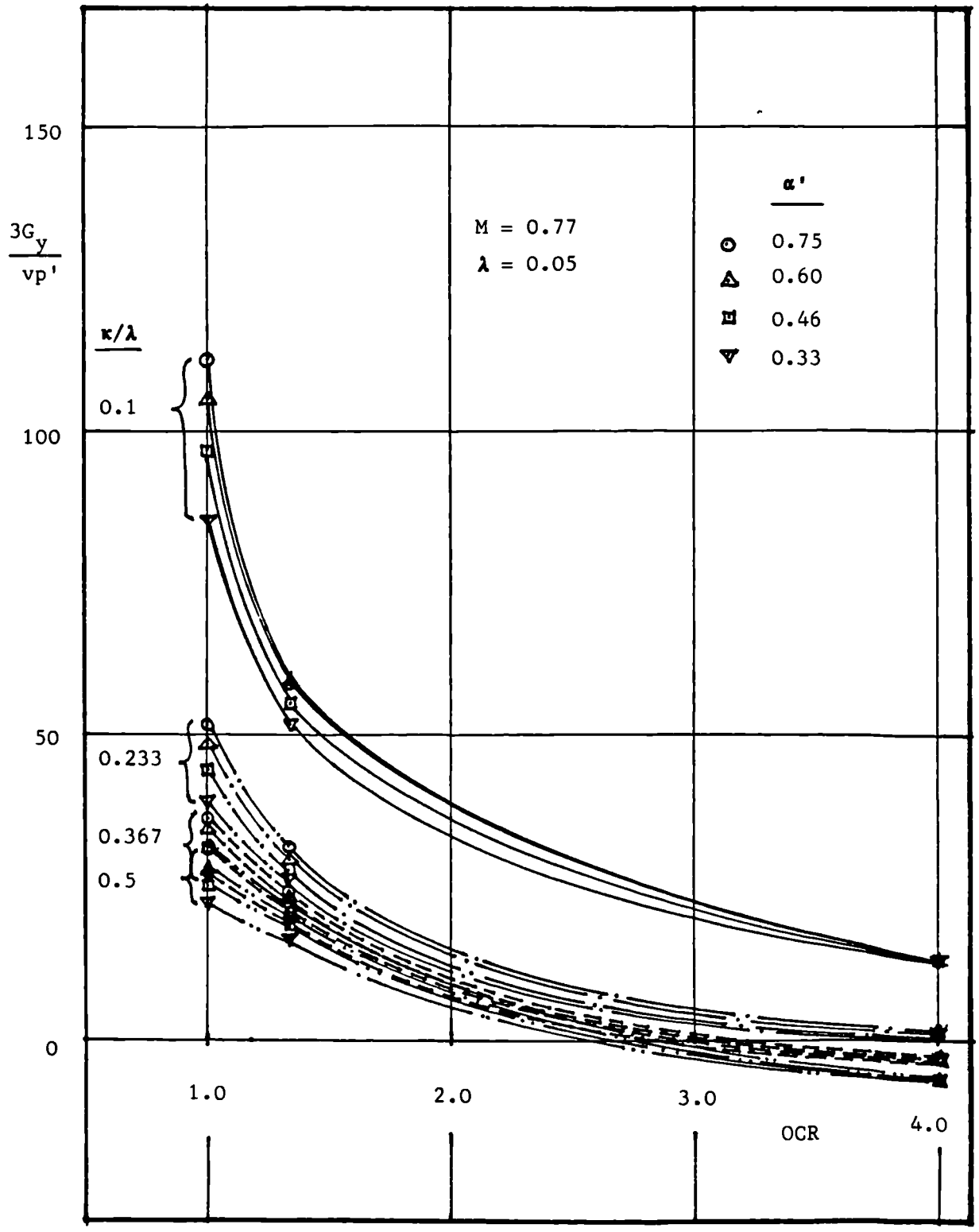

Figure 5.10 Variations of normalised tangent modulus $3G_y/(vp')$ immediately after yield with OCR for fixed values of α' and κ/λ

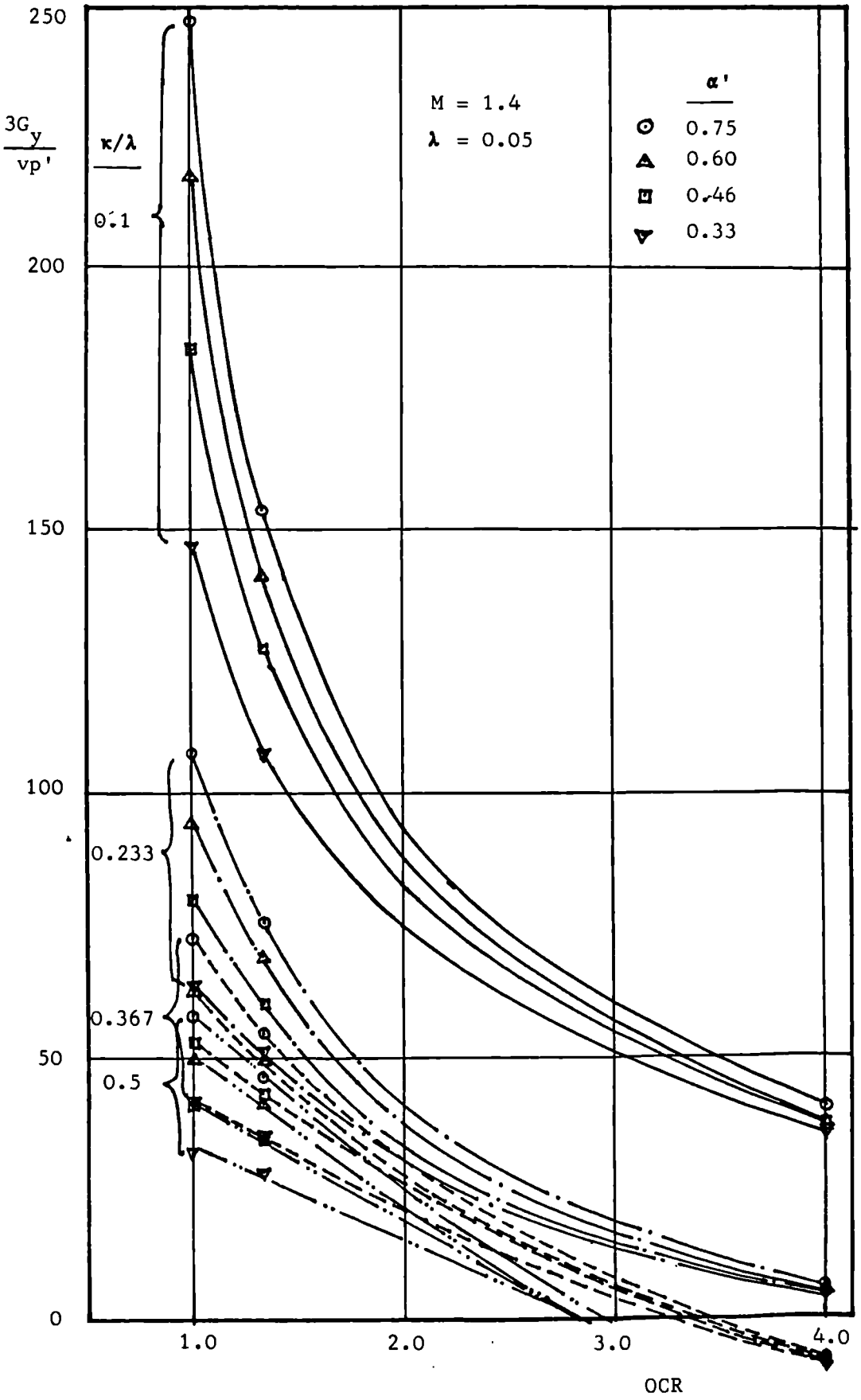

Figure 5.11 Variations of normalised tangent modulus $3G_y/(vp')$ immediately after yield with OCR for fixed values of α' and κ/λ

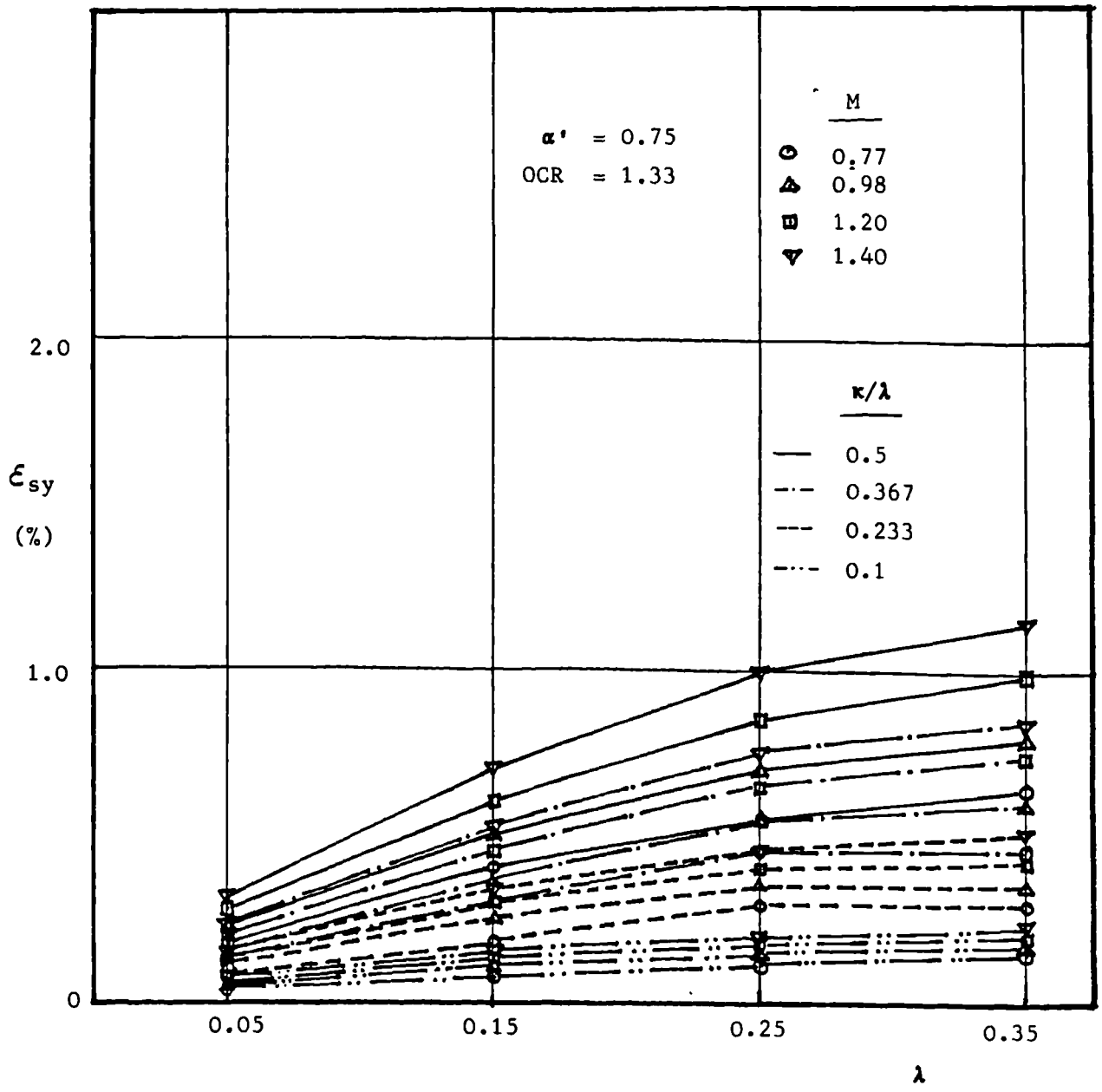

Figure 5.12 Variations of shear strains ε_{sy} immediately after yield with λ for fixed values of M and κ/λ

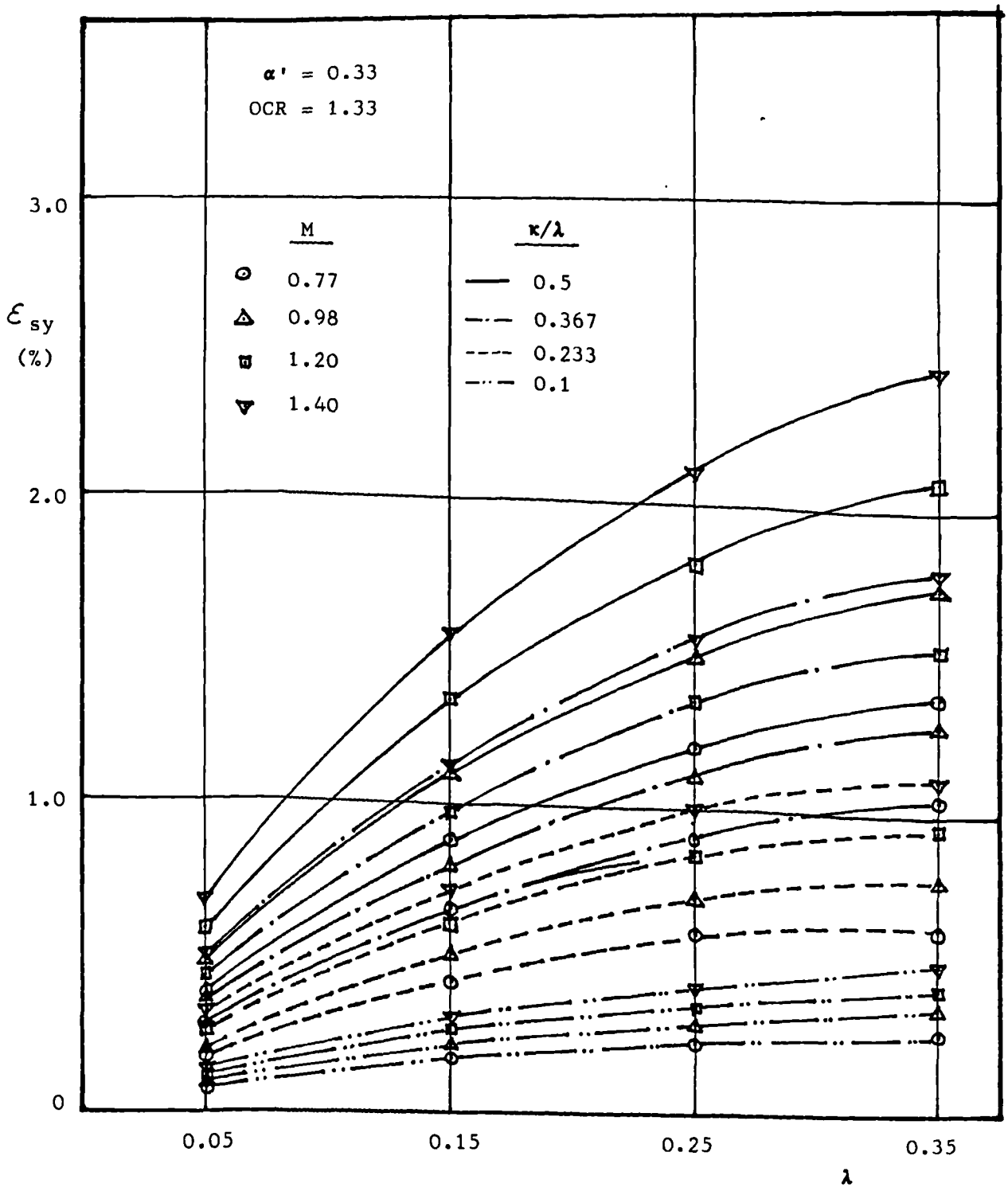

Figure 5.13 Variations of shear strains ε_{sy} immediately after yield with λ for fixed values of M and κ/λ

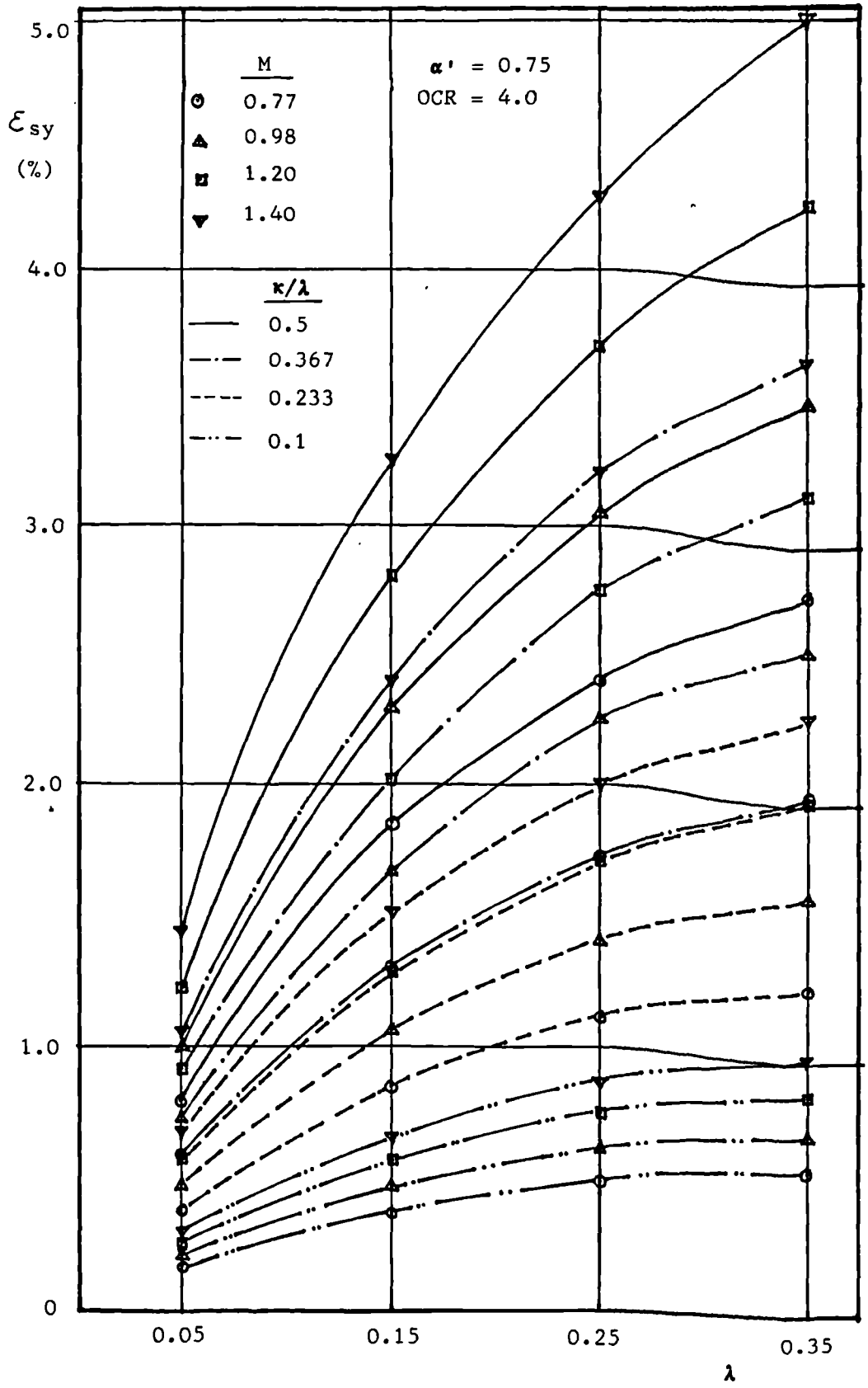

Figure 5.14 Variations of shear strain ε_{sy} immediately after yield with λ for fixed values of M and κ/λ

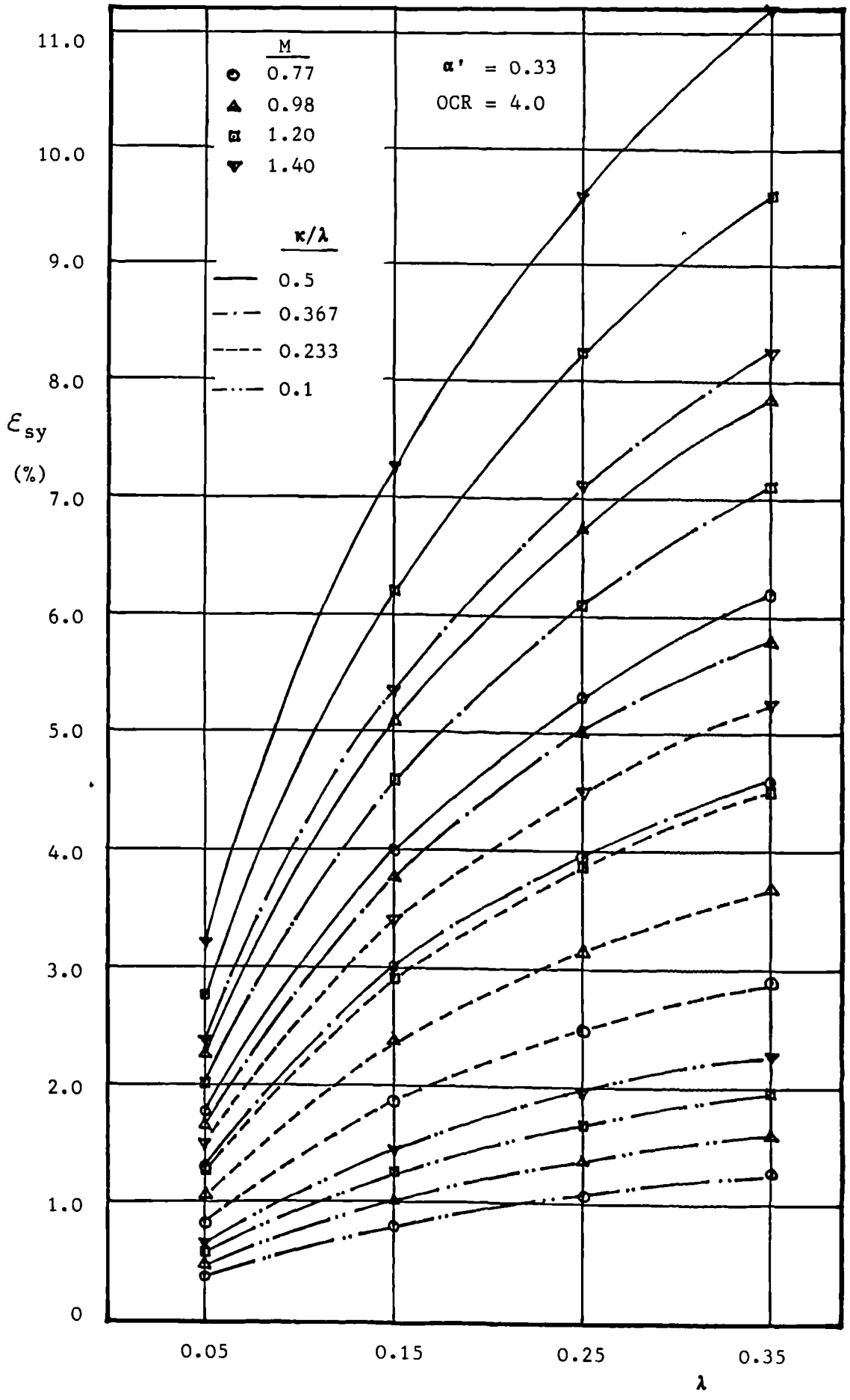

Figure 5.15 Variations of shear strain ε_{sy} immediately after yield with λ for fixed values of M and κ/λ

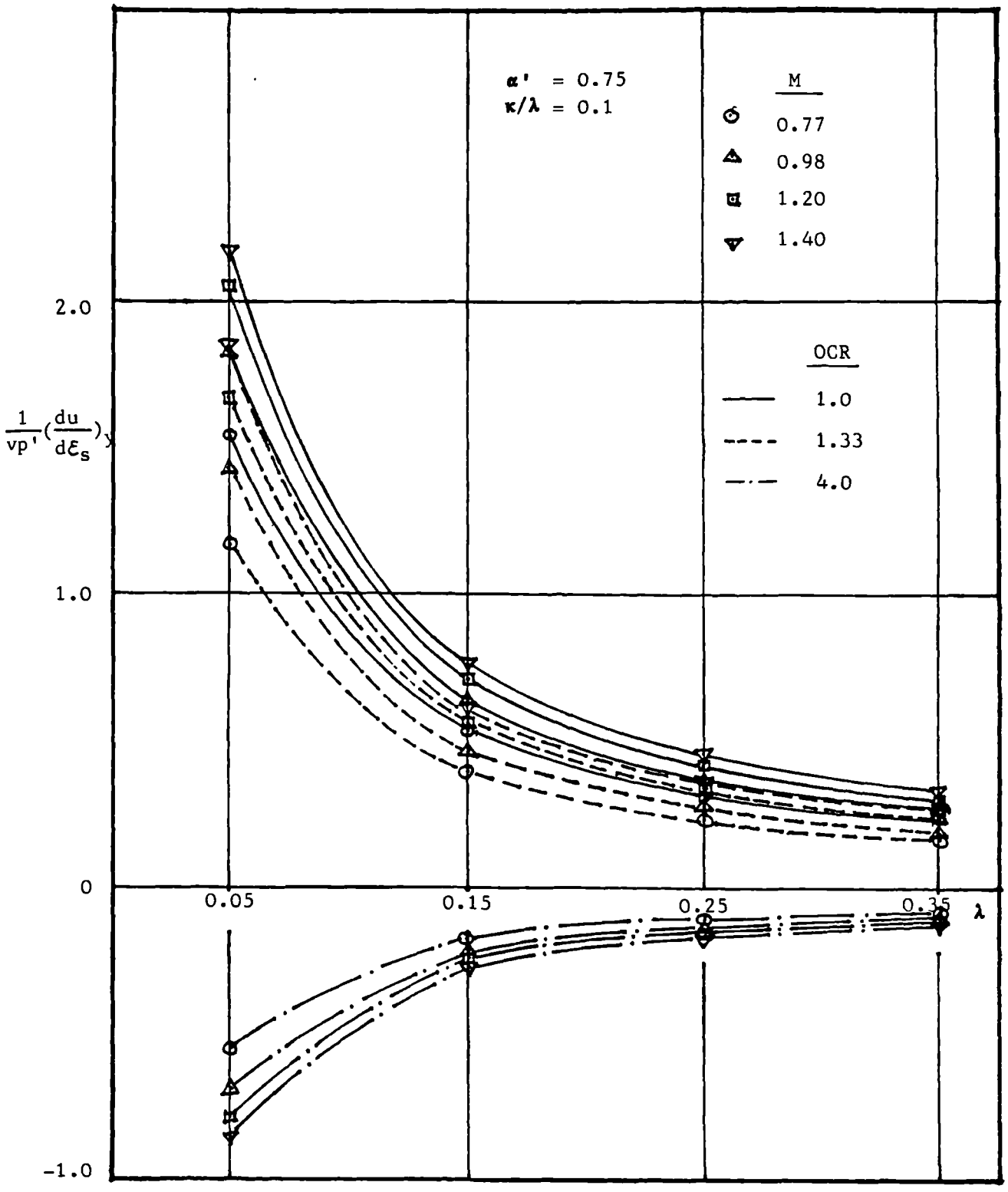

Figure 5.16 Variations of normalised rate of pore pressure change $[du/(vp'd\varepsilon_s)]_y$ immediately after yield with λ for fixed values of M and OCR

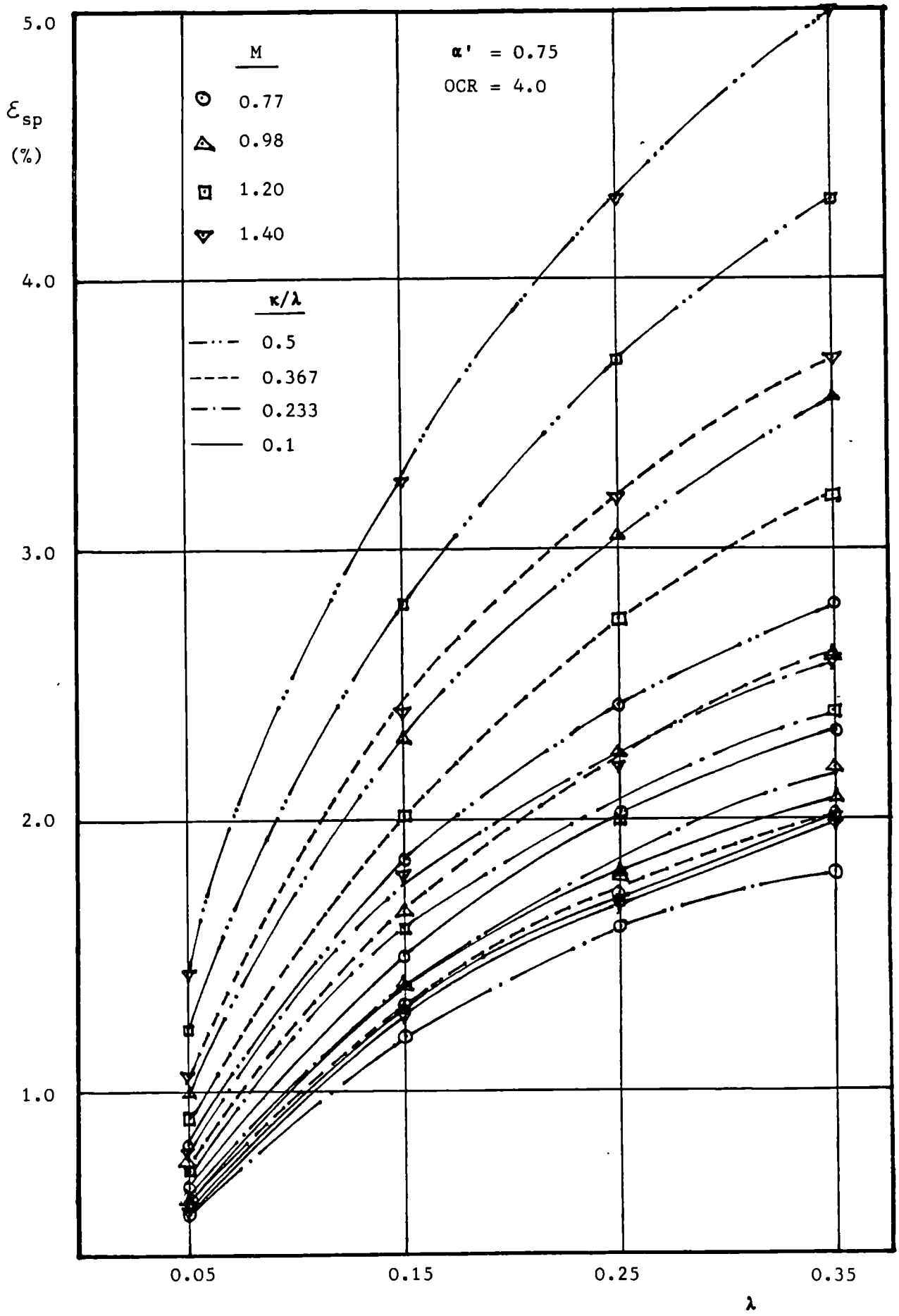

Figure 5.17 Variations of shear strains ε_{sp} at peak deviator stress with λ for fixed values of κ/λ and M

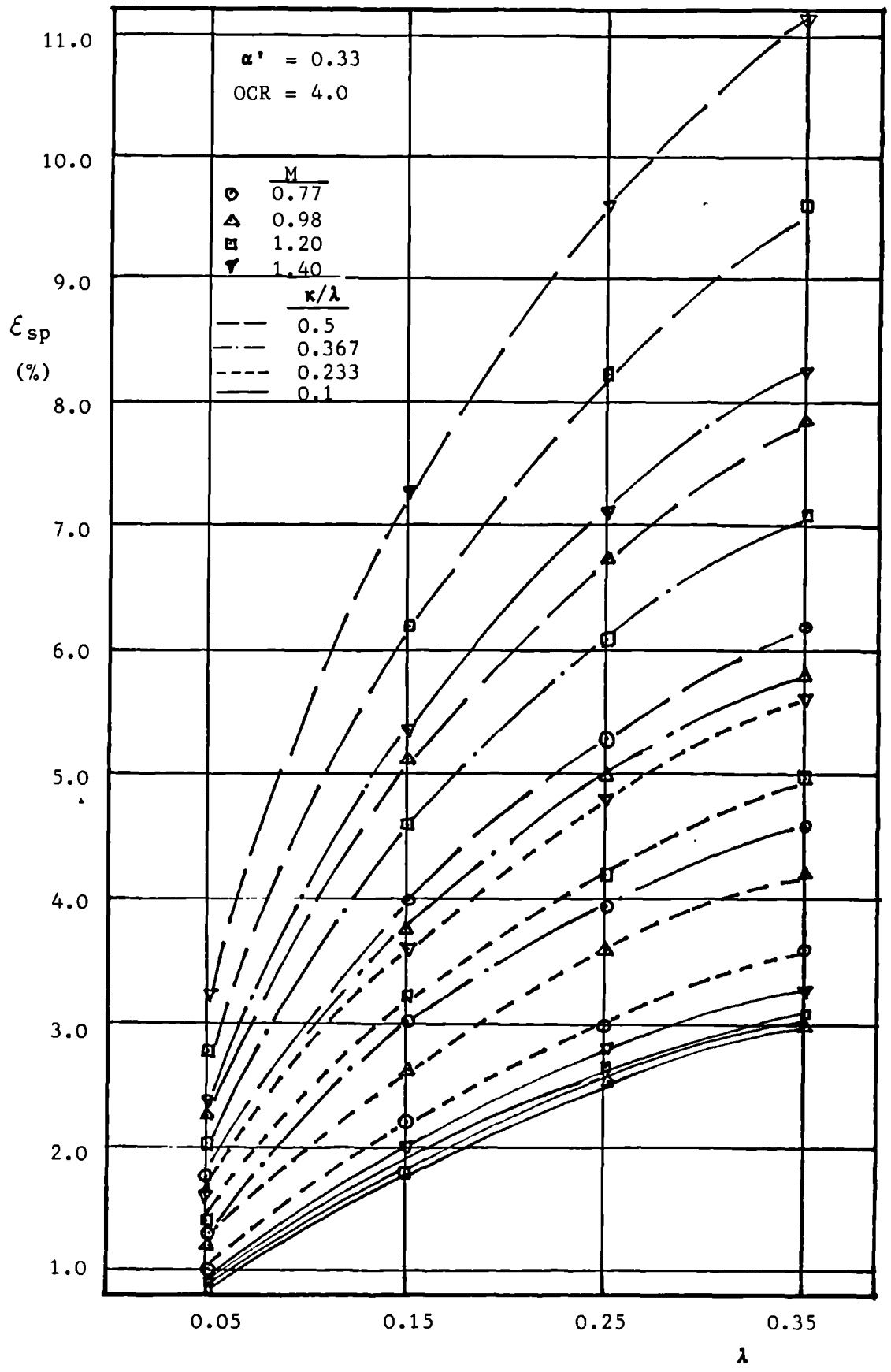

Figure 5.18 Variations of shear strains ε_{sp} at peak deviator stress with λ for fixed values of κ/λ and M

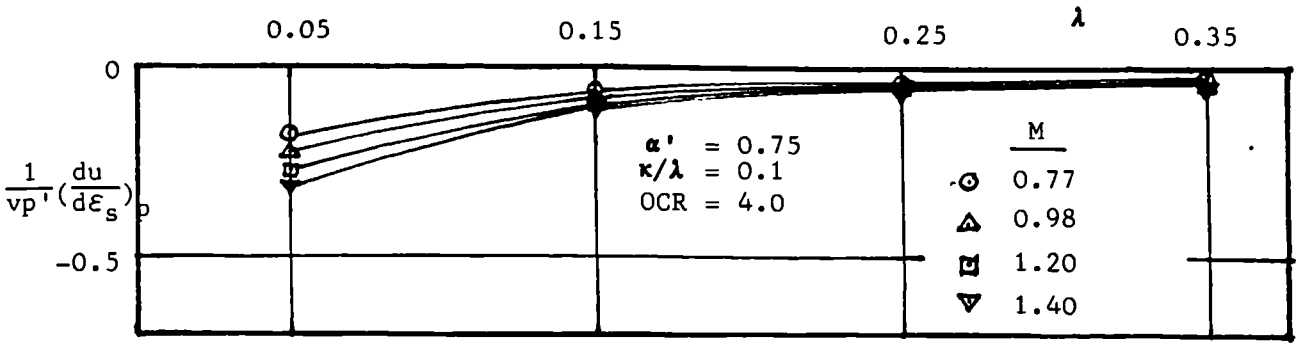

Figure 5.19 Variations of peak normalised rate of pore pressure change $[du/(vp'd\varepsilon_s)]_p$ with λ for fixed values of M

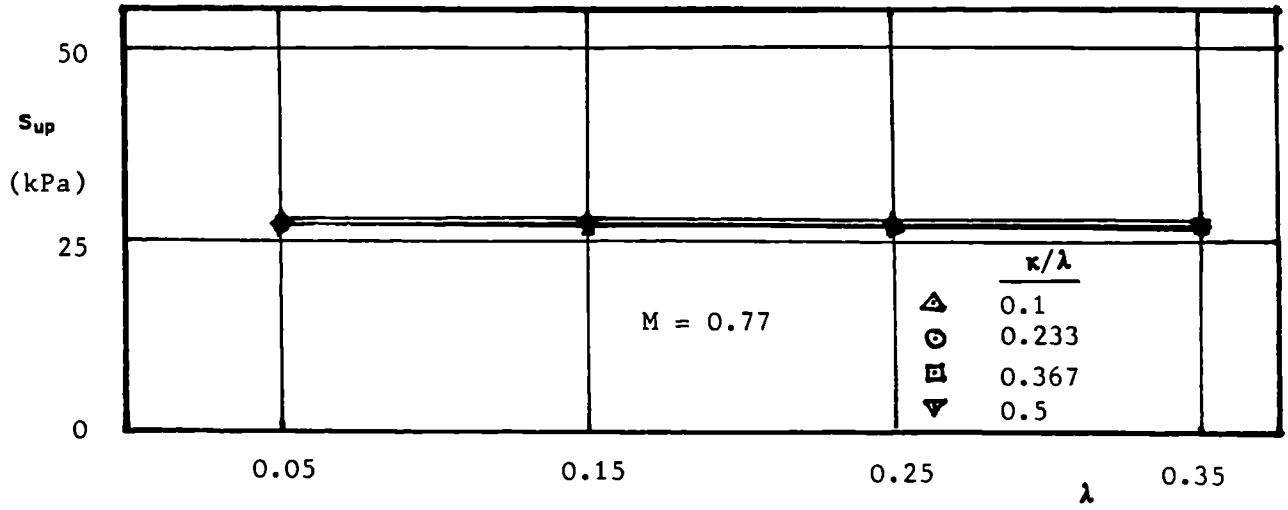

Figure 5.20 Variations of peak shear strength s_{up} with λ for fixed values of κ/λ

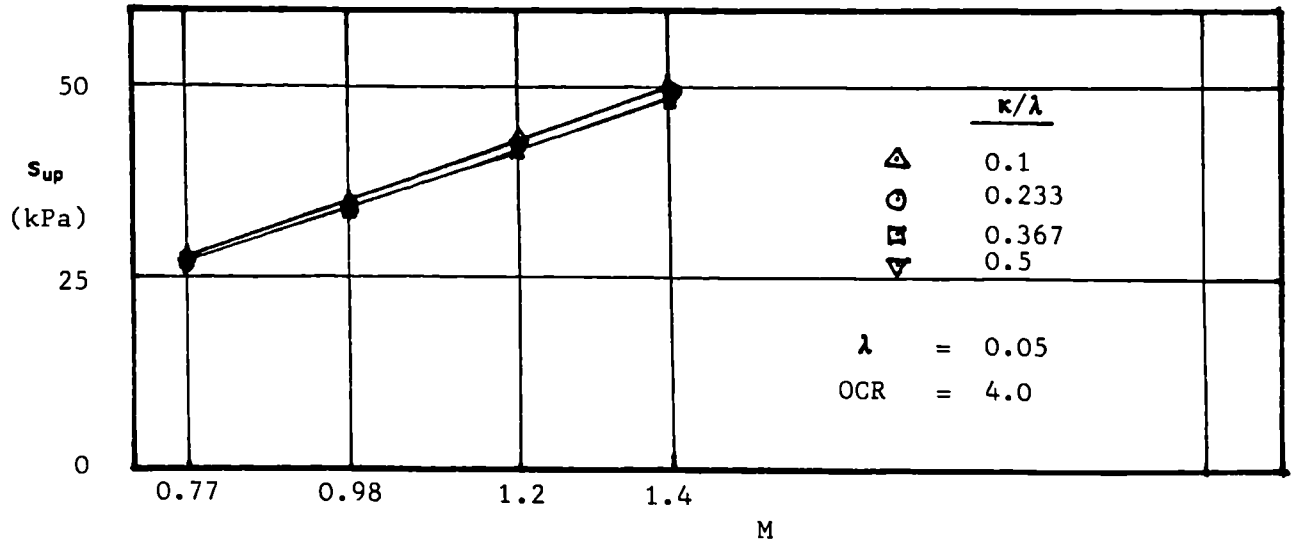

Figure 5.21 Variations of peak shear strength s_{up} with M for fixed values of κ/λ

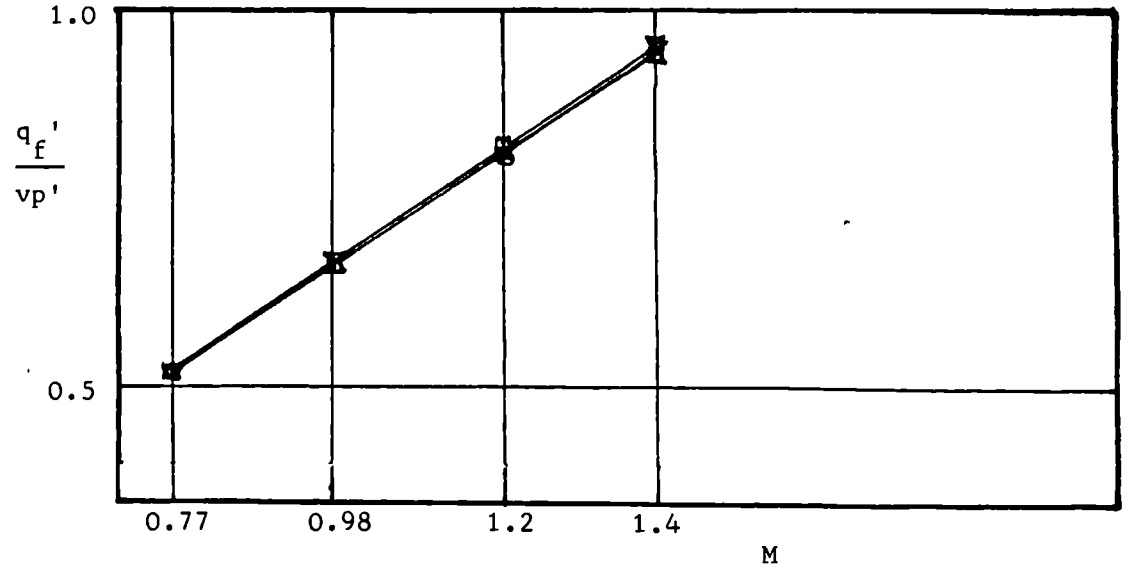

Figure 5.22(a) Variations of ultimate deviator stress with M for fixed values of κ/λ

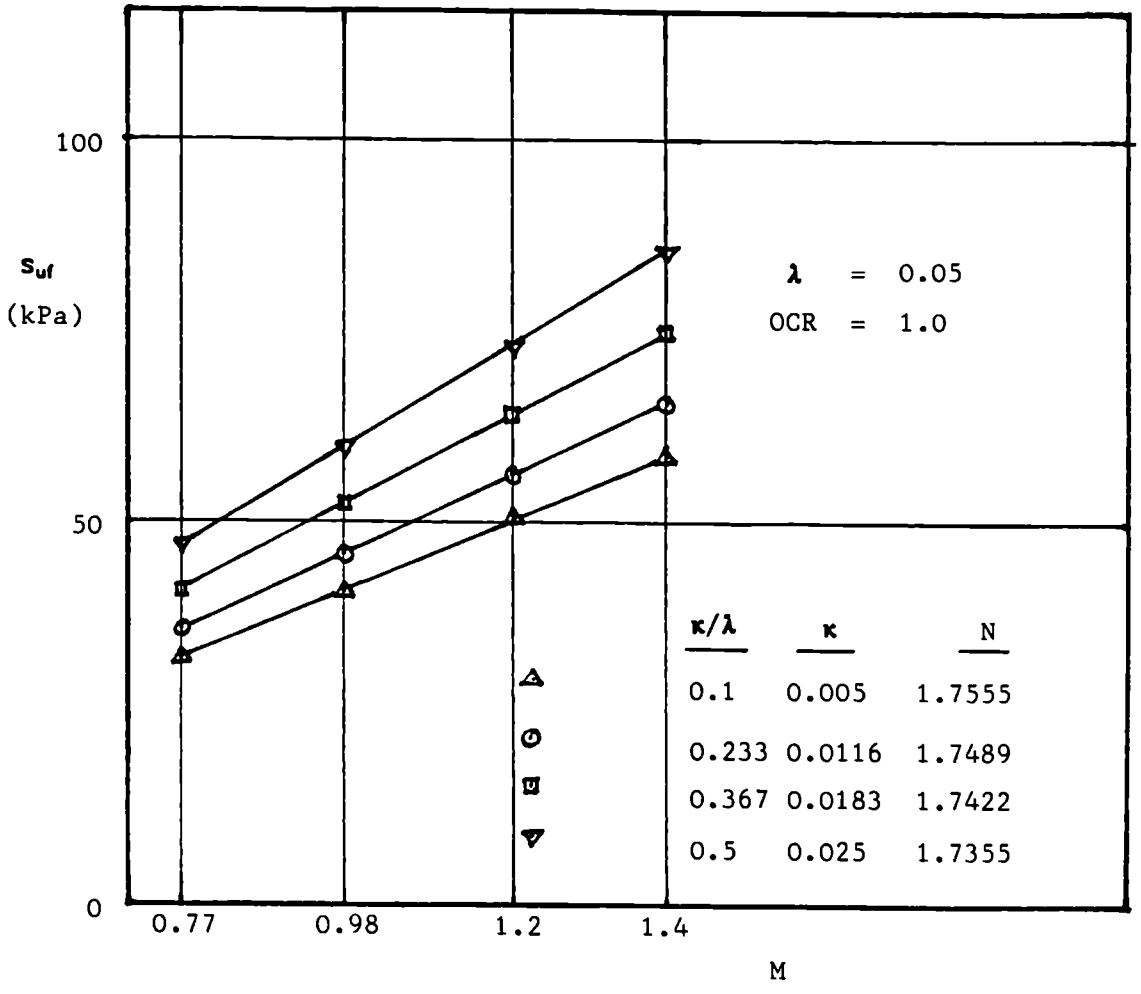

Figure 5.22(b) Variations of ultimate shear strength with M for fixed values of κ/λ

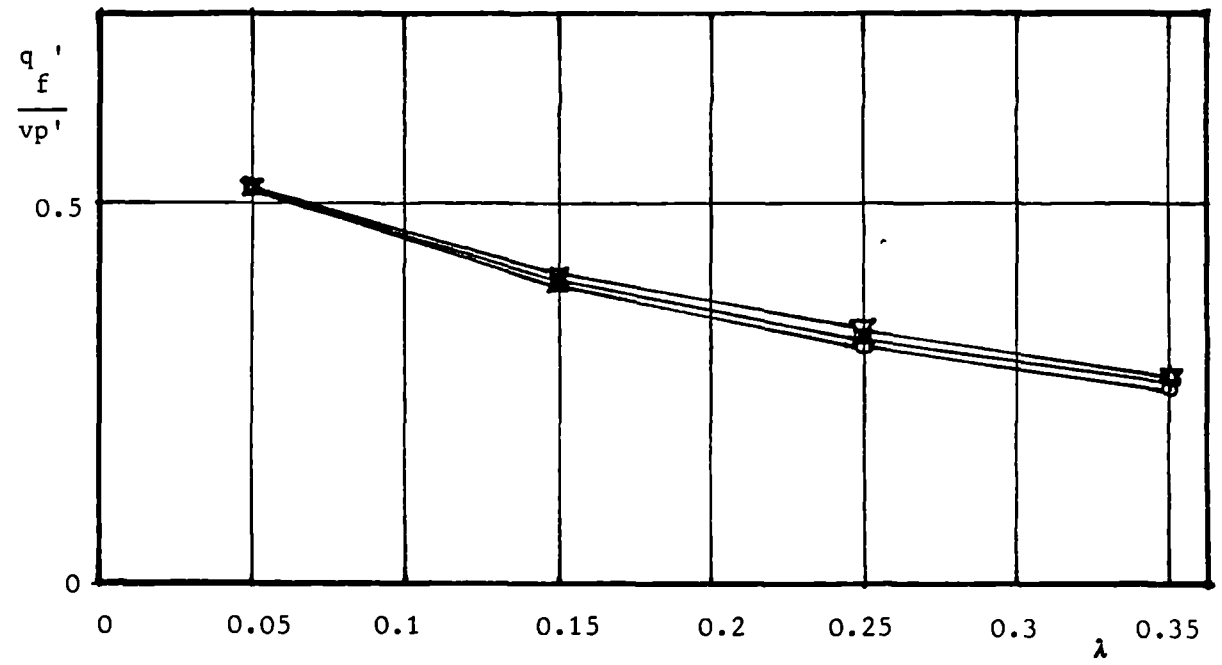

Figure 5.23(a) Variations of ultimate deviator stress with λ and κ/λ

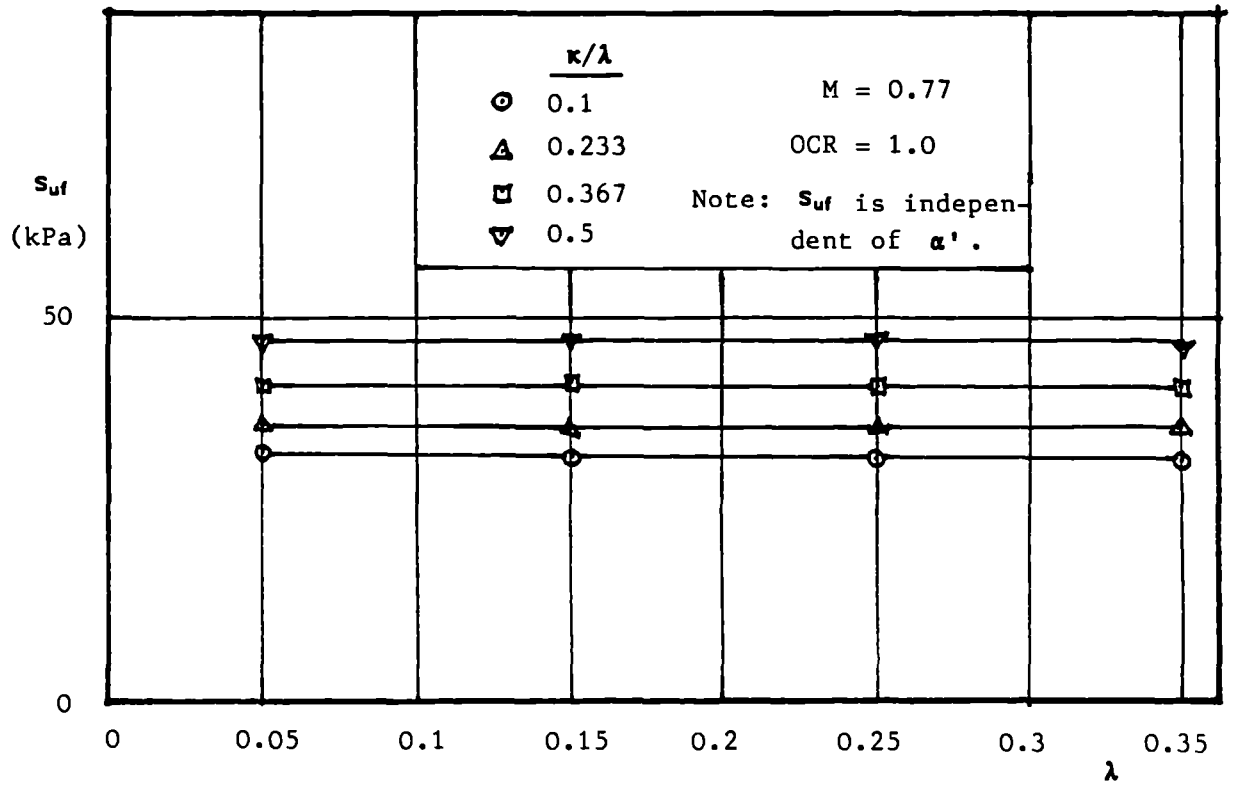

Figure 5.23(b) Variations of ultimate shear strength with λ and κ/λ

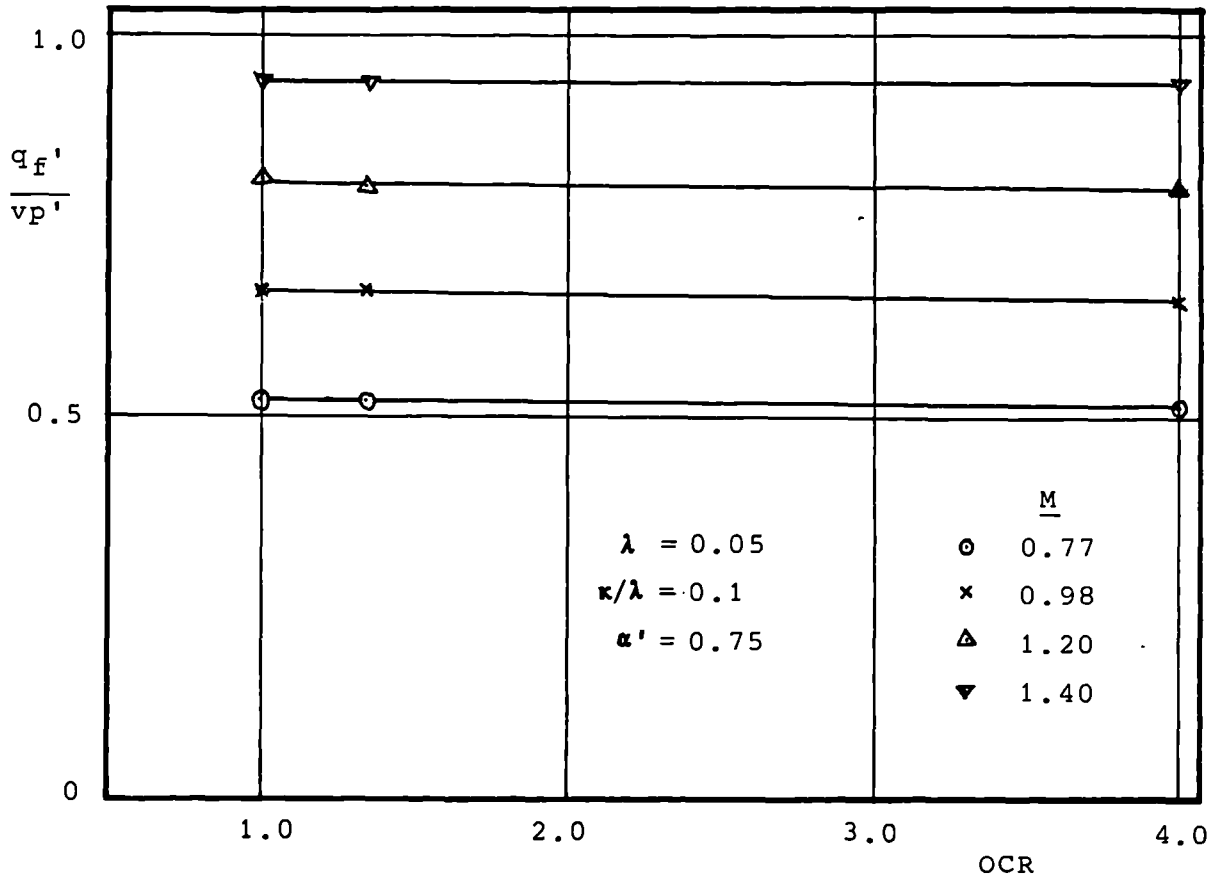

Figure 5.24(a) Variations of normalised ultimate deviator stress with OCR and M

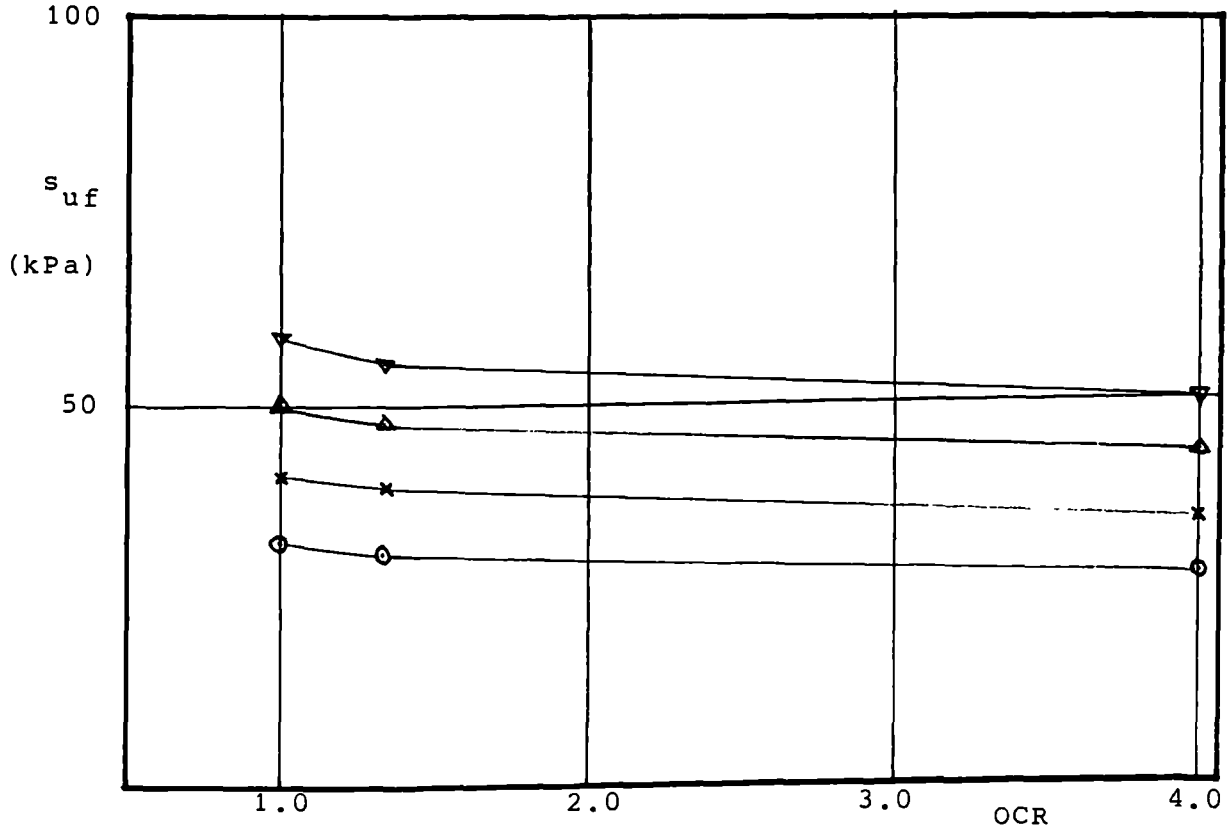

Figure 5.24(b) Variations of ultimate shear strength with OCR and M

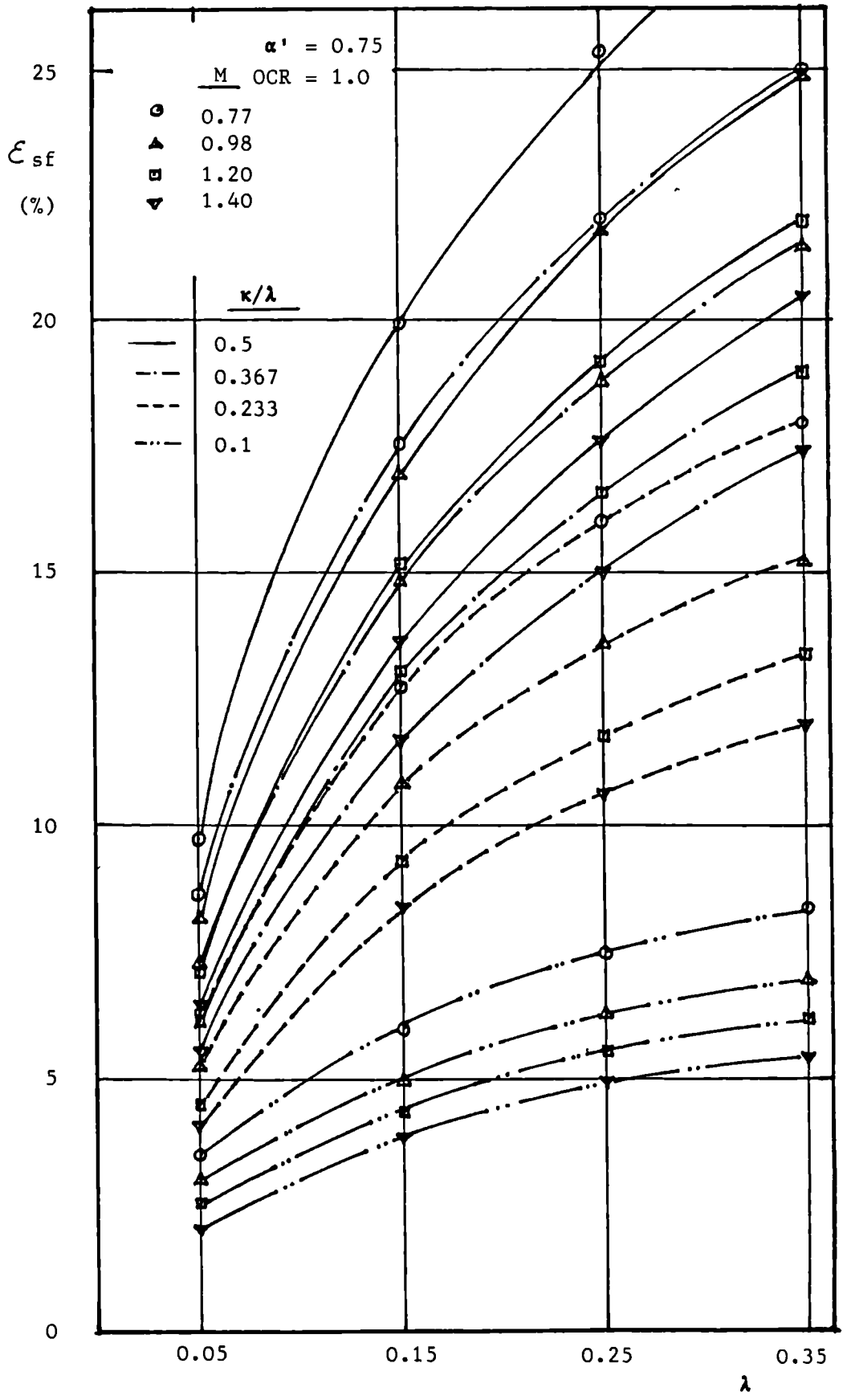

Figure 5.25 Variations of ultimate shear strain ε_{sf} with λ for fixed values of M and κ/λ

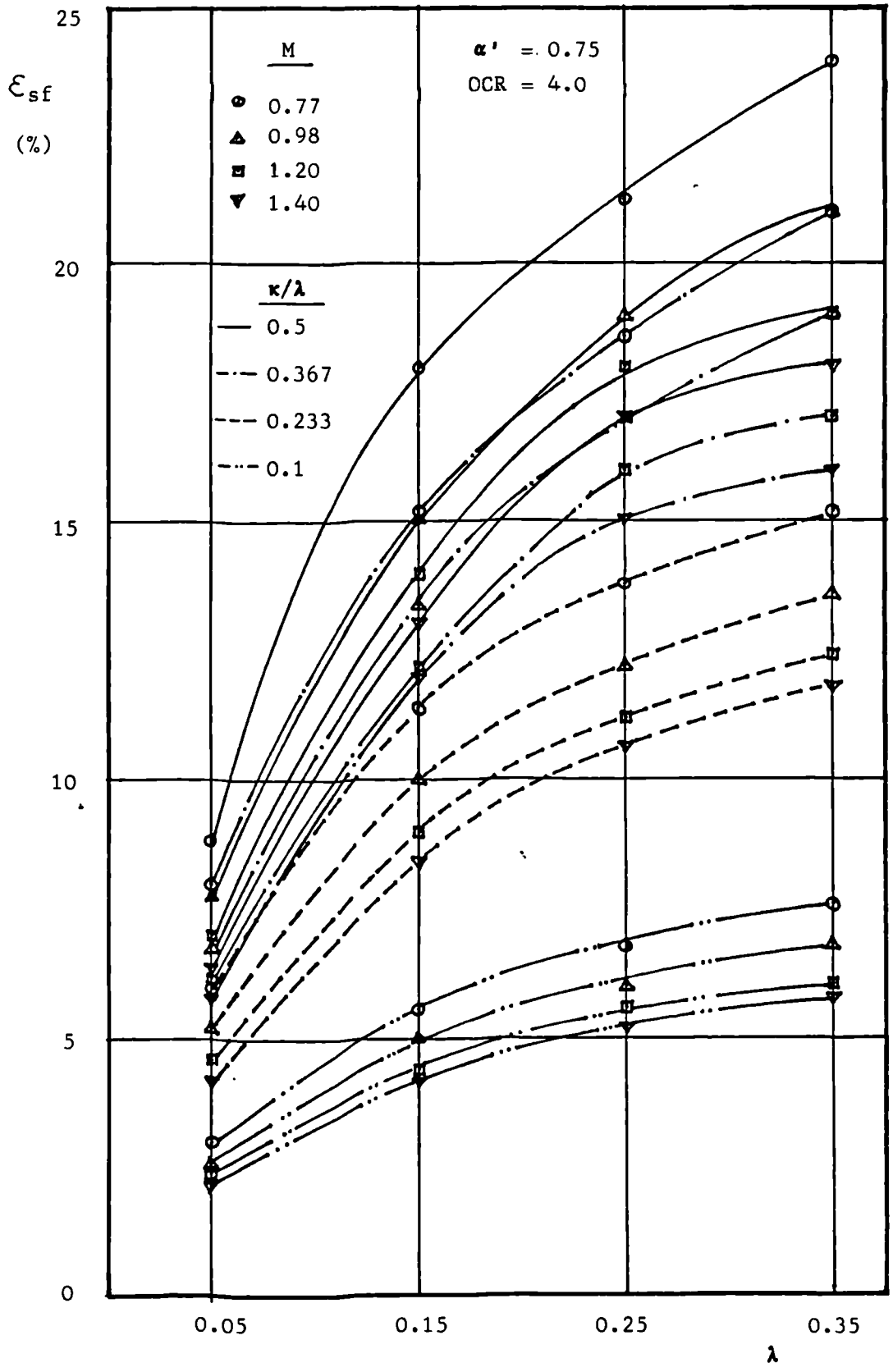

Figure 5.26 Variations of ultimate shear strain ε_{sf} with λ for fixed values of M and κ/λ

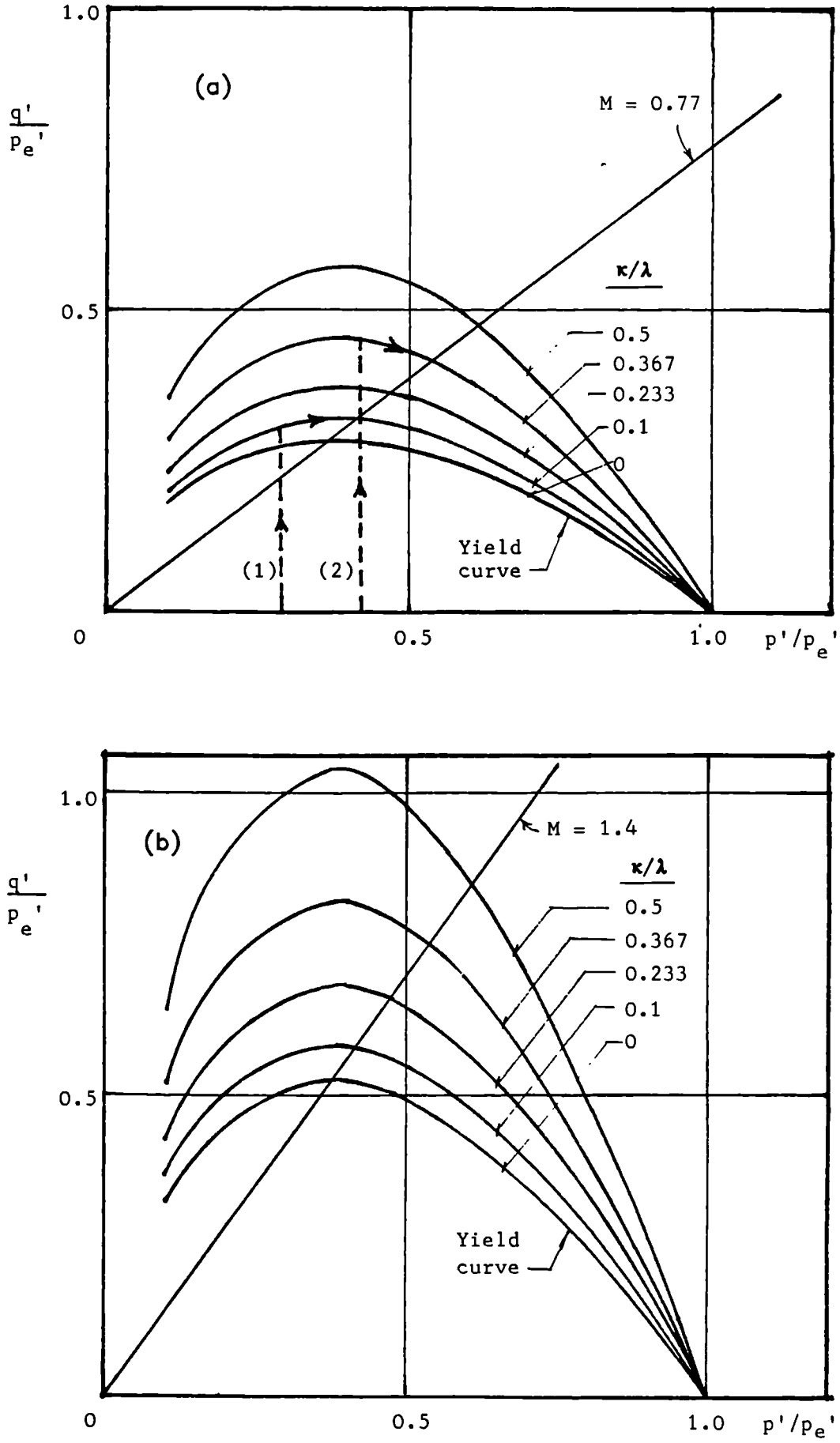

Figure 5.27 Constant volume sections through normalised state boundary surfaces with changing κ/λ (a) M = 0.77 (b) M = 1.4

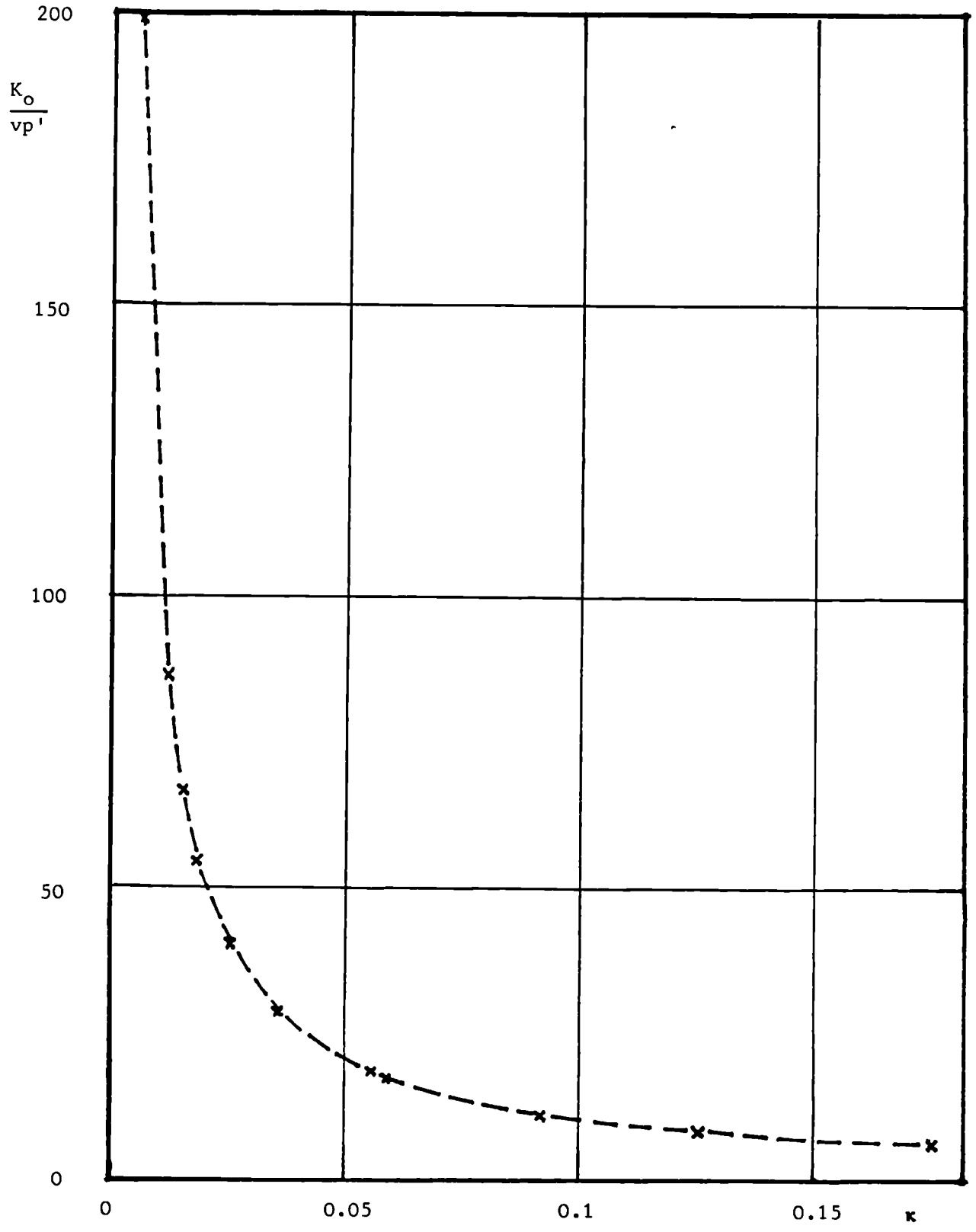

Figure 5.28 Variations of initial normalised bulk modulus $K_o/(vp')$ with κ

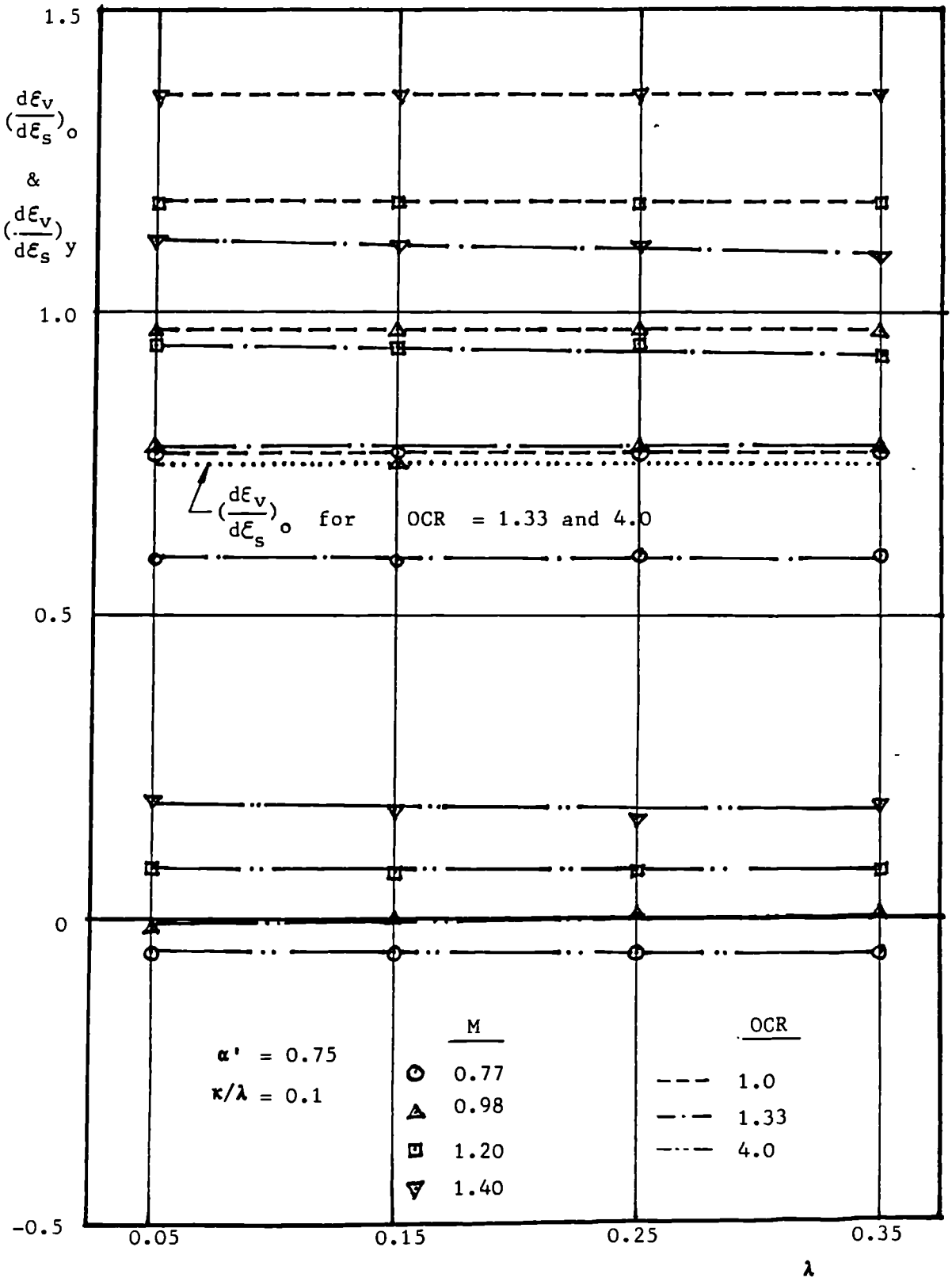

Figure 5.29 Variations of rate of dilatancy $(d\varepsilon_v/d\varepsilon_s)_o$ at initial state and $(d\varepsilon_v/d\varepsilon_s)_y$ immediately after yield with λ for fixed values of M and OCR

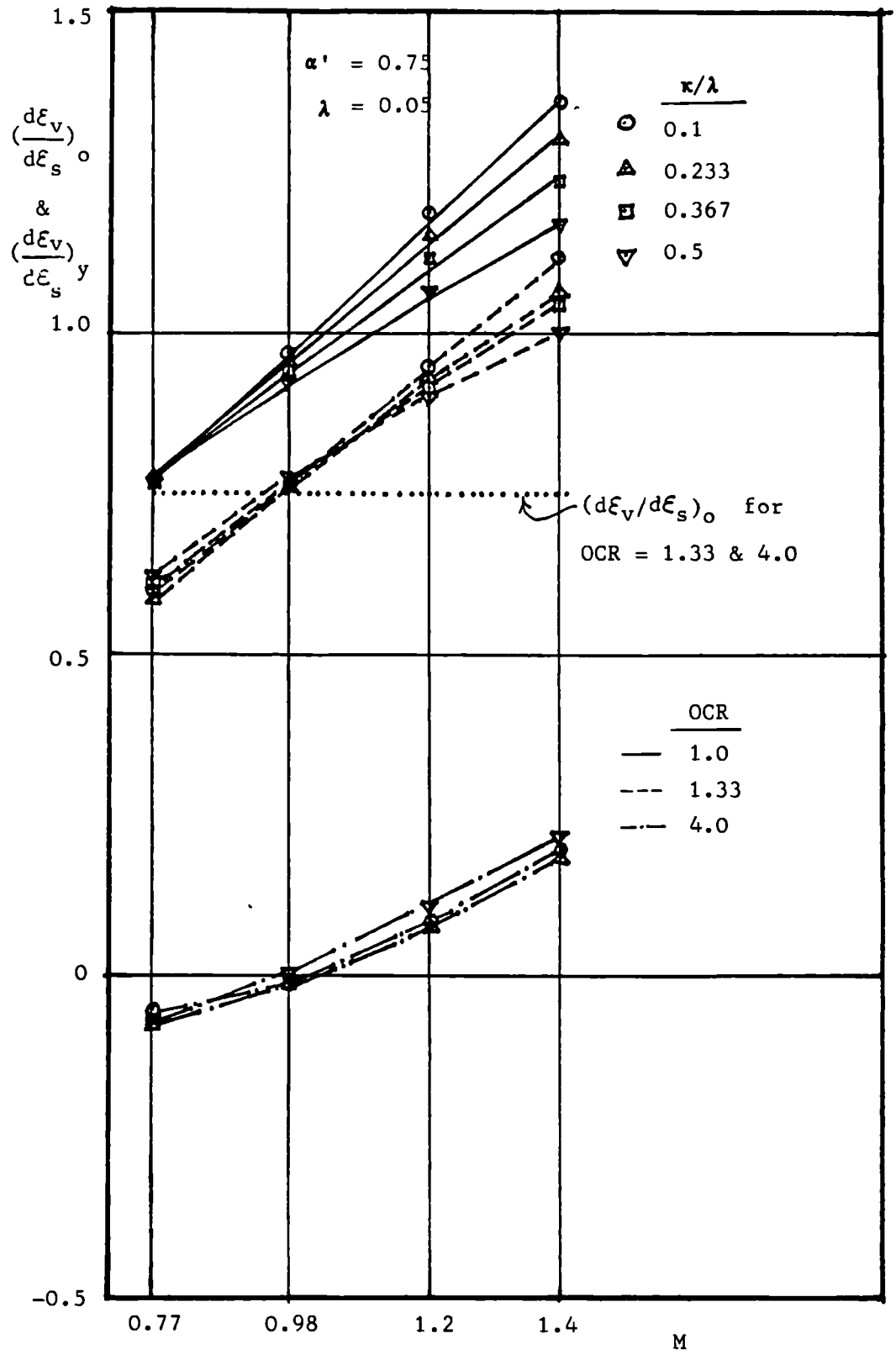

Figure 5.30 Variations of rate of dilatancy $(d\varepsilon_v/d\varepsilon_s)_o$ at initial state and $(d\varepsilon_v/d\varepsilon_s)_y$ immediately after yield with M for fixed values of κ/λ and OCR

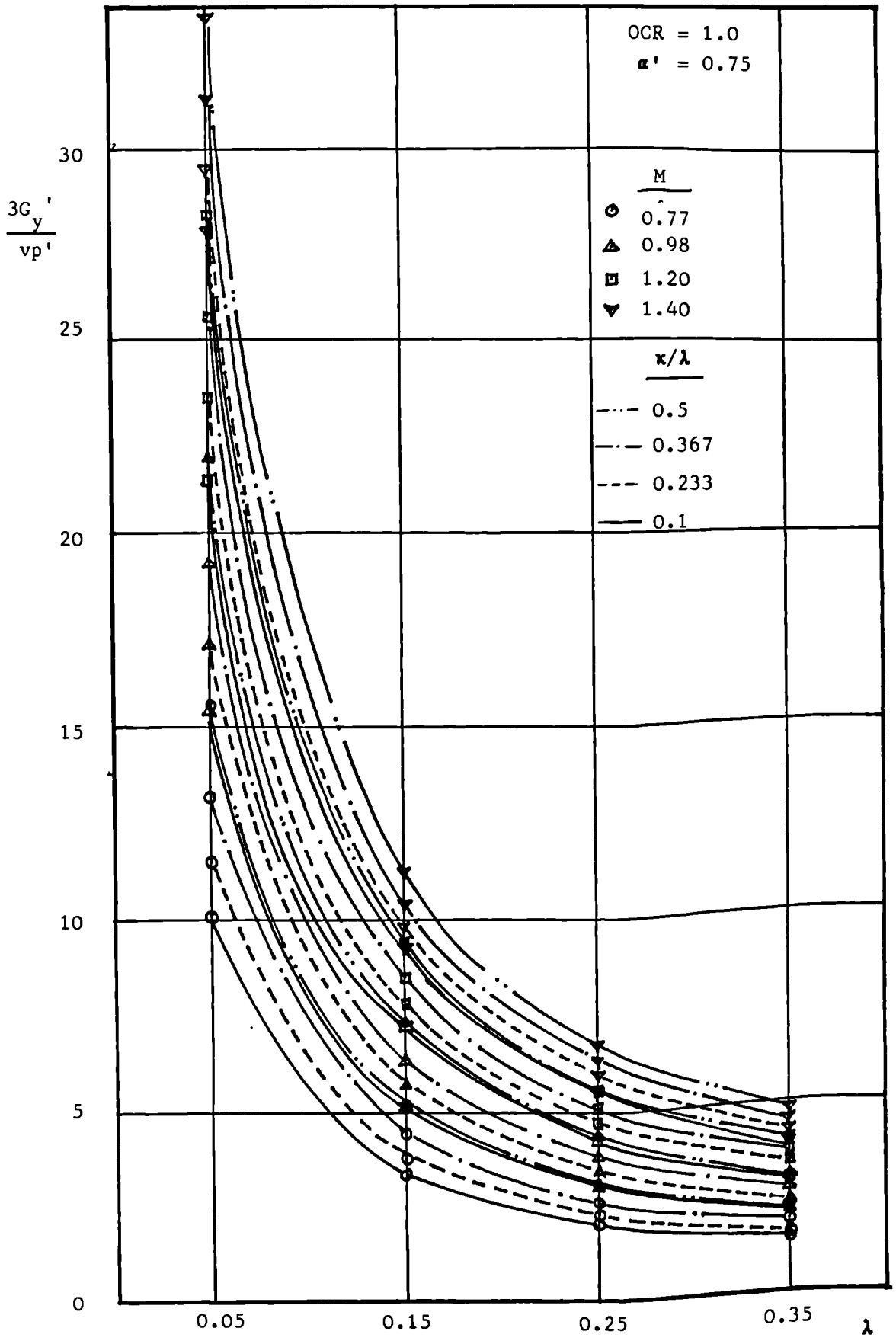

Figure 5.31 Variations of normalised tangent modulus $3G_y'/(vp')$ immediately after yield with λ for fixed values of κ/λ and M

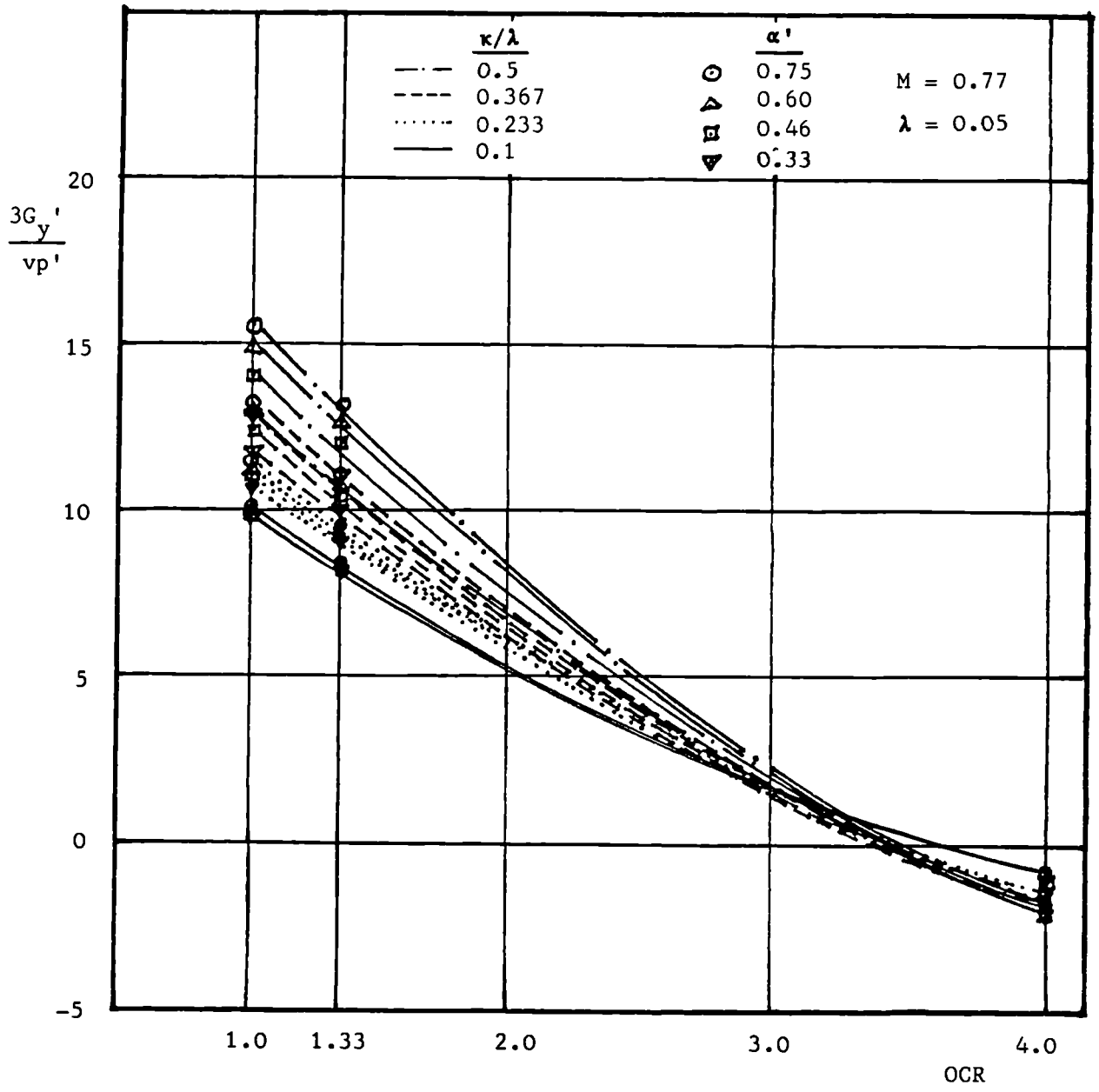

Figure 5.32 Variations of normalised tangent modulus $3G_y'/(vp')$ immediately after yield with OCR for fixed values of κ/λ and α'

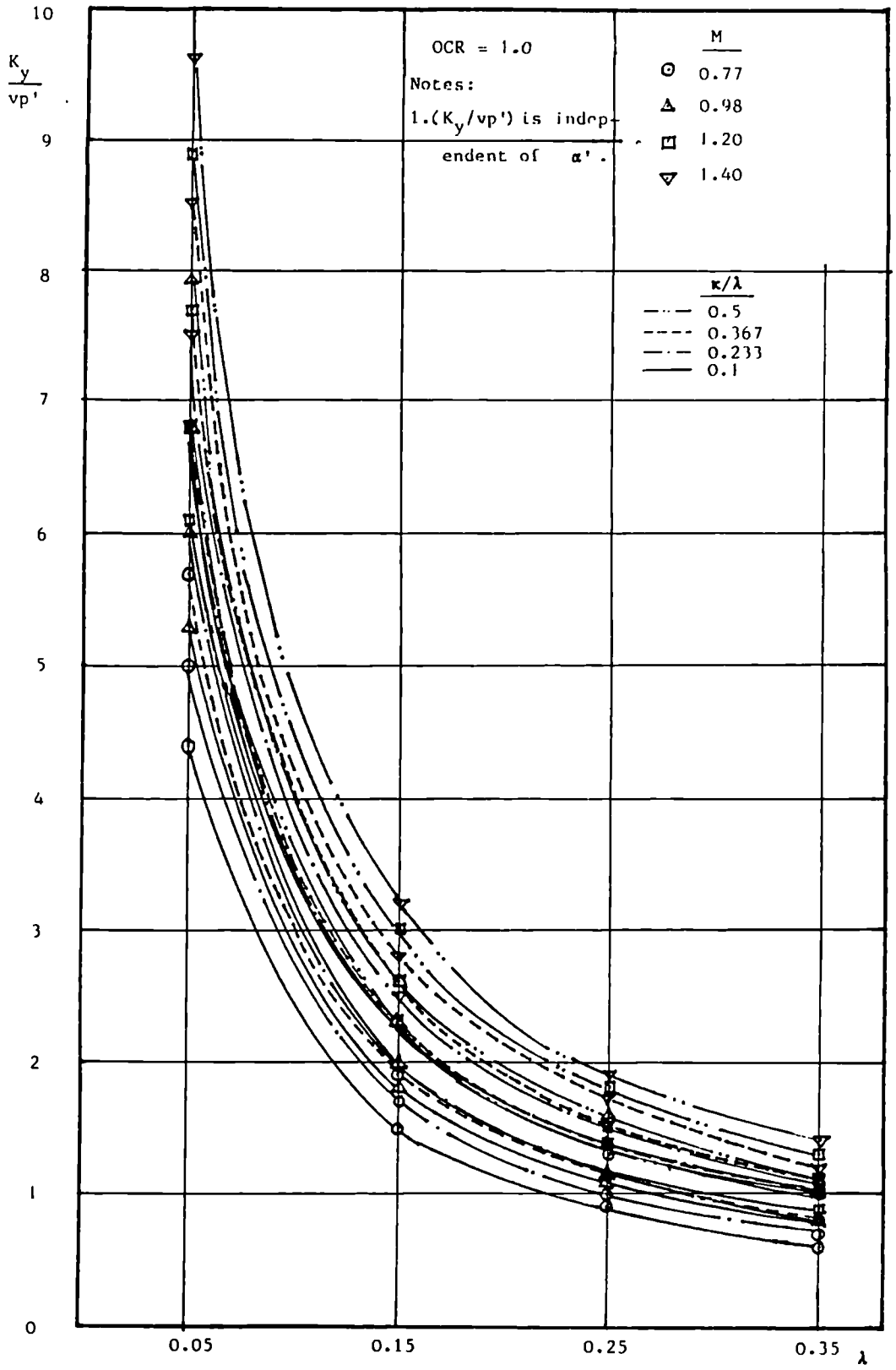

Figure 5.33 Variations of normalised bulk modulus $K_y'/(vp')$ immediately after yield with λ for fixed values of κ/λ and M

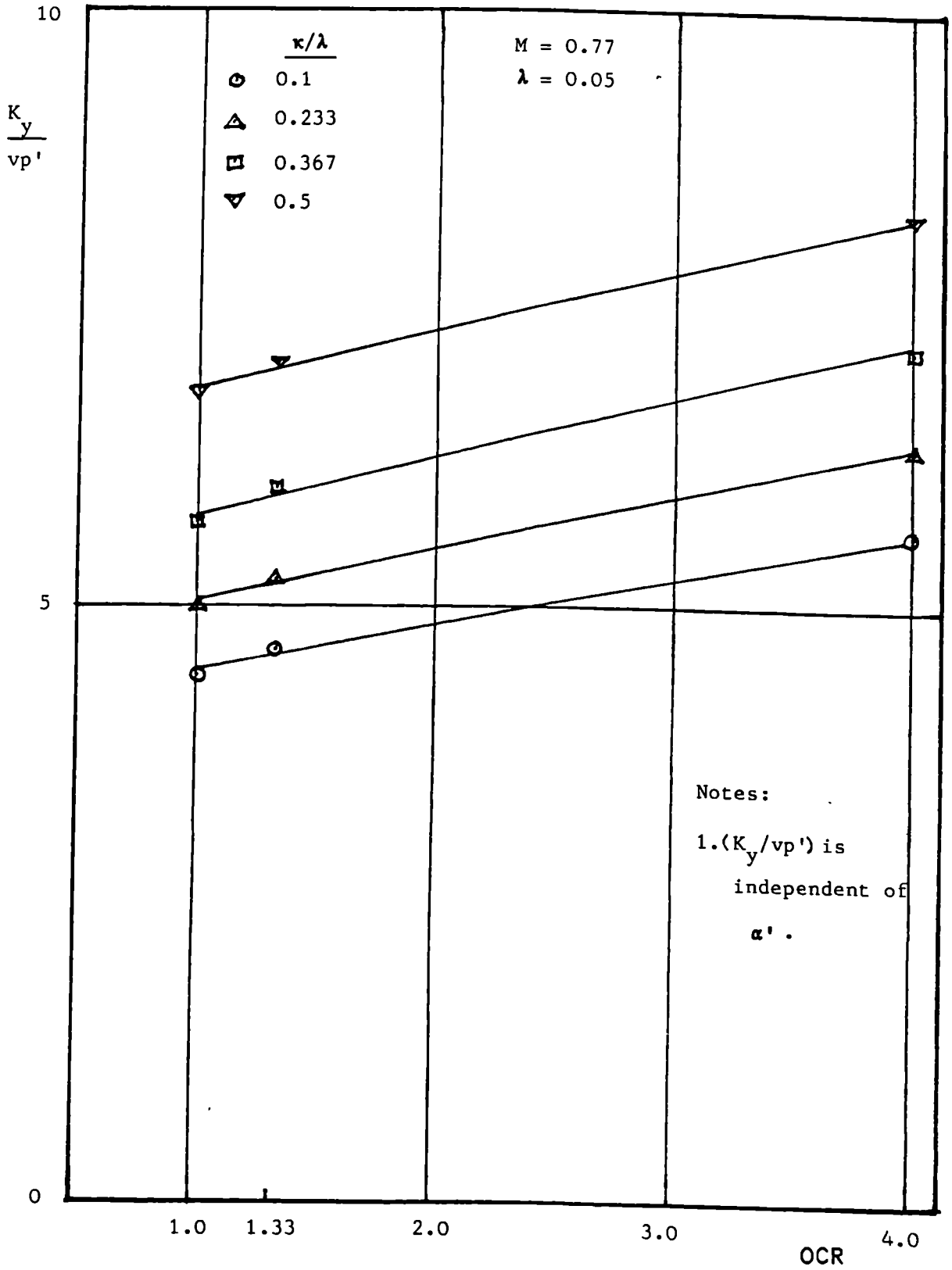

Figure 5.34 Variations of normalised bulk modulus $K_y'/(vp')$ immediately after yield with OCR for fixed values of κ/λ

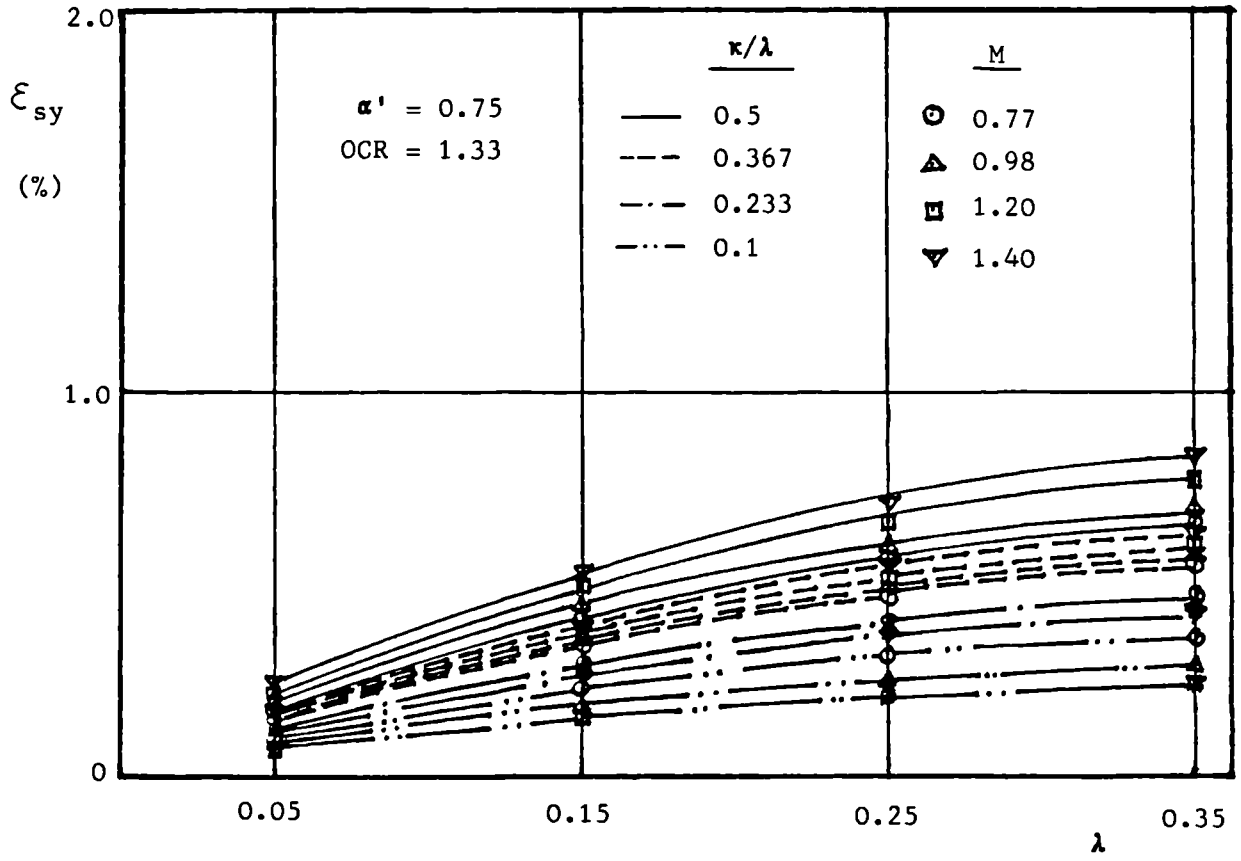

Figure 5.35 Variations of shear strain ε_{sy} immediately after yield with λ for fixed values of κ/λ and M

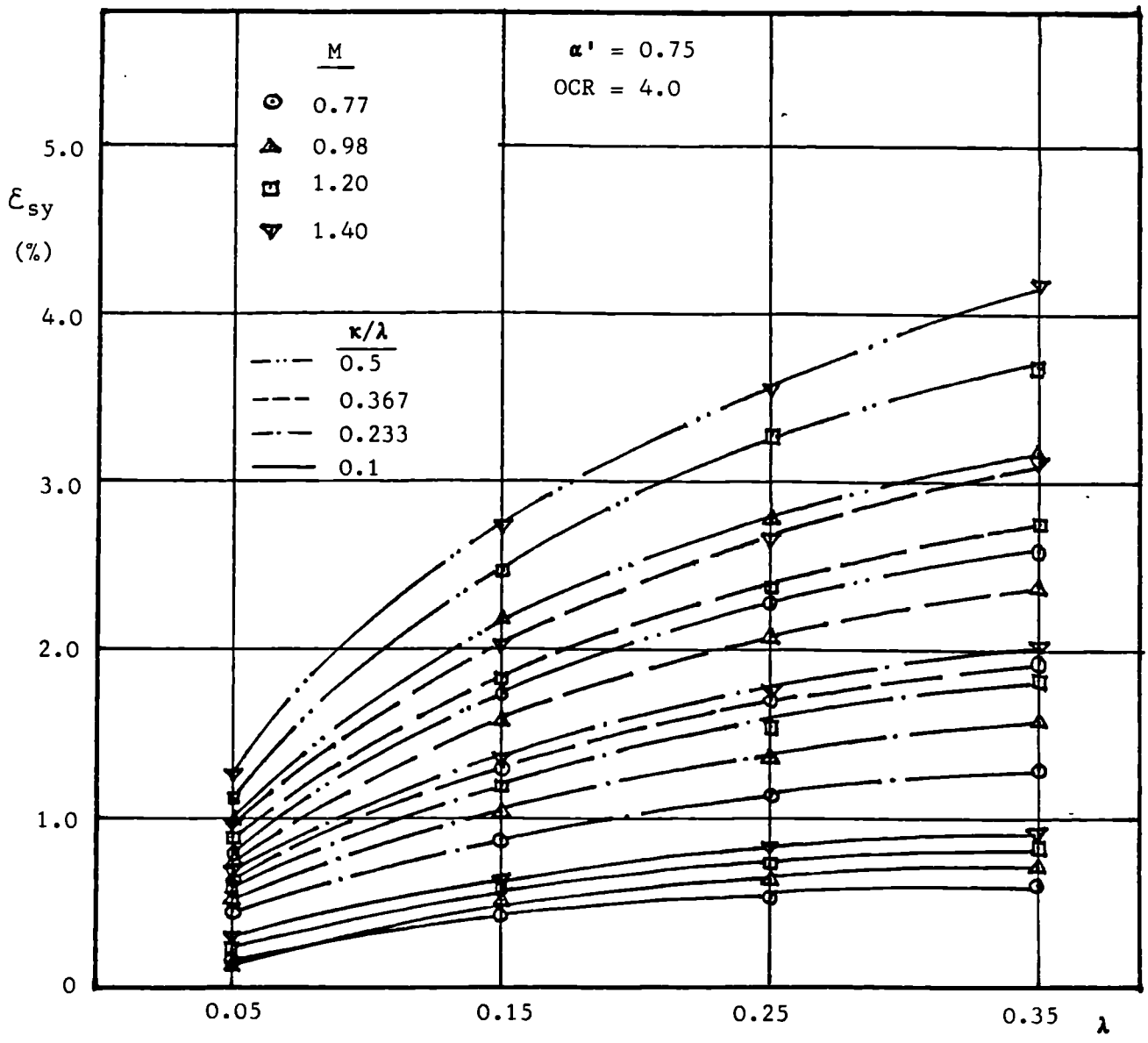

Figure 5.36 Variations of shear strain ε_{sy} immediately after yield with λ for fixed values of κ/λ and M

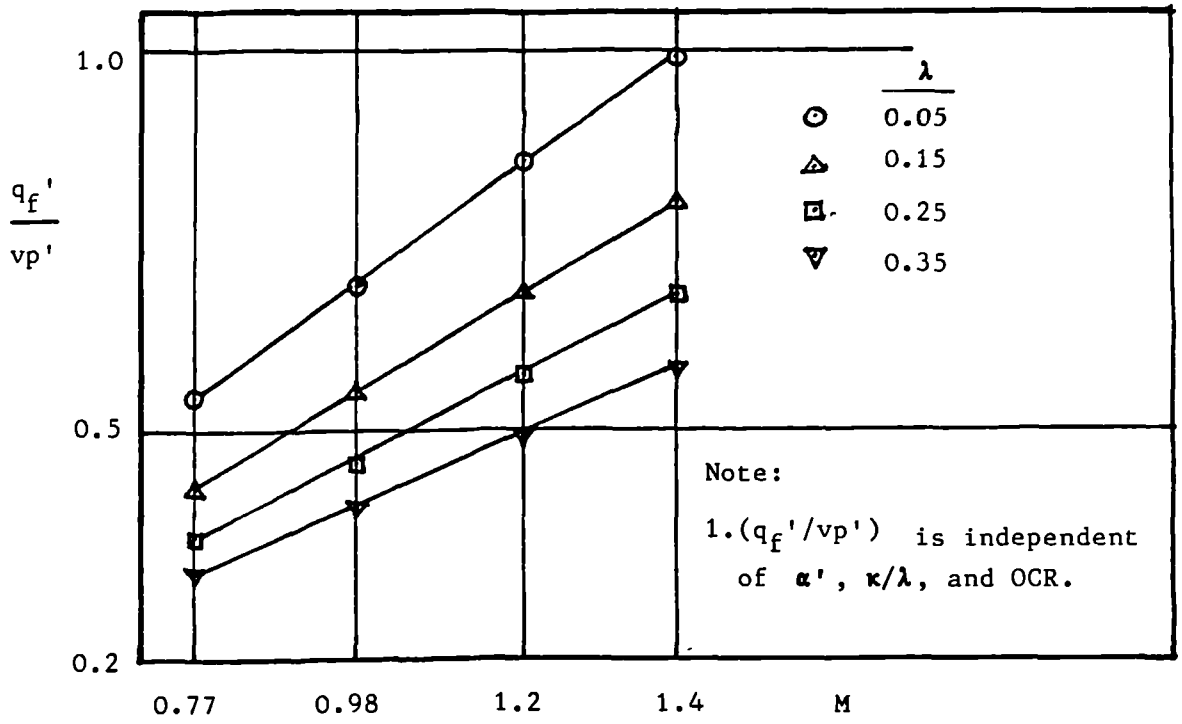

Figure 5.37(a) Variations of normalised ultimate deviator stress with M for fixed values of λ

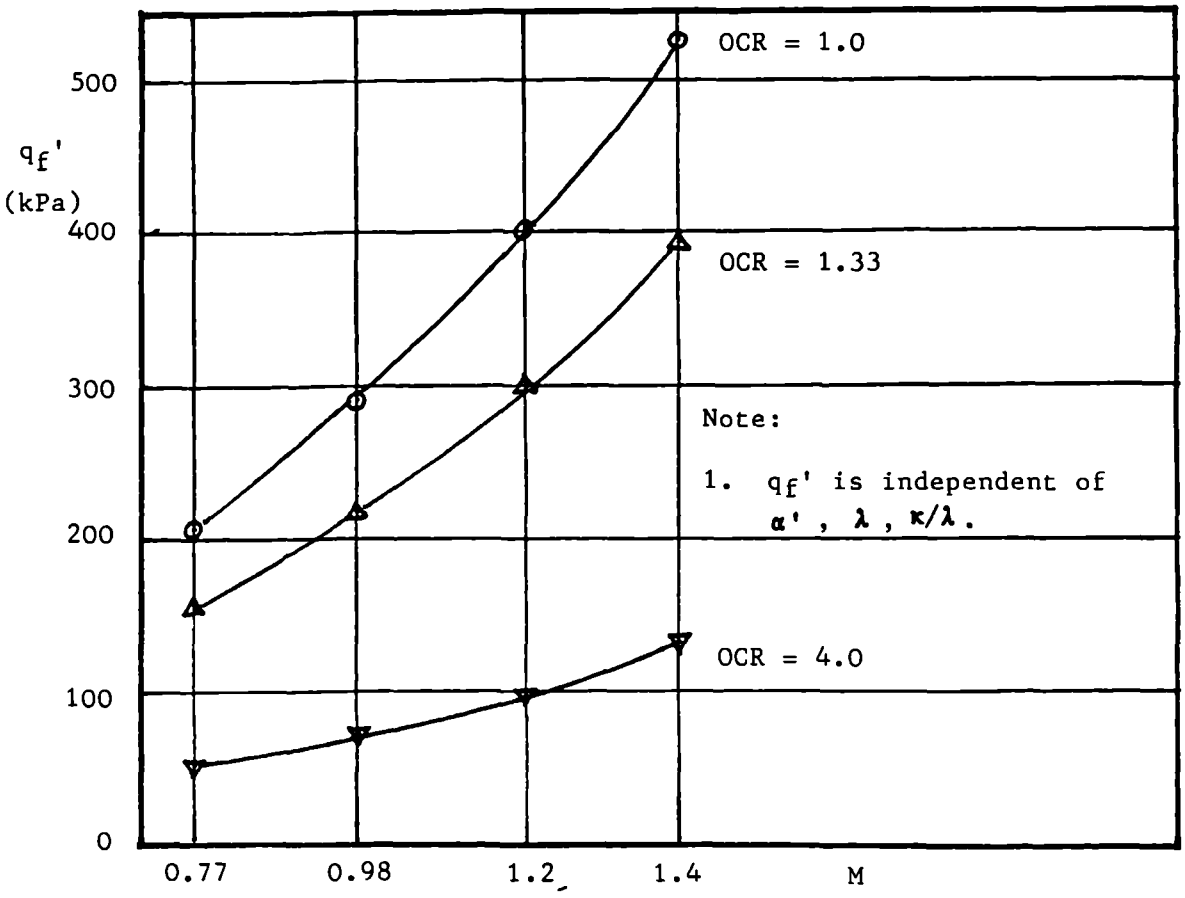

Figure 5.37(b) Variations of ultimate deviator stress with M for fixed values of OCR

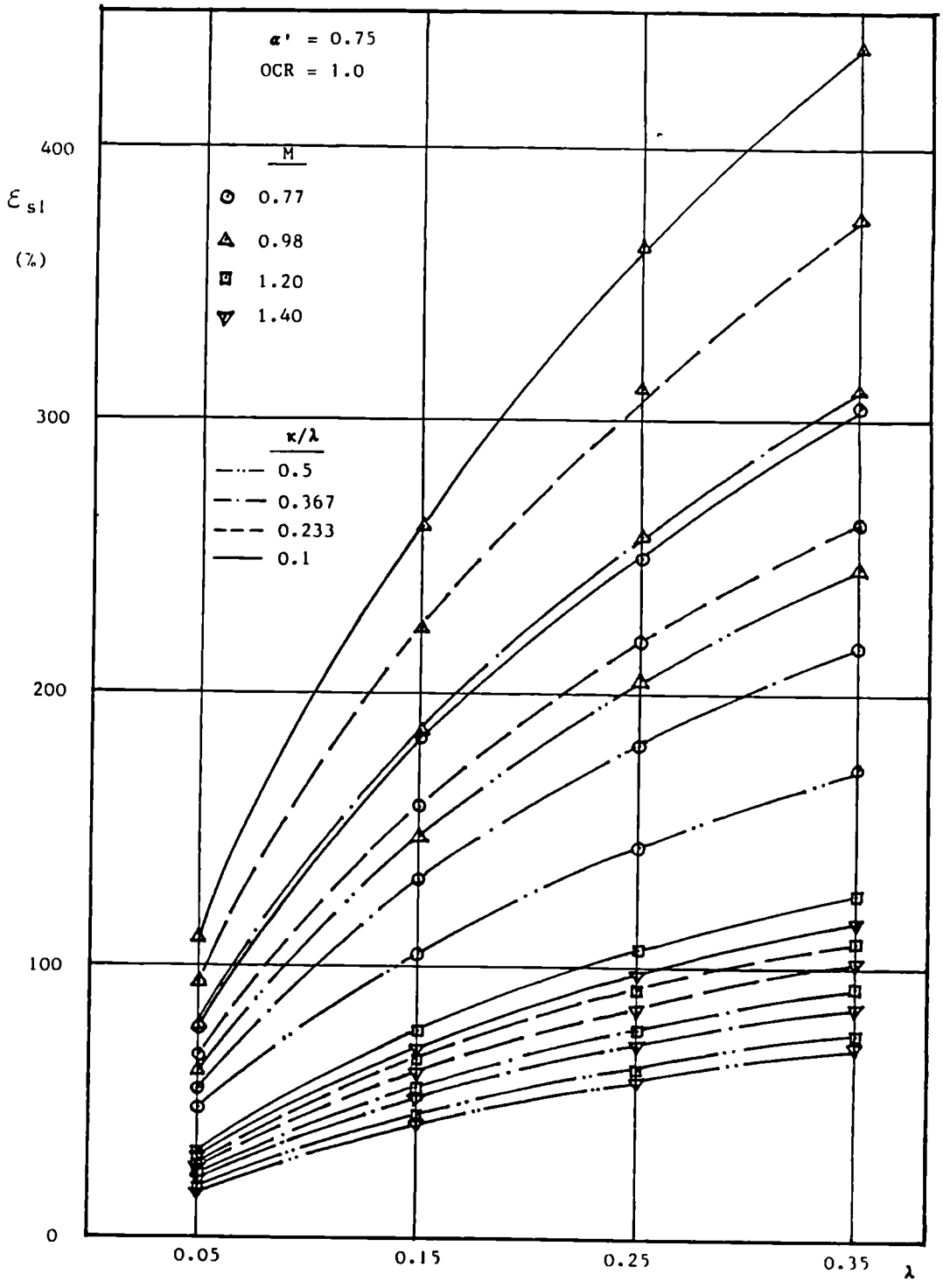

Figure 5.38 Variations of ultimate shear strain ε_{sf} with λ for fixed values of κ/λ and M

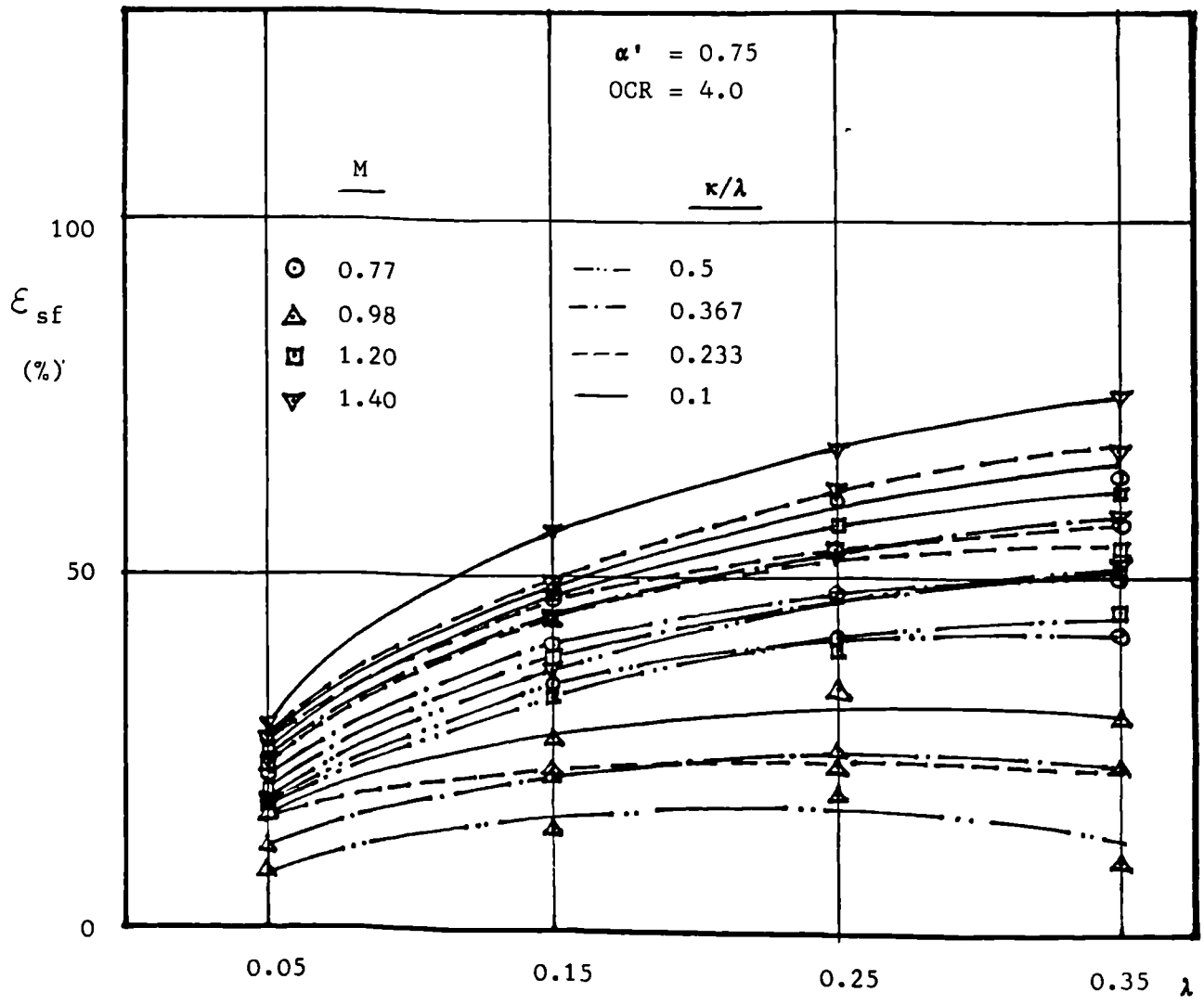

Figure 5.39 Variations of ultimate shear strain ε_{sf} with λ for fixed values of κ/λ and M

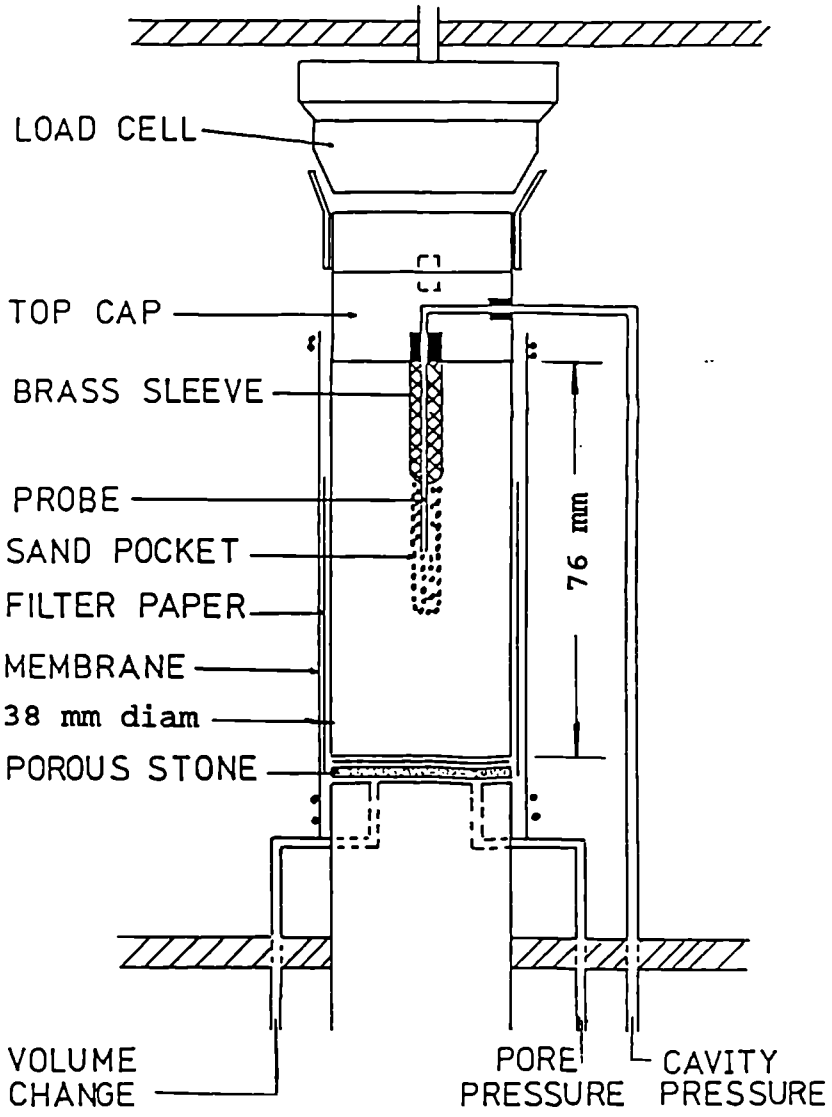

Figure 6.1 Laboratory sample set-up in hydraulic fracturing experiments (after Mhach, 1991)

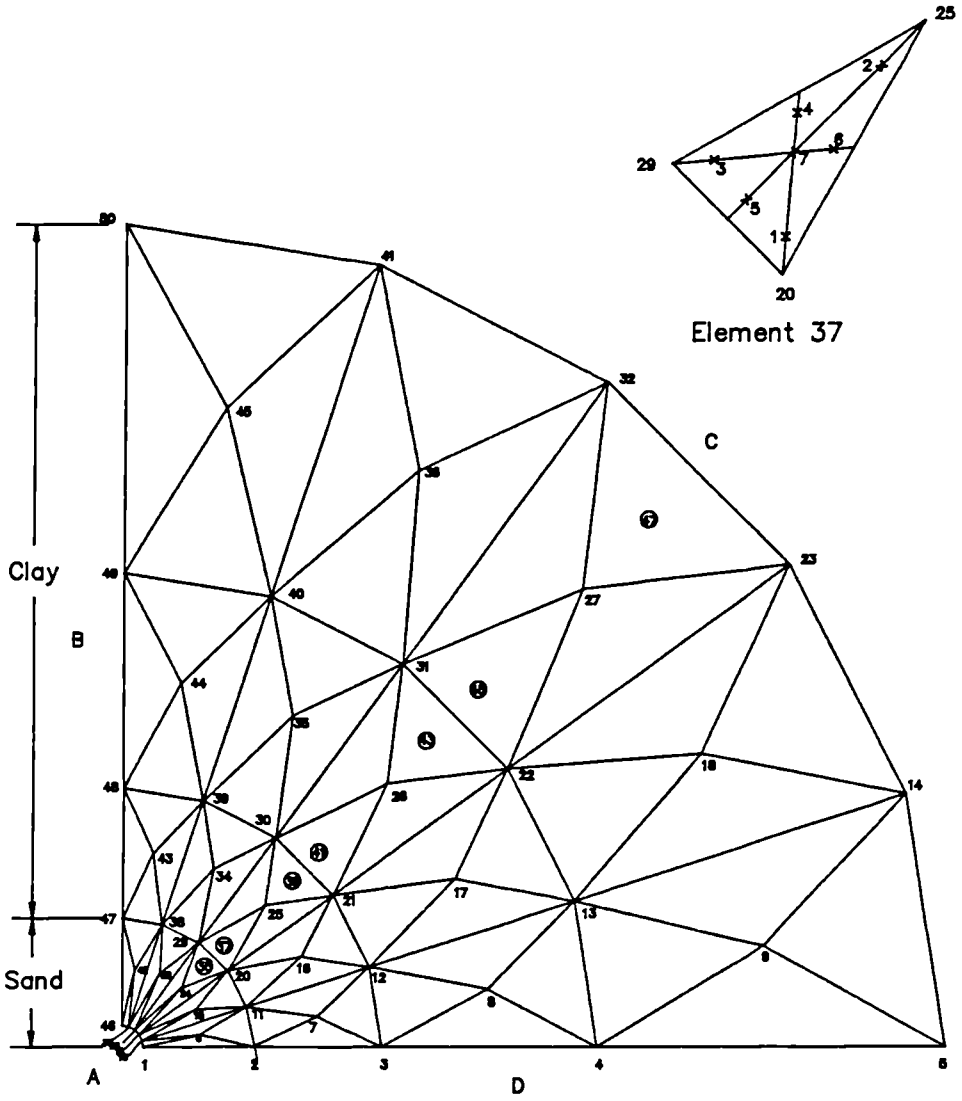

Figure 6.2(a) Finite element mesh HF005 – plane strain case (6 mm bore)

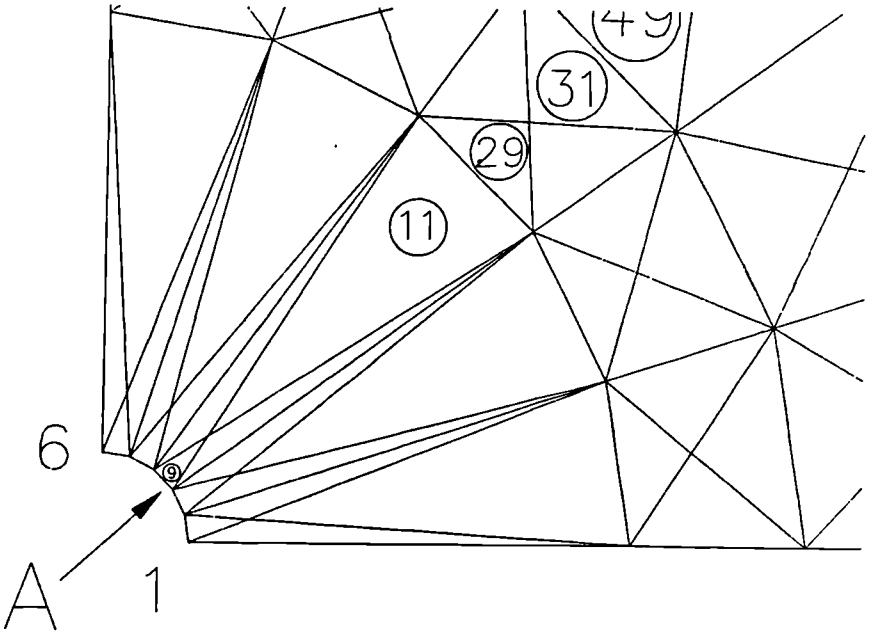

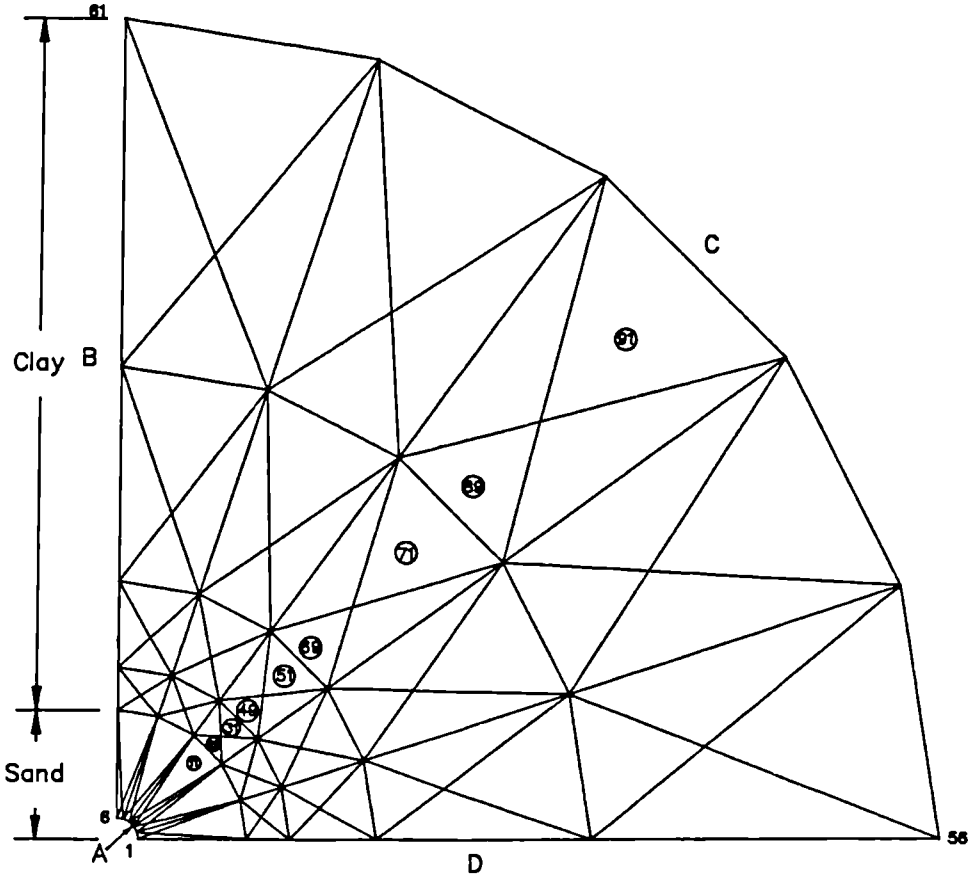

Figure 6.2(b) Finite element mesh HF105 – plane strain case (6 mm bore)

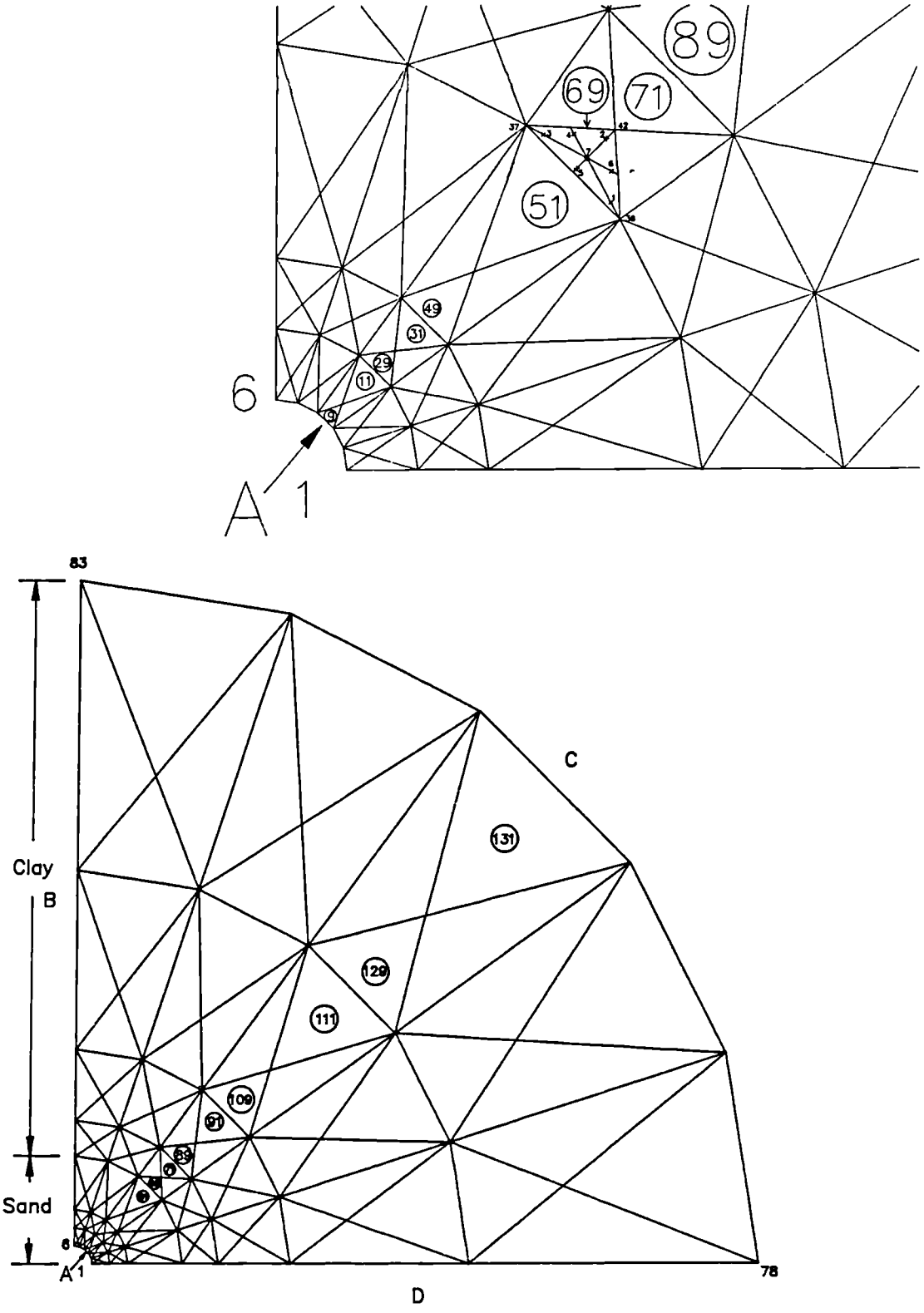

Figure 6.2(c) Finite element mesh HF205 – plane strain case (6 mm bore)

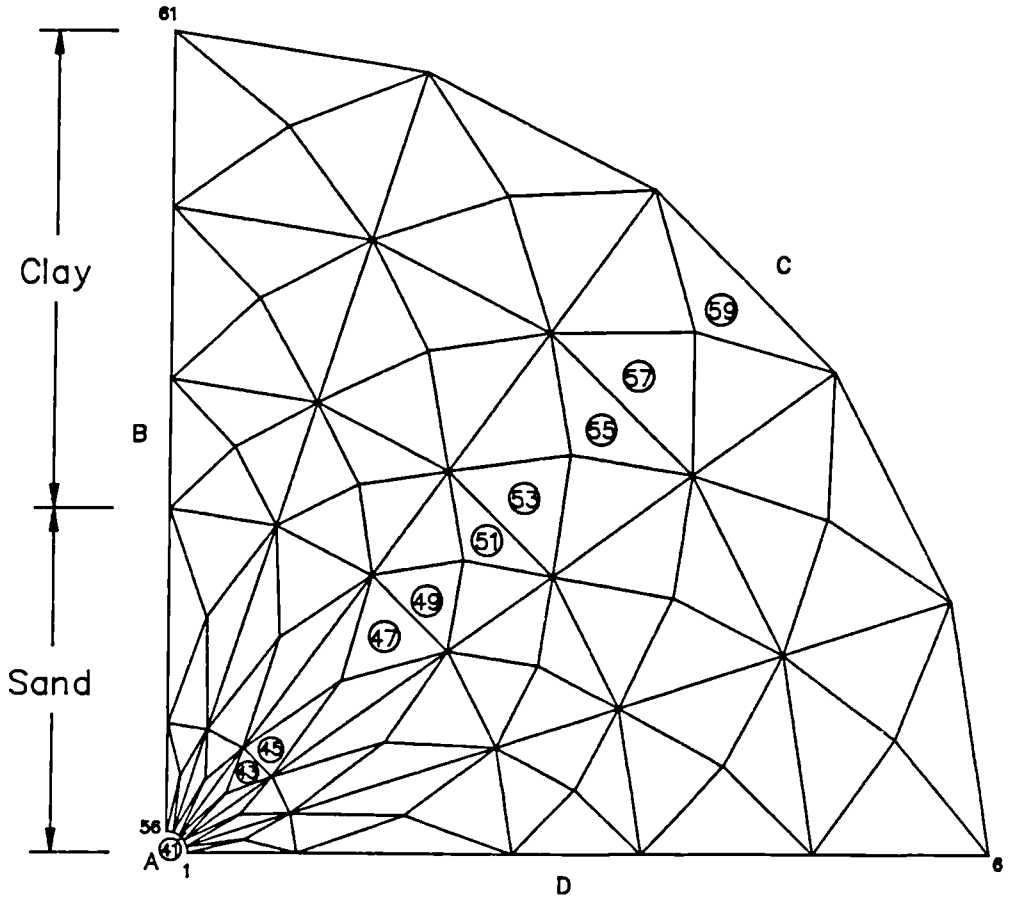

Figure 6.2(d) Finite element mesh HF211 – plane strain case (16 mm bore)

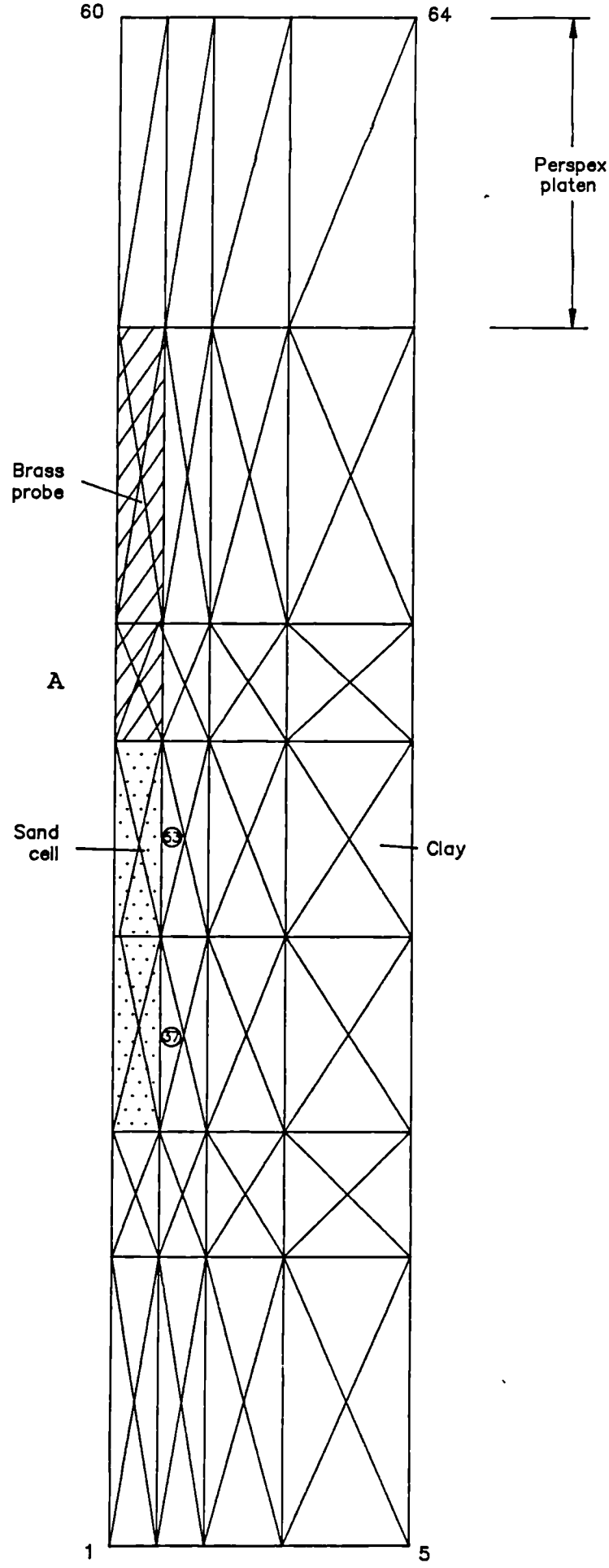

Figure 6.3(a) Finite element mesh HF100 – axisymmetric case (6 mm bore)

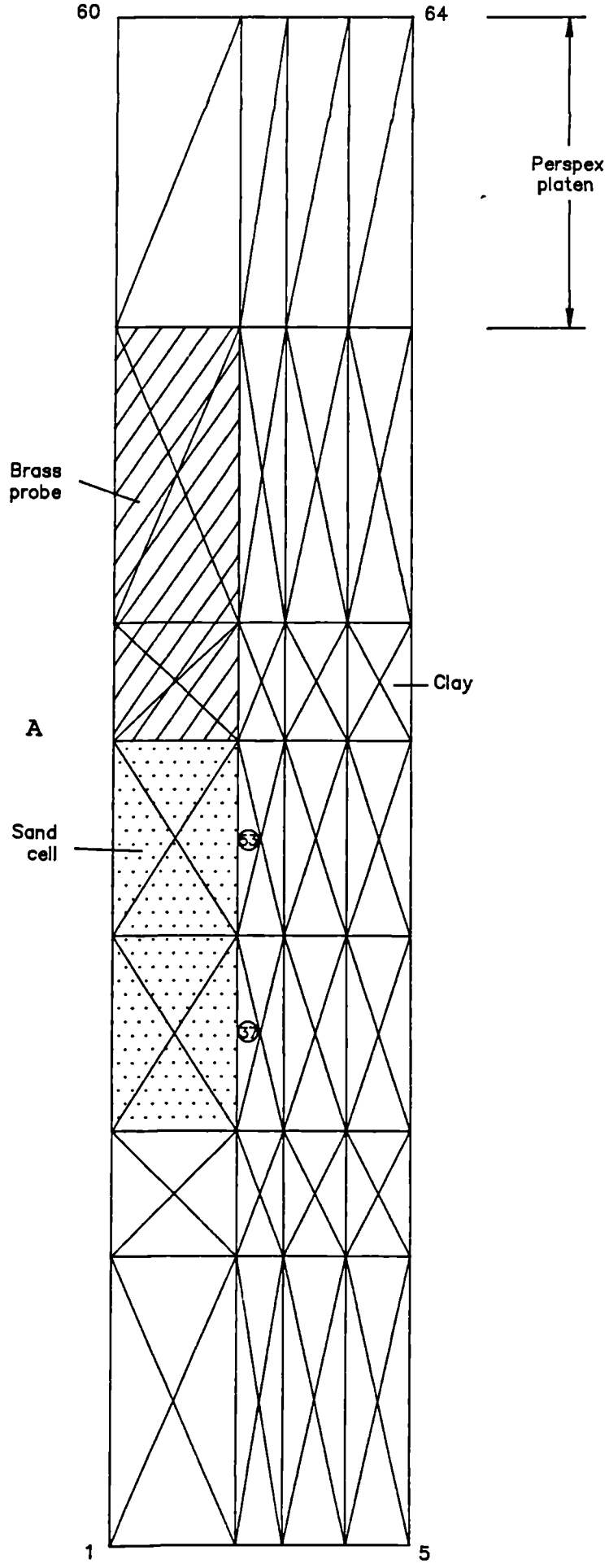

Figure 6.3(b) Finite element mesh HF 101 – axisymmetric case (16 mm bore)

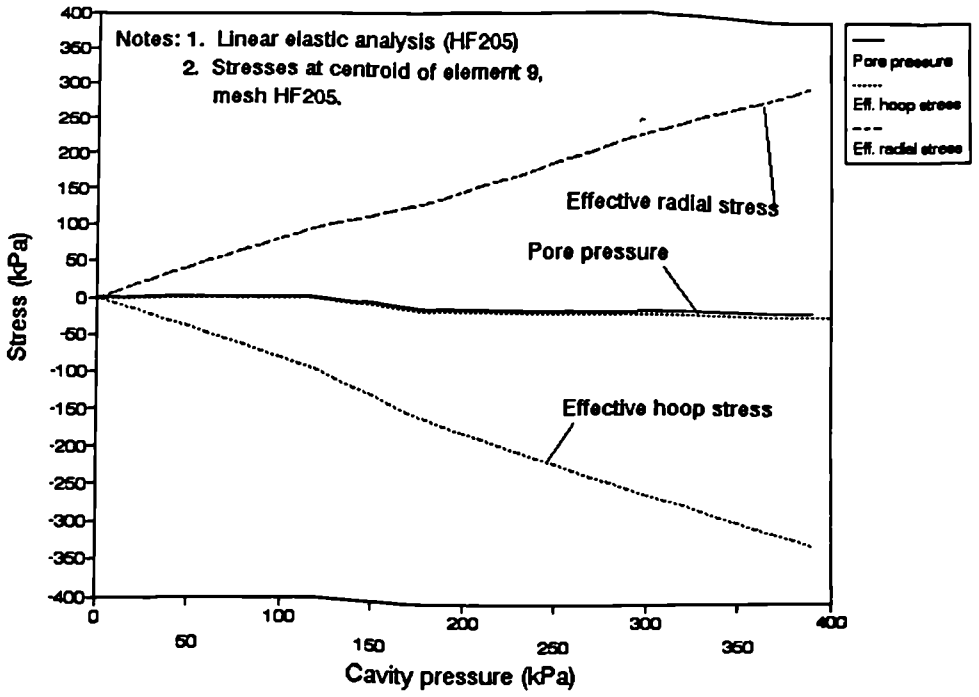

Figure 6.4 Variations of internal stresses at the centroid of element 9 with cavity pressure increase in undrained elastic analysis

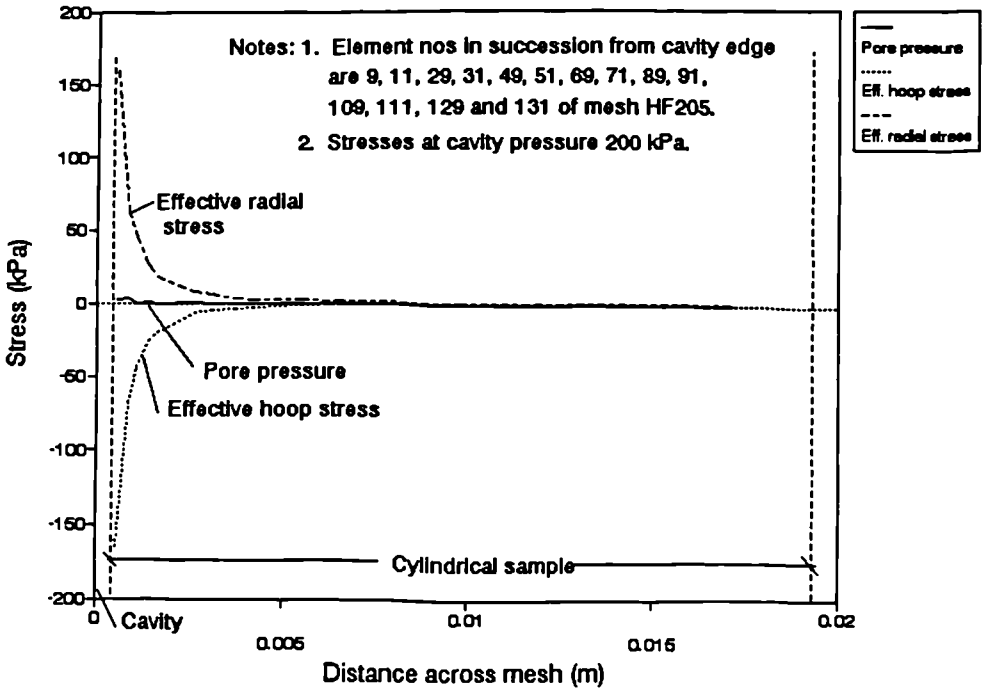

Figure 6.5 Distribution of effective radial and hoop stresses and pore pressures at centroids across the mesh

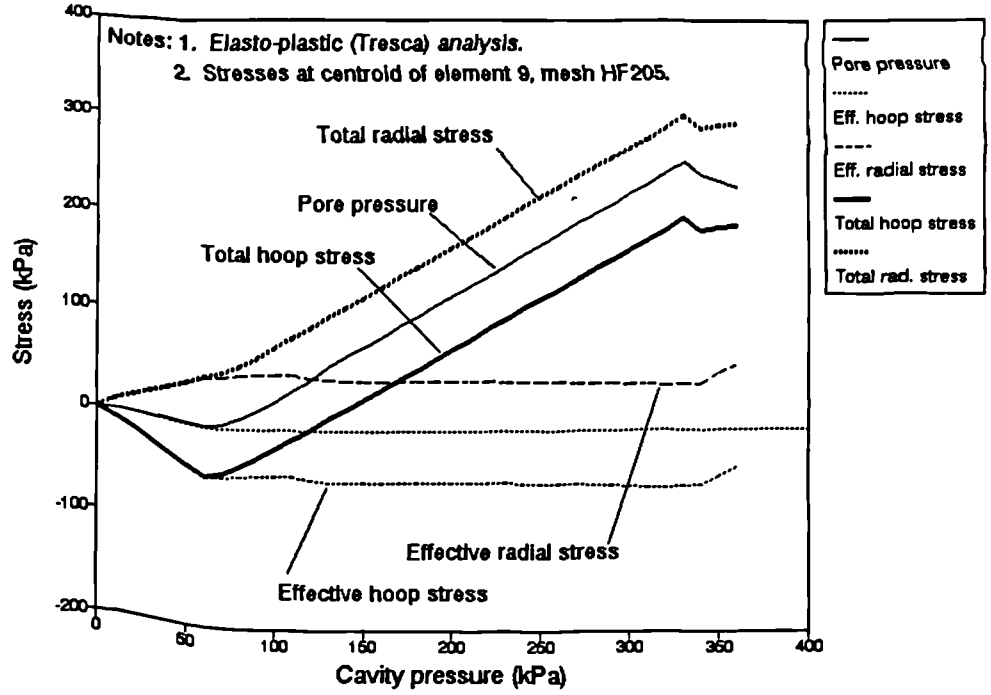

Figure 6.6 Variations of internal stresses at the centroid of element 9 with cavity pressure increase in undrained elasto-plastic analysis

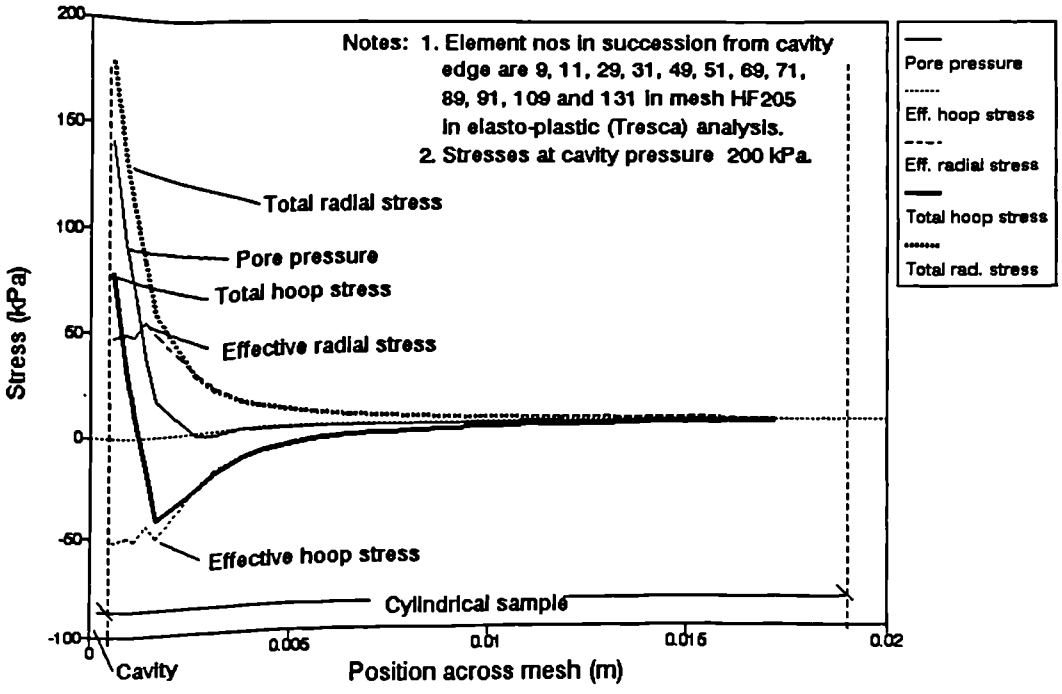

Figure 6.7 Distribution of total and effective radial and hoop stresses and pore pressures at centroids across the mesh

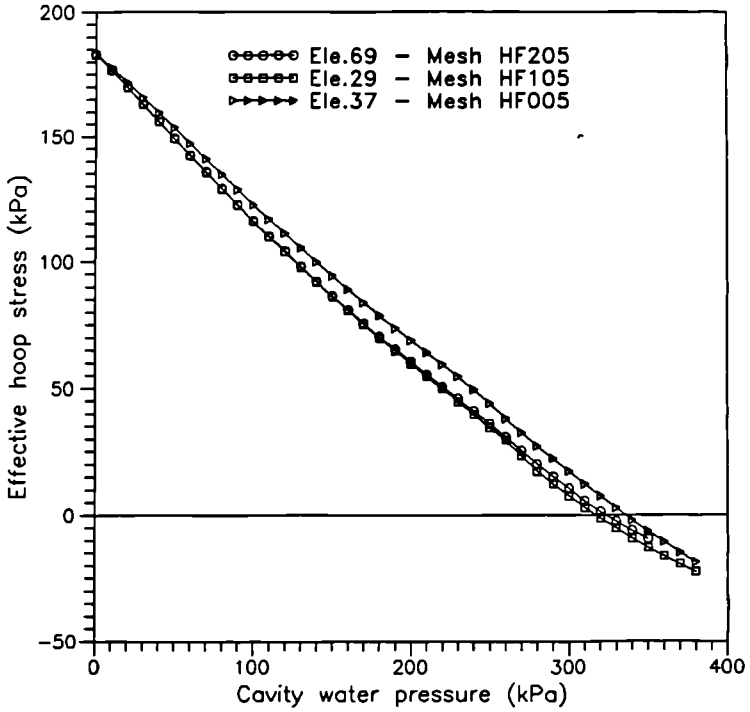

Figure 6.8 Variations of effective hoop stress with cavity water pressure at element centroids for Meshes HF205, HF105 and HF005 (Case D1)

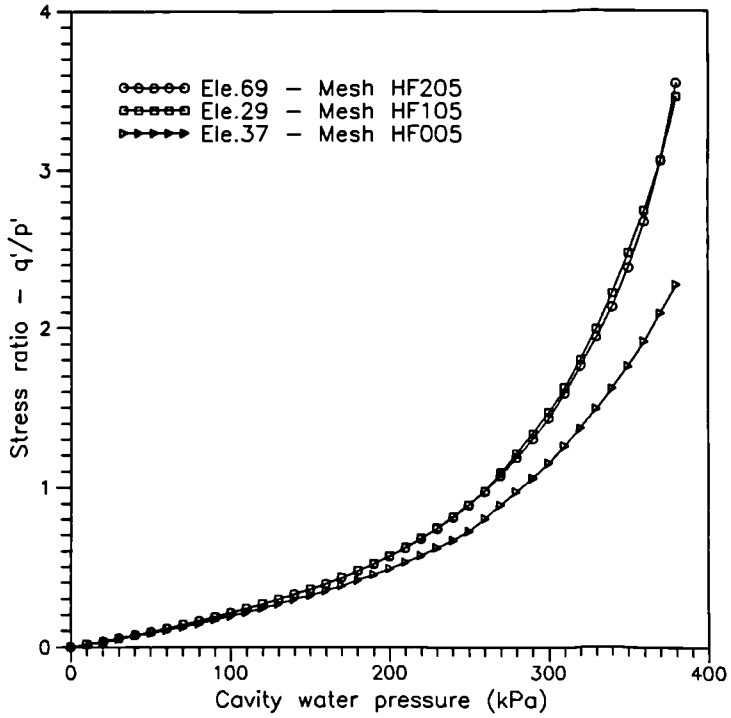

Figure 6.9 Variations of stress ratio q'/p' with cavity water pressure at element centroids for Meshes HF205, HF105 and HF005 (Case D1)

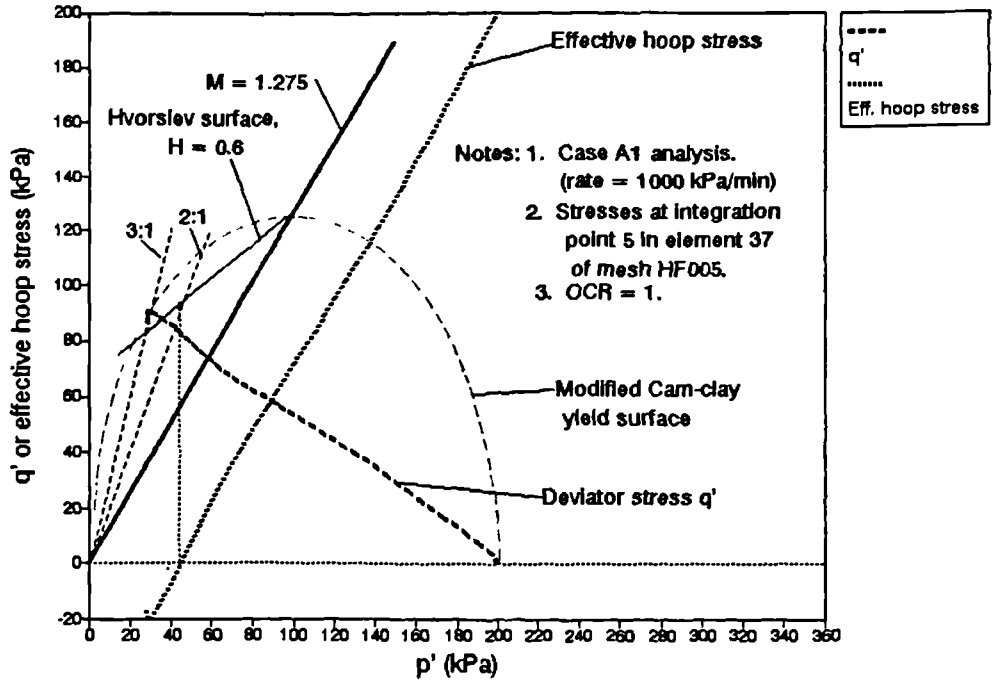

Figure 6.10 Variations of effective hoop stress in p':q' space at integration point 5 in element 37 of mesh HF005

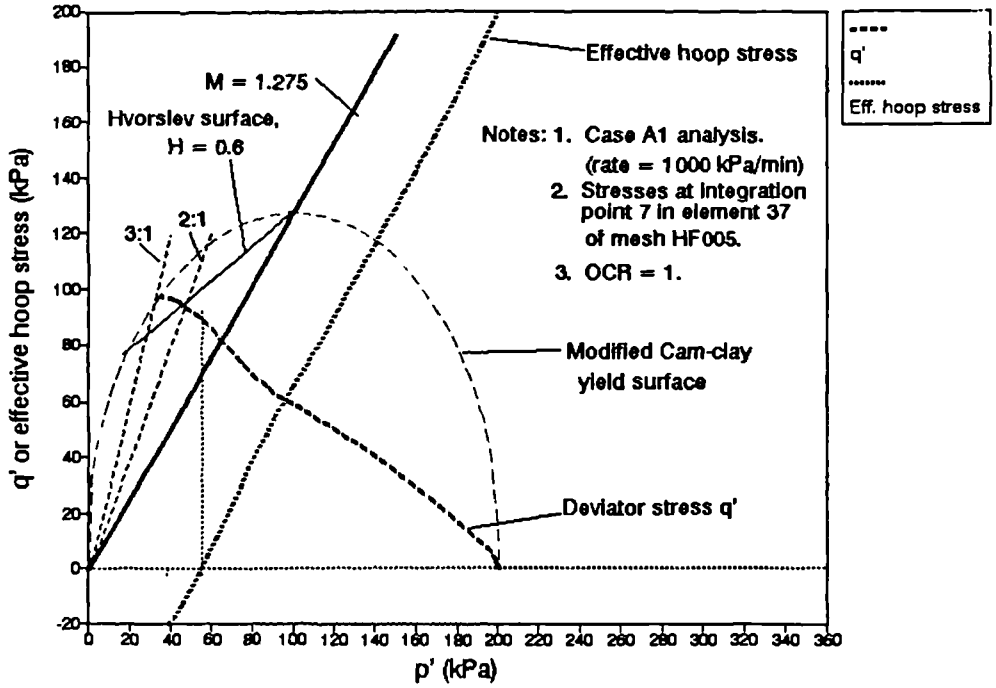

Figure 6.11 Variations of effective hoop stress in p':q' space at integration point 7 in element 37 of mesh HF005

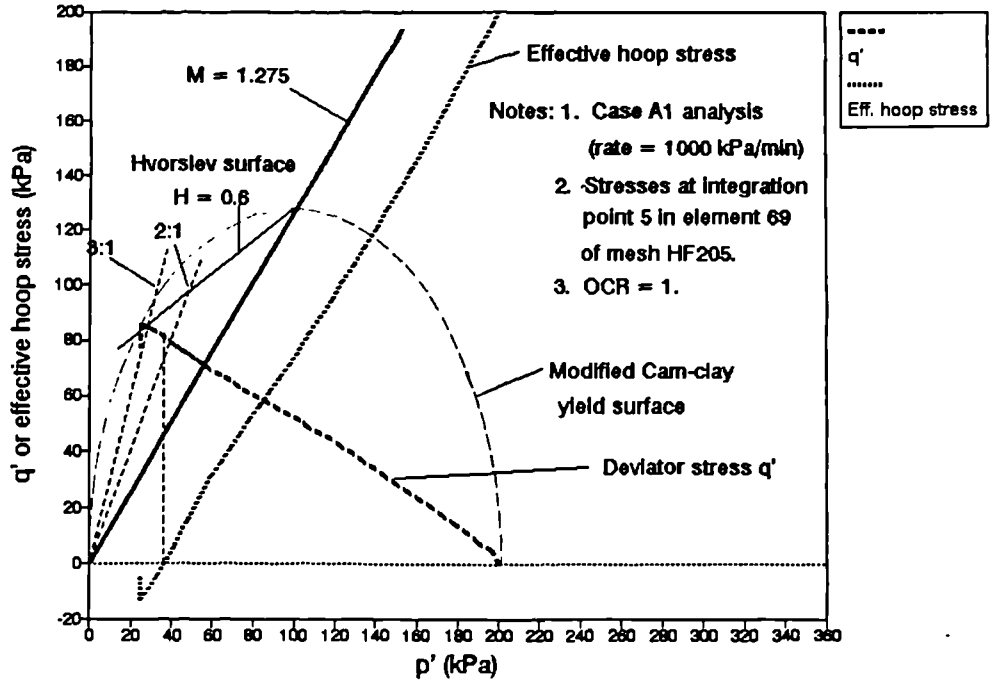

Figure 6.12 Variations of effective hoop stress in p':q' space at integration point 5 in element 69 of mesh HF205

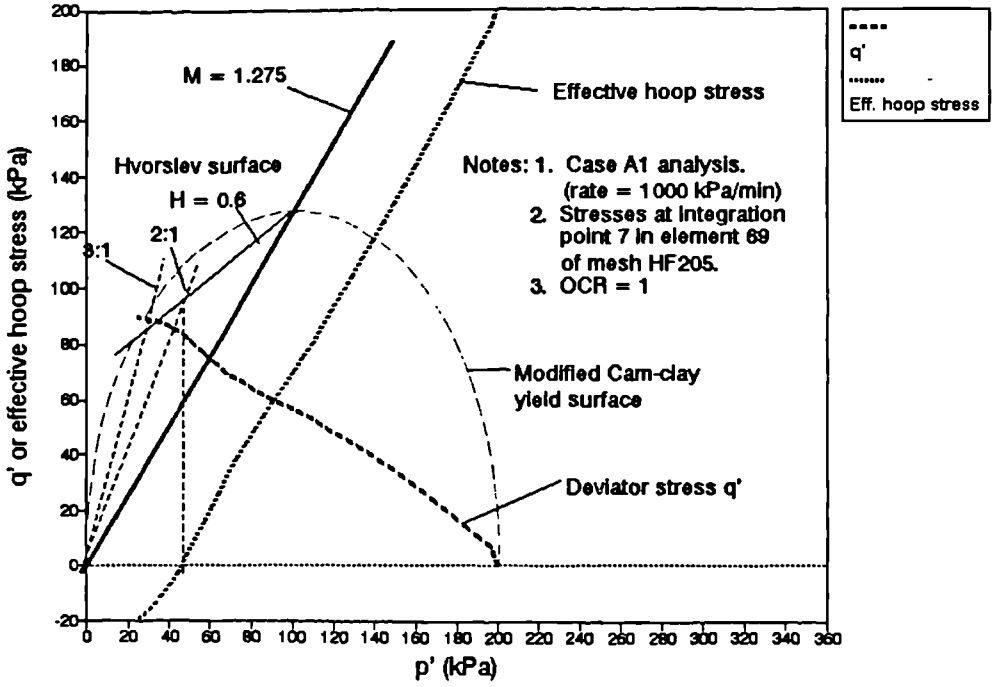

Figure 6.13 Variations of effective hoop stress in p':q' space at integration point 7 in element 69 of mesh HF205

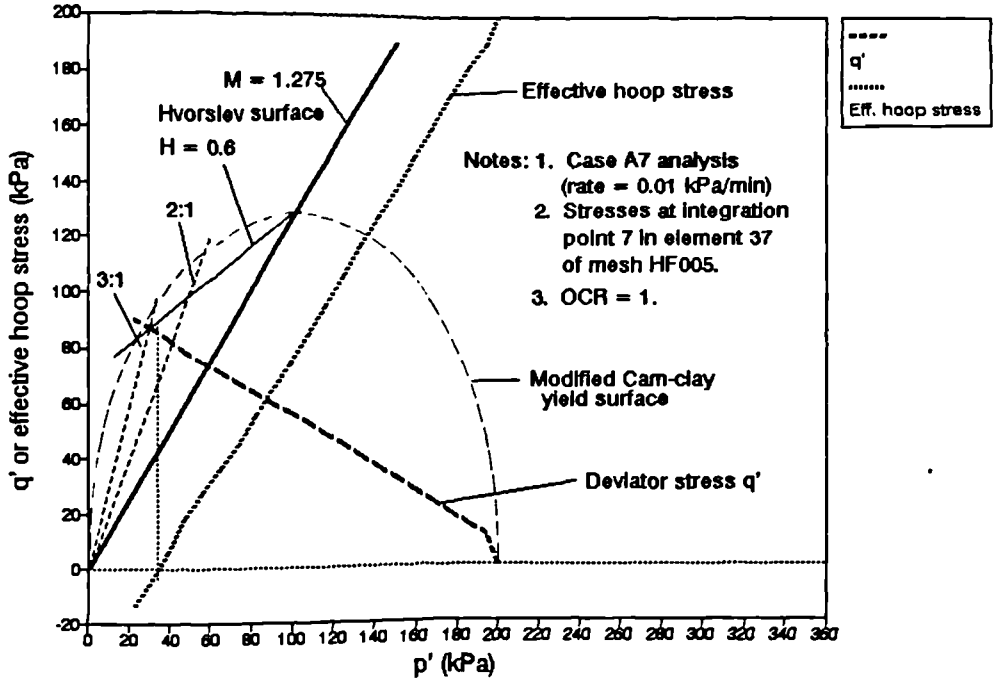

Figure 6.14 Variations of effective hoop stress in p':q' space at integration point 7 in element 37 of mesh HF005

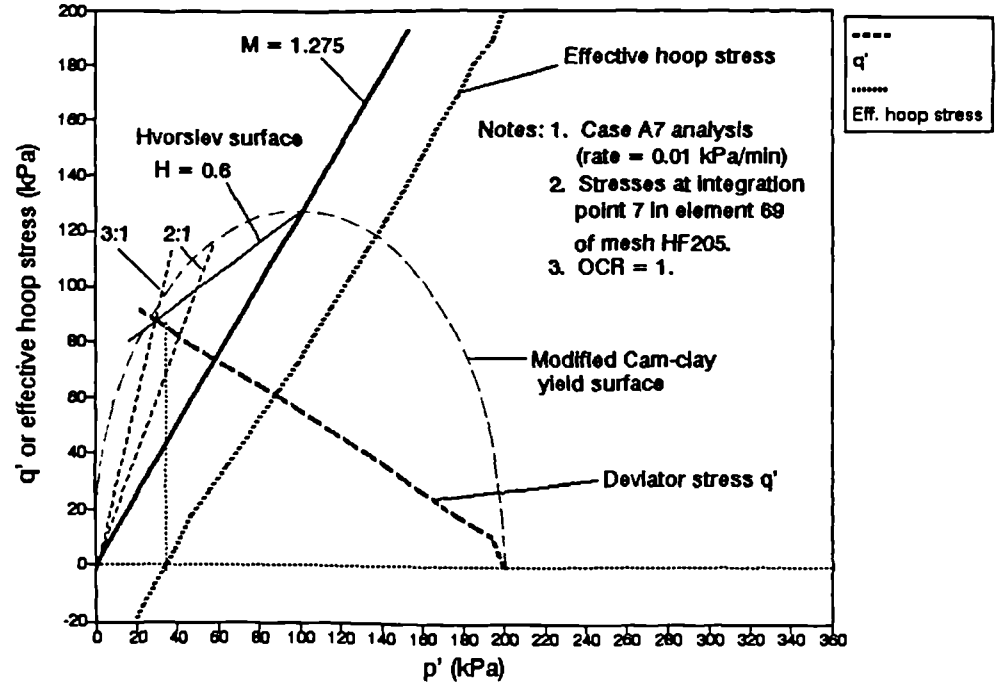

Figure 6.15 Variations of effective hoop stress in p':q' space at integration point 7 in element 69 of mesh HF205

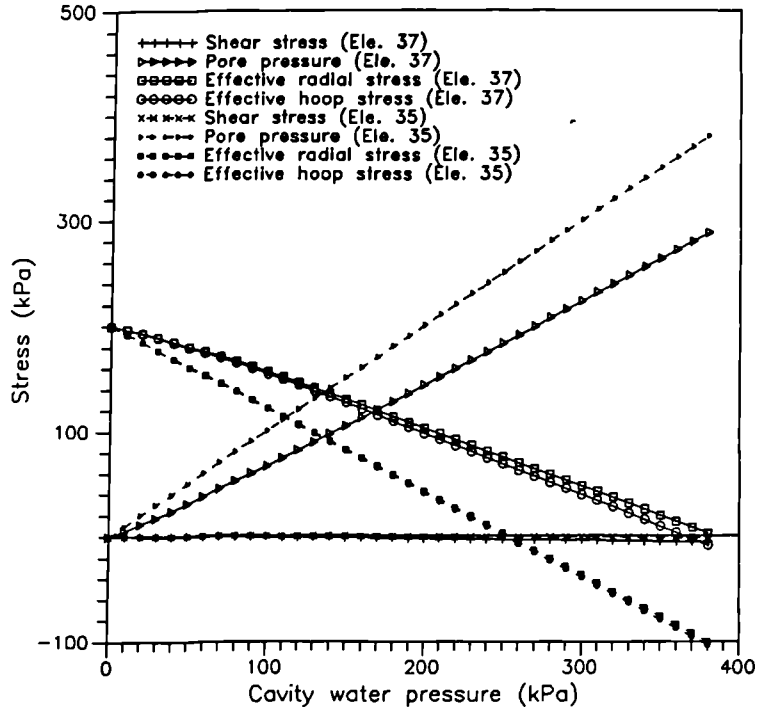

Figure 6.16 Variations of stresses at centroids of elements 37 (clay) and 35 (sand) with cavity water pressure increase for mesh HF005 – linear elastic analysis (Case A1)

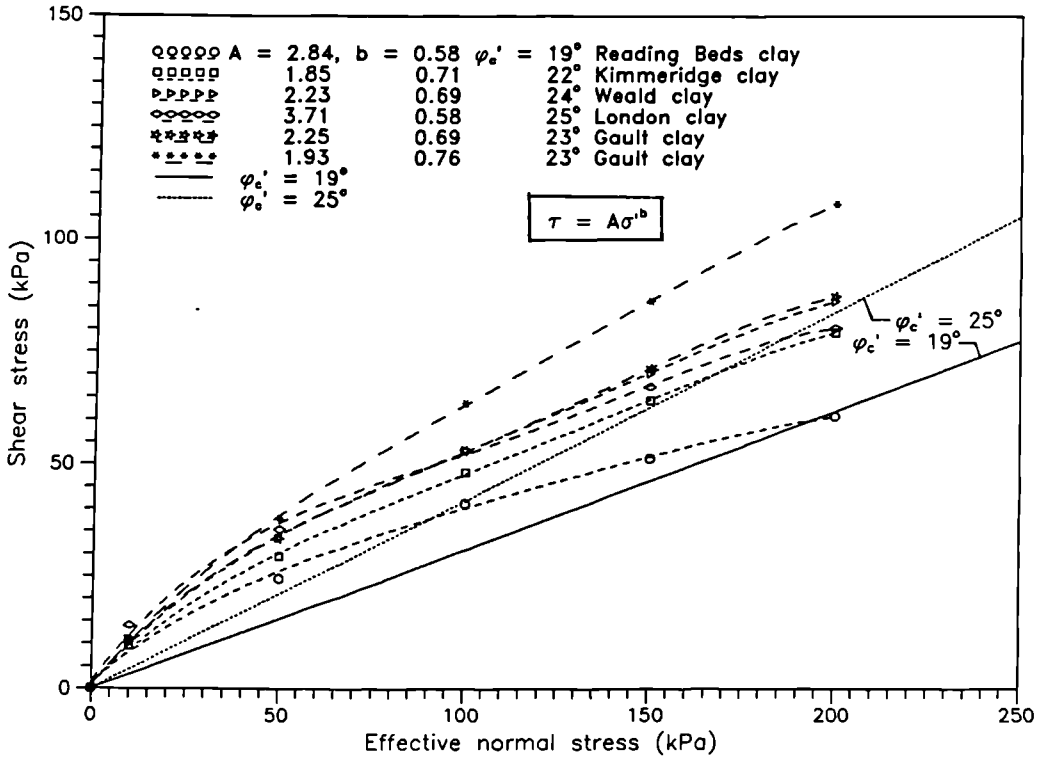

Figure 6.17 Derivation of the peak friction angles φ_p' for different types of clays based on the correlation in Atkinson and Crabb (1991)

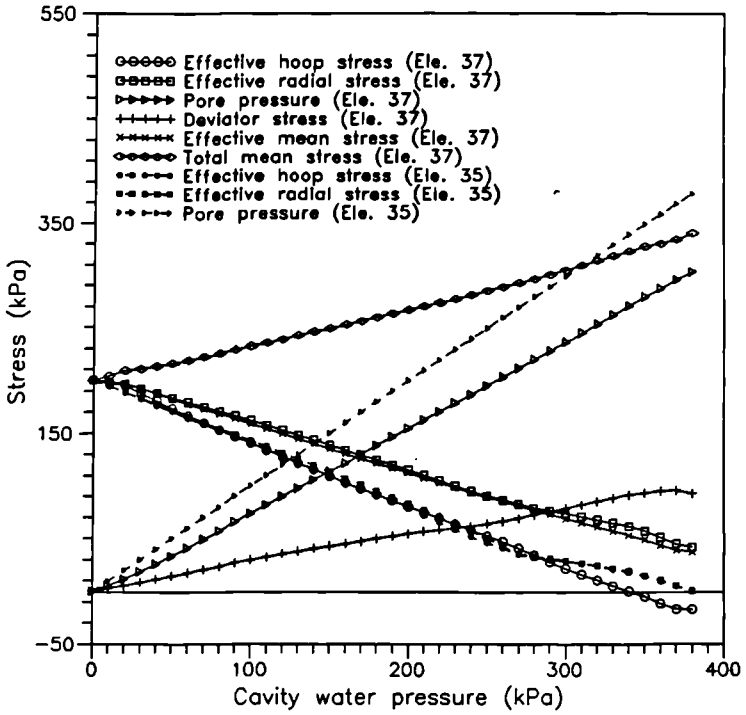

Figure 6.18 Variations of stresses at centroids of elements 37 (clay) and 35 (sand) with cavity water pressure increase – hydraulic fracturing analysis using modified Cam-clay (Case A1)

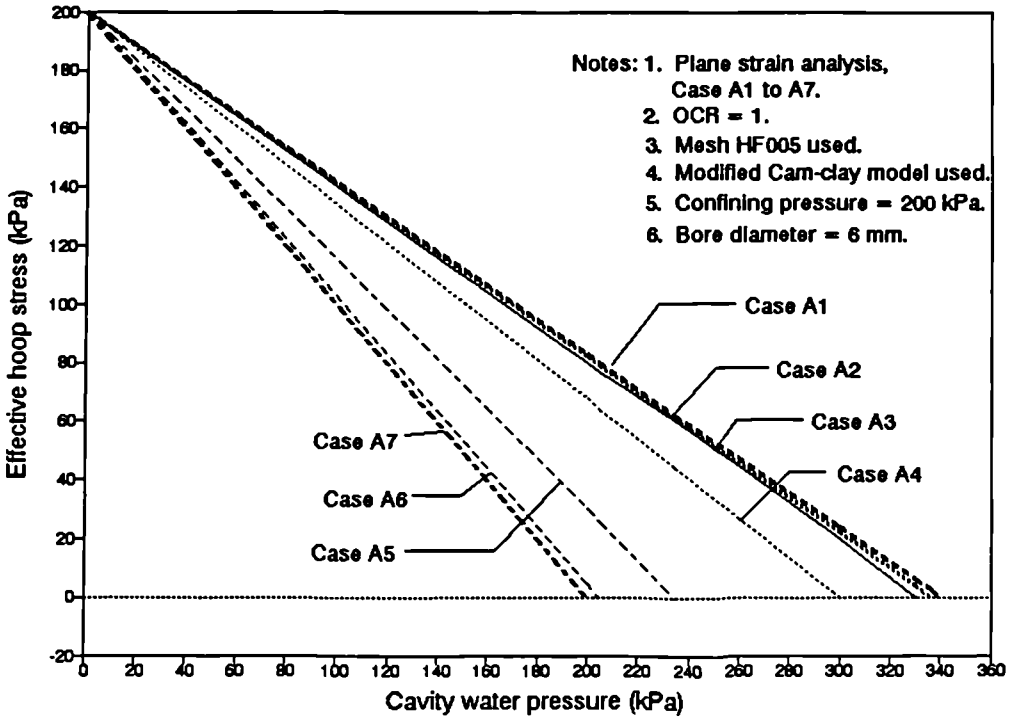

Figure 6.19 Variations of effective hoop stresses with cavity water pressure at the centroid in element 37 for confining pressure of 200 kPa - Case A1 to A7

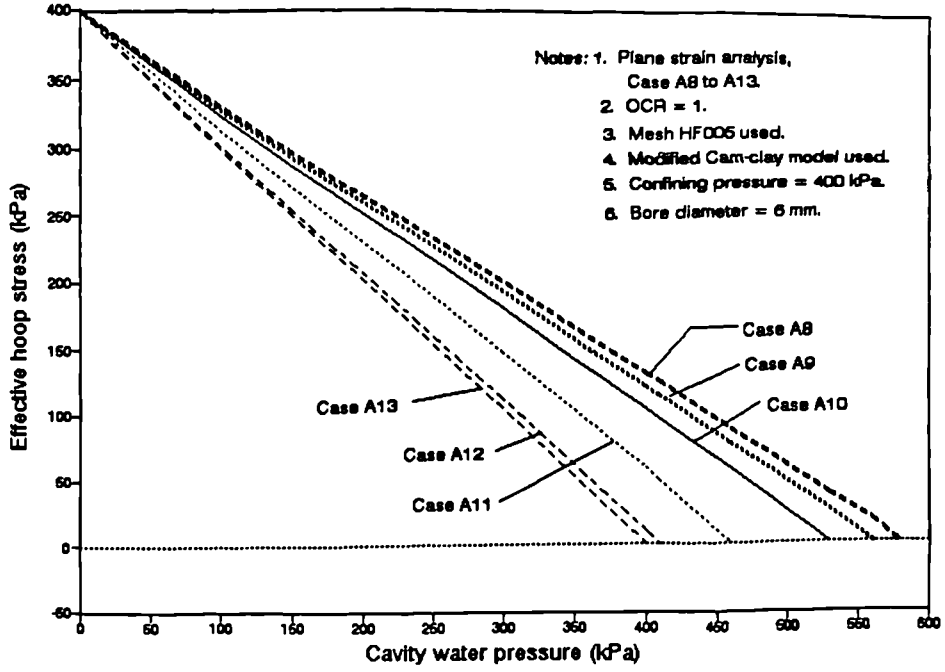

Figure 6.20 Variations of effective hoop stresses with cavity water pressure at the centroid in element 37 for confining pressure of 400 kPa - Case A8 to A13

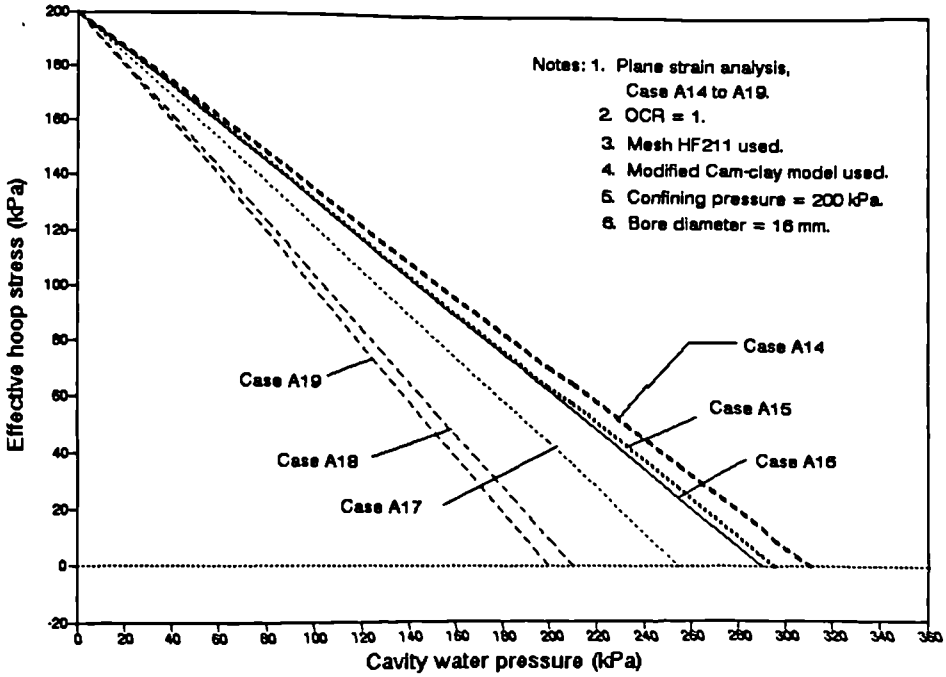

Figure 6.21 Variations of effective hoop stresses with cavity water pressure at the centroid in element 37 for confining pressure of 200 kPa - Case A14 to A19

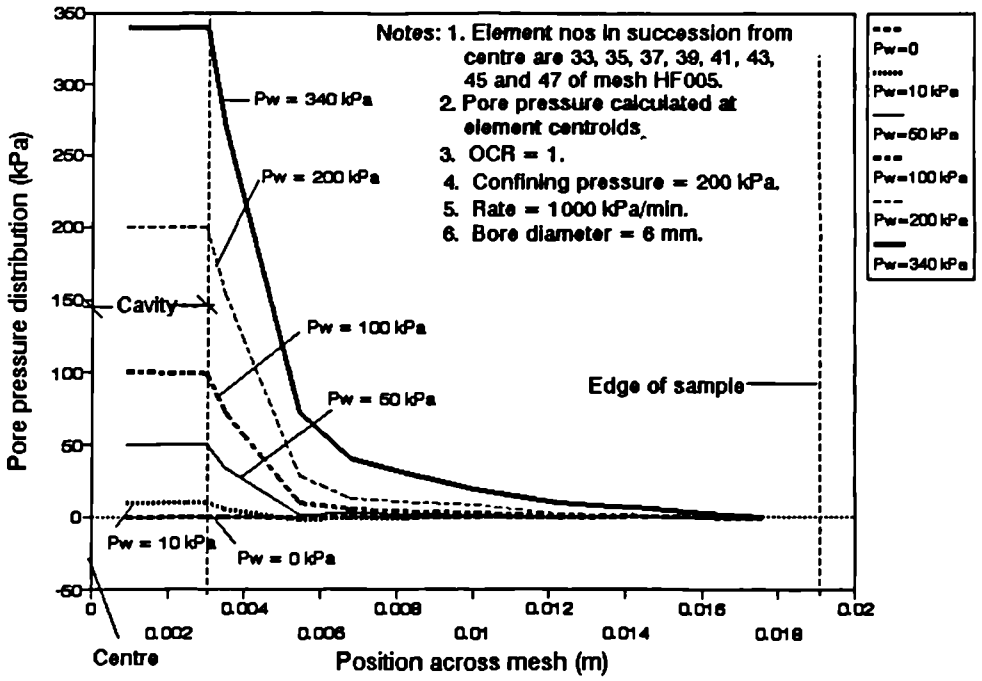

Figure 6.22 Variations of pore pressure across the mesh as the cavity water pressure Pw increases (Case A1)

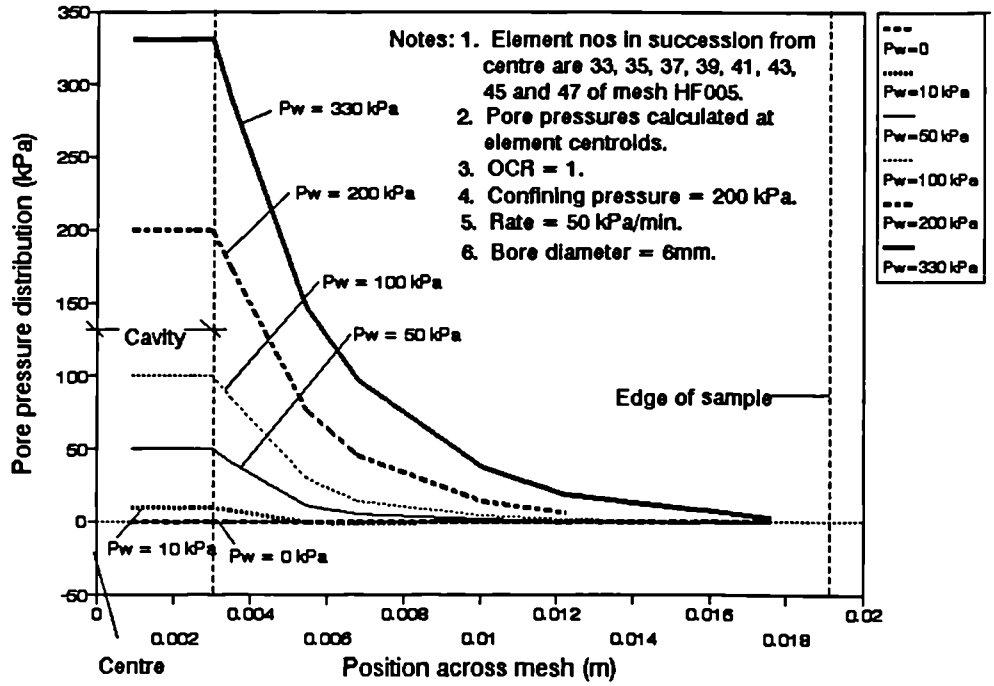

Figure 6.23 Variations of pore pressure across the mesh as the cavity water pressure Pw increases (Case A3)

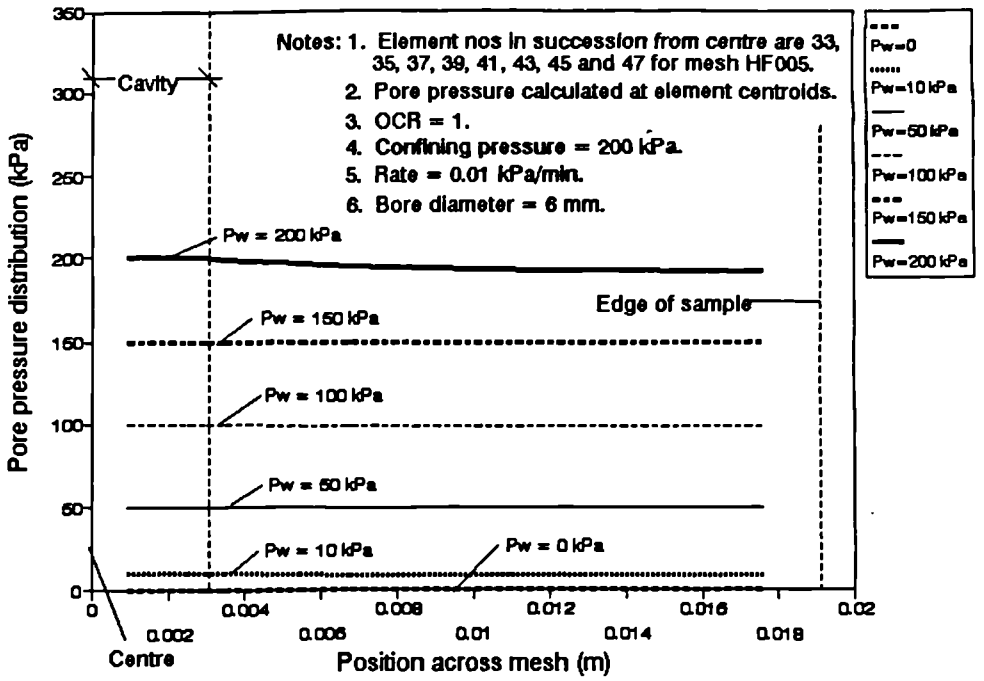

Figure 6.24 Variations of pore pressure across the mesh as the cavity water pressure Pw increases (Case A7)

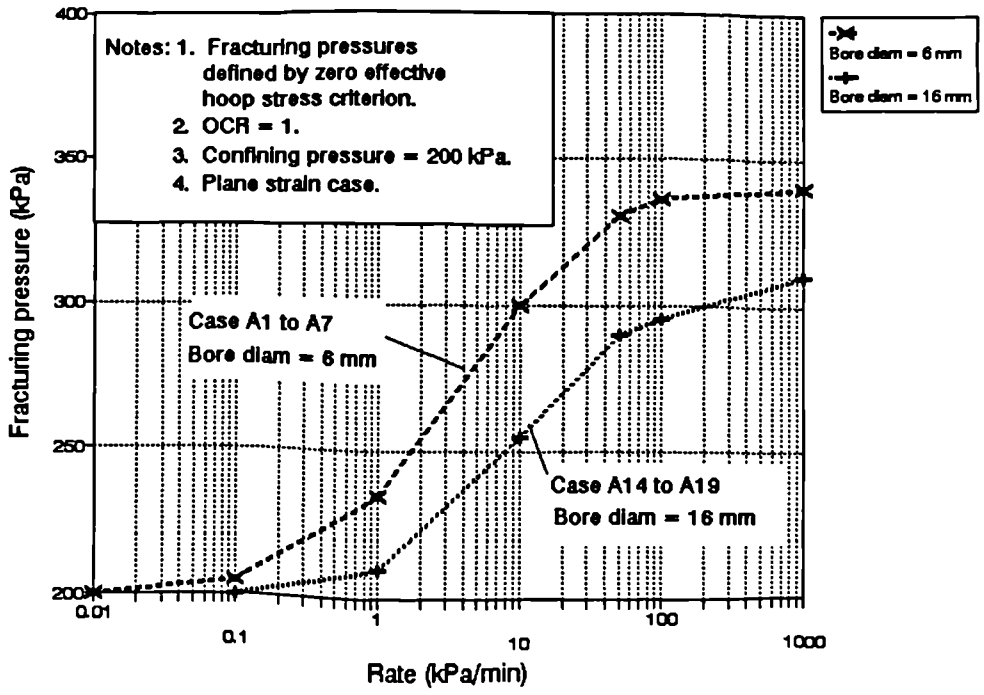

Figure 6.25 Variations of fracturing pressure with rates of cavity water pressure increase (Case A1 to A7 and A14 to A19)

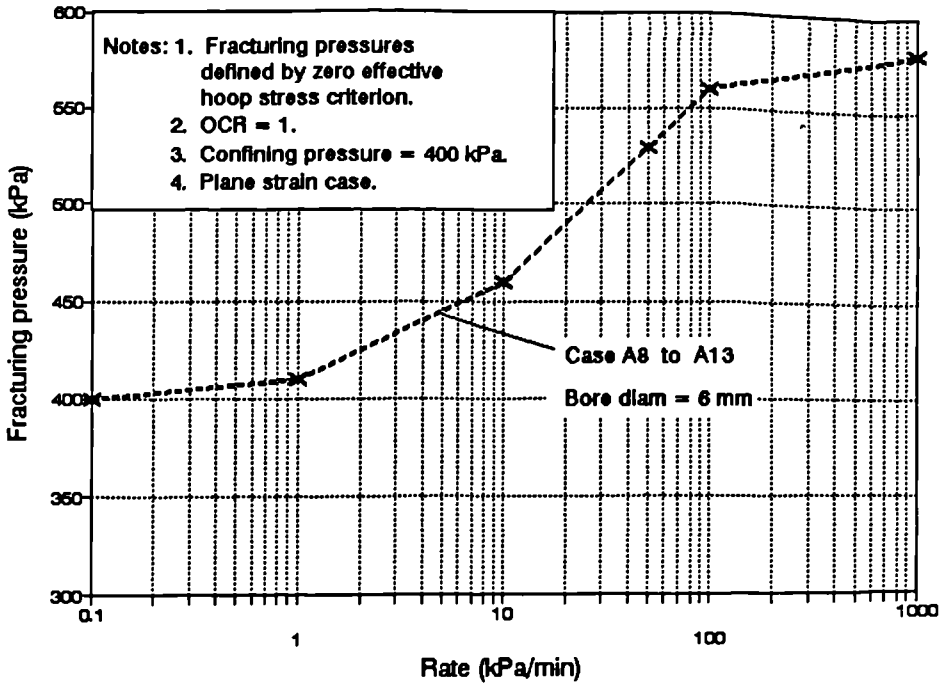

Figure 6.26 Variations of fracturing pressure with rates of cavity water pressure increase (Case A8 to A13)

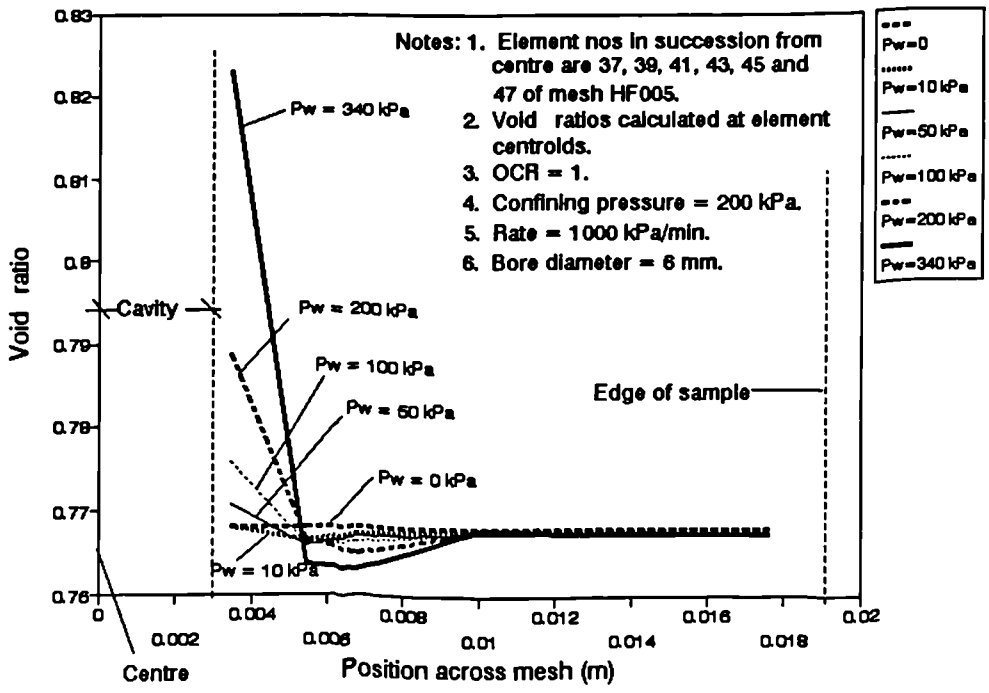

Figure 6.27 Variations of void ratio across the mesh as the cavity water pressure Pw increases (Case A1)

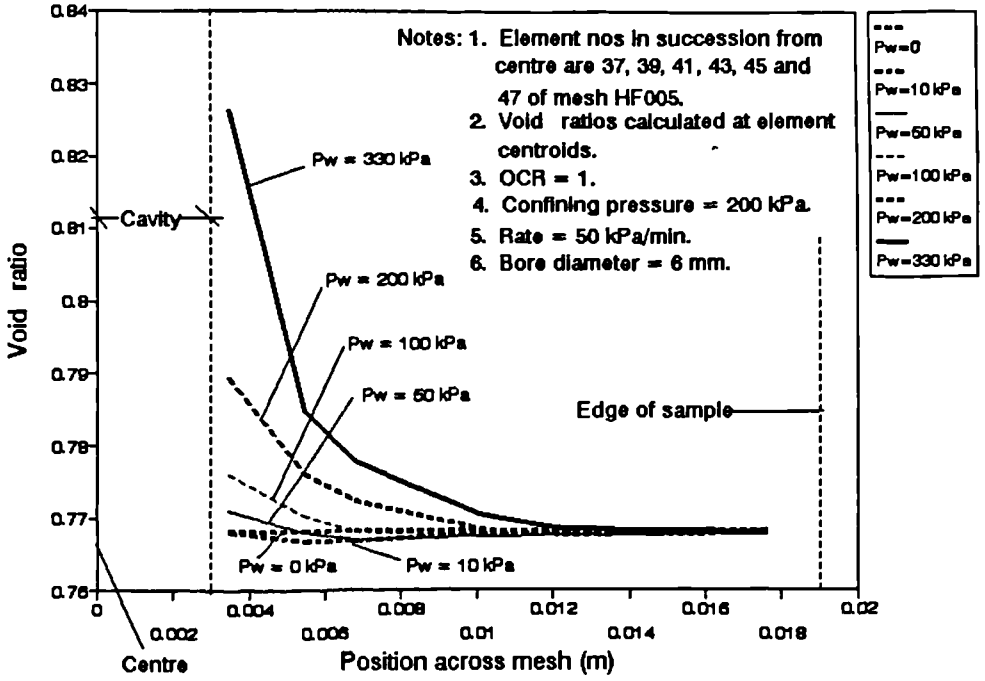

Figure 6.28 Variations of void ratio across the mesh as the cavity water pressure Pw increases (Case A3)

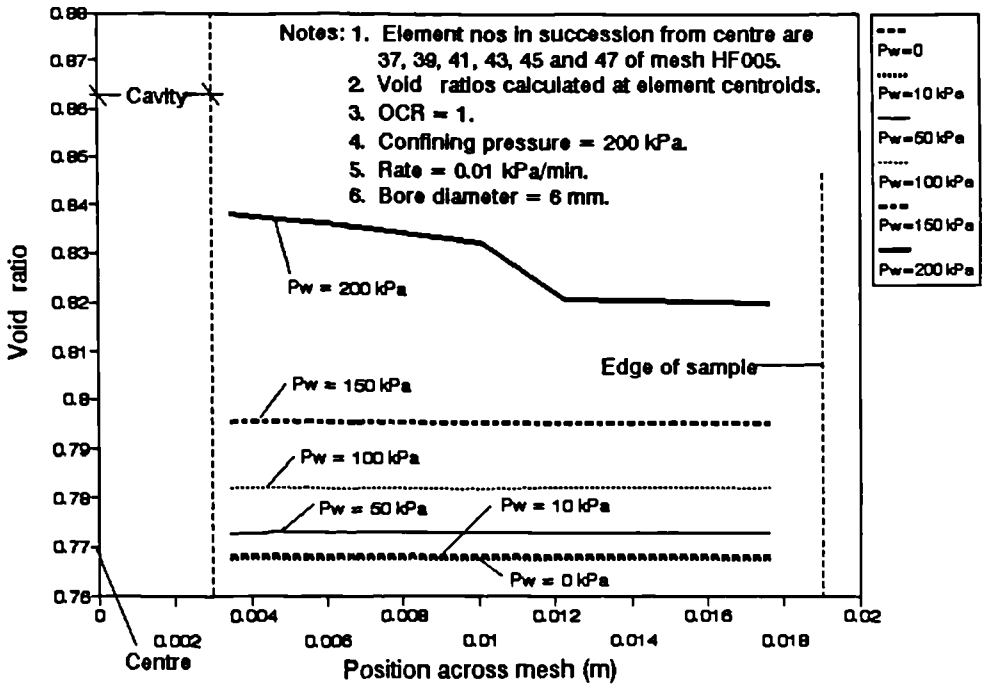

Figure 6.29 Variations of void ratio across the mesh as the cavity water pressure Pw increases (Case A7)

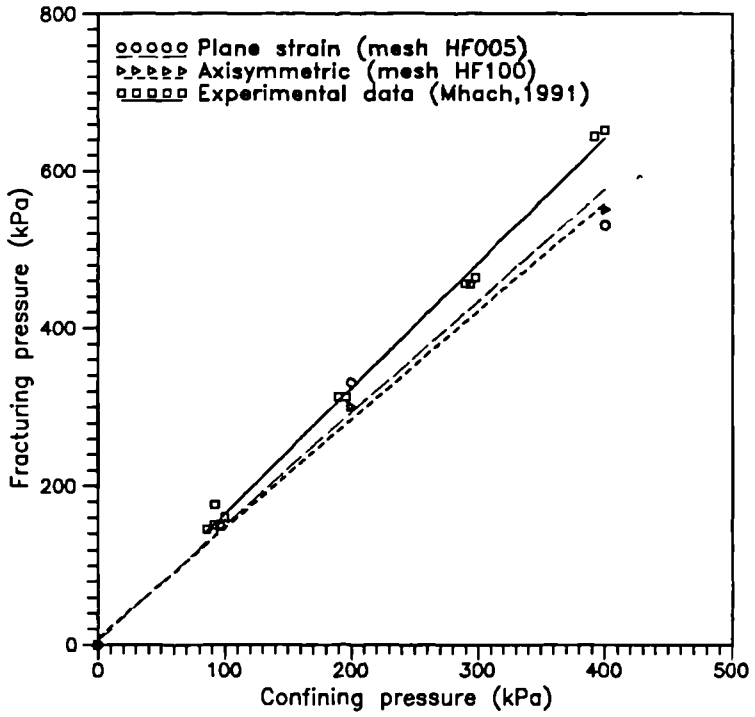

Figure 6.30 Variations of fracturing pressures with confining pressures (Plane strain and axisymmetric cases)

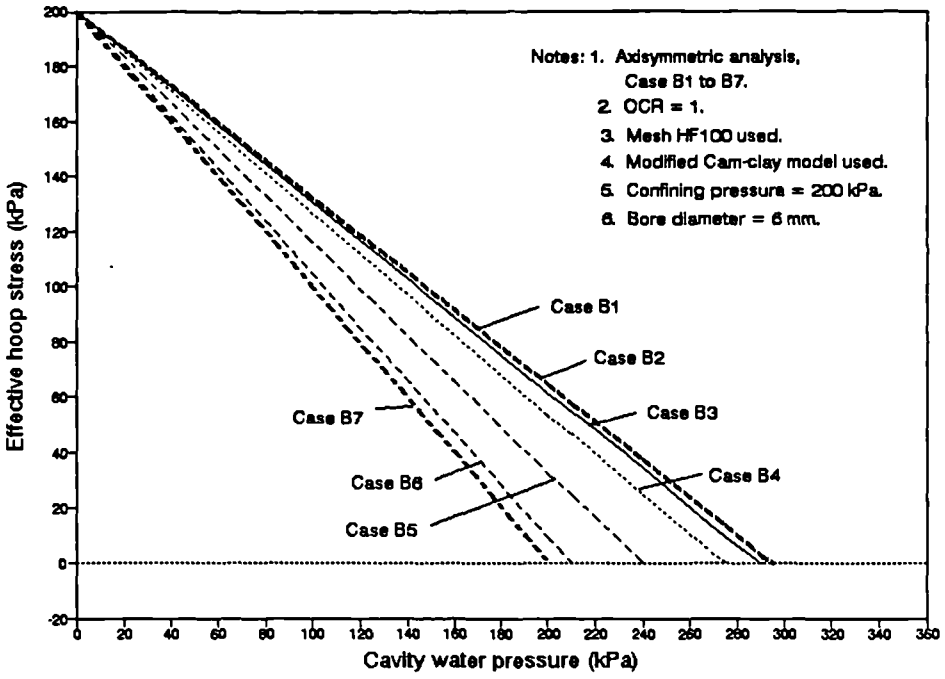

Figure 6.31 Variations of effective hoop stresses with cavity water pressure at the centroid in element 53 for confining pressure of 200 kPa - Case B1 to B7

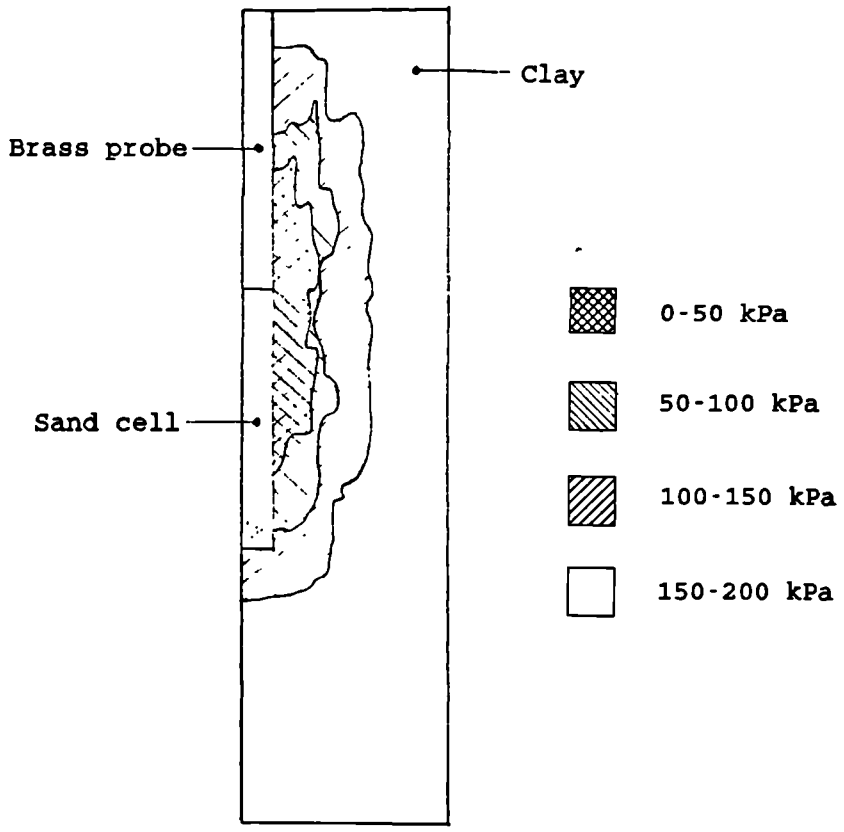

Figure 6.32 Contours of effective hoop stress σ_θ' at fracturing pressure of 290 kPa (Case B3)

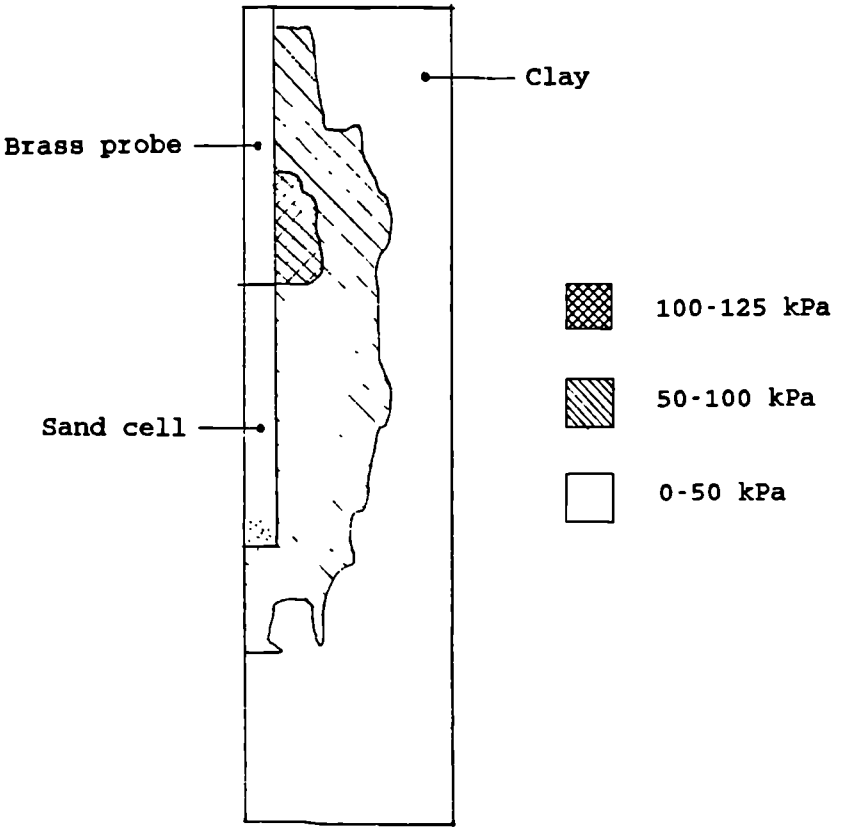

Figure 6.33 Contours of deviator stress q' at fracturing pressure of 290 kPa (Case B3)

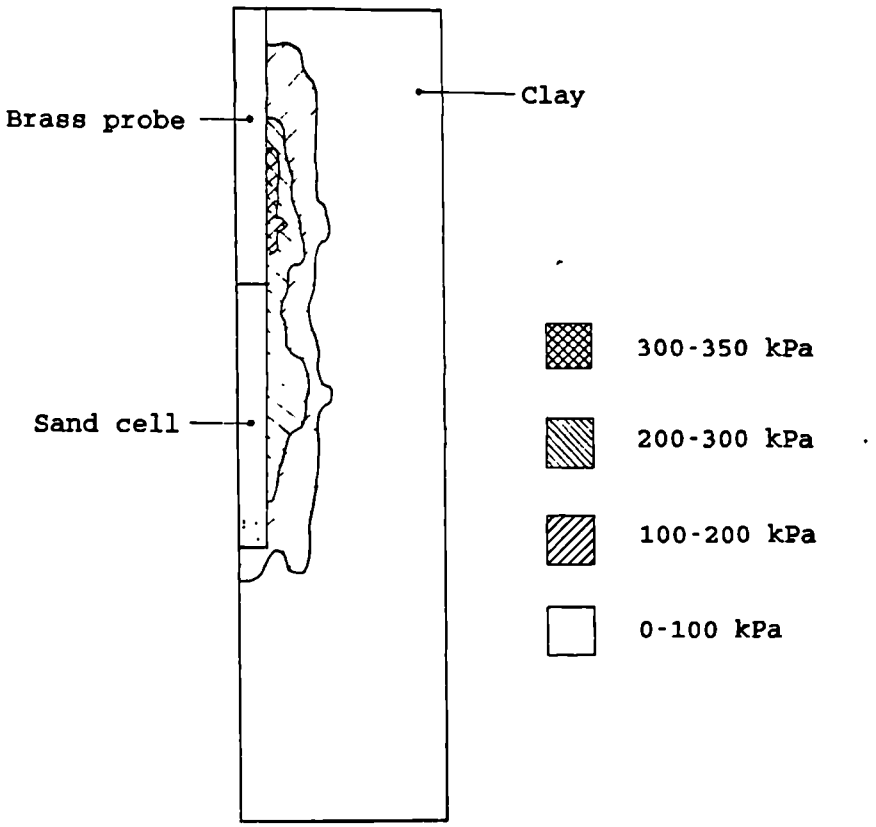

Figure 6.34 Contours of pore pressure u at fracturing pressure of 290 kPa (Case B3)

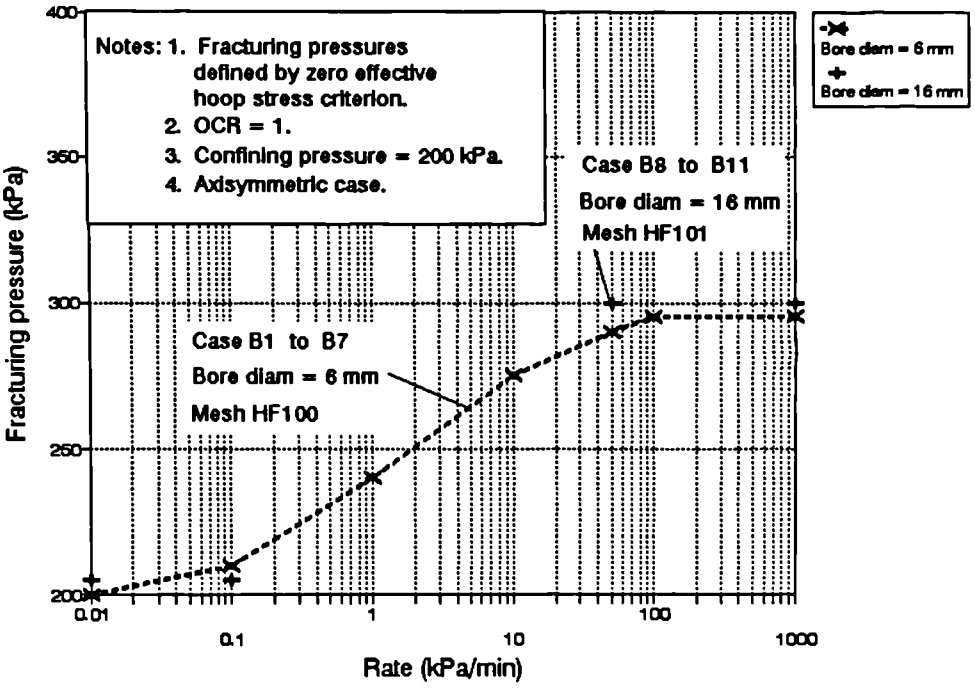

Figure 6.35 Variations of fracturing pressure with rates of cavity water pressure increase (Case B1 to B7 & B8 to B11)

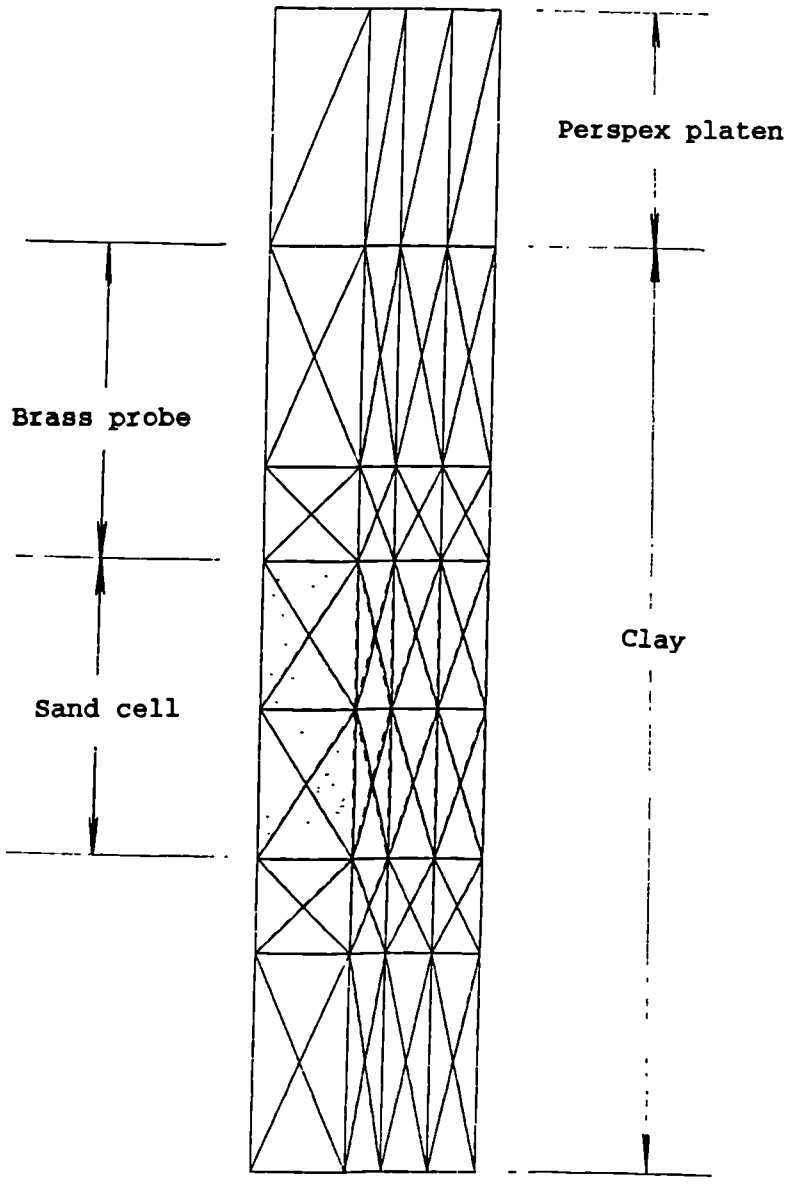

Figure 6.36 Deformed mesh at fracturing pressure of 300 kPa (Case B8)

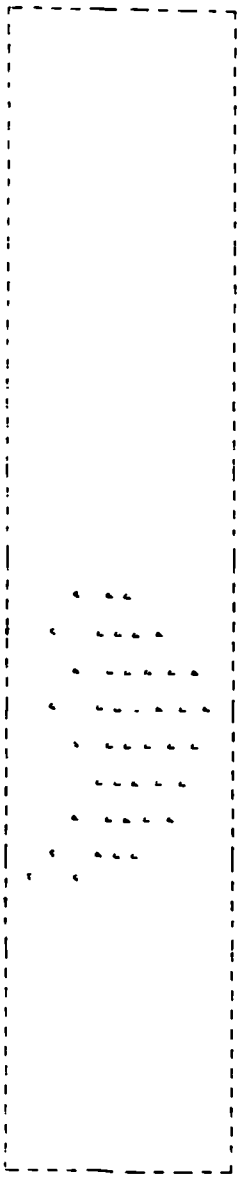

Figure 6.37 Nodal displacement vectors at fracturing pressure of 300 kPa (Case B8)

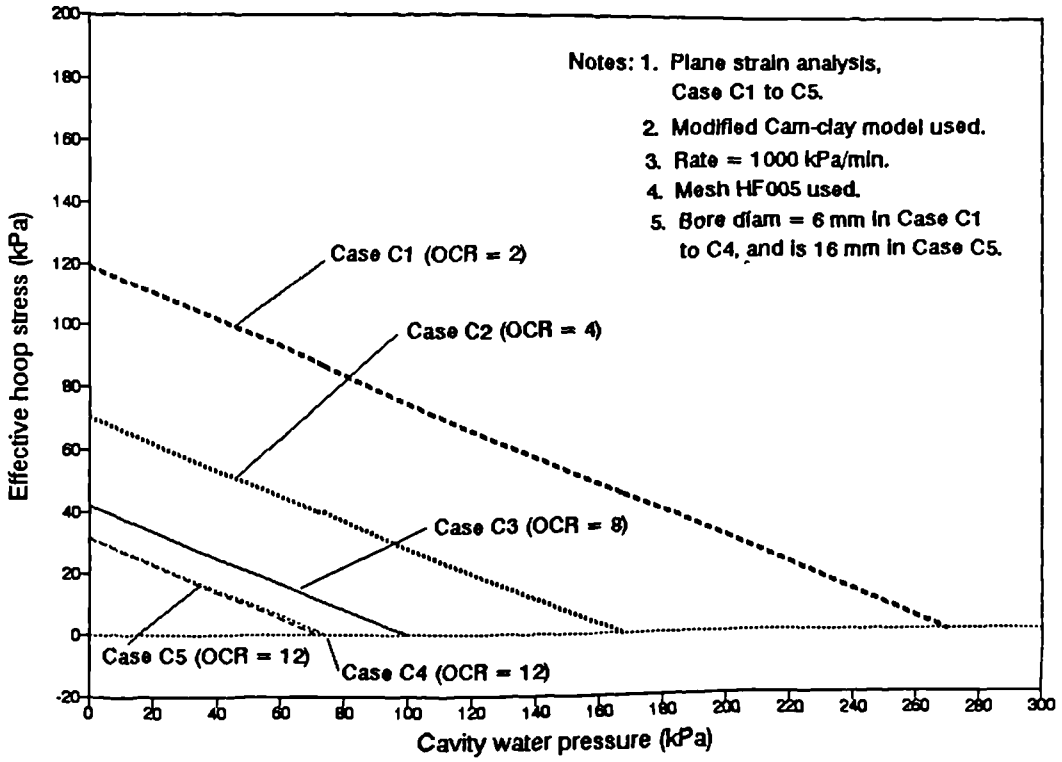

Figure 6.38 Variations of effective hoop stresses with cavity water pressure at the centroid in element 37 for different overconsolidation ratios and bore diameters - Case C1 to C5

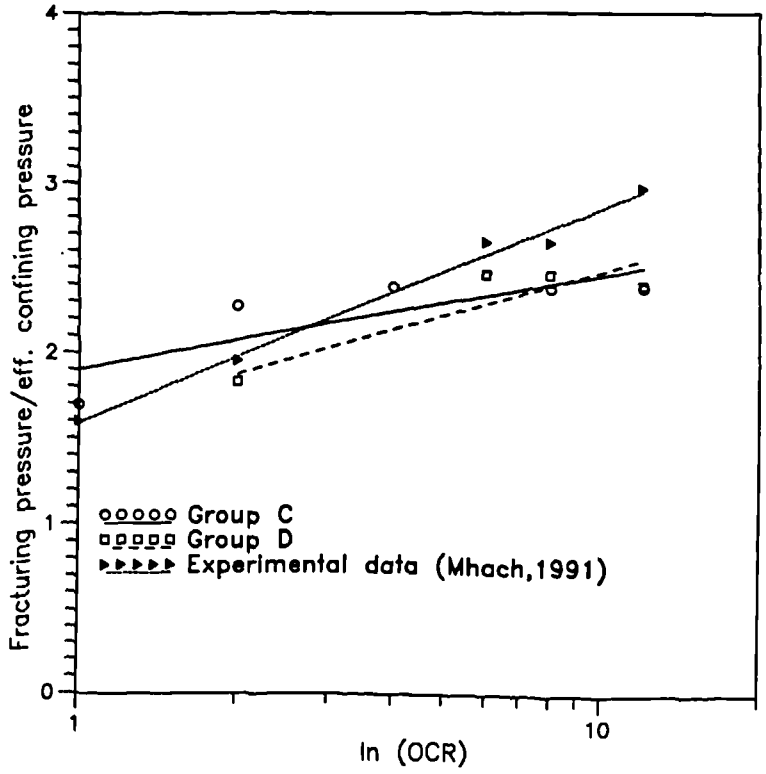

Figure 6.39(a) Variations of fracturing pressure normalised by effective confining pressure $(U_F-u_o)/(\sigma_c-u_o)$ with ln (OCR)

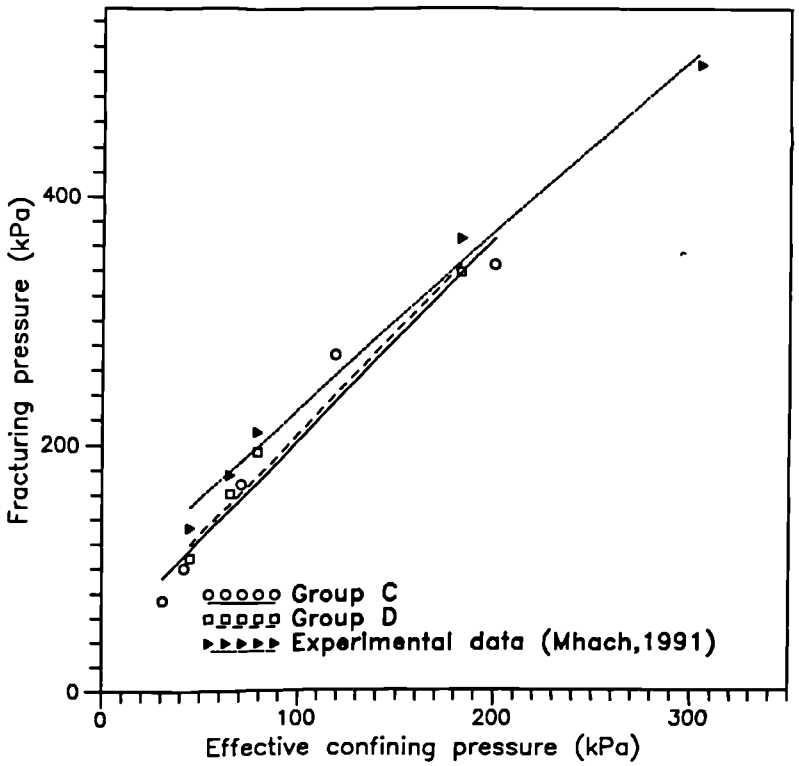

Figure 6.39(b) Variations of fracturing pressure $(U_F - u_o)$ with effective confining pressure $(\sigma_c - u_o)$

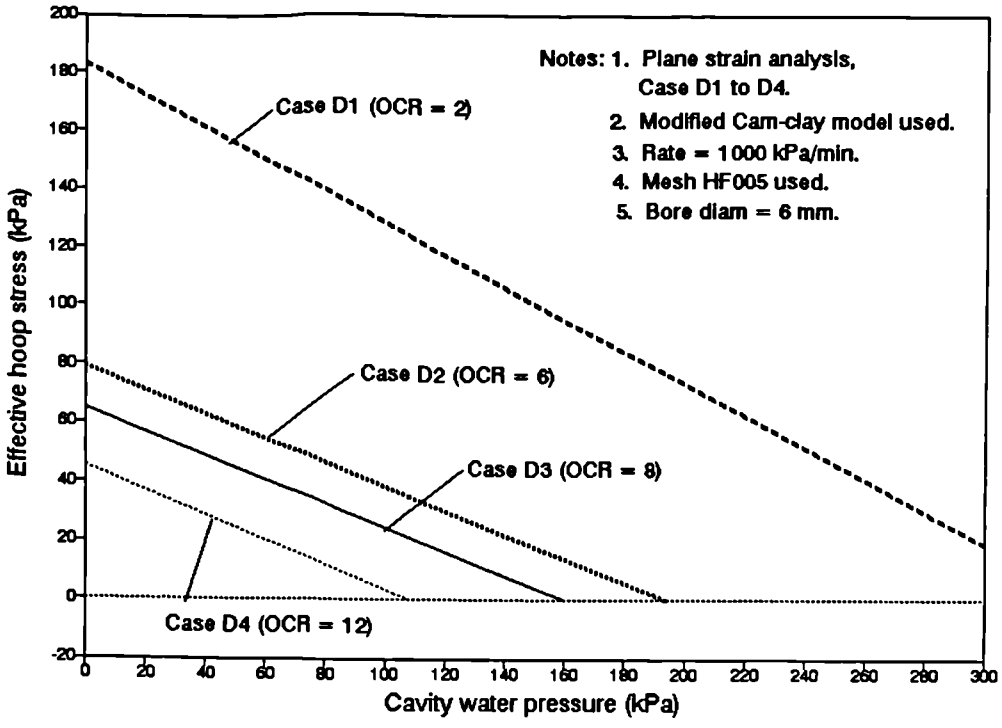

Figure 6.40 Variations of effective hoop stresses with cavity water pressure at the centroid in element 37 for different overconsolidation ratios - Case D1 to D4

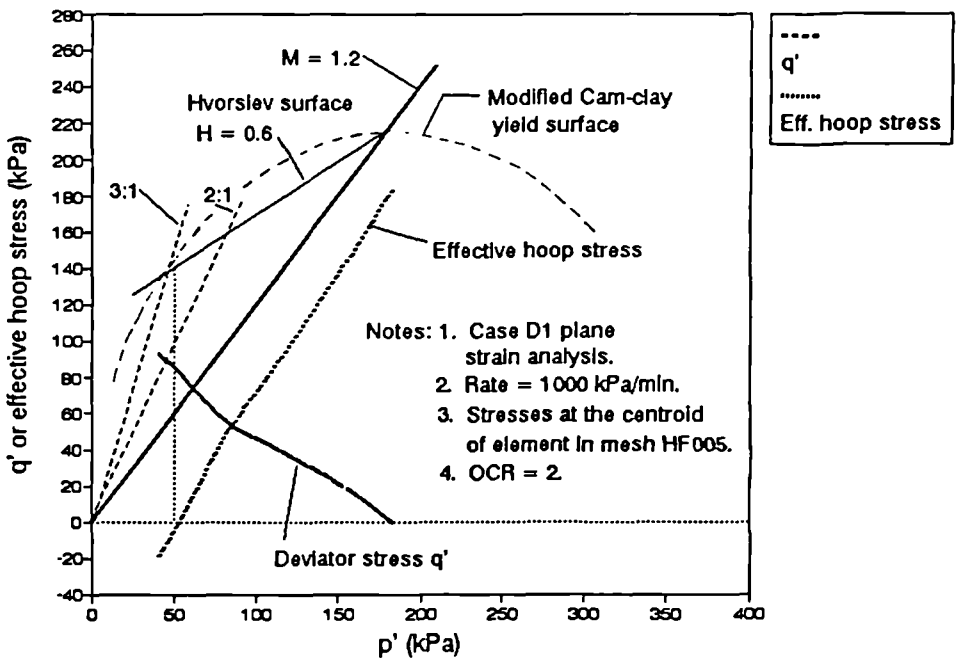

Figure 6.41 Variations of effective hoop stress in p':q' space at the centroid of element 37 in mesh HF005 (Case D1)

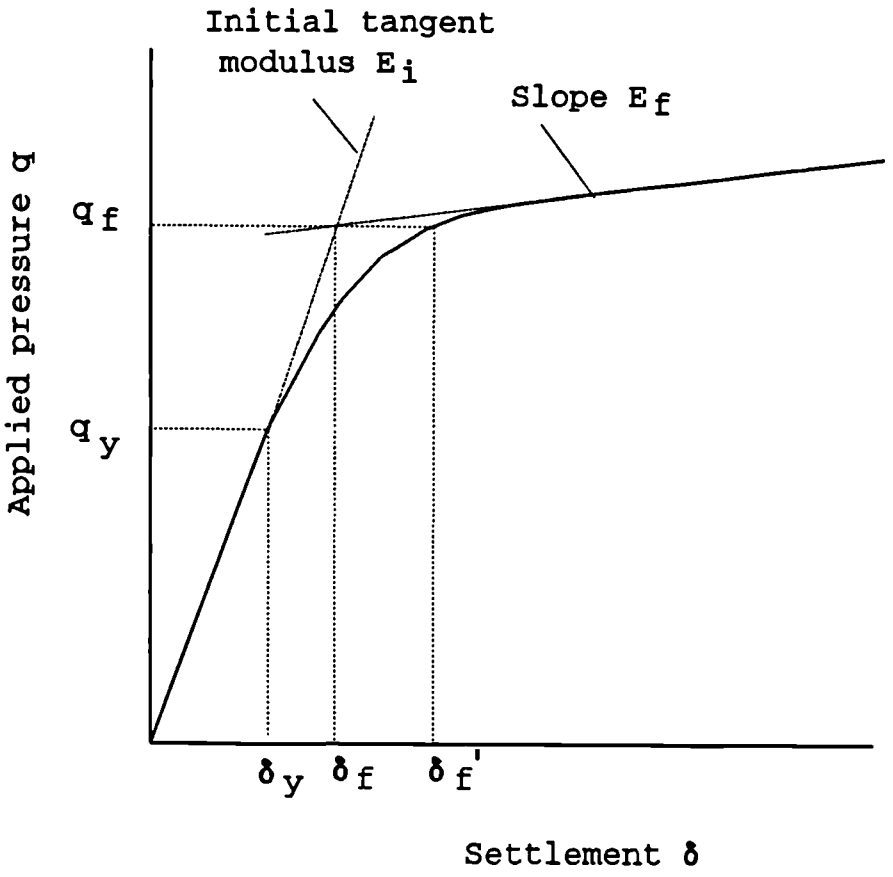

Figure 7.1 Idealised pressure-settlement curve

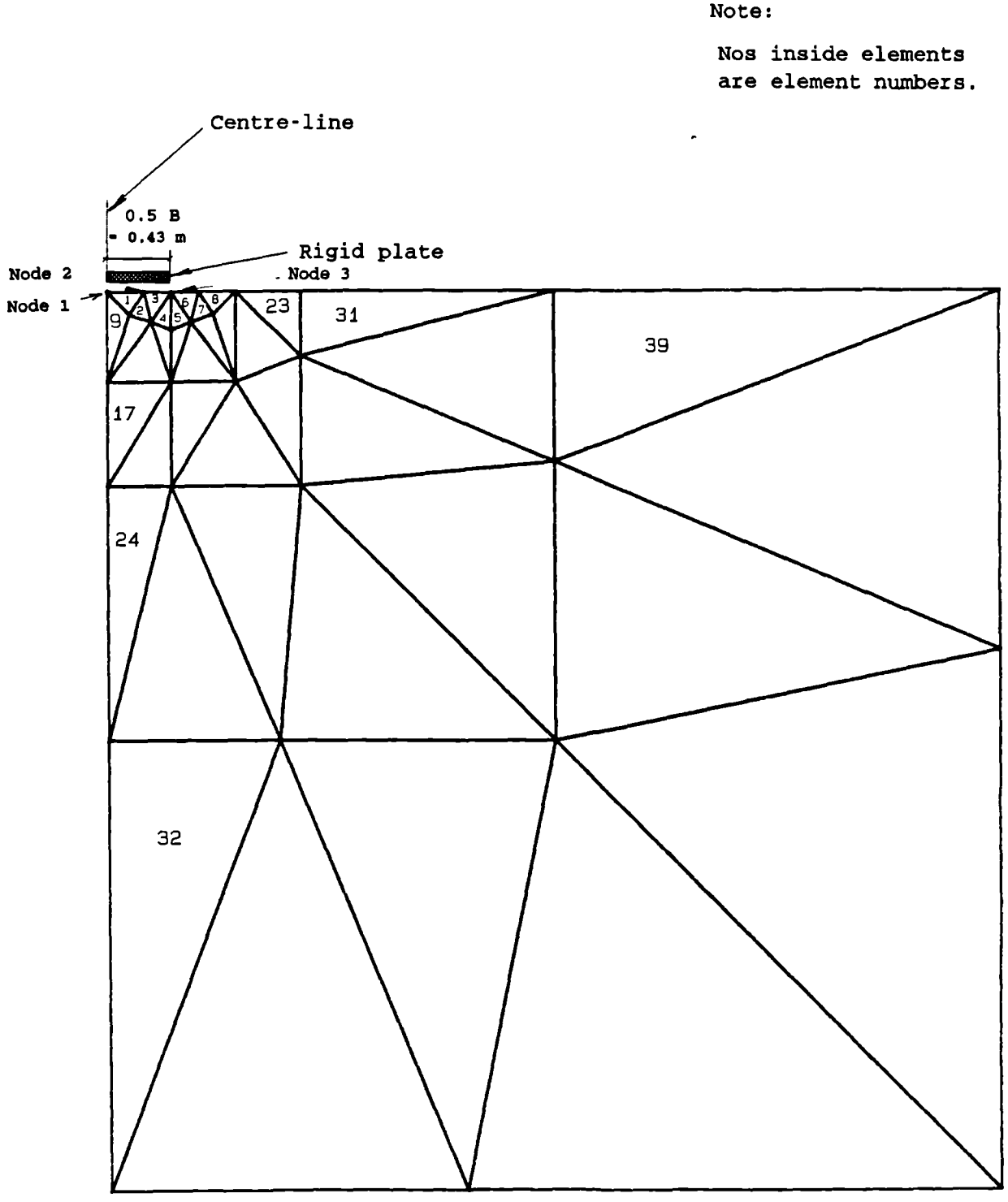

Figure 7.2 Finite element mesh CP–07 (axisymmetric) for surface plate loading analysis

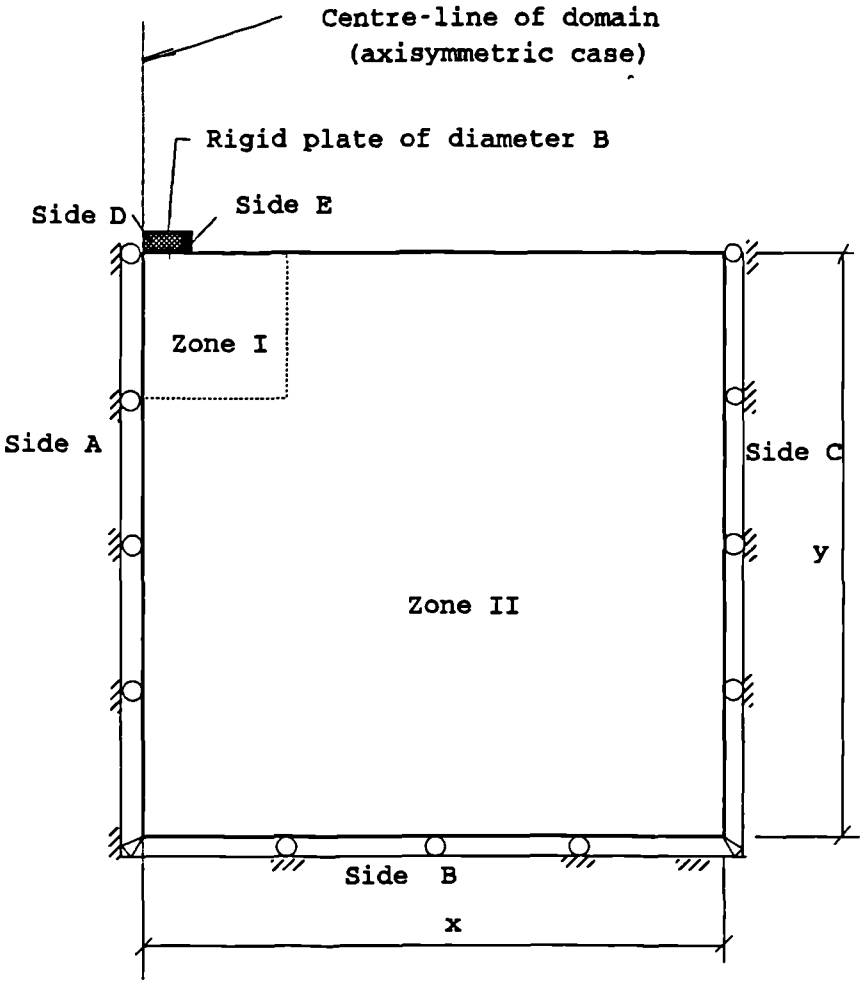

$x = y = 7B$

Figure 7.3 Boundary conditions of Mesh CP-07

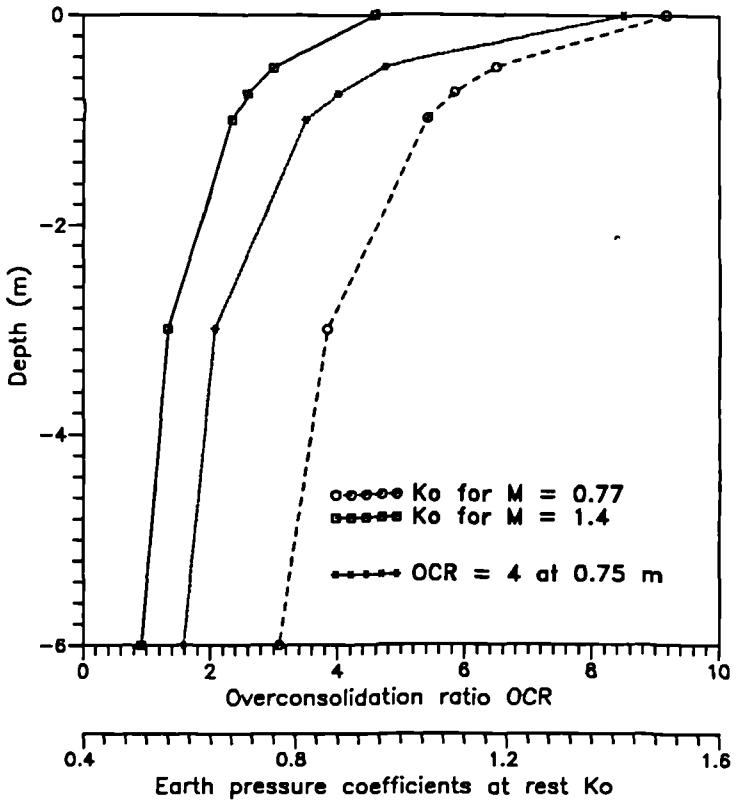

Figure 7.4(a) Variations of overconsolidation ratio and earth pressure coefficients at rest with depth for M = 0.77 and 1.4

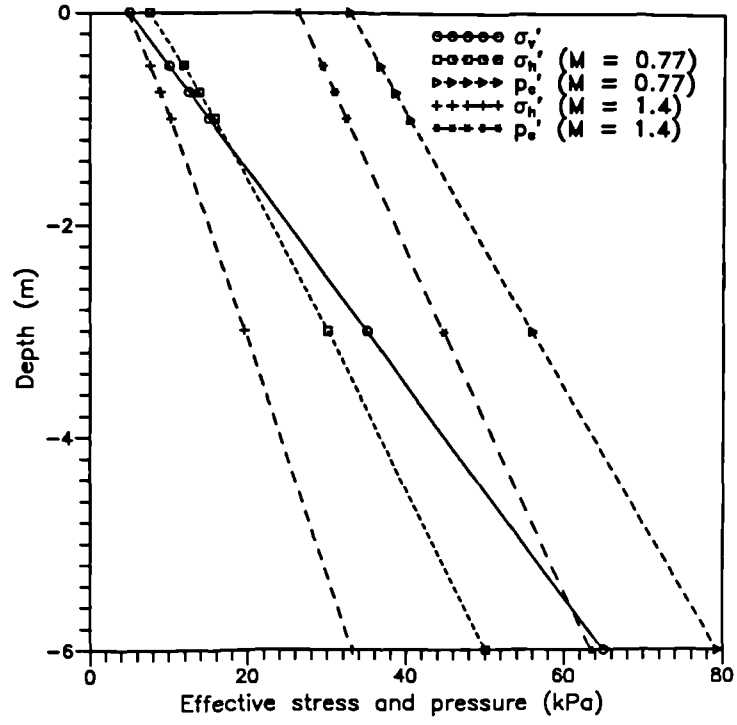

Figure 7.4(b) Variations of effective vertical and horizontal stresses and preconsolidation pressures with depth for M = 0.77 and 1.4 assuming K_o conditions

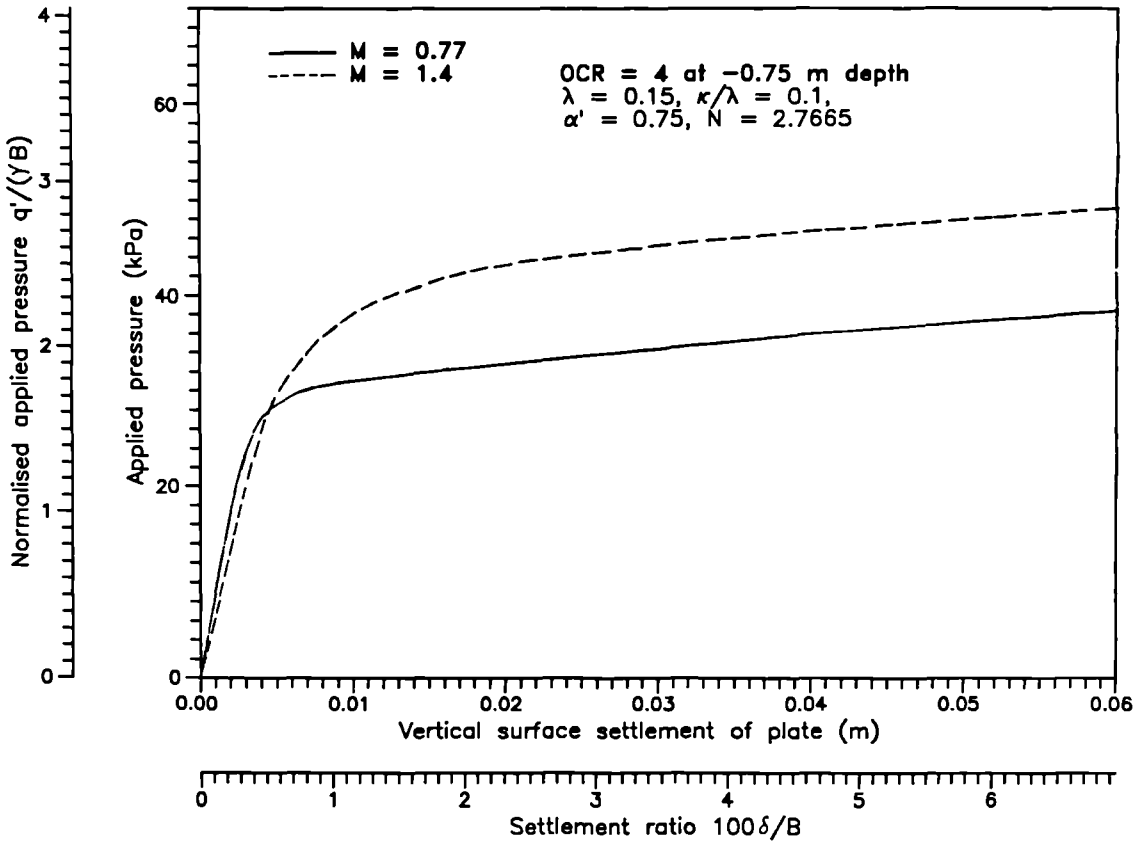

Figure 7.5 Pressure–settlement curves of two plate loading analyses with M = 0.77 or 1.4 having Ko in-situ stress conditions

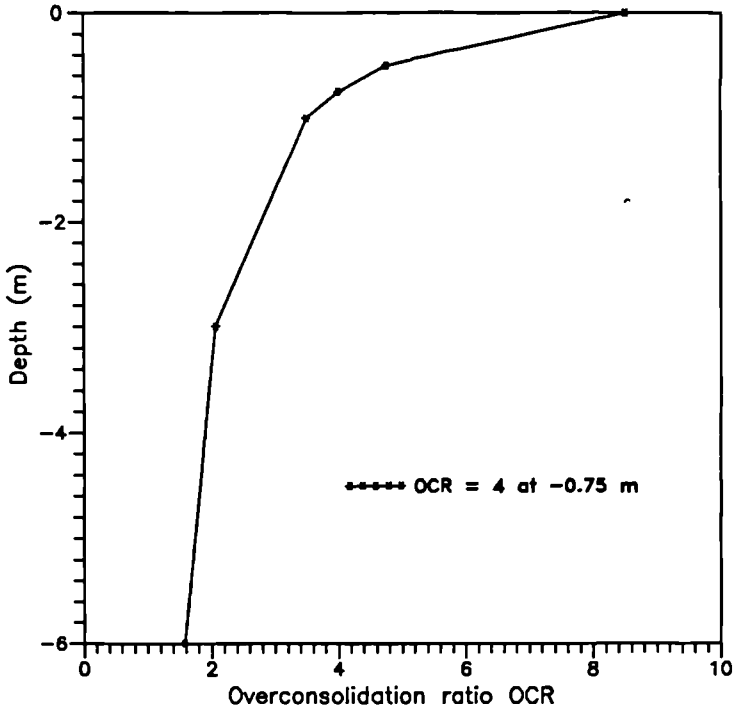

Figure 7.6(a) Variations of overconsolidation ratio with depth assuming isotropic in-situ stresses (Ko = 1), OCR = 4 at -0.75 m depth and ground water table at -0.5 m depth

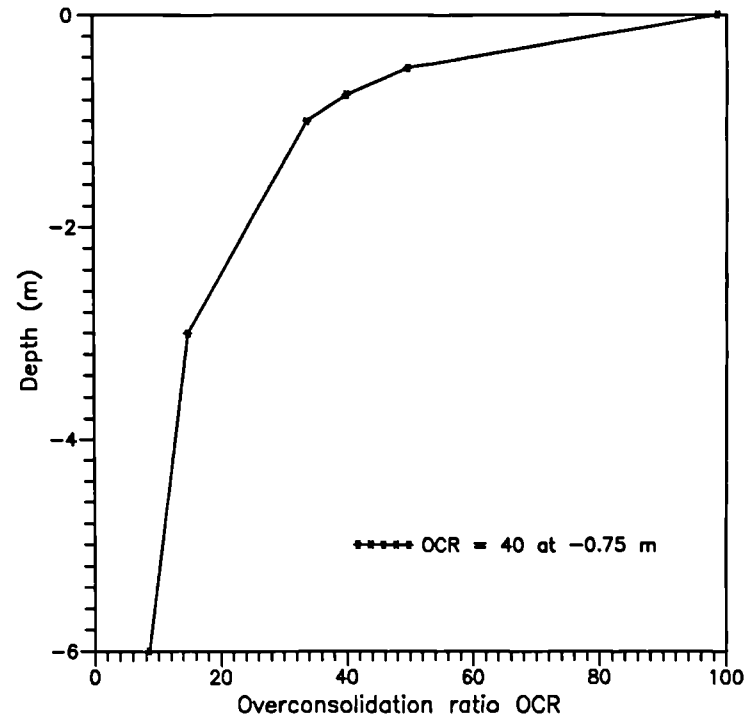

Figure 7.6(b) Variations of overconsolidation ratio with depth assuming isotropic in-situ stresses (Ko = 1), OCR = 40 at -0.75 m depth and ground water table at -0.5 m depth

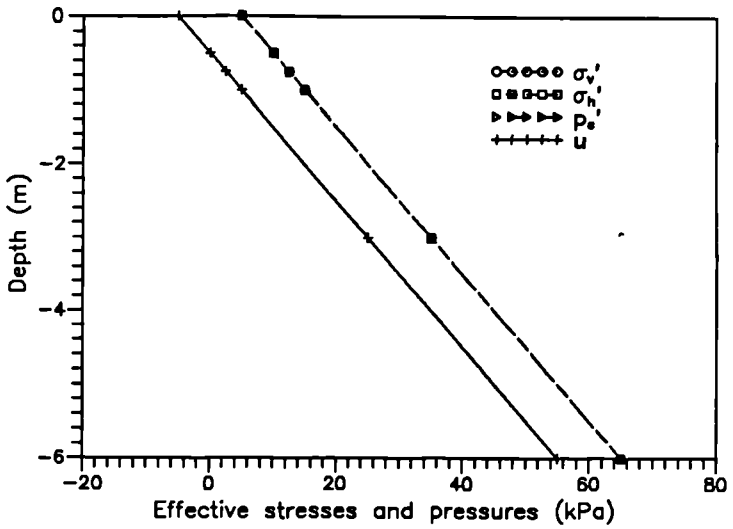

(a) OCR = 1 at −0.75 m depth

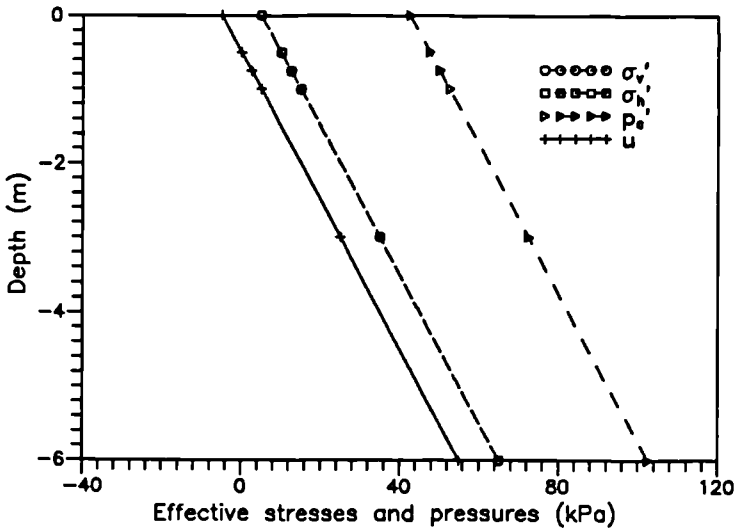

(b) OCR = 4 at −0.75 m depth

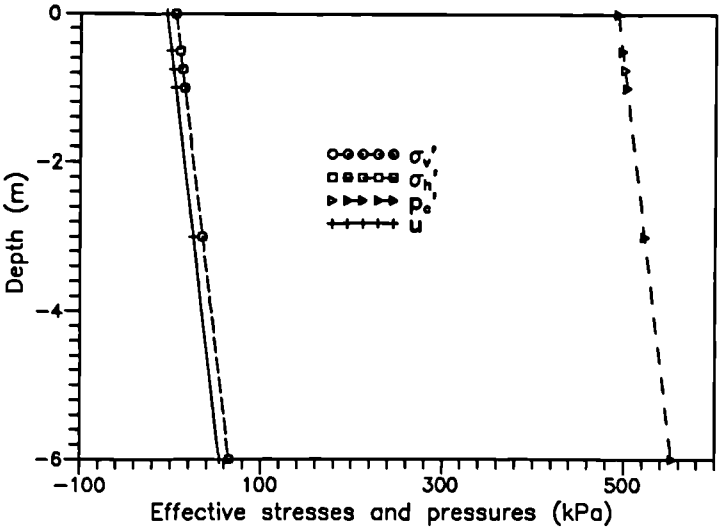

(c) OCR = 40 at −0.75 m depth

Figure 7.7 Variations of effective vertical & horizontal stresses, preconsolidation and pore pressures with depth assuming isotropic in−situ stress conditions for three different OCR's

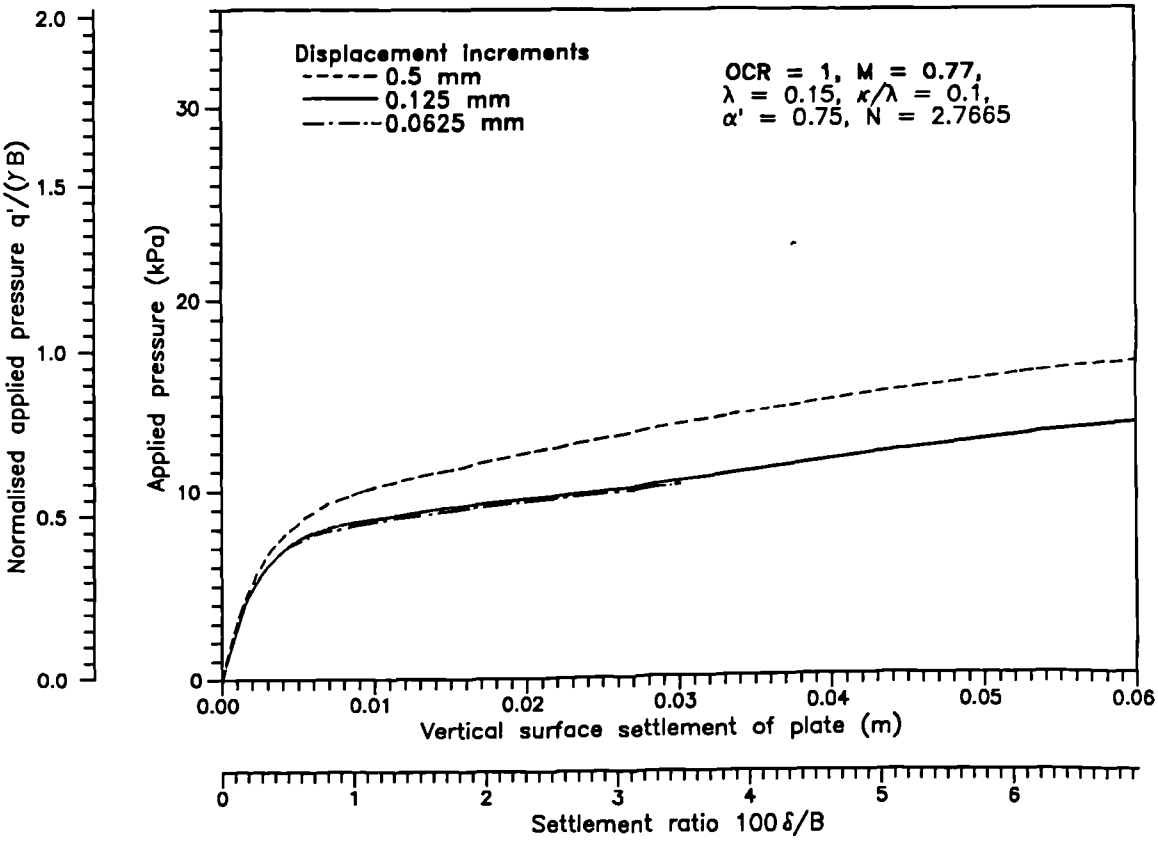

Figure 7.8 Pressure–settlement curves checking the convergence of solutions for different displacement increment sizes

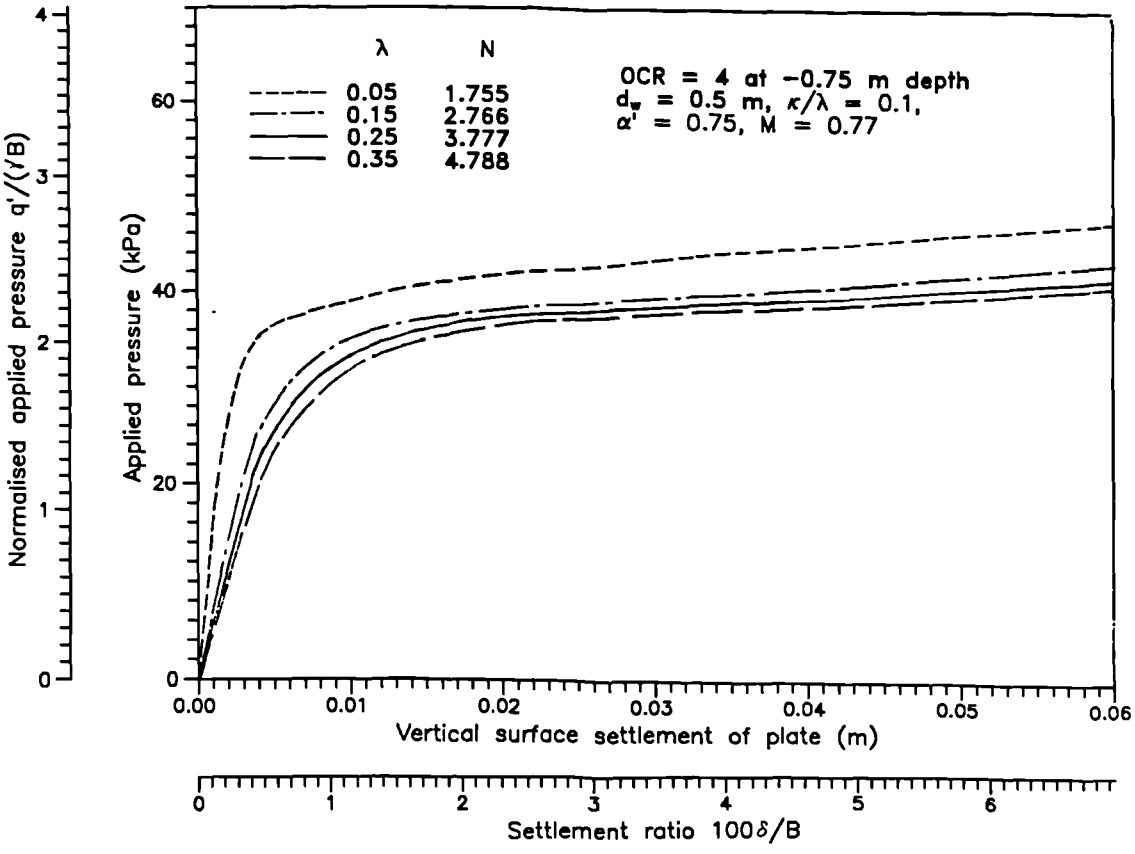

Figure 7.9 Pressure–settlement curves for varying λ values

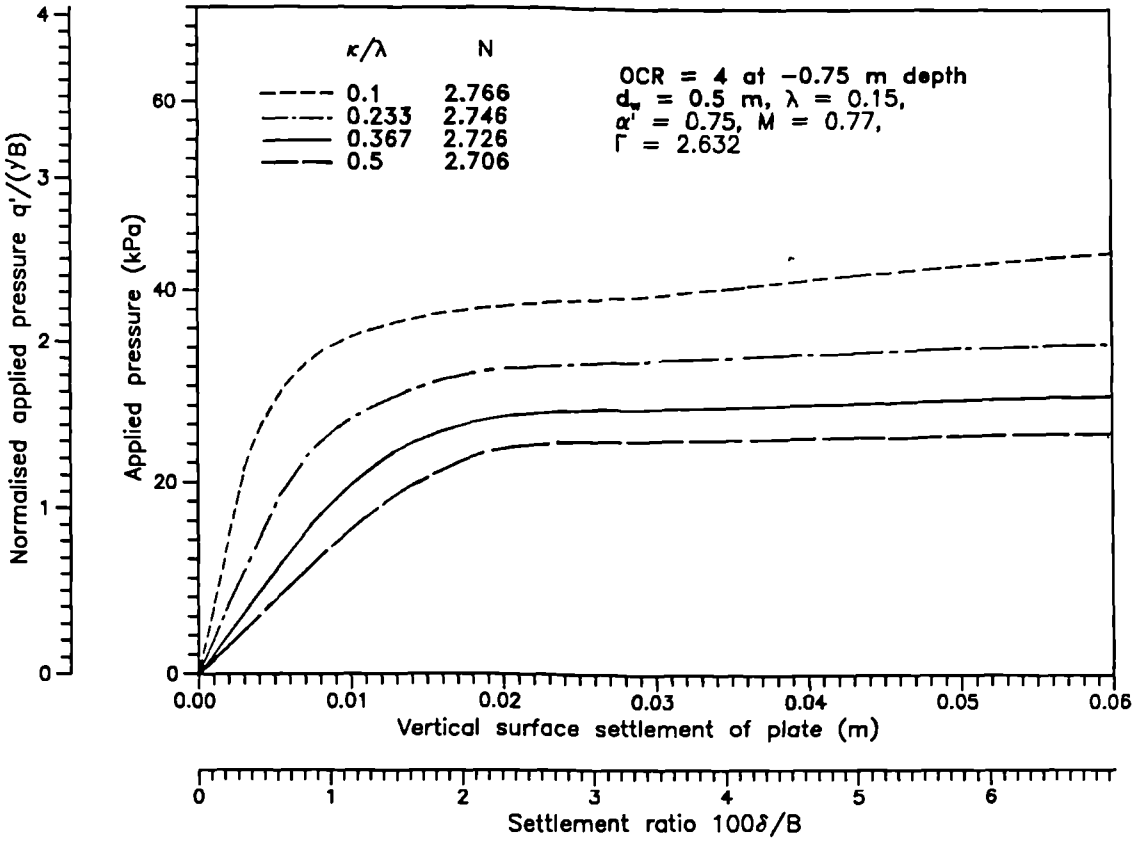

Figure 7.10 Pressure–settlement curves for varying κ/λ values

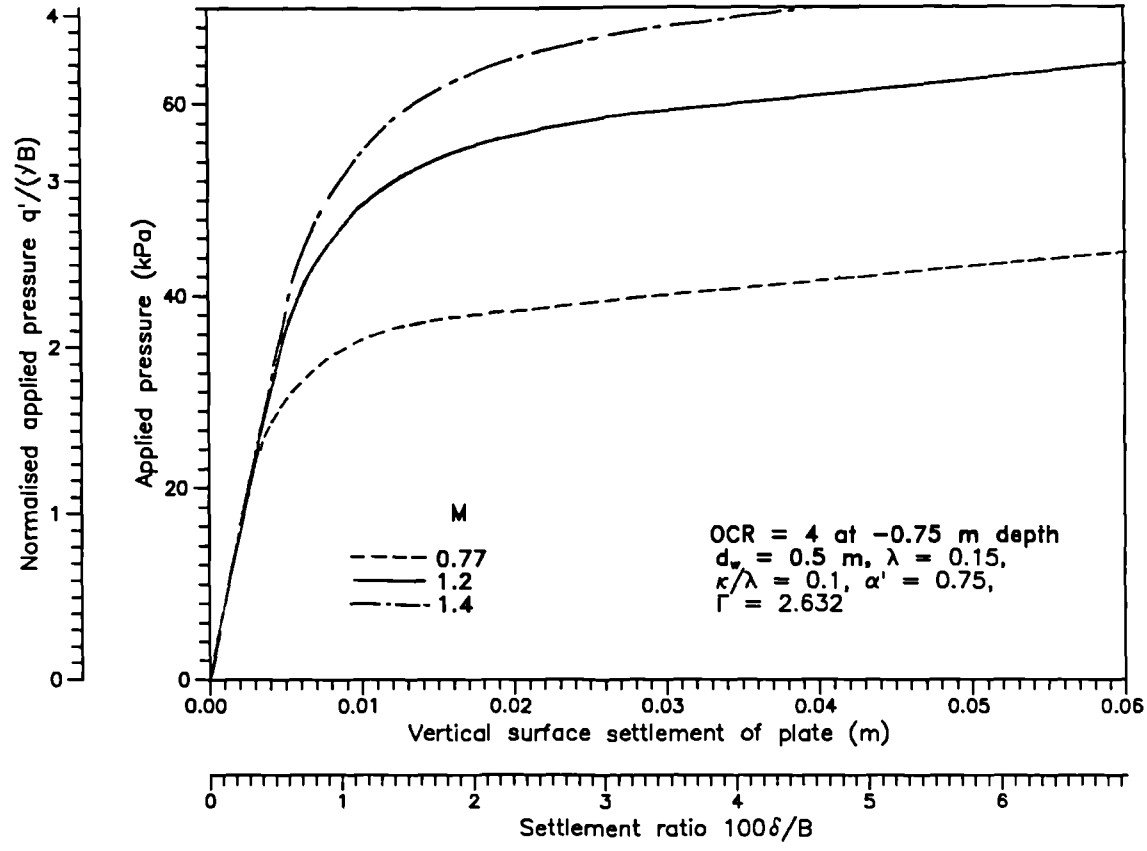

Figure 7.11 Pressure–settlement curves for varying M values

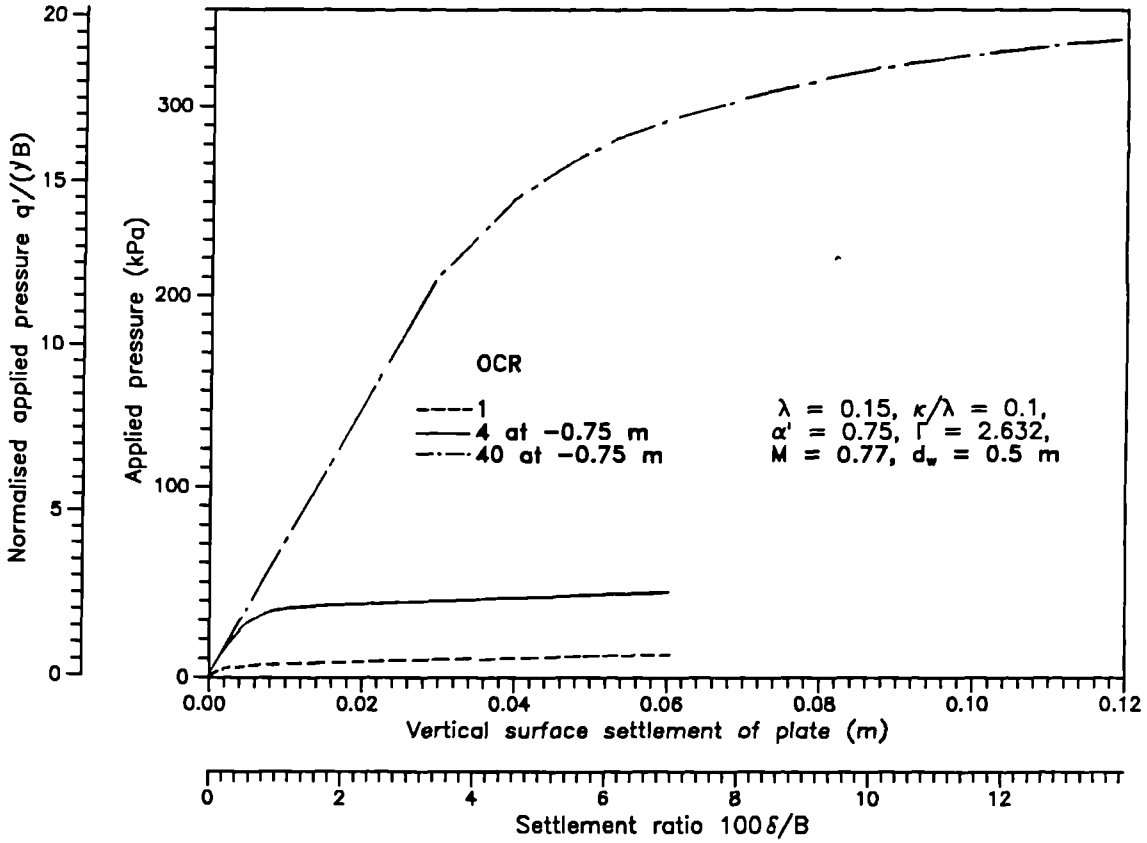

Figure 7.12 Pressure–settlement curves for varying OCR values

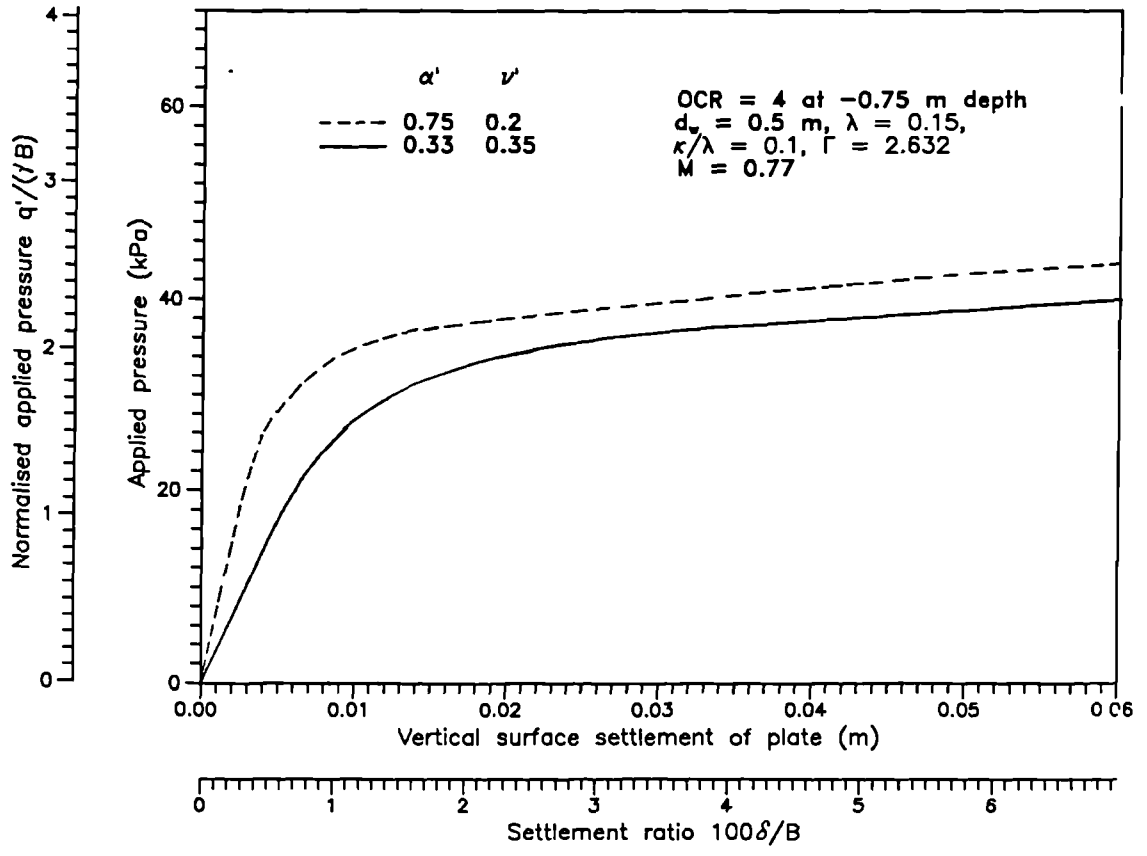

Figure 7.13 Pressure–settlement curves for varying α' values

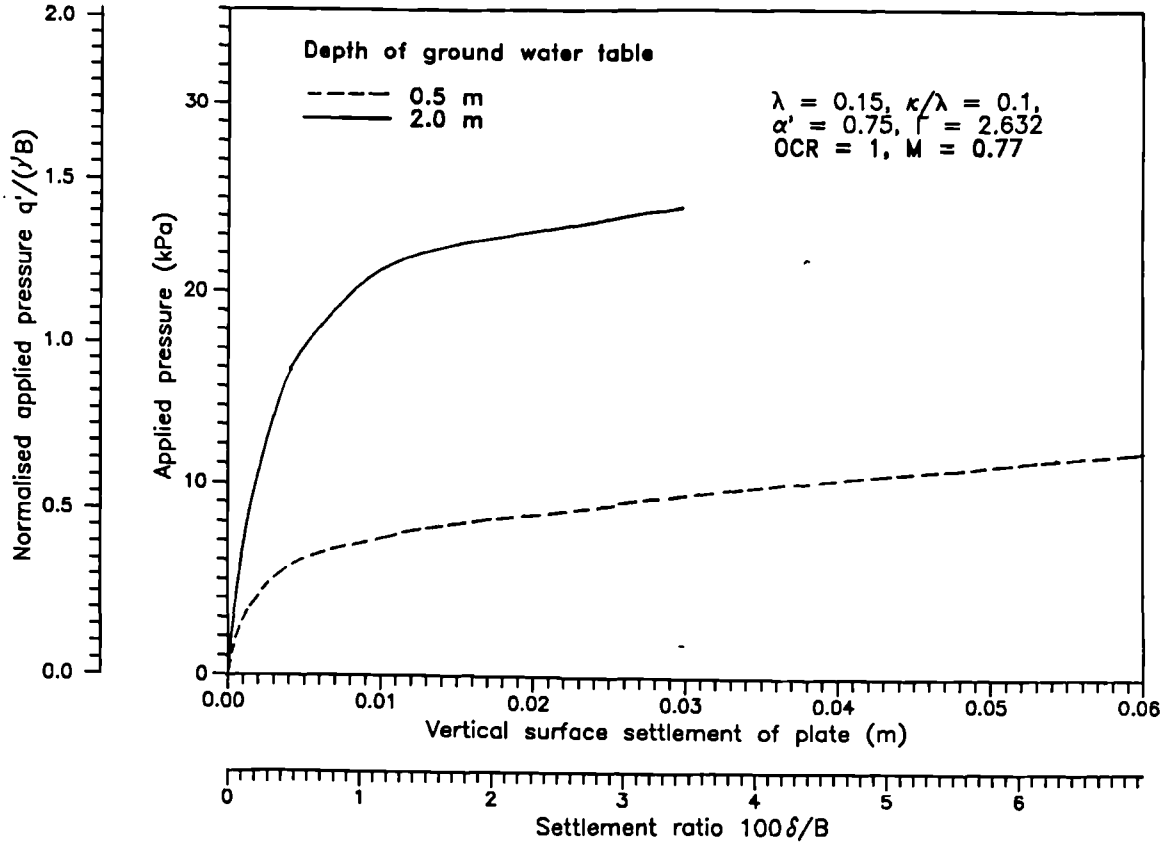

Figure 7.14 Pressure–settlement curves for varying depths of ground water table d_w

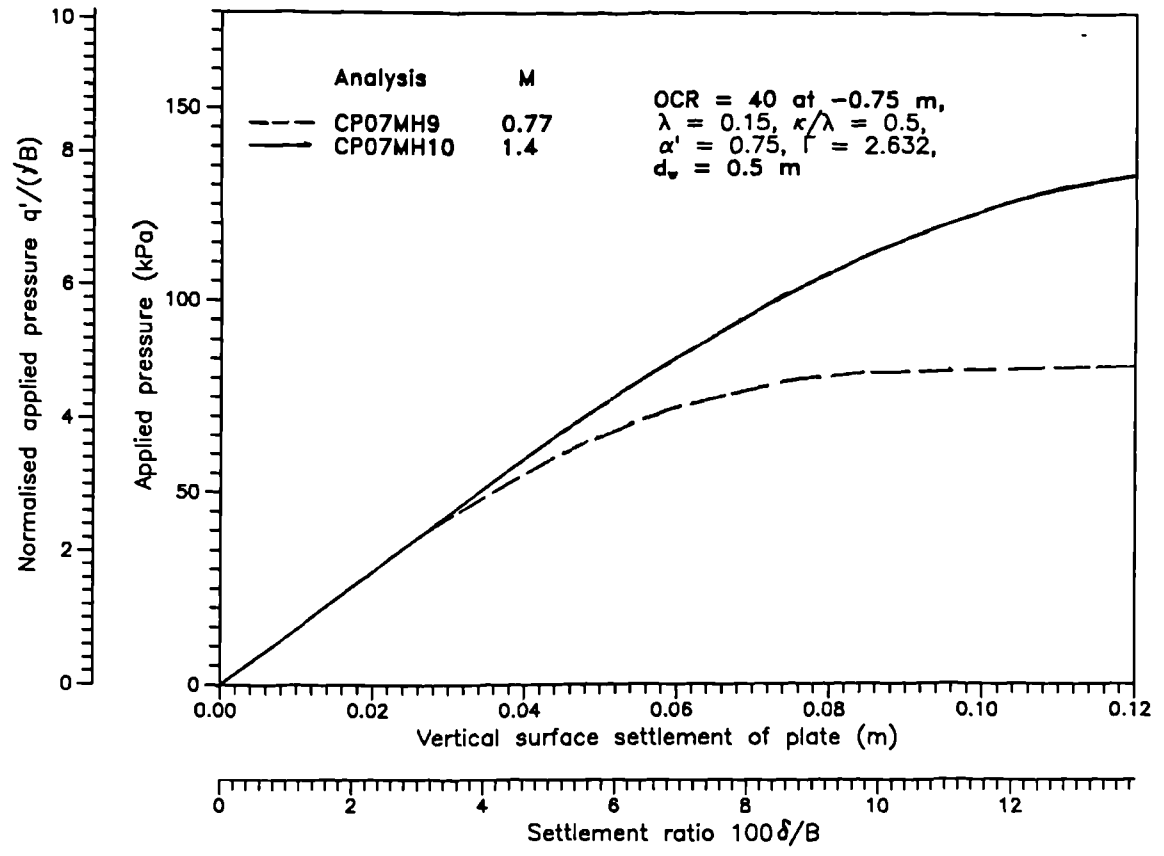

Figure 7.15 Pressure–settlement curve showing no clearly defined failure point for an analysis with an OCR of 40

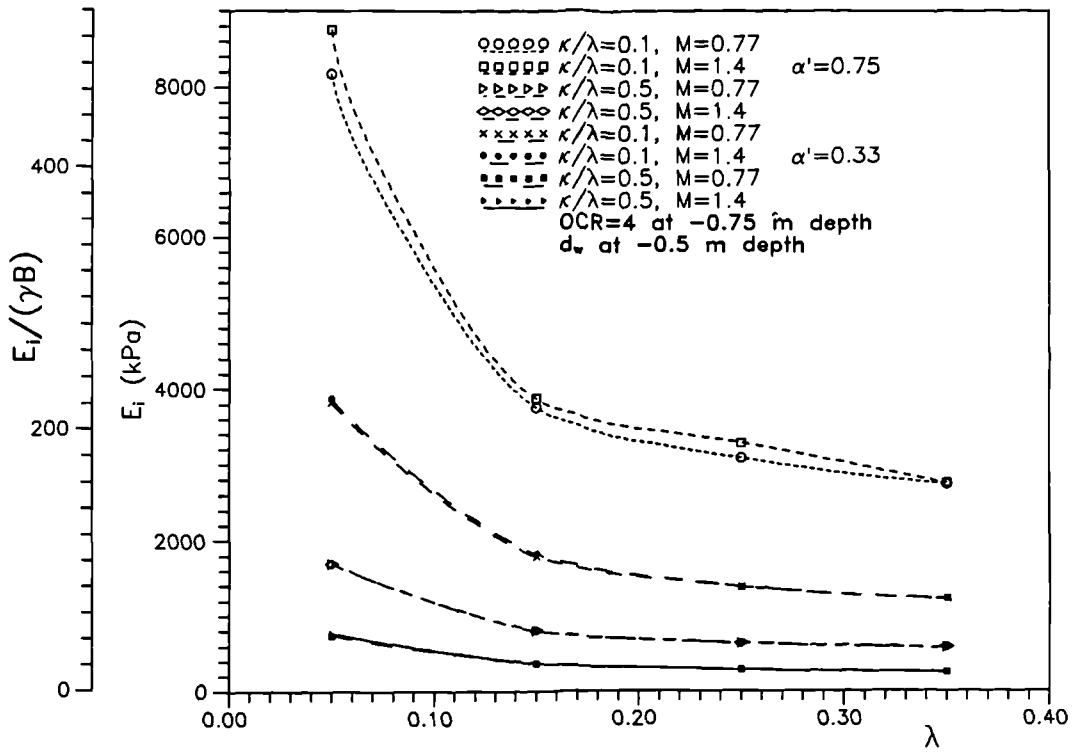

Figure 7.16 Variations of initial tangent modulus E_i and normalised initial tangent modulus $E_i/(\gamma B)$ with λ for fixed values of κ/λ, M and α'

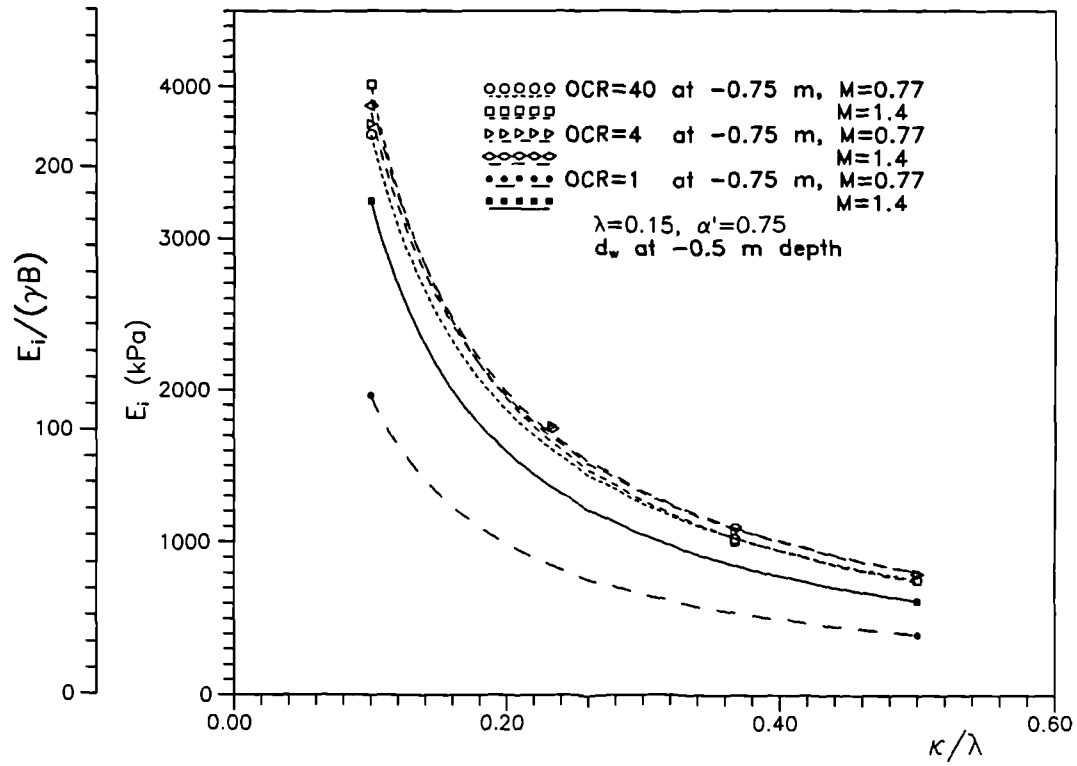

Figure 7.17 Variations of initial tangent modulus E_i and normalised initial tangent modulus $E_i/(\gamma B)$ with κ/λ for fixed values of λ, M and α'

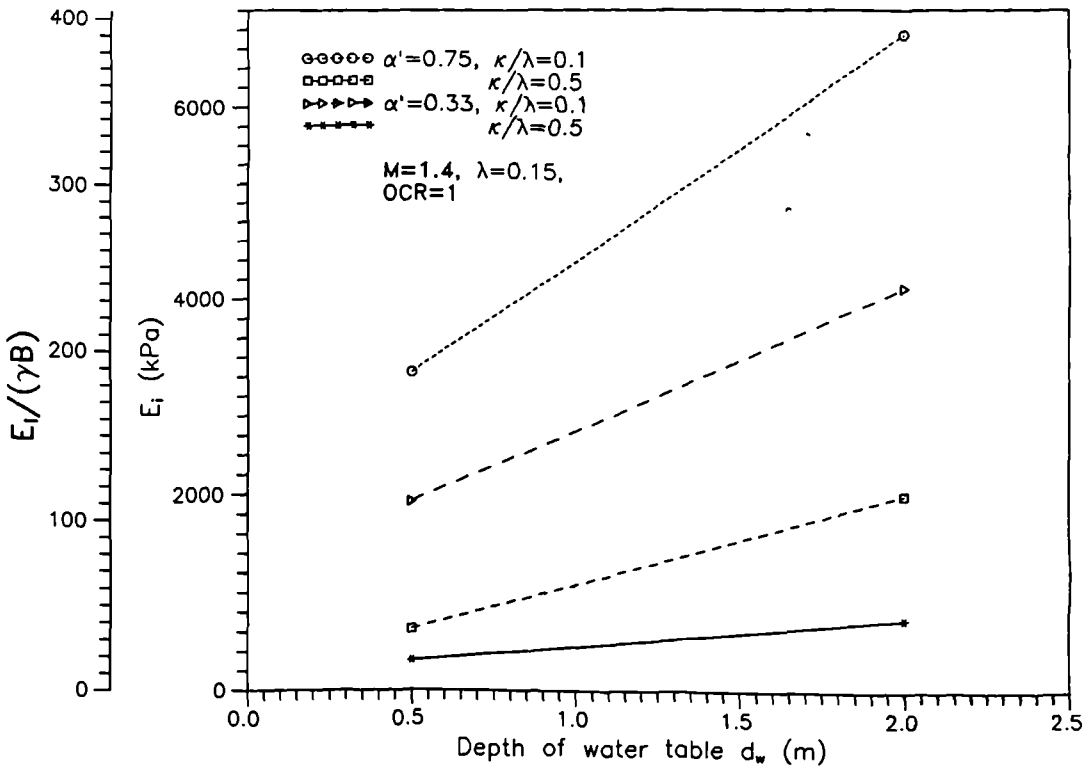

Figure 7.18 Variations of initial tangent modulus E_i and normalised initial tangent modulus $E_i/(\gamma B)$ with depth of water table d_w for fixed values of λ, κ/λ, M and α'

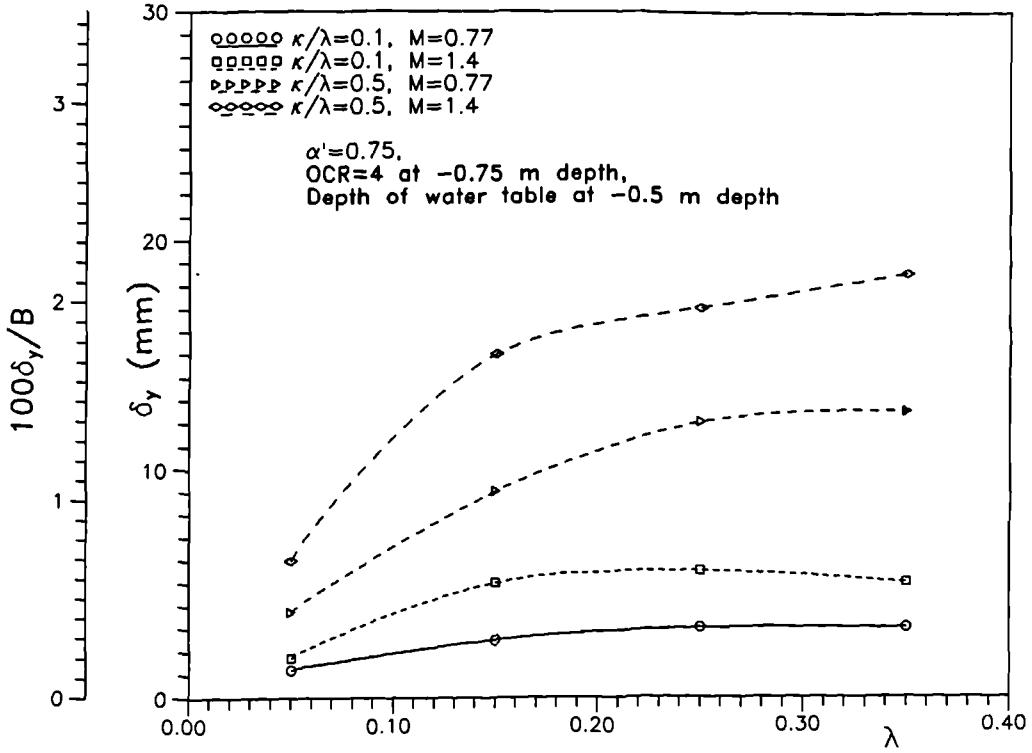

Figure 7.19 Variations of settlement δ_y and settlement ratio $100\delta_y/B$ immediately after yield with λ for fixed values of κ/λ, M and α'

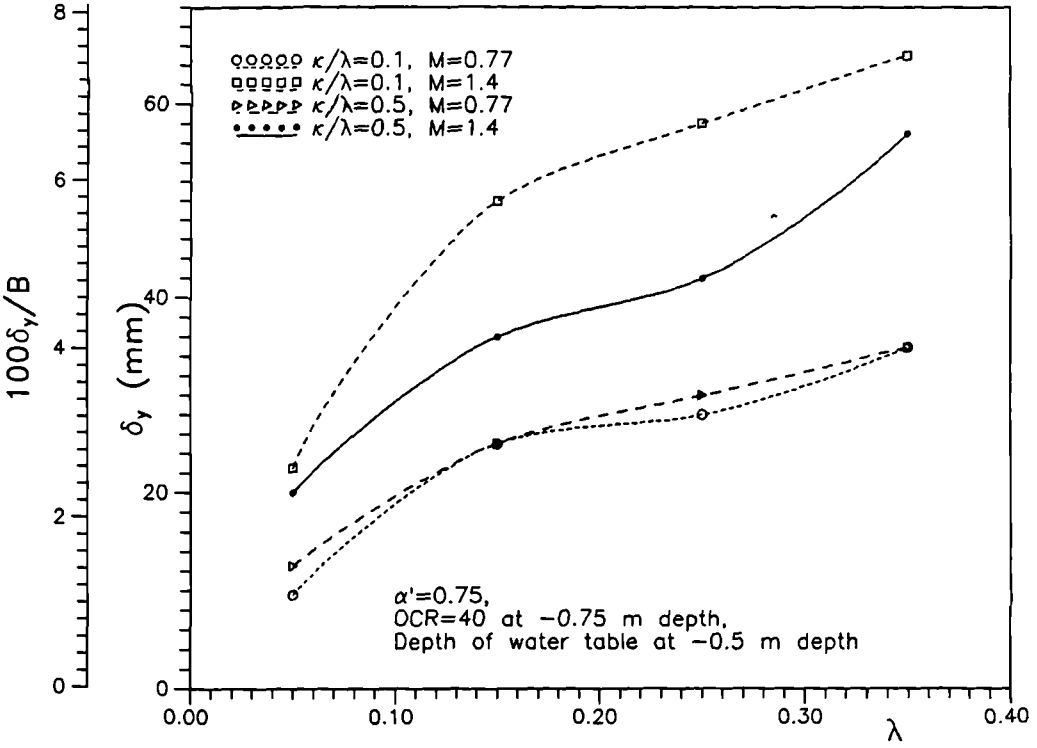

Figure 7.20 Variations of settlement δ_y and settlement ratio $100\delta_y/B$ immediately after yield with λ for fixed values of κ/λ, M and α'

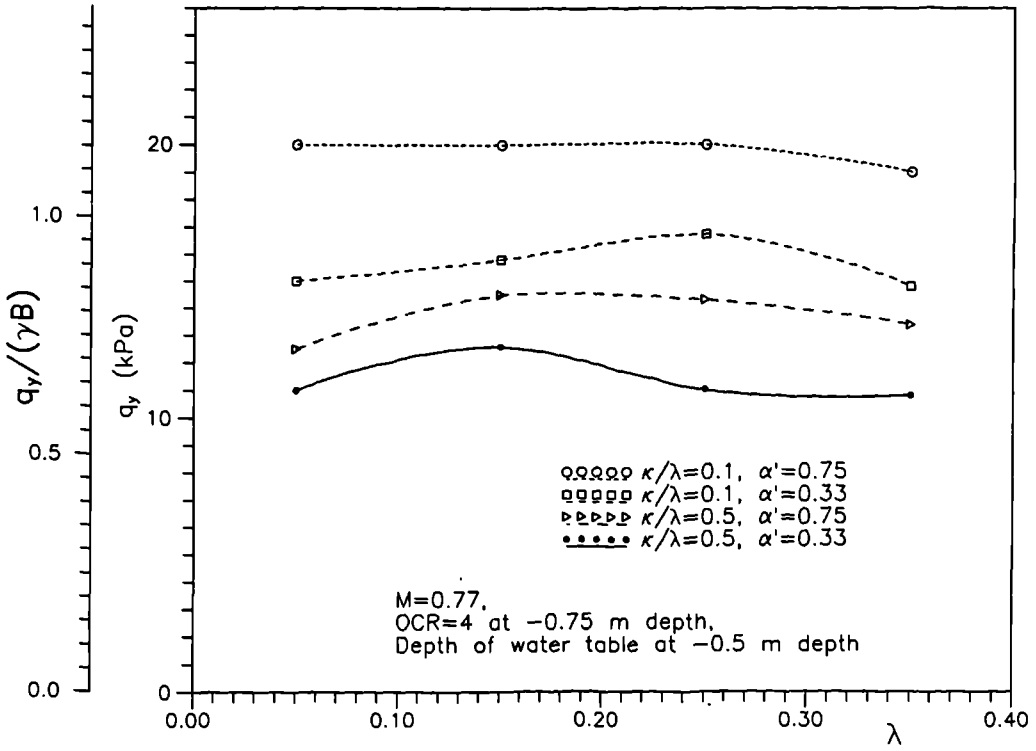

Figure 7.21 Variations of bearing pressure q_y and normalised bearing pressure $q_y/(\gamma B)$ immediately after yield with λ for fixed values of κ/λ, M and α'

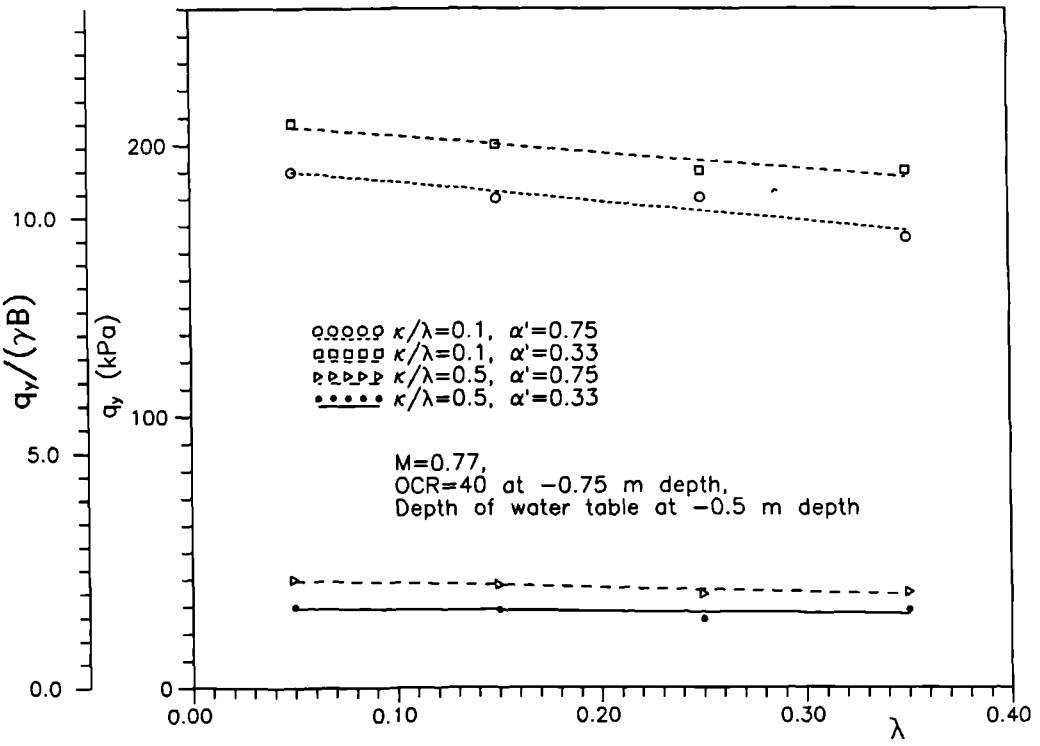

Figure 7.22 Variations of bearing pressure q_y and normalised bearing pressure $q_y/(\gamma B)$ immediately after yield with λ for fixed values of κ/λ, M and α'

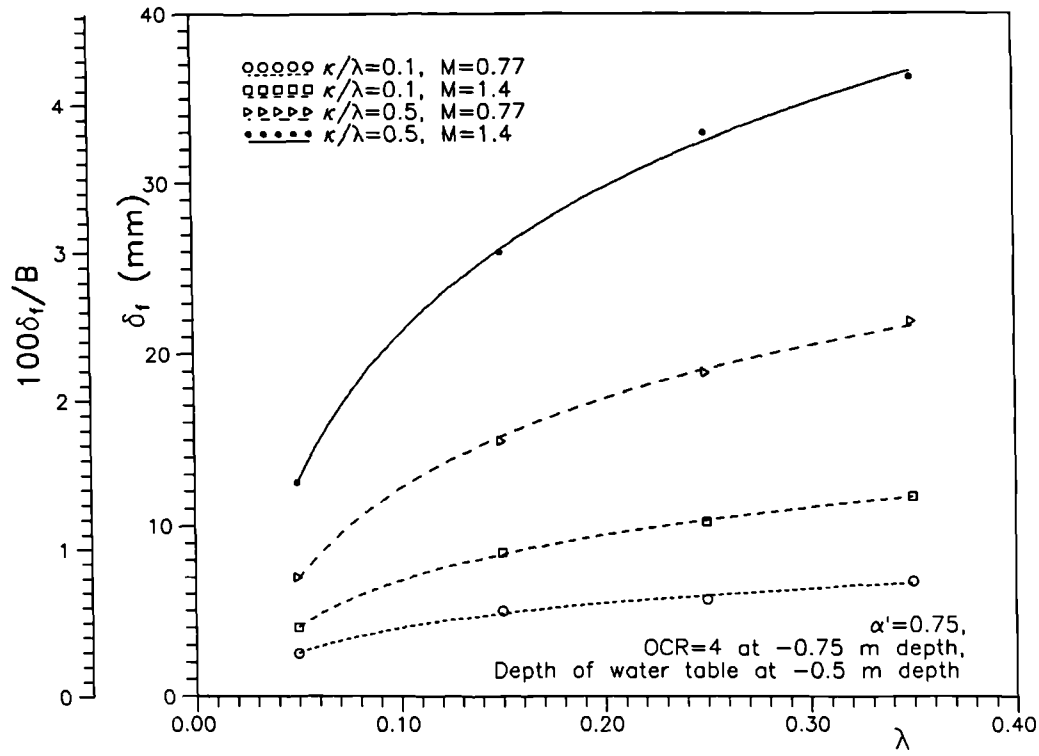

Figure 7.23 Variations of settlement δ_f and settlement ratio $100\delta_f/B$ at failure with λ for fixed values of κ/λ, M and α'

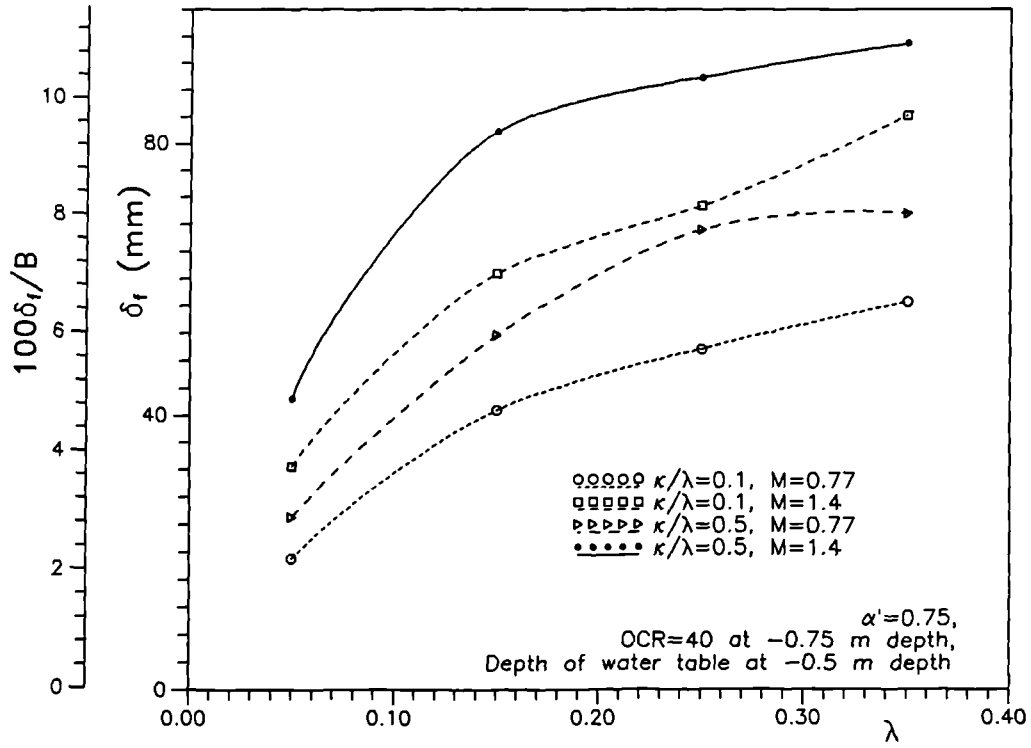

Figure 7.24 Variations of settlement δ_f and settlement ratio $100\delta_f/B$ at failure with λ for fixed values of κ/λ, M and α'

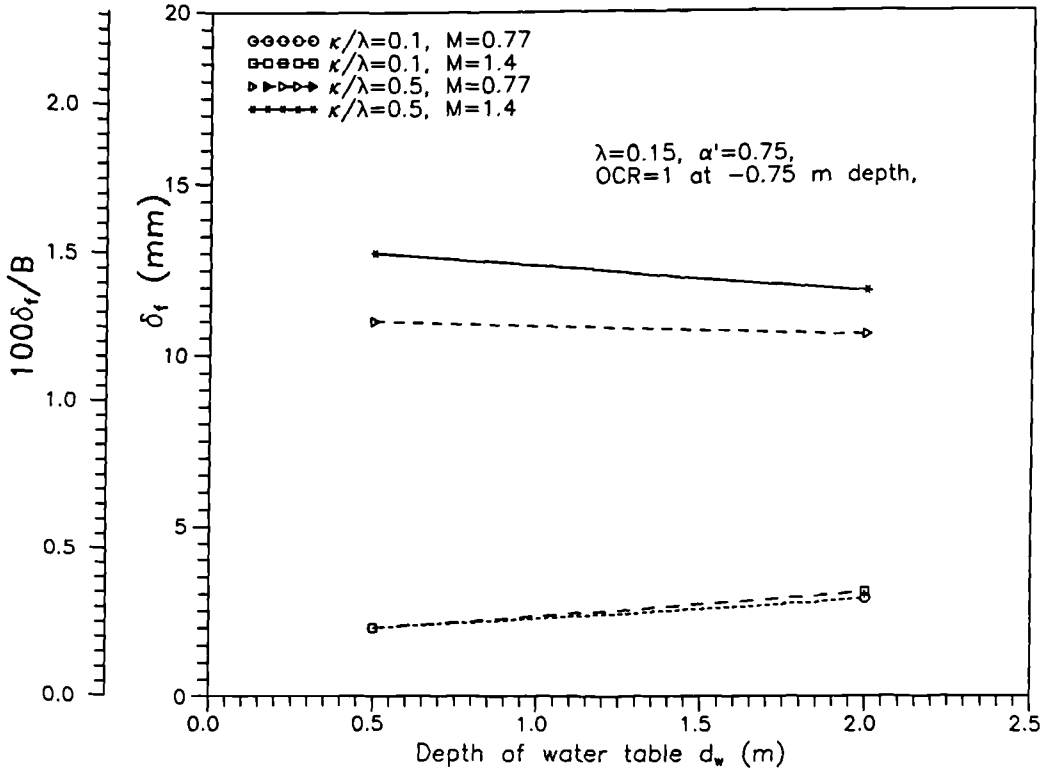

Figure 7.25 Variations of settlement δ_f and settlement ratio $100\delta_f/B$ at failure with depth of water table d_w for fixed values of λ, κ/λ, M and α'

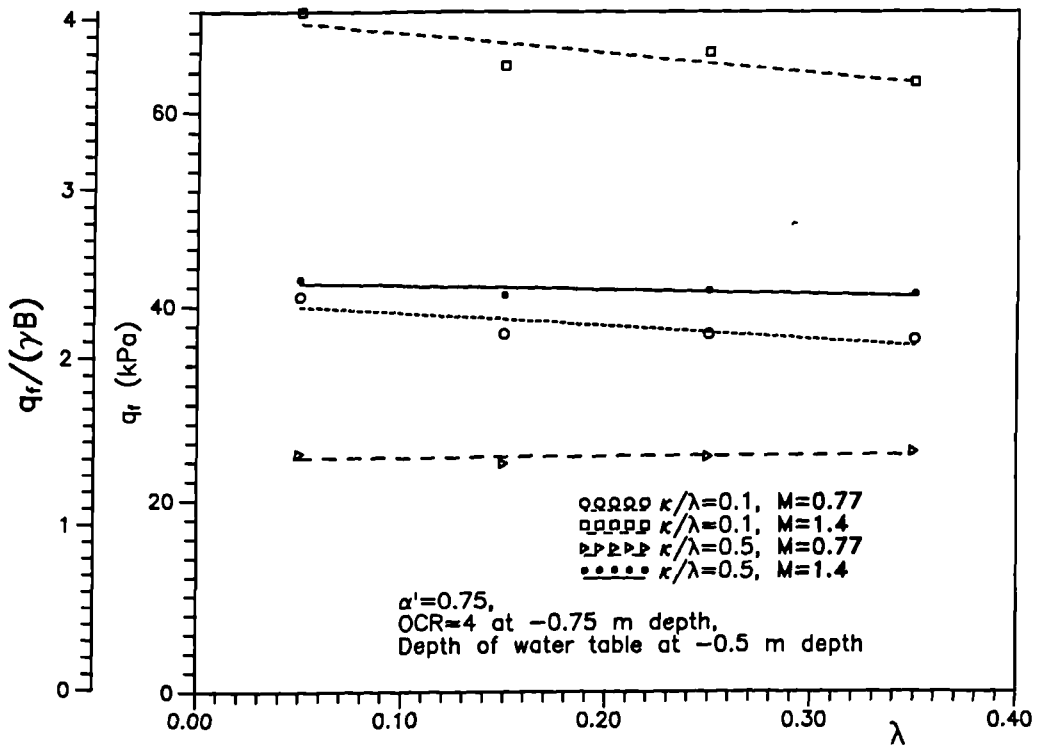

Figure 7.26 Variations of bearing pressure q_f and normalised bearing pressure $q_f/(\gamma B)$ at failure with λ for fixed values of κ/λ, M and α'

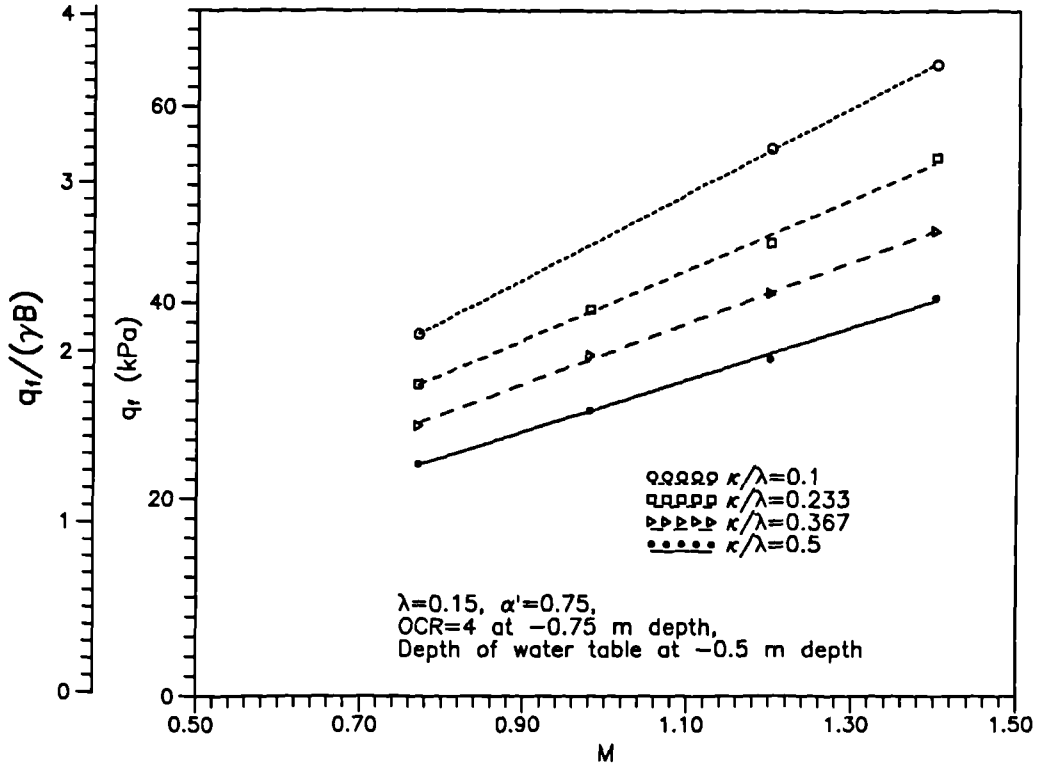

Figure 7.27 Variations of bearing pressure q_f and normalised bearing pressure $q_f/(\gamma B)$ at failure with M for fixed values of λ, κ/λ and α'

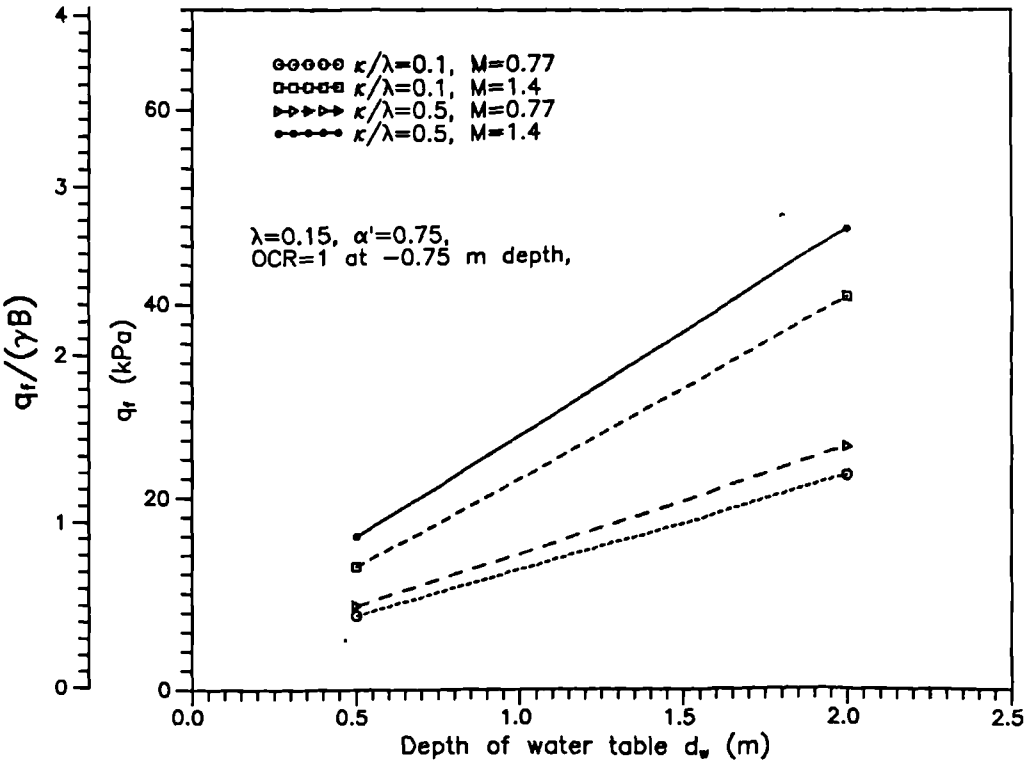

Figure 7.28 Variations of bearing pressure q_f and normalised bearing pressure $q_f/(\gamma B)$ at failure with depth of water table d_w for fixed values of λ, κ/λ, M and α'

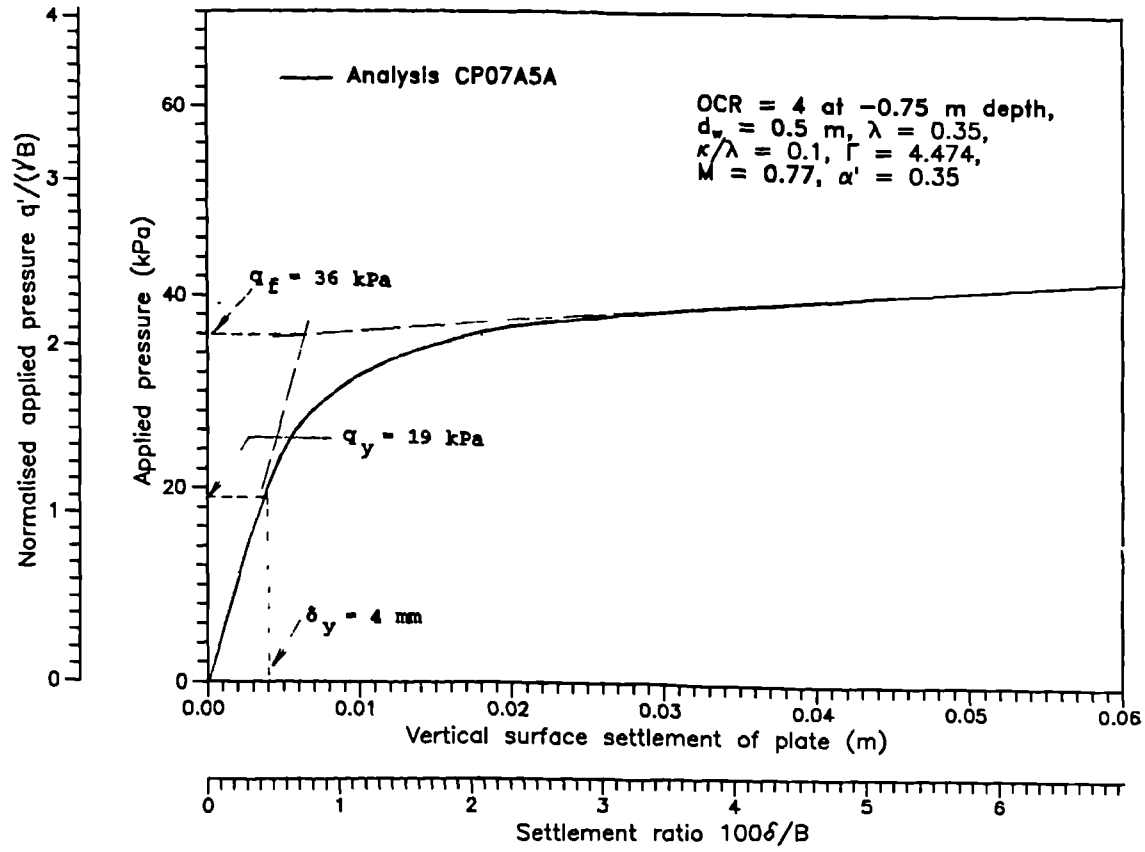

Figure 7.29 Pressure–settlement curve for the plate loading analysis CP07A5A

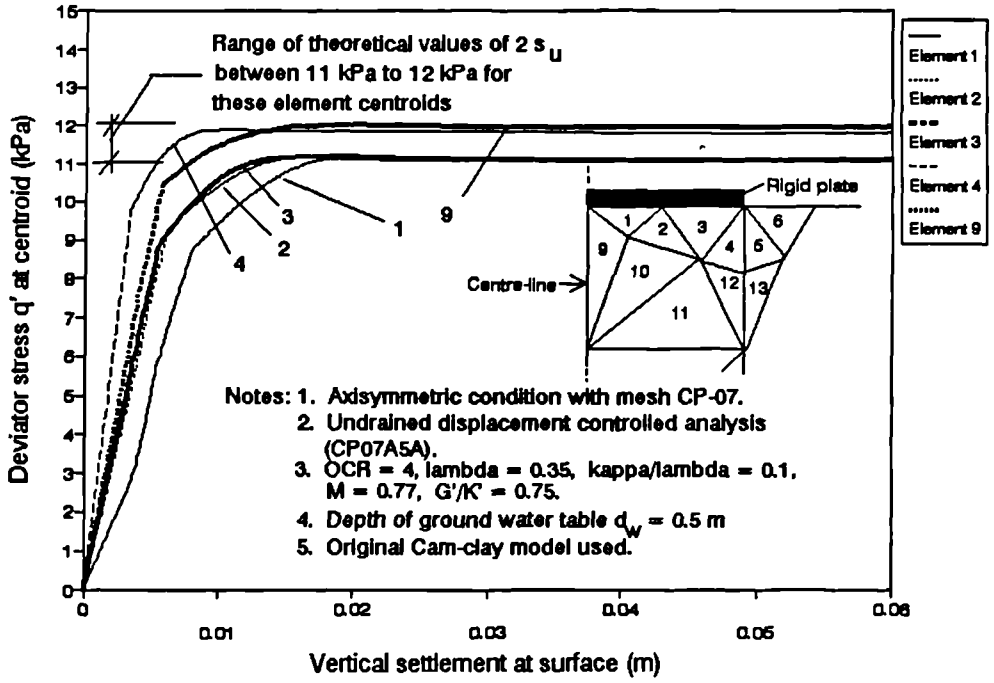

Figure 7.30 Deviator stress at element centroids versus vertical ground surface settlement (Analysis CP07A5A)

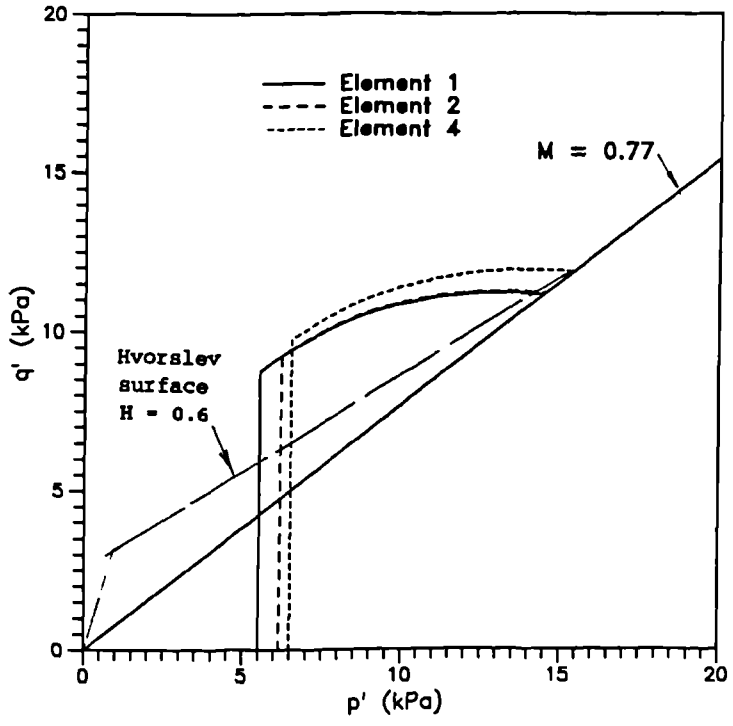

Figure 7.31 Effective stress paths in p':q' space for centroids of elements 1, 2 and 4 (Analysis CP07A5A)

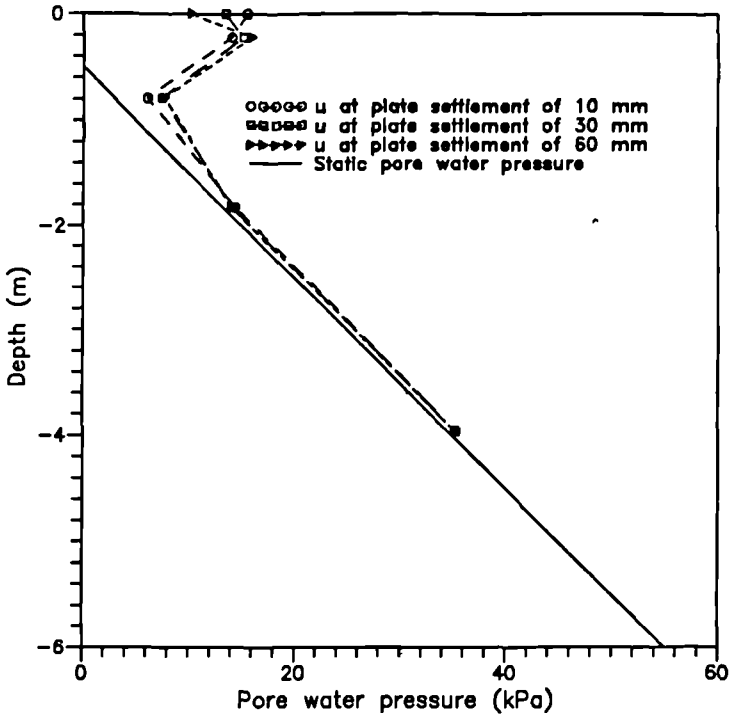

Figure 7.32 Pore pressure distribution with depth near centre-line at plate settlements of 10 mm, 30 mm and 60 mm - (Analysis CP07A5A)

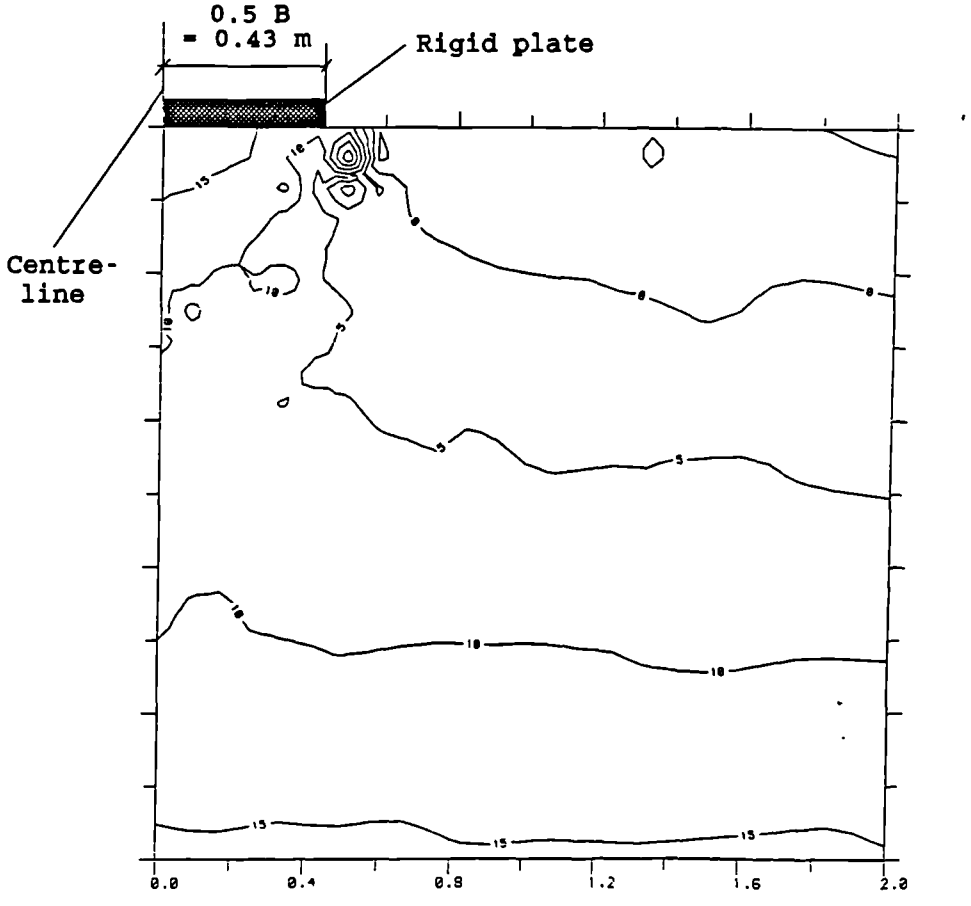

Figure 7.33 Pore pressure contours (in kPa) within a 2 m square cross-section under the plate at a settlement of 10 mm (Analysis CP07A5A)

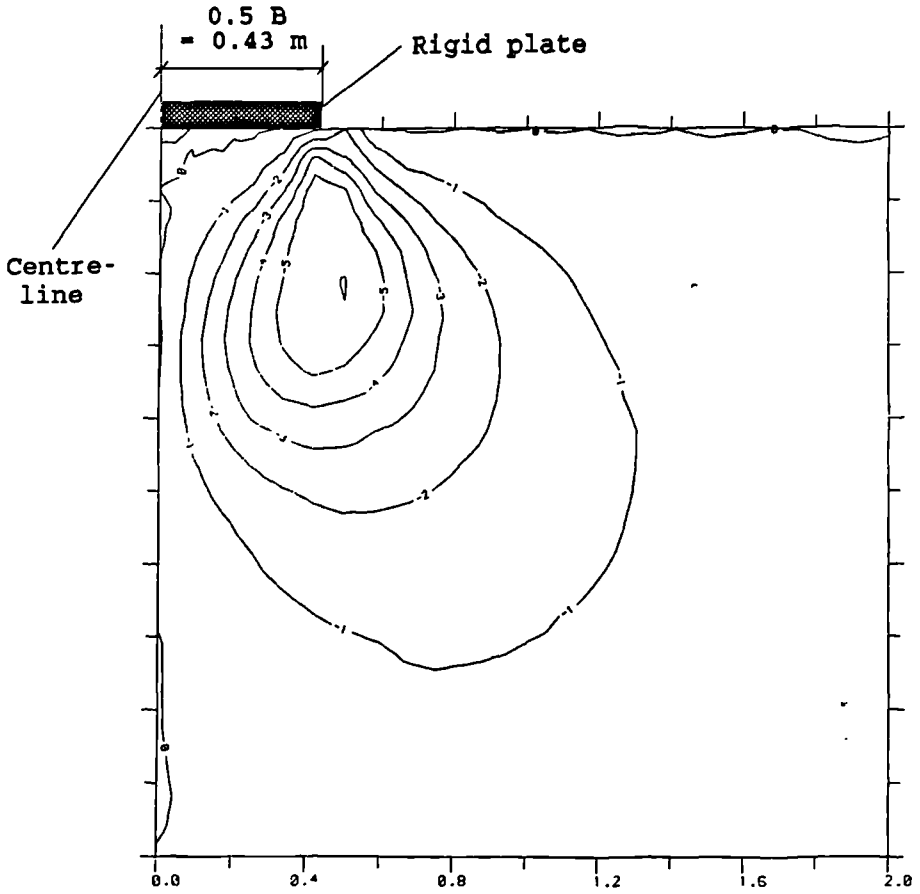

Figure 7.34 Shear stress contours (in kPa) within a 2 m square cross-section under the plate at a settlement of 10 mm (Analysis CP07A5A)

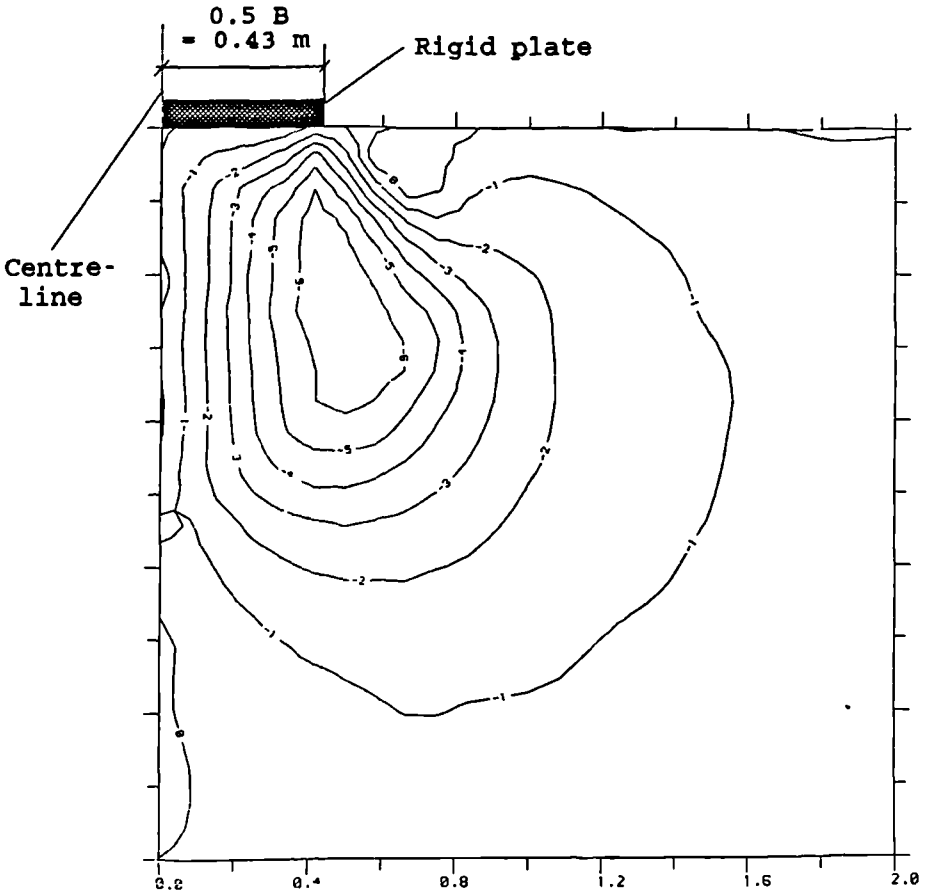

Figure 7.35 Shear stress contours (in kPa) within a 2 m square cross-section under the plate at a settlement of 30 mm (Analysis CP07A5A)

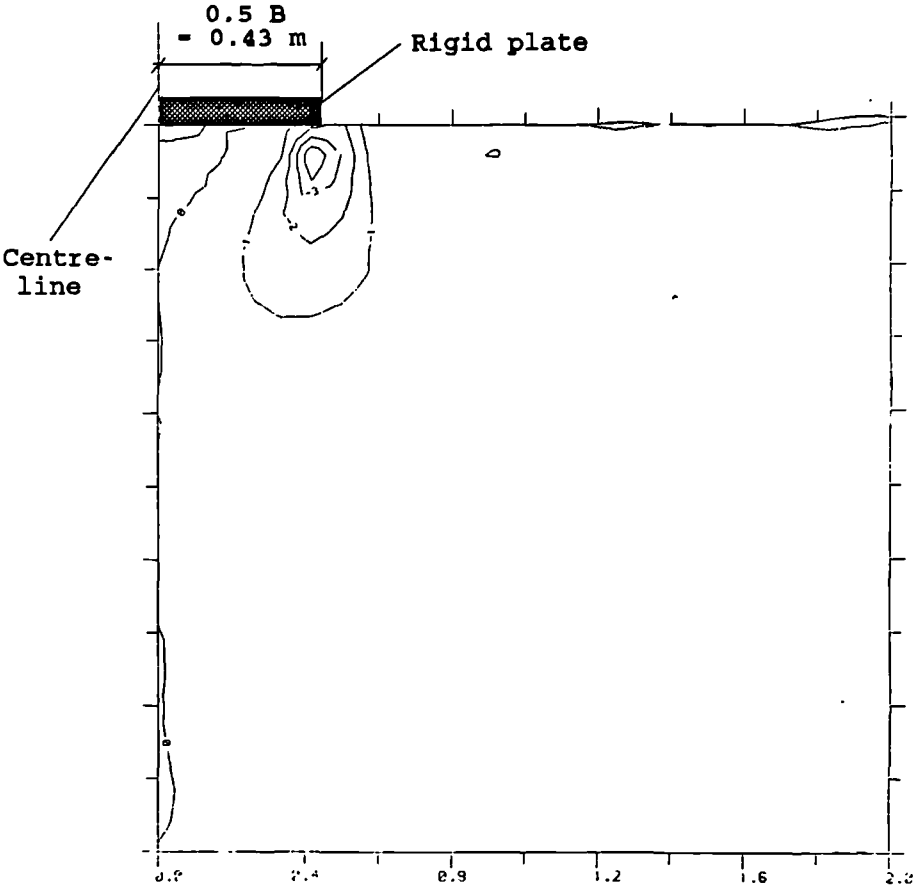

Figure 7.36 Shear strain contours (in %) within a 2 m square cross-section under the plate at a settlement of 10 mm (Analysis CP07A5A)

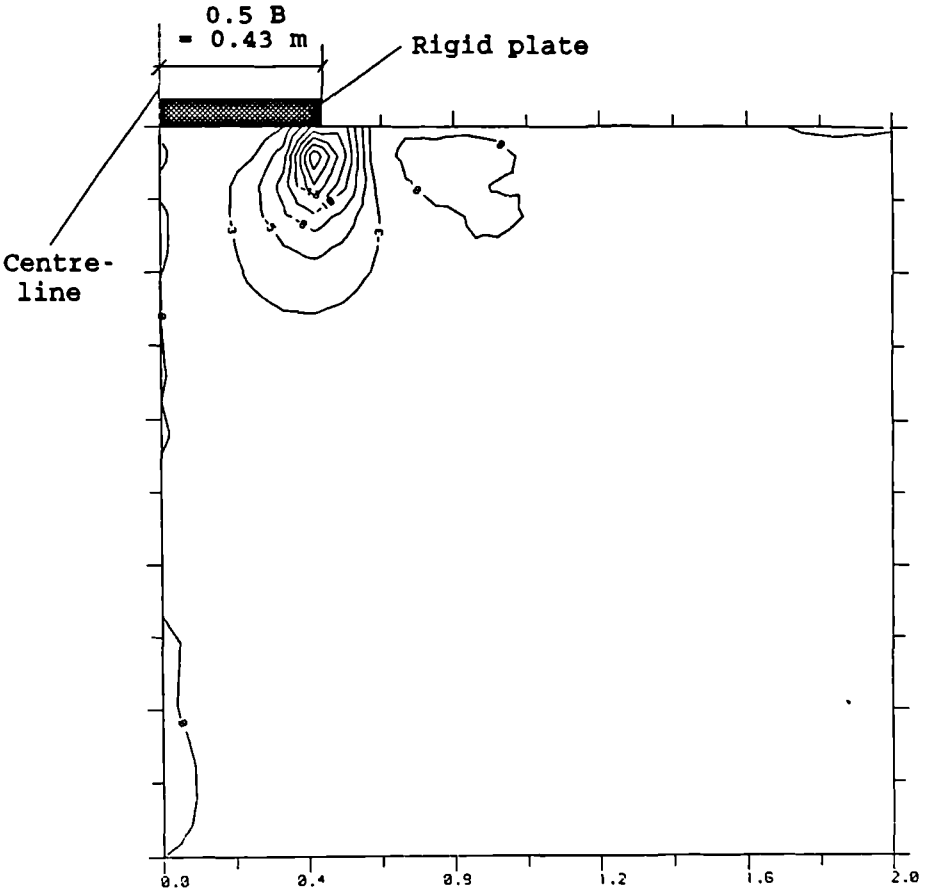

Figure 7.37 Shear strain contours (in %) within a 2 m square cross-section under the plate at a settlement of 30 mm (Analysis CP07A5A)

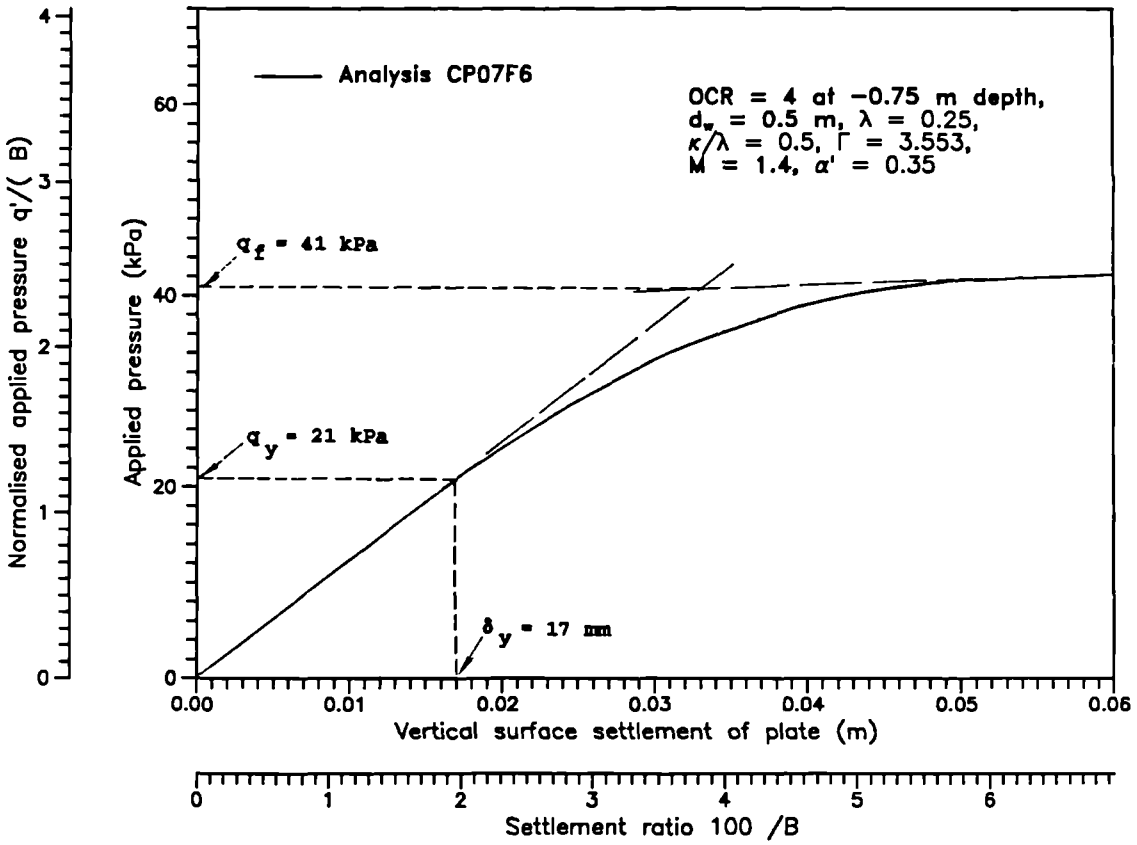

Figure 7.38 Pressure–settlement curve for the plate loading analysis CP07F6

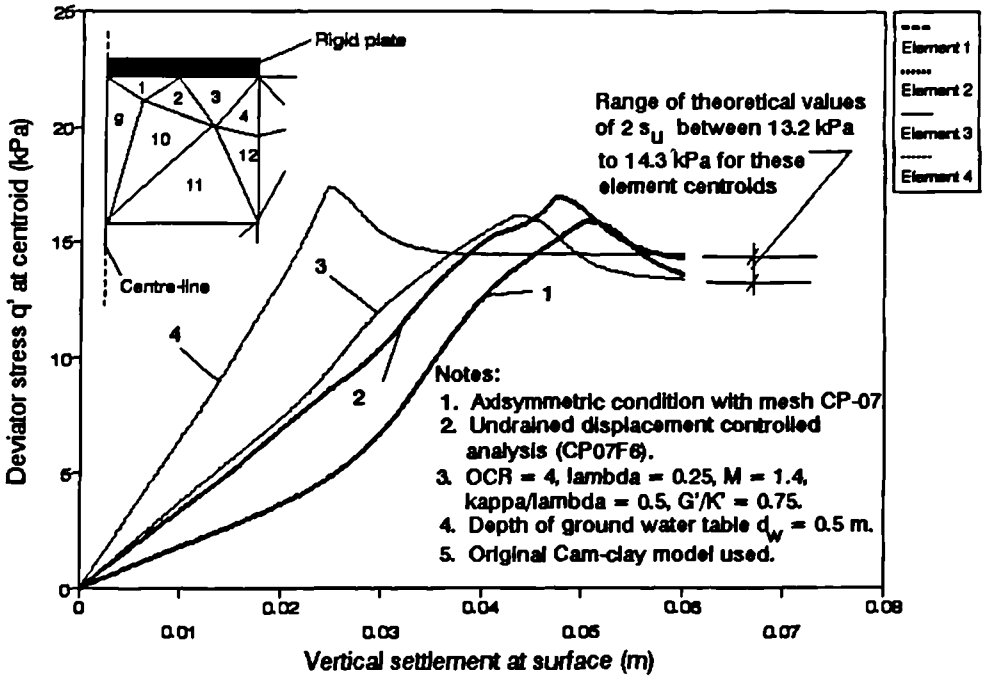

Figure 7.39 Deviator stress at element centroids versus vertical ground surface settlement (Analysis CP07F6)

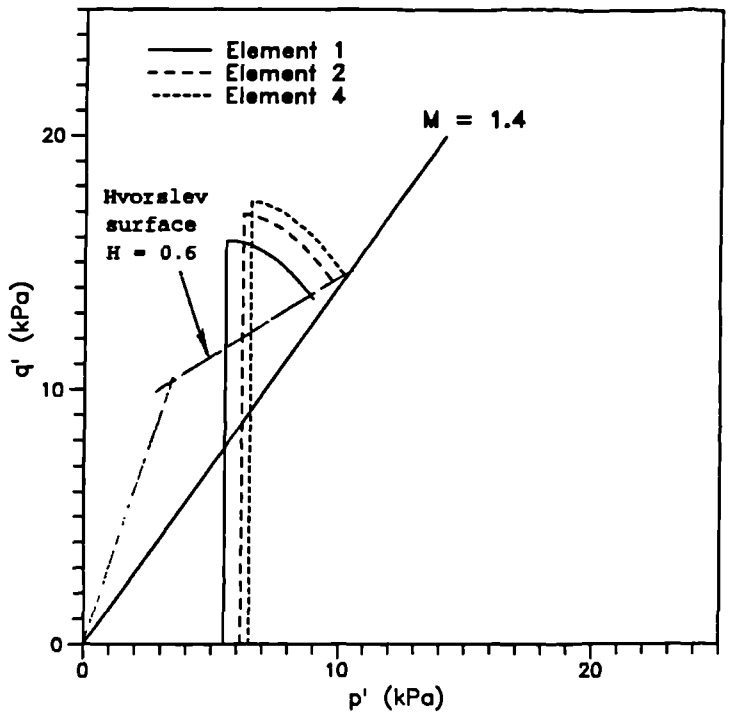

Figure 7.40 Effective stress paths in p':q' space for centroids of elements 1, 2 and 4 (Analysis CP07F6)